Ionization of Molecular Hydrogen in Ultrashort Intense Laser Pulses

DISSERTATION

zur Erlangung des akademischen Grades

Dr. Rer. Nat.
im Fach Physik

eingereicht an der
Mathematisch-Wissenschaftlichen Fakultät I
Humboldt-Universität zu Berlin

von
Dipl.-Phys. Yulian V. Vanne
geboren am 18.12.1979 in Kritschew, Belarus

Präsident der Humboldt-Universität zu Berlin:
Prof. Dr. Dr. h.c. Christoph Markschies

Dekan der Mathematisch-Wissenschaftlichen Fakultät I:
Prof. Dr. Lutz-Helmut Schön

Gutachter:
1. P.D. Dr. Alejandro Saenz
2. Dr. Wilhelm Becker
3. Prof. Dr. Eva Lindroth

eingereicht am: 08.12.2009
Tag der mündlichen Prüfung: 18.03.2010

Dedication

To my wife, Aliona, and my daughter, Nicole.

Abstract

A novel *ab initio* numerical approach is developed and applied that solves the time-dependent Schrödinger equation describing two-electron diatomic molecules (e.g. molecular hydrogen) exposed to an intense ultrashort laser pulse. The method is based on the fixed-nuclei and the non-relativistic dipole approximations and aims to accurately describe both correlated electrons in full dimensionality. The method is applicable for a wide range of the laser pulse parameters and is able to describe both few-photon and many-photon single ionization processes, also in a non-perturbative regime. A key advantage of the method is its ability to treat the strong-field response of the molecules with arbitrary orientation of the molecular axis with respect to the linear-polarized laser field. Thus, this work reports on the first successful orientation-dependent analysis of the multiphoton ionization of H_2 performed by means of a full-dimensional numerical treatment. Besides the investigation of few-photon regime, an extensive numerical study of the ionization by ultrashort frequency-doubled Ti:sapphire laser pulses (400 nm) is presented. Performing a series of calculations for different internuclear separations, the total ionization yields of H_2 and D_2 in their ground vibrational states are obtained for both parallel and perpendicular orientations. A series of calculations for 800 nm laser pulses are used to test a popular simple interference model.

Besides the discussion of the *ab initio* numerical method, this work considers different aspects related to the application of the strong-field approximation (SFA) for investigation of a strong-field response of an atomic and molecular system. Thus, a deep analysis of the gauge problem of SFA is performed and the quasistatic limit of the velocity-gauge SFA ionization rates is derived. The applications of the length-gauge SFA are examined and a recently proposed generalized Keldysh theory is criticized.

Zusammenfassung

Ein neuer numerischer *ab initio* Ansatz wurde entwickelt und zur Lösung der zeitabhängigen Schrödingergleichung für zweiatomig Moleküle mit zwei Elektronen (z.B. molekularer Wasserstoff), welche einem intensiven kurzen Laserpuls ausgesetzt sind, angewandt. Die Methode basiert auf der Näherung fester Kernabstände und der nicht-relativistischen Dipolnäherung und beabsichtigt die genaue Beschreibung der beiden korrelierten Elektronen in voller Dimensionalität. Die Methode ist anwendbar für eine große Bandbreite von Laserpulsparamtern und ist in der Lage, Einfachionisationsprozesse sowohl mit wenigen als auch mit vielen Photonen zu beschreiben, sogar im nicht-störungstheoretischen Bereich. Ein entscheidender Vorteil der Methode ist ihre Fähigkeit, die Reaktion von Molekülen mit beliebiger Orientierung der molekularen Achse im Bezug auf das linear polarisierte Laserfeld in starken Feldern zu beschreiben. Dementsprechend berichtet diese Arbeit von der ersten erfolgreichen orientierungsabhängigen Analyse der Multiphotonenionisation von H_2, welche mit Hilfe einer numerischen Behandlung in voller Dimensionalität durchgeführt wurde. Neben der Erforschung des Bereichs weniger Photonen wurde eine ausführliche numerische Untersuchung der Ionisation durch ultrakurze frequenzverdoppelte Titan:Saphir-Laserpulse (400 nm) präsentiert. Mit Hilfe einer Serie von Rechnungen für verschiedene Kernabstände wurden die totalen Ionisationsausbeuten für H_2 und D_2 in ihren Vibrationsgrundzuständen sowohl für parallele als auch für senkrechte Ausrichtung erhalten. Eine weitere Serie von Rechnungen für 800 nm Laserpulse wurde benutzt, um ein weitverbreitetes einfaches Interferenzmodel zu falsifizieren.

Neben der Diskussion der numerischen *ab initio* Methode werden in dieser Arbeit verschiedene Aspekte im Bezug auf die Anwendung der Starkfeldnäherung [Englisch Strong-Field Approximation (SFA)] für die Erforschung der Reaktion eines atomaren oder molekularen Systems auf ein intensives Laserfeld betrachtet. In diesem Kontext wurde eine tiefgehende Analyse des Eichproblems der SFA durchgeführt und der quasistatische Limes der SFA-Ionisationsraten in Geschwindigkeitseichung hergeleitet. Die Anwendungen der SFA in Längeneichung wurden untersucht und es wurde ein Fehler in einer kürzlich vorgeschlagenen, verallgemeinerten Keldysh-Theorie aufgedeckt.

Contents

II. Investigation of ionization process 65

Introduction

In the past two decades, the technology of ultra-short pulsed lasers has advanced enormously. The discovery of Kerr-lens mode locking in novel solid-state gain media (various host crystals, e.g. sapphire, doped with transition-metal ions, e.g. titanium) with enormous bandwidths on the order of 100 THz, followed by the technological advances in precision broadband dispersion control (e.g. by chirped multilayer mirrors) culminated in the generation of intense ultrashort pulses with durations approaching the light oscillation period [1, 2]. Generation of octave-spanning optical frequency combs by means of photonic crystal fiber or directly from the laser oscillator has revolutionized the art of counting the frequency of light [3]. Moreover, by means of a so-called f-to-$2f$ interferometer and feedback loops exploited for stabilizing the frequency comb it became possible to yield intense few-cycle pulses with stabilized carrier-envelope (CE) phase [4]. Meanwhile, new techniques for CE-phase stabilization directly in the usable laser output have pushed the degree of stabilization of the CE phase to the level of accuracy of its measurement [5]. The pulse train consisting of pulses with constant (but unknown) CE phase can further be used for measurement of CE phase exploiting various phase-sensitive phenomena. Most promising technique is the so-called stereo-ATI method that is based on simultaneous detection of energy distribution of backscattered electrons ejected in two opposite directions along the laser polarization [6]. Although typically such measurements are made by averaging over a large number of phase-stabilized laser pulses, very recent experiment has demonstrated the possibility of a single-shot CE phase measurement [7]. Thus, the complete control and characterization of light waveform enable the in-depth study of ultrafast electronic processes in light-matter interactions. Using phenomenon known as high harmonic generation (HHG), i.e. generation of extreme ultraviolet light by recombination of ionized electrons [8], and a variety of clever techniques to compensate a frequency chirp appeared during recombination of electrons, the researches were able to generate sub-100-as pulses [9].

Development of sources of ever shorter light flashes and techniques for their measurement has driven the progress in time-resolved measurements. It permitted the initiation and recording of snapshots of chemical reactions with femtosecond time resolution and paved the way to the birth of real-time laser femtochemistry [10]. Femtosecond laser pulses has been successfully used for real-time observation of the breakage of chemical bonds, and revealing details about the intermediate products that form during chemical reactions, which cannot be deduced from observing the starting and end products. Combining a time-resolved measurement with photoelectron spectroscopy resulted in time-resolved photoelectron spectroscopy (TRPES), which is capable to provide a deeper insight into dynamical processes occurring in molecules [11]. The measurement of photoelectron distributions can be detected not only as a function of time and energy, but also as a function of angular variables [12]. This measurement, however, is usually made in the laboratory frame, where averaging over the random orientations of the molecule generally leads to a loss of information. One way to circumvent this problem is to pre-align the molecule before studying, e.g. by means of intense laser field [13]. A more general approach is time-resolved coincidence imaging spectroscopy (TRCIS), which measures fully correlated photofragment and photoelectron recoil distributions as a function of time, thereby permitting dynamical observations from the molecule's point of view [14].

Besides a direct investigation of molecule by its ionization, the imaging of molecular structure was performed also by means of the strong-field induced high-harmonic radiation [15] or the electrons ejected in the ionization process [16]. These successful pioneering experiments have driven the development of various imaging techniques that aim for the time-resolved imaging of changes of the electronic structure during chemical reactions. A prerequisite for the success of these techniques is a full understanding of the influence of the molecular structure on the strong-field response what still remains an outstanding goal.

Molecular hydrogen (and its heavier isotope, deuterium) being the simplest neutral stable molecule can be used as a test system for verifying our knowledge of the molecular strong-field response. Whereas the other molecular systems require some approximative treatment like strong-field approximation (SFA) based additionally on the single-active electron approximation (SAE) [17–20] or an effective independent-particle model like the time-dependent density-functional theory (TD-DFT) [21], molecular hydrogen is the perfect candidate to go beyond these approximations. Only recently *ab initio* calculations for H_2 exposed to strong fields became available in which both electrons are treated in full dimensionality. This includes calculations of the ionization and dissociation behavior of H_2 exposed to an intense static or quasi-static electric field [22–27] which revealed the possible occurrence of bond softening and enhanced ionization in *neutral* H_2 due to a field-induced avoided crossing of the neutral ground state with the ion-pair state

H^+H^-. Shortly thereafter, a full time-dependent calculation confirmed this finding [28–30]. These latter calculations were based on a judiciously chosen grid on which the electronic wavefunctions were expanded. In a different approach the electronic wavepacket is expanded in terms of field-free eigenstates of H_2 using a one-center expansion for the electronic orbitals [31]. All these works did, however, only consider a parallel orientation of the linear polarized laser field and the molecular axis. The reason is rather simple: in this case the problem of 6 spatial dimensions describing two electrons moving in the field of the laser and the two nuclei reduces effectively to a 5-dimensional one, because the quantum number of angular momentum along the molecular axis, M, is conserved or, equivalently, the cylindrical symmetry of H_2 is not broken by the electromagnetic field.

The achievements reached by this dissertation are threefold. First, the present work has developed a new molecular *ab initio* method employing the prolate spheroidal coordinate system, B-spline basis set, and configuration interaction (CI) approach. The method has been purposely developed to overcome limitations of existing techniques when describing diatomic molecules or atom-atom collisions. Although its current implementation is limited to two-electron diatomics, the numerical treatment of alkali diatomics is also possible by means of a proper model potential describing the interaction of ionic core and valence electron. The main advantage of the present method is the ability to calculate both electronic bound states and continuum of diatomics for the whole range of interatomic separations. Owing to the high precision of the method, considerable advances have been made in understanding of the collisional properties of metastable hydrogen atoms [32, 33].

Second, the present dissertation has developed and applied a tool for numerical solution of the time-dependent Schrödinger equation (TDSE) describing molecular hydrogen exposed to ultrashort laser pulses. For the first time, the orientation-dependent analysis has been performed based on a non-perturbative treatment where all six spatial dimensions of the two correlated electrons are explicitly considered [34, 35]. This study is of great importance for interpretation of a series of recent experiments where orientational dependence of ionization [36–38] or angular distribution of ejected electrons [39] was recently experimentally investigated. It also represents a substantial advancement in the field of time-resolved imaging of electron dynamics, since the orientation-dependent analysis is a key issue for imaging to work. Thus, the energy-resolved electron spectra extracted from the TDSE calculation were used to check the validity of a simple interference picture predicted by the molecular SFA formulated in the velocity gauge. Besides, the obtained two-electron results have made it possible to numerically check the validity of SAE, as well as other simplified models like the molecular Ammosov-Delone-Krainov tunneling model [40]. Undoubtedly, the tool will be in a good demand also in the future providing the results serving as benchmarks for other theoretical approaches and simplified models.

Finally, a considerable contribution to the field of laser-matter interaction has been made by investigation of different aspects of the SFA. Thus, a clear argumentation has been provided against the existing statement that the residue theorem can be used for calculation of the transition amplitude in the length gauge SFA in order to avoid the necessity of applying the saddle-point approximation [41]. In addition, the quasistatic limit of the velocity-gauge SFA describing the total ionization rate of atomic and molecular systems exposed to linearly polarized laser fields is derived [42]. It has been shown for the first time, that in contrast to the previous belief, the velocity-gauge SFA yields an ionization rate which is proportional to the laser frequency, if a Coulombic long-range interaction is present. Finally, the gauge problem in the SFA has been investigated by introducing a generalized gauge and partitioning of the Hamiltonian. It has been demonstrated that the S-matrix expansion obtained in the SFA depends on both gauge and partitioning in such a way that two gauges always yield the same S-matrix expansion, if the partitioning is properly chosen [43].

The thesis is organized as followed. The first part of the thesis deals with electronic structure calculations. Chapter 1 describes B-spline basis set and briefly discusses how this basis set is used to solve the stationary Schrödinger equation. Furthermore, the properties of the discretized continuum are considered and the basic aspects of the convergence behavior with respect to B-spline parameters are demonstrated. Chapter 2 introduces the two-center B-spline based CI method, where the calculation of ionic molecular orbitals is followed by their subsequent use in constructing symmetry-adapted configurations and implementation of CI approach. Chapter 3 provides a discussion of different configuration-selection schemes and their influence on computed electronic bound states. Besides, the CI method is applied for calculation of single-photon ionization cross section and the numerical investigation of the doubly excited states of H_2 converging to the $\mathrm{H}(n{=}2) + \mathrm{H}(n'{=}2)$ limit.

The second part of the thesis is devoted to the treatment of atomic and molecular ionization in intense, ultra-short laser fields. Chapter 4 reviews the main advances in understanding of ionization mechanisms, discusses gauge invariance and introduces the concept of a generalized field-free Hamiltonian. Chapter 5 gives a brief account of results obtained by the investigation of different aspects of the strong-field approximation.

Chapter 6 demonstrates the influence of laser parameters of the ionization response of the H atom, discusses the AC Stark shift of atomic states and compares the results obtained by different approaches. Chapter 7 introduces the TDSE method for H_2, gives a detailed account of used basis set parameters and discusses the orientational dependence of ionization in different regimes. Finally, main conclusions are summarized and an outlook for future research is presented. Atomic units are used in this work unless otherwise specified.

Part I.

Electronic structure calculation

1. *B*-spline basis set

B splines are the main building stones of the approach used in the present thesis. This chapter gives a brief introduction to what is meant by *B* splines and how they are used to solve a physical problem. Since convergence and accuracy are important issues when discussing a numerical approach, main features of reaching converged results with *B* splines are demonstrated by means of simple applications. Also, properties of a discretized continuum emerged from the box boundary conditions are discussed in detail.

1.1. *B* splines in physics

The Schrödinger equation which is the main equation in atomic, molecular and optical (AMO) physics can be solved analytically only in a few cases. In order to solve most of the occurring problems one must resort to approximation methods. Their development started just after the quantum mechanics was established and it still continues nowadays. Such techniques as the perturbation theory and variational methods allow to bridge a real physical problem to a simpler, exactly solvable one. Among other implementations of the variational principle, the usage of "unphysical" basis sets [1] has become one of the most popular implementations with the development of electronic computers. The Rayleigh-Ritz-Galerkin method allows to transform the solution of a differential equation into an algebraic eigenvalue problem, which then can be very efficiently solved using modern linear algebra packages. Numerous types of basis sets have been tested in the past but they can be classified into two groups, *local* and *global* basis sets. While the *global* basis functions, such as Slater type orbitals (STO) or Gaussians, are spread over the entire space domain, the *local* basis functions are non-zero only in a small part of the space domain. If these functions are piecewise polynomial, they are called *finite elements* or *splines*. It is commonly accepted that the first mathematical reference to splines is the 1946 paper by Schoenberg [44], which is probably the first place where the word "spline" is

---

[1] This term is used to distinguish from those basis sets, whose basis functions are defined as solutions of an unperturbed Hamiltonian

used in connection with smooth, piecewise polynomial approximation. Splines of various types have been used in numerical analysis for a long time, e.g. cardinal splines, Bézier splines, Hermite splines. All of them are L^2 integrable functions defined in a restricted space usually referred to as a box. In the box, a knot sequence is defined and the freedom to define the knots to suit the particular problem is one of the important advantages of the method. Every kind of splines is characterized by its degree, smoothness, and knot sequence and can be represented as a linear combination of basis splines, in short *B splines*. A B-spline basis is the most compact (local) spline basis (i.e. for a given degree, smoothness, and knot sequence its basis functions are non-zero on the shortest intervals compared to other spline basis sets) and B splines are positive defined functions. These two important properties are of great advantage in matrix calculations, since resulting matrices are sparse (often banded) and easier to diagonalize.

The application of B splines to atomic physics started in the 1970s and was strengthened by the publication of the monograph by de Boor [45] containing also FORTRAN routines that make it possible to define and manipulate B splines of arbitrary order (degree of the involved polynomials plus one) and knot sequences. The extension of B splines to higher orders became straightforward and allowed to obtain a competitive degree of accuracy in the solution of the Schödinger equation. B splines have been applied to calculate orbitals for subsequent many-body perturbation theory (MBPT) and configuration interaction (CI) calculations of electronic structure. In 1992, B-spline basis sets were used for the first time to describe the electronic states of H_2^+ and HeH_2^+ molecular systems [46]. Among other advantages, B splines are able to provide a very accurate representation of continuum states, which makes them superior to more conventional L^2 basis sets. This property is important for calculation of dynamic properties and led to success in description of such effects as multiphoton excitation, above-threshold ionization and high-order harmonic generation. An extensive review [47] on the use of B splines in atomic and molecular physics contains more than five hundred references to different applications employing them.

1.2. Definition of *B* splines

A complete description of B splines and their properties can be found in [45]. Being a very flexible mathematical object, B splines have a quite extensive general definition, therefore, only the minimum required for understanding of their use in physical applications is given below.

To visualize B splines and their properties, consider a one-dimensional space specified by a coordinate x. To define a B-spline basis set over an interval (box) $I = [a, b]$ with endpoints $x = a$ and $x = b$, the following characteristics must be specified.

- One of the main characteristics is the choice of $s-1$ interior points which divide the interval I into s subintervals and construct, together with endpoints, the sequence of $s + 1$ strict ascending points called *breakpoints*. For example, division of an interval [0,8] into $s = 8$ equal subintervals (spans) results in the following sequence of breakpoints $\{0, 1, 2, 3, 4, 5, 6, 7, 8\}$.

- The second characteristic is the order k of B splines determining the order (maximum degree $k - 1$) of polynomial pieces,

  $$p(x) = a_{k-1}x^{k-1} + \cdots + a_1 x + a_0$$

  which the B splines are composed of.

- Finally, the last characteristic is the order of continuity at the breakpoints. This is achieved by construction of another sequence of points $\{x_i\}$ called *knots*. With every breakpoint is associated one or more knots, where multiplicity of the knots at the breakpoint determines the continuity as follows. The unity corresponds to maximum continuity for given order k of B splines, that is C^{k-2} (a function is continuous together with its derivatives up to order $k - 2$). Higher multiplicity μ reduces the continuity to $C^{k-1-\mu}$, and a function becomes discontinuous for the multiplicity $\mu = k$. The most standard way employed throughout present work is to use the multiplicity μ equal to k for the endpoints and equal to unity for all interior breakpoints. With this choice the number of knots is equal to $s + 2k - 1$. For the given example and $k = 4$ the obtained knot sequence $\{x_i\} = \{0, 0, 0, 0, 1, 2, 3, 4, 5, 6, 7, 8, 8, 8, 8\}$ contains 15 knots.

To support n B splines of order k the number of knots in the knot sequence must be equal to $n + k$. With the discussed choice of continuity conditions, the number of B splines is thus given by

$$n = s + k - 1. \tag{1.1}$$

A full set consisting of 11 B splines is shown in Fig. 1.1. The following important properties are apparent:

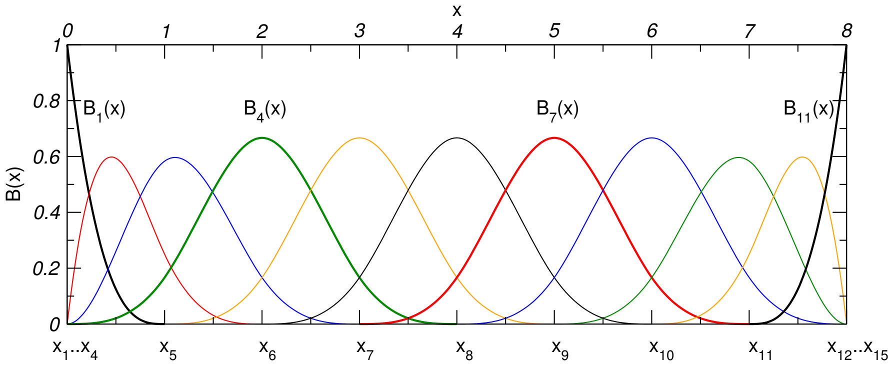

Figure 1.1.: Full set of 11 B splines of order $k = 4$ defined for the knot sequence $\{x_i\} = \{0, 0, 0, 0, 1, 2, 3, 4, 5, 6, 7, 8, 8, 8, 8\}$.

- Every B spline is non-zero over maximum k spans,

$$B_i(x) \neq 0 \quad \text{for} \quad x \in (x_i, x_{i+k}).$$

- Over each span (x_i, x_{i+1}) exactly k B splines are non-zero,

$$B_j(x) \neq 0 \quad \text{for} \quad j = i - k + 1, \ldots, i$$

- Every B spline overlaps only with a limited number of other B splines,

$$B_i(x) \cdot B_j(x) = 0 \quad \text{for} \quad |i - j| \geqslant k$$

- B-spline basis sets are normalized,

$$\sum_i B_i(x) = 1 \quad \text{for} \quad x \in [a, b]$$

- For simple equidistant breakpoints all B splines $B_i(x), k - 1 < i < n - k$ are just translations of each other by one or more spans. (For example, in Fig. 1.1 the B spline $B_7(x)$ is just a translation of $B_4(x)$).

Sets of polynomial coefficients $\{a_i\}$ differ for different B splines and different spans. They can be found using a recursion relation [47], although this is rarely needed. For example, the explicit representation of $B_1(x)$ shown in Fig. 1.1 reads

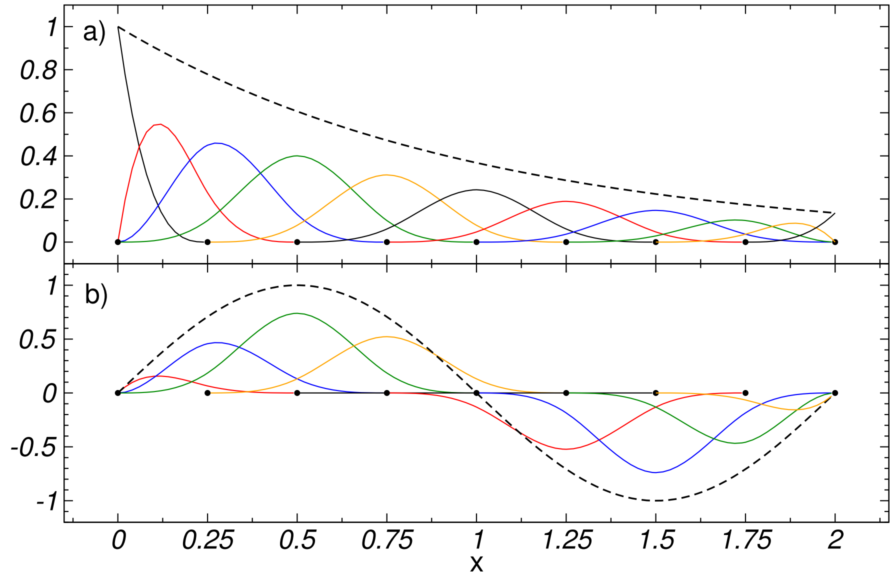

Figure 1.2.: Expansion of (a) $\exp(-x)$ and (b) $\sin(\pi x)$ functions (dashed curves) in the B-spline basis ($k = 4$, $s = 8$, linear breakpoint sequence on $I = [0, 2]$). Solid curves show contributions of every B spline.

$$B_1(x) = \begin{cases} -x^3 + 3x^2 - 3x + 1 & 0 \leqslant x < 1 \\ 0 & \text{otherwise} \end{cases}, \tag{1.2}$$

whereas the explicit representation of $B_4(x)$ is given by

$$B_4(x) = \begin{cases} x^3/6 & 0 \leqslant x < 1 \\ -x^3/2 + 2x^2 - 2x + 2/3 & 1 \leqslant x < 2 \\ x^3/2 - 4x^2 + 10x - 22/3 & 2 \leqslant x < 3 \\ -x^3/6 + 2x^2 - 8x + 32/3 & 3 \leqslant x < 4 \\ 0 & \text{otherwise} \end{cases}. \tag{1.3}$$

It is easy to verify that B spline $B_4(x)$ is continuous with its first two derivatives at $x = 1$. Indeed, their limits from both sides are equal,

$$B_4(1^-) = B_4(1^+) = 1/6, \quad B_4'(1^-) = B_4'(1^+) = 1/2, \quad B_4''(1^-) = B_4''(1^+) = 1,$$

whereas the third derivative is discontinuous,

$$B_4'''(1^-) = 1, \qquad B_4'''(1^+) = -3.$$

Due to the locality and continuity of B splines, functions with different qualitative behavior (e.g., oscillating and exponentially decaying functions) can be accurately represented with the same B-spline basis, as demonstrated in Fig. 1.2. The sum of contributions of all B splines is visually indistinguishable from the function, projected onto the B-spline basis. The figure demonstrates also another important feature of B splines, namely, that there are no large cancellations between contributions of the various B splines. This is not the case for basis sets employing global basis functions, where the cancellations can be extremely large and may result in numerical instability.

1.3. Solving the Schrödinger equation with *B* splines

1.3.1. Solving the single-electron Schrödinger equation

To demonstrate basic aspects of B-splines based techniques, consider an application of B splines for solving the reduced Schrödinger equation determining eigenstates of a single-electron atom,

$$\left[-\frac{d^2}{2dr^2} + \frac{l(l+1)}{2r^2} + V(r)\right]\psi_{El}(r) = E\psi_{El}(r) \quad , \tag{1.4}$$

where the boundary condition $\psi_{El}(r=0) = 0$ is imposed. For the sake of simplicity, the potential $V(r)$ is supposed to vanish at $r \to \infty$.

Specifying the box $[0, r_{\max}]$, the order k_r of B-splines, and knot sequence $\{r_i\}$, the basis set is constructed consisting of n_r B splines. Any solution of (1.4) is then approximated by the linear combination

$$\psi_{El}(r) = \sum_{\alpha=1}^{n_r} C_\alpha^{El} B_\alpha(r) \quad . \tag{1.5}$$

Since only $B_1(0) \neq 0$, the boundary condition is fulfilled by requiring that $C_1^{El} = 0$.

Before proceeding further, it should be reminded that the exact energy spectra is discrete for negative energies $E < 0$ describing bound states, and continuous for positive energies

$E > 0$ describing continuum states. Whereas for $E > 0$ it is sufficient to specify a value of energy E in order to solve Eq. 1.4, for $E < 0$ an additional condition must be imposed in order to obtain physical solutions,

$$\psi_{El}(r) \to 0 \qquad \text{for} \qquad r \to \infty \quad .$$

In the case of the continuum, there are two ways to handle the problem with B splines:
i) Specify the energy $E > 0$ and transform the problem to one determining the coefficient set $\{C_i^{El}\}$ (so-called Galerkin, or free boundary condition approach).
ii) Impose an additional (artificial) condition $\psi_{El}(r = r_{\max}) = 0$ and transform the problem to the eigenvalue problem yielding the set of discretized energies and corresponding coefficients (box-discretization approach).

In the present work, the second approach will mainly be used. It allows to obtain a set of orthogonal solutions which is able to represent both bound and continuum states. Similar to imposing the boundary condition at $r = 0$, the additional condition at $r = r_{\max}$ is fulfilled by requiring that $C_{n_r}^{El} = 0$. Further, substituting (1.5) in (1.4) and projecting on every B spline $B_\beta(r)$, the differential equation is reduced to a system of $n_r - 2$ linear equations. This system can be written in the matrix form as follows,

$$\underline{\mathbf{H}}^{(l)} \cdot \mathbf{C} = E\,\underline{\mathbf{S}} \cdot \mathbf{C} \tag{1.6}$$

where for $\alpha, \beta = 2, \ldots, n_r - 1$

$$\underline{\mathbf{H}}^{(l)}_{\alpha\beta} = \underline{\mathbf{T}}_{\alpha\beta} + \frac{l(l+1)}{2} \int\limits_0^{r_{\max}} \frac{B_\alpha(r) B_\beta(r)}{r^2} dr + \int\limits_0^{r_{\max}} B_\alpha(r) V(r) B_\beta(r) dr \tag{1.7}$$

$$\underline{\mathbf{T}}_{\alpha\beta} = -\frac{1}{2} \int\limits_0^{r_{\max}} B_\alpha(r) B''_\beta(r) dr = \frac{1}{2} \int\limits_0^{r_{\max}} B'_\alpha(r) B'_\beta(r) dr \tag{1.8}$$

$$\underline{\mathbf{S}}_{\alpha\beta} = \int\limits_0^{r_{\max}} B_\alpha(r) B_\beta(r) dr \tag{1.9}$$

All matrix elements can be computed very accurately (or exactly) applying the Gauss-Legendre quadrature on each span and summing the obtained results. The resulting matrices are symmetric and banded, with bandwidth $2k - 1$. Due to the fact that the overlap matrix $\underline{\mathbf{S}}$ is positive defined, solution of the generalized eigenvalue problem with the standard linear-algebra methods is straightforward.

Since the accuracy of the quadrature and the diagonalization procedure is of the order of the machine accuracy, there are only two reasons for the result to be inaccurate.

- The first reason is the incompleteness of the B-spline basis. Indeed, its span is only a subspace of the Hilbert space, therefore not every vector of the Hilbert space can be represented by a given B-spline basis. However, the degree of incompleteness can be easily controlled by a variation of the parameters of B-spline basis as will be discussed in Sec. 1.5.

- The second reason is connected with the use of the box-boundary condition. Its imposition influences those exact solutions for which the reduced wavefunctions $\psi_{El}(r)$ are non-zero at $r = r_{\max}$. Either such solutions are completely absent in the set of the computed solutions (in the case of energies above the ionization threshold it results in the discretization of the continuum) or their wavefunctions are slightly modified and their eigenvalues are increased due to an additional confinement. The larger the used box size $r_{\max}$, the more states can be described quite accurately.

1.3.2. Solving coupled Schrödinger equations

Various physical processes in nuclear, atomic, and molecular physics give rise to a system of coupled Schrödinger equations. For example, the two-body collision dynamics is described by coupled Schrödinger equations, where the appropriate scattering boundary conditions are applied. In order to solve these equations one often has to resort to numerical techniques. Many different numerical methods have been developed over the years. They can be broadly divided into two categories, explicit (or 'propagators') and implicit approaches. Explicit methods (e.g. Numerov, see [48] and references therein) require the solution of the dependent variable at the preceding grid point to determine its value at the next adjacent point. These approaches are generally fast and are not memory limited. Implicit methods typically require the solution of a large set of linear equations (or an eigensystem) and thereby determine the value at all grid points simultaneously. Therefore, they have much higher memory needs but, on the other hand, are inherently more stable and often provide better accuracy.

An implicit method to solve the coupled-channel Schrödinger equations has been developed by the author especially for the numerical treatment of ultracold atomic collisions. The method is based on using a B-spline basis set and the eigenchannel R-matrix approach [49]. It has been implemented in the FORTRAN package CNUCRMAT. The package was successfully employed for interpretation of Feshbach resonances experimentally observed in collisions between ultracold Li and Rb atoms [50] as well as for a systematic investigation of the applicability of single-channel approximations [51]. Within the method, the total wavefunction $\Psi(r,\omega)$ is decomposed as

$$\Psi(r,\omega) = \sum_i \frac{1}{r}\,\Phi_i(\omega)\,F_i(r) \tag{1.10}$$

using a complete and ortho-normalized basis set $\{\Phi_i(\omega)\}$ with $i = 1..N$. The variable r specifies the distance between the atoms and the variable ω incorporates spin degrees of freedom as well as the other spatial degrees of freedom. A substitution of Eq. (1.10) into the Schrödinger equation describing the collision of two atoms results in a system of coupled second-order ordinary differential equations

$$-\frac{\mathrm{d}^2 F_i(r)}{\mathrm{d}r^2} + \sum_{j=1}^{N} Q_{ij}(r)\,F_j(r) = 0. \tag{1.11}$$

where the condition $F_i(0) = 0$ has to be fulfilled.

In order to impose appropriate scattering boundary conditions, the basis functions $\{\Phi_i(\omega)\}$ are chosen as a direct product of the one-atom states and thus describe physical collisional channels. In this case, the functions $Q_{ij}(r)$ have the asymptotic behavior

$$Q_{ij}(r) \overset{r\to\infty}{\longrightarrow} \delta_{ij}\Delta_i \tag{1.12}$$

where $\Delta_i > 0$ for the energetically open channels and $\Delta_i < 0$ for the energetically closed ones. Physically relevant solutions are then obtained by imposing incoming-wave boundary conditions for the functions $F_i(r)$ describing open channels and requiring the functions $F_i(r)$ for closed channels to exponentially decay at $r \to \infty$.

If the coupling between channels occurs only due to electron exchange interaction, it is localized in some volume with radius r_0 so that

$$Q_{ij}(r > r_0) = \delta_{ij} Q_i(r) \tag{1.13}$$

where the functions $Q_i(r)$ incorporate, for example, a long-range van der Waals interaction between the atoms and the centrifugal barrier. The present method uses this advantage by dividing the radial domain r into two boxes A ($r \in [0, r_0]$) and B ($r \in [r_0, r_{\mathrm{as}}]$), where r_{as} is selected large enough so that for $r > r_{\mathrm{as}}$ the asymptotic behavior (1.12) is reached and the functions $F_i(r)$ for the closed channels vanish. For each of the two boxes a B-spline basis set is constructed in such a way that the multiplicity for the endpoints is equal to the order of B splines. Projecting the functions $F_i(r)$ onto these two B-spline basis sets and using the Galerkin approach, the system (1.11) can be reduced to a set of linear-algebra problems which yield relations between the values of the functions $F_i(r)$ and their derivatives $F_i'(r)$ at the box boundaries. A detailed description of the method would require introduction of the techniques used for matching and constructing of a set of solutions with imposed boundary conditions and is beyond the scope of the present work.

1.4. Properties of the discretized continuum

1.4.1. Density of states

Although the diagonalization procedure provides only a discrete set of electronic wavefunctions with energies above the ionization threshold, these functions can be used to represent the true electronic continuum. For a better understanding of this issue, consider sets of discretized continuum states yielded by a diagonalization for different values of the box size $r_{\max}$. The points in Figure 1.3 present the momenta $\kappa = \sqrt{2E}$ of the discretized continuum states of the H atom, with $l = 0$, obtained by varying $r_{\max}$ from $200\,a_0$ to $230\,a_0$ (lower part) as well as from $400\,a_0$ to $410\,a_0$ (upper part), with a stepsize of $1\,a_0$. Points lying upon the same horizontal line belong to the set obtained for the same box size. The following conclusion can be drawn from Fig. 1.3:

- The value of $r_{\max}$ allows to control the energy of each discretized continuum state and, consequently, the spacing between states. For any given energy E several values of $r_{\max}$ can be found that yield a discretized continuum state with the required energy.
- The spacing between discretized continuum states decreases with increasing the box size $r_{\max}$.
- The momenta κ of the discretized continuum states become uniformly spaced as the index of the discretized state increases.

In order to understand this behavior, consider the asymptotic behavior of a Coulomb partial continuum wavefunction, which in the limit $\kappa r \to \infty$ reads

$$\psi_{El}(r) = \sqrt{\frac{2}{\pi\kappa}} \sin\left(\kappa r + \frac{Z}{\kappa}\ln(2\kappa r) - \frac{l\pi}{2} + \arg\Gamma\left(l + 1 - \frac{\mathrm{i}Z}{\kappa}\right) + \sigma_l\right) \tag{1.14}$$

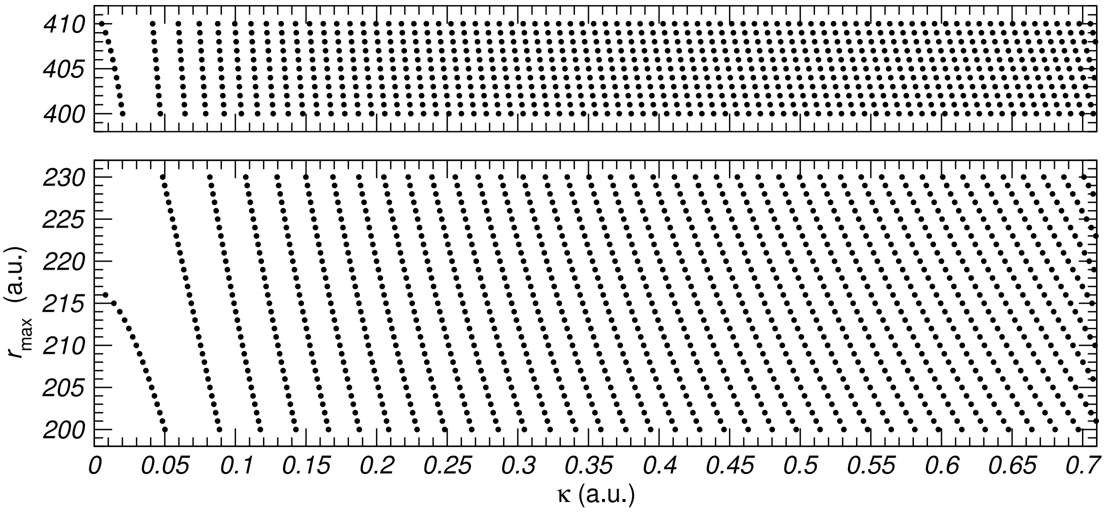

Figure 1.3.: Momenta of discretized continuum states of the H atom, $\kappa = \sqrt{2E}$, for different values of box size $r_{\max}$.

where $\kappa = \sqrt{2E}$, Z is the nuclear charge, $\arg\Gamma(l+1-\mathrm{i}Z/\kappa)$ is the Coulomb phase and σ_l is the non-Coulombic phase ($\sigma_l = 0$ for hydrogen). Imposition of the boundary condition $\psi_{El}(r_{\max}) = 0$ results in the quantization relation

$$\kappa r_{\max} + \frac{Z}{\kappa}\ln(2\kappa r_{\max}) - \frac{l\pi}{2} + \arg\Gamma\left(l+1-\frac{\mathrm{i}Z}{\kappa}\right) + \sigma_l = \pi N \tag{1.15}$$

where N is an integer. Given Z, l and $r_{\max}$, the relation (1.15) yields the set of energies $E_N = \kappa_N^2/2$. In a first approximation (if $\kappa r_{\max}$ is larger than all remaining terms) this relation leads to the energy of a free particle in a box,

$$E_N = \frac{N^2\pi^2}{2r_{\max}^2} \quad . \tag{1.16}$$

The density of states defined as the number of states per unit energy (momentum) interval,

$$\rho(E) = \frac{\partial N}{\partial E} = \frac{\rho(\kappa)}{\kappa}\,, \qquad \rho(\kappa) = \frac{\partial N}{\partial \kappa}\,, \tag{1.17}$$

can be evaluated from the equation (1.16) as

$$\rho(E) = \frac{1}{\pi\sqrt{2}}\frac{r_{\max}}{\sqrt{E}}\,, \qquad \rho(\kappa) = \frac{r_{\max}}{\pi} \tag{1.18}$$

giving the difference in the momentum of two adjacent states, $\Delta\kappa = \rho^{-1}(\kappa) = \pi/r_{\max}$. For example, the box size $r_{\max} = 200\,a_0$ yields $\Delta\kappa = 0.016\,\text{a.u.}$ (see Fig. 1.3).

A major problem emerging in any discretization technique is the so-called *normalization problem.* Whereas continuum states $\{\psi_E\}$ ($\{\psi_\kappa\}$) normalized on the continuous energy (momentum) scale satisfy the condition

$$\langle\psi_E|\psi_{E'}\rangle = \delta(E - E'), \qquad \langle\psi_\kappa|\psi_{\kappa'}\rangle = 2\pi\delta(\kappa - \kappa'), \tag{1.19}$$

the computed discretized continuum states $\{\psi_N\}$ are normalized (together with the obtained bound states) to unity,

$$\langle\psi_N|\psi_{N'}\rangle = \delta_{NN'} \quad . \tag{1.20}$$

Therefore, a renormalization has to be performed in order to compute measurable quantities involving a continuum state as the final state (e.g., cross-section, ionization rate). Two methods are commonly used with B splines. The first one employs a fit of a discretized state to the corresponding exact solution in the asymptotic region ($\kappa r \gg 1$) where the analytical expression is often available (see equation (1.14) as an example). The other technique extracts the normalization factor from the set of eigenenergies without the need for external information. It is based on using the density of states and it is self-consistent with the box discretization procedure. This technique will mainly be employed in the present work and is the topic of the following subsection.

1.4.2. Normalization using the density of states

Consider a box with the size tending to infinity, so that the discretized continuum is sufficiently dense. In this limit, the projection operator to the continuum can be written as

$$\hat{\mathrm{P}}_{\mathrm{c}} = \int \mathrm{d}E\,|\psi_E\rangle\langle\psi_E| \approx \sum_N |\psi_N\rangle\langle\psi_N|, \tag{1.21}$$

where $\{\psi_E\}$ and $\{\psi_N\}$ are normalized according to the conditions (1.19), (1.20), respectively. Assume that $E(\tilde{N})$ is a monotonic function of $\tilde{N}$ yielding for a positive integer value of the variable, $\tilde{N} = N$, the energy of the correspondingly discretized continuum state, $E(N) = E_N$. Introducing the density of states, defined by Eq.(1.17), the integration over the energy can be substituted with a summation over N,

$$\int \mathrm{d}E \cdots = \int \frac{\partial E}{\partial \tilde{N}}\, \mathrm{d}\tilde{N} \cdots = \int \frac{\mathrm{d}\tilde{N}}{\rho(E)} \cdots \approx \sum_N \frac{1}{\rho(E)} \cdots \bigg|_{E=E_N}. \tag{1.22}$$

It follows from equations (1.22) and (1.21) that

$$|\psi_{E_N}\rangle = [\rho(E_N)]^{1/2}\, |\psi_N\rangle \tag{1.23}$$

For example, applying (1.23) to discretized continuum states describing a free particle in a box,

$$\kappa_N r_{\max} = \pi N, \qquad \psi_N(r) = \sqrt{\frac{2}{r_{\max}}} \sin \kappa_N r, \qquad \rho(E_N) = \frac{r_{\max}}{\pi \kappa_N} \tag{1.24}$$

one obtains

$$\psi_{E_N}(r) = \sqrt{\frac{2}{\pi \kappa_N}} \sin \kappa_N r \tag{1.25}$$

which is exactly the continuum wavefunction normalized according to (1.19).

The value of $\rho(E_N)$ can be approximately obtained using the Taylor expansion of $E(\tilde{N})$ in the vicinity of $\tilde{N} = N$. Indeed, applying the expansion

$$\begin{aligned} E(\tilde{N}) = E(N) &+ \frac{\partial E}{\partial \tilde{N}}\bigg|_{\tilde{N}=N} (\tilde{N} - N) + \frac{1}{2}\frac{\partial^2 E}{\partial^2 \tilde{N}}\bigg|_{\tilde{N}=N} (\tilde{N} - N)^2 \\ &+ \frac{1}{6}\frac{\partial^3 E}{\partial^3 \tilde{N}}\bigg|_{\tilde{N}=N} (\tilde{N} - N)^3 + \dots \end{aligned} \tag{1.26}$$

to the case $\tilde{N} = N \pm 1$ results in

$$E(N \pm 1) = E_{N\pm1} = E_N \pm \frac{1}{\rho(E_N)} + \frac{1}{2}\frac{\partial^2 E}{\partial^2 \tilde{N}}\bigg|_{\tilde{N}=N} \pm \frac{1}{6}\frac{\partial^3 E}{\partial^3 \tilde{N}}\bigg|_{\tilde{N}=N} + \dots \tag{1.27}$$

Subtracting E_{N-1} from E_{N+1} as well as neglecting third and higher derivatives (according to Eq. (1.16) they are equal to zero for a free particle in a box), the following expression for the density of states is obtained

$$\rho(E_N) = \frac{2}{E_{N+1} - E_{N-1}}. \tag{1.28}$$

1.5. Convergence study and control over accuracy

Convergence is an important issue when performing a numerical computation employing a B-spline basis. Whereas the flexibility of the B splines allows one to adjust the parameters for a particular problem in a most appropriate way, their improper usage may lead to significantly wrong results. In general, there are different approaches to obtain converged results, requiring however a different computational cost. The latter increases with the increase of the number and order of B splines. Although some experience is required to find an optimal set of parameters, in general it is not as tricky as, for example, with global basis sets.

In AMO physics a wavefunction of a system is usually an analytic function, i.e. it can be given locally by a convergent power series. Being expanded in a Taylor series at a point, the function can be represented at another point using a part of this series as better as shorter is the distance between points and as higher is the order of employed polynomial. Similarly, using B splines one obtains as better a representation of a function upon an interval between breakpoints as shorter the length of the interval and as higher the order of the B splines is. To adjust the length of the interval it is also important to know the expected behavior of the solution. For example, a rapidly oscillating function requires shorter intervals than a slowly varying one. Making use of a B-spline basis, one can locally increase the density of breakpoints where it is required, but keeping it low otherwhere. In the following the convergence issue is illustrated in the context of atomic hydrogen ($V(r) = 1/r$).

To disentangle different effects, the independent parameters are chosen as follows:
1) the box size $r_{\max}$,
2) the order k of the B splines,
3) the number s of non-zero intervals,
4) the breakpoint sequence (for fixed $r_{\max}$ and s).

Note that the number of B splines is related to k and s by means of Eq.(1.1) and therefore is not an independent parameter. Since the convergence of wavefunctions is not necessary identical to the convergence of energies, the dipole-operator matrix element will be tested as well.

Table 1.1.: Energies of the 1S and 2P states of the hydrogen atom as well as the matrix element of the dipole operator z between them, $\langle 1\mathrm{S}\,|z|\,2\mathrm{P}\rangle$, computed with different B-spline basis sets

a) Varying the order k of B-splines for fixed parameters $r_{\max} = 200\,a_0$, $s = 200$ and linear breakpoint sequence

k	$E_{1\mathrm{S}}$, a.u.	$E_{2\mathrm{P}}$, a.u.	$\langle 1\mathrm{S}\,\lvert z\rvert\,2\mathrm{P}\rangle$
4	-0.499 795 494 109	-0.124 996 698 185	0.745 215 738 417
5	-0.499 995 954 665	-0.124 999 968 005	0.744 940 341 192
6	-0.499 999 861 143	-0.124 999 999 472	0.744 935 682 096
7	-0.499 999 993 986	-0.124 999 999 992	0.744 935 542 807
8	-0.499 999 999 826	-0.125 000 000 000	0.744 935 539 038
9	-0.499 999 999 998	-0.125 000 000 000	0.744 935 539 026
10	-0.500 000 000 000	-0.125 000 000 000	0.744 935 539 028

b) Varying the number s of non-zero intervals for fixed parameters $r_{\max} = 200\,a$, $k = 10$ and linear breakpoint sequence

s	$E_{1\mathrm{S}}$, a.u.	$E_{2\mathrm{P}}$, a.u.	$\langle 1\mathrm{S}\,\lvert z\rvert\,2\mathrm{P}\rangle$
20	-0.486 357 949 853	-0.124 911 107 813	0.744 755 371 528
50	-0.499 997 311 184	-0.124 999 986 129	0.744 939 265 844
80	-0.499 999 936 078	-0.124 999 999 989	0.744 935 556 290
110	-0.499 999 999 222	-0.125 000 000 000	0.744 935 538 505
140	-0.499 999 999 983	-0.125 000 000 000	0.744 935 539 012
170	-0.499 999 999 999	-0.125 000 000 000	0.744 935 539 027
200	-0.500 000 000 000	-0.125 000 000 000	0.744 935 539 028

c) Varying parameter g of geometrically progressive breakpoint sequence for fixed parameters $r_{\max} = 200\,a_0$, $s = 20$ and $k = 10$.

g	$E_{1\mathrm{S}}$, a.u.	$E_{2\mathrm{P}}$, a.u.	$\langle 1\mathrm{S}\,\lvert z\rvert\,2\mathrm{P}\rangle$
1.0	-0.486 357 949 853	-0.124 911 107 813	0.744 755 371 528
1.1	-0.499 997 311 184	-0.124 999 993 906	0.744 946 798 433
1.2	-0.499 999 999 965	-0.125 000 000 000	0.744 935 539 048
1.3	-0.499 999 999 992	-0.124 999 999 988	0.744 935 539 136
1.4	-0.499 999 999 527	-0.124 999 997 832	0.744 935 601 286
1.5	-0.499 999 982 060	-0.124 999 914 451	0.744 938 131 096
Exact	-0.500 000 000 000	-0.125 000 000 000	0.744 935 539 028

Table 1.2.: Energies of nS states of the hydrogen atom computed using linear breakpoint sequence, $k = 10$, $r_{\max} = 200\,a_0$, $s = 200$ and compared to exact values.

n	$E_{n\mathrm{S}}$, a.u.	$E_{n\mathrm{S}}^{\mathrm{exact}}$, a.u.
1	-0.500 000 000 000	-0.500 000 000 000
2	-0.125 000 000 000	-0.125 000 000 000
3	-0.055 555 555 556	-0.055 555 555 556
4	-0.031 250 000 000	-0.031 250 000 000
5	-0.020 000 000 000	-0.020 000 000 000
6	-0.013 888 888 889	-0.013 888 888 889
7	-0.010 204 081 567	-0.010 204 081 633
8	-0.007 812 381 089	-0.007 812 500 000
9	-0.006 157 272 715	-0.006 172 839 506
10	-0.004 760 808 277	-0.005 000 000 000

1.5.1. Accuracy of computed bound states

First consider the case when the box size is chosen to be sufficiently large, so that the box boundary does not influence the investigated solutions. Table 1.1 presents the energies of the 1S and 2P states of the hydrogen atom as well as the matrix element of the dipole operator z between these two states. The exact result (see bottom row) is compared with results obtained varying one of the parameters while the others are fixed. As can be seen from Table 1.1 a, convergence with respect to the order k of the B splines is achieved within 12 significant digits for $k = 10$ for both energies and matrix element, whereas for $k = 4$ (simple cubic splines) the accuracy is rather poor, especially for the 1S state. In general, the optimal order of B splines can vary between 7 and 10. Having fixed the values of k and the box size $r_{\max}$, the number s of non-zero intervals is gradually decreased from 200 to 20 and the obtained results are shown in Table 1.1 b. Since the wavefunction of the 1S state is more localized, its accuracy decreases faster than the accuracy of a more spread 2P state. For $s = 20$ the energy of the 1S state deviates from the exact value by about 3%, whereas for the 2P state the deviation is only about 0.1%. Nevertheless, even for such small value of s the accuracy can be significantly improved employing a non-linear breakpoint sequence, as shown in Table 1.1 c where results are obtained employing a geometrically progressive breakpoint sequence ($r_{i+1} - r_i = g(r_i - r_{i-1}), g \geqslant 1$). With an increase of the parameter g, the density of segments increases for smaller r and decreases for larger r. This leads to a much higher accuracy, for example for the optimal value $g = 1.2$ it is on 9 significant digits better than for $g = 1.0$ representing the linear breakpoint sequence. However, a further increase of g worsens the accuracy since the density at larger r becomes insufficient.

Having shown and discussed the inaccuracy due to the incompleteness of the B-spline basis, the effect of the imposed box boundary condition on the energies of the bound states is now considered. Table 1.2 presents the energies of the bound nS states of the hydrogen atom computed using B splines and compared to the exact values. The parameters of the B-spline basis set are chosen to guarantee that results are converged to the number of significant figures given (compare to Table 1.1 a and b). As one can see, the agreement is perfect for the principal quantum number $n = 1 - 6$, while for higher n the computed energies lie above the exact ones and their deviation increases with increasing n. This deviation is caused by the additional confinement due to the box boundary, which transforms the atomic Hamiltonian into the atomic Hamiltonian within the box by adding a potential step of an infinite height at $r = r_{\max}$. Since for the nS states of the hydrogen atom one has $\langle r \rangle_n = 1.5n^2$, the box size $r_{\max}$ must be set larger to describe states with higher principal quantum numbers n. 'Unphysical' high-n eigenstates of the modified Hamiltonian with the energy lying below the ionization threshold are often referred to as *pseudo-states*. While the exact Hamiltonian can have an infinite number of bound eigenstates (as for the hydrogen atom), imposition of the box will limit the number of computed bound states proportionally to the square of its size $r_{\max}$, as shown in Table 1.3.

1.5.2. Numerical stability of the computed discretized continuum

The diagonalization procedure yields a finite number of discretized continuum states, despite the existence of an infinite number of box discretized continuum states. The latter may have a very high energy E so that their wavefunctions are highly oscillating. It is obvious that such states cannot be represented with a limited number of B splines. Figure 1.4 shows how the range of numerically stable results can be ascertained by means of the density of states. A plain evidence of the numerical instability can be found comparing the density of states computed using Eq. (1.28) with its analytical expression for a free particle in a box given by Eq. (1.18). This comparison is shown

Table 1.3.: The number of computed bound nS states (including pseudo-states) of the hydrogen atom, n_{bnd}, for different box sizes $r_{\max}$.

$r_{\max}, a_0$	100	400	900	1600	2500	3600	4900	6400
n_{bnd}	8	17	26	35	44	53	62	71

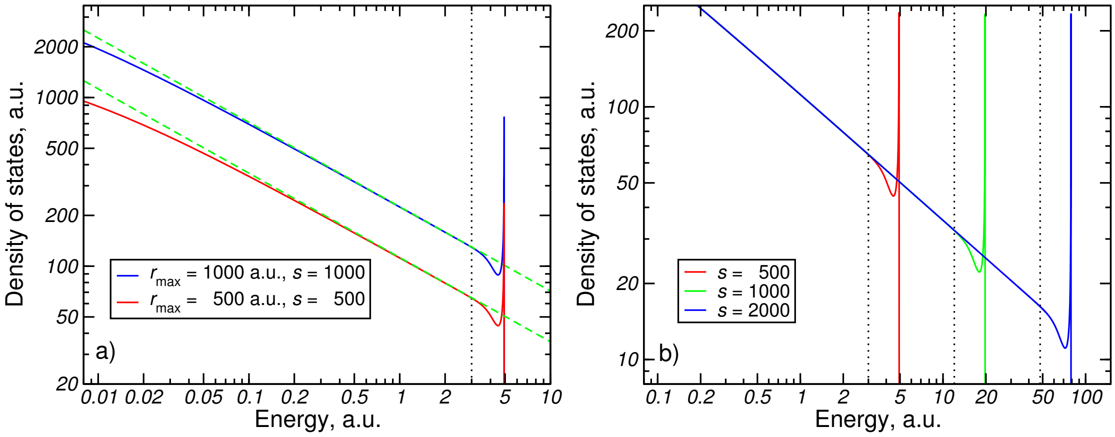

Figure 1.4.: Computed density of continuum S states of the H atom, $\rho(E)$, as a function of the energy E for different parameters of the B-spline basis set. Dotted curves restrict the range of numerically stable results. a) Solid curves present results of the calculation performed for two different values of the box size $r_{\max}$ keeping the length $r_{\max}/s$ of the segments in the linear breakpoint sequence fixed. Dashed lines depict the density of states (see equation (1.18)) of a free particle in a box for the corresponding box size. b) Increase of the range of numerical stability by increasing the number of segments s and keeping the box size fixed at $r_{\max} = 500\,a_0$

in Fig. 1.4 a where results for two different box sizes are presented. As the energy E increases, the computed density of S states of the H atom approaches the density of states of a free particle in a box, so that they become visually indistinguishable at $E = 0.5$ a.u. However, the computed density starts to deviate at $E_{\text{cr}} = 3$ a.u. exhibiting first a minimum followed by a sharp maximum and having a nearly zero value afterwards. The critical energy E_{cr} is equal for both computations performed with different box sizes. It is however due to the fact that the length of the segments is chosen to be the same for both computations, $\Delta r = r_{\max}/s = 1\,a_0$. The wavelength $\lambda = 2\pi/\sqrt{2E}$ for energies $E > E_{\text{cr}}$ is less than $2.6\,a_0$. Therefore, to obtain numerically stable results the number of segments per wavelength must be larger than the critical value $t_{\text{cr}} = 2\pi s/(\sqrt{2E_{\text{cr}}}r_{\max}) = 2.6$. Given the value of t_{cr}, the critical energy can be obtained for an arbitrary box size and a number of segments as

$$E_{\text{cr}} = \frac{2\pi^2}{t_{\text{cr}}^2}\left(\frac{s}{r_{\max}}\right)^2 \approx 3\left(\frac{s}{r_{\max}}\right)^2 . \tag{1.29}$$

The applicability of Eq. (1.29) is tested in Fig. 1.4 b, where the computation is performed for a different number of segments s keeping the box size fixed. As can be seen, the onset of numerically unstable results is well predicted by the values of critical energy calculated using Eq. (1.29). Note that the factor 3 in Eq. (1.29) holds true for $k = 10$, which was used to perform the computations shown in Fig. 1.4. The value of the factor changes with the order of the B splines, from 1.5 for $k = 5$ to 4 for $k = 30$, since the critical value t_{cr} decreases with increasing k.

The knowledge of the critical energy E_{cr} is important for the numerical treatment of the ionization process of an atom or molecule. It also provides a good measure for cutting off unphysical states with a high energy in order to make the time propagation in an external field faster, as is discussed in Sec. 7.2.

2. Two-center *B*-spline based CI method

This chapter discusses a new method that is capable of treating two-electron diatomic molecules using a B-spline basis in prolate-spheroidal (elliptic) coordinates. The method has been developed and coded in order to overcome the limitations of the previously existing *ab initio* codes for diatomic molecules. These limitations are discussed in Sec. 2.1. After introducing the prolate spheroidal coordinate system in Sec. 2.2, the solution of the one-electron Schrödinger equation in this coordinate system is discussed in Sec. 2.3. Although a B-spline based one-electron approach in prolate spheroidal coordinates had already been implemented [52, 53], a new code was written from scratch. Section 2.4 describes the implementation of the configuration-interaction approach and the calculation of the arising two-electron integrals. The chapter closes with a discussion of how the present method was extended for the numerical treatment of alkali dimers.

2.1. Motivation

The existing in principle exact *ab initio* electronic-structure codes for diatomic molecules may be classified as explicitly correlated (geminal) methods or configuration interaction (CI). In the former case the basis functions contain some functional form of the interelectronic coordinate explicitly. The James-Coolidge type basis functions of Kołos and coworkers have already long time ago succeeded in providing tremendously accurate potential curves for the low lying states of H_2, especially its ground state [54]. The use of elliptic coordinates allows full use of the diatomic symmetry. The electron-nucleus Coulombic cusp condition is automatically fulfilled and electronic correlation is efficiently included using some power of the interelectronic coordinate in the basis. Altogether, very accurate results can be obtained with an impressively small number of basis functions. A problem of this approach is the tendency of the basis set to run into numerically caused linear dependencies. This makes systematic basis-set convergence investigations very difficult or even impossible. Although a canonical orthogonalization of the basis helps and prevents a crash of the program, experience shows that a further improvement of the result remains difficult. Even more severely, there is a fluent transition from the physical into the unphysical regime. Therefore, it is impossible to determine a well-defined cut-off value for the orthogonalization. Since the occurring integrals are rather complicated, and every new type of matrix element leads always to two-electron integrals due to the explicit dependence of the basis set on the interelectronic coordinate, the extension to more than two electrons appears to demand heroic efforts, even if core electrons should only be considered by means of some model potential. The complicated form of the integrals limits also the range of quantum numbers of angular momentum that can be considered in the existing codes, and the number of highly excited (Rydberg) states that is available with a given basis is rather limited. Due to the linear dependencies it is difficult to obtain a number of states with a comparable accuracy using a single basis set. The use of different basis sets for different states is on the other hand rather tedious, if many states are considered.

Rather recently, Gaussian geminals have been successfully implemented and used for very accurate calculations for small molecular systems (see, e. g., [55]). Their advantages are the much simpler (though by far non-trivial) integrals that have to be solved. This allows extensions to more than two electrons and also more than two nuclei. Also, the calculation of new properties can easier be implemented than in the case of the Kołos approach, though the problem remains that rather complicated two-electron integrals have to be solved. The deficiency of Gaussians with respect to a correct representation of the cusp condition has to be overcome by correspondingly large basis-set expansions which are possible due to nowadays available computer power. As is the case with the Kołos approach, the basis-set optimization and convergence investigation is nevertheless very difficult and hampered by numerically caused linear dependencies.

There are essentially two types of configuration-interaction (or variants of it like multi-configuration self-consistent field, coupled cluster etc.) codes in use. The multipurpose quantum-chemistry codes based on Gaussians are highly optimized, but do not consider symmetry groups with an infinite rotation axis as it is present in diatomic molecules. Very accurate results require very large expansions, partly due to the incomplete use of symmetry, but mainly due to the deficiency of Gaussians to represent the cusp and due to the slow convergence of angular correlation. Large expansions are, however, only possible, because in those quantum chemistry codes the used Davidson routine [56] (or variants of it) avoids the need for a full diagonalization of the CI matrix. A disadvantage of the Davidson routine is the limited number of excited states that can be obtained. There exist also some specialized diatomic codes using either Gaussians or, preferentially, exponential basis functions [57]. The latter fulfill the cusp condition and may easily be expressed in prolate-spheroidal coordinates, as the integrals are anyhow usually calculated in that coordinate system. The main advantage of the multipurpose codes compared to the specialized codes for diatomic molecules is the tremendous efforts that have been spent in their efficiency optimization. This allows even all-electron calculations for alkali dimers. However, it has to be kept in mind that for heavier alkalis a good model or pseudo potential describing the core electrons may give more accurate results than all-electron calculations. This is due to the fact that the model or pseudo potentials stem from very accurate atomic calculations that use spherical symmetry and thus even allow the very accurate inclusion of relativistic effects, far beyond the ability of present days molecular codes. Although it is not as bad as for the explicitly correlated basis functions, also the CI methods are hampered by numerically caused linear dependencies of the (now one-particle) basis functions. The main problem arises from diffuse functions centered at different atoms, and thus single-centered even-tempered Gaussians help to perform some convergence studies, but do not fully solve the problem.

There is one property that is common to all methods described so far. They are based on global basis functions, i. e. they use basis functions that are defined within the complete position space. Although this globality is part of the success story of quantum chemistry as this appears to be the only way to handle large molecular systems within available computer resources, there are some disadvantages to it. One of them is the already discussed linear-dependency problem. It complicates (or even prevents) systematic basis-set convergence studies. Related to this problem is the difficulty of obtaining a well-defined number of molecular Rydberg states or getting a well-defined and dense representation of the electronic continuum. The evident solution to this problem is provided by local basis functions. In atomic electronic structure calculations B splines have proven to combine locality with a very high degree of flexibility [47]. This flexibility allows a very good description of any type of wave function, both bound and continuum ones. The locality avoids the problem of linear dependencies. The inherent box discretization provided by the local basis leads to a well-defined discretization of the electronic continuum. With a given box size only those states that have a node at the box boundary appear in the calculation. The variation of the box size offers thus a tuning knob that determines the number of Rydberg states and the density of continuum states. This does not only provide the ability to calculate bound to continuum transitions within the same basis set (and thus consistently), but is also very practical when calculating quantities using a summation over complete sets of eigenstates, as is required in the calculation of perturbative expressions. One example is the calculation of multiphoton transition rates [58].

The success of the B-spline methods especially for the calculation of multiphoton processes in atoms (both perturbatively and non-perturbatively by solving the time-dependent Schrödinger equation of the atom in a laser pulse) has motivated the extension to molecules. For two-electron molecules, this was done by adopting a one-center approximation where only the radial coordinate is expanded in B splines, while the angular part is expressed in terms of spherical harmonics. The absence of spherical symmetry in molecules couples the different angular momenta, and thus convergence becomes increasingly more difficult to achieve, if the anisotropy of the system increases. For molecular hydrogen very impressive results could be obtained for dissociative photoionization at internuclear distances smaller than about $4\,a_0$ [47, 59]. However, this distance is unlikely to be sufficient for studies involving competitive ionization and dissociation, e. g. in strong laser fields. It appears also difficult or even impossible to extend those one-center methods to alkali dimers, if very accurate results are required, since their equilibrium internuclear distance is relatively large. Also, for calculations of low-temperature scattering of excited hydrogen atoms [60] one is interested in the complete range of internuclear distances, especially the large ones.

Thus, the present development and implementation of a two-center B-spline basis CI method was motivated by the need to preserve the advantages of the B-spline based methods and overcome the limitations of the previously used one-center approach.

2.2. Prolate spheroidal coordinate system

Consider two nuclei A and B separated by the internuclear distance R. Introduce the Cartesian coordinate system with the origin in the midpoint between the nuclei and the axis z pointing along the internuclear axis, with the nucleus A at $z_A = -R/2$ and the nucleus B at $z_B = R/2$ (see Fig. 2.1). For an electron e with coordinates (x, y, z), its radial distance from the axis z is given by $r_z = \sqrt{x^2 + y^2}$, while the distances to the nuclei are

$$r_A = \sqrt{r_z^2 + (z + R/2)^2} \quad \text{and} \quad r_B = \sqrt{r_z^2 + (z - R/2)^2}, \tag{2.1}$$

respectively. The first two prolate-spheroidal (elliptical) coordinates $\xi \in [1, \infty)$, $\eta \in [-1, 1]$ can then be simply defined in terms of r_A, r_B as

$$\xi = \frac{r_A + r_B}{R} \quad \text{and} \quad \eta = \frac{r_A - r_B}{R}. \tag{2.2}$$

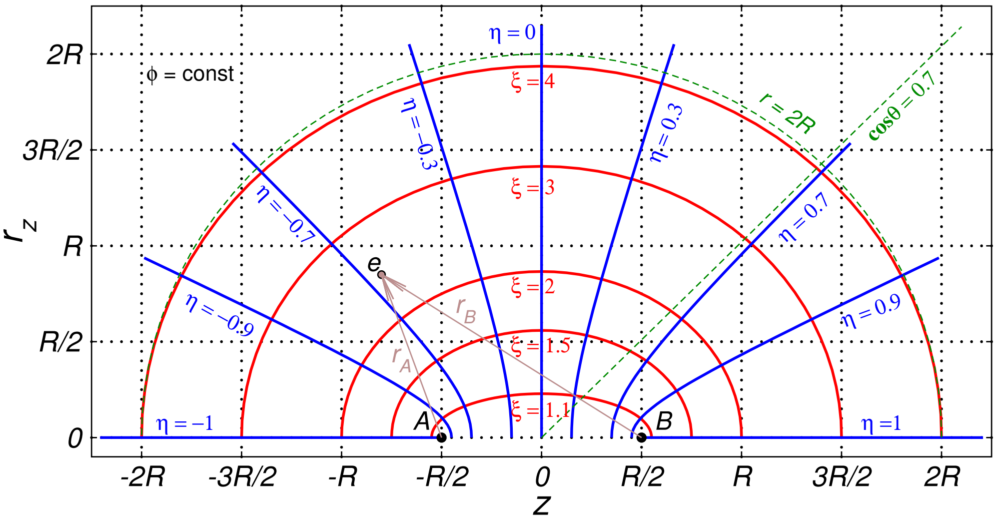

Figure 2.1.: Prolate spheroidal coordinate system. Cuts of various prolate spheroids (hyperboloids) are shown by red (blue) curves. For the sake of comparison, cuts of surfaces with the given value of spherical coordinate r or θ are presented by dashed green curves.

The third prolate-spheroidal coordinate is the angle $\phi \in [0, 2\pi]$ around the internuclear axis defined analogous to the azimuthal angle ϕ in the spherical coordinates (r, θ, ϕ) as

$$x = r_z \cos\phi, \qquad y = r_z \sin\phi. \tag{2.3}$$

A variation of the coordinates η and ϕ for a constant value of ξ yields a prolate spheroid, i.e., an ellipsoid with the equal equatorial radii (along the x and y axes) which are smaller than the polar radius (along z axes). Conversely, the surface with fixed η is a hyperboloid. Cuts of various prolate spheroids and hyperboloids for a fixed value of ϕ are presented in Fig. 2.1.

The expressions for r_z and z obtained from the equations (2.1), (2.2) are given by

$$r_z = \frac{R}{2}\sqrt{(\xi^2 - 1)(1 - \eta^2)}, \qquad z = \frac{R}{2}\xi\eta \tag{2.4}$$

Using their expressions in spherical coordinates,

$$r_z = r\sin\theta, \qquad z = r\cos\theta, \tag{2.5}$$

one can deduce the relations between both coordinate systems:

$$r = \frac{R}{2}\sqrt{\xi^2+\eta^2-1}, \quad \cos\theta = \frac{\xi\eta}{\sqrt{\xi^2+\eta^2-1}}. \tag{2.6}$$

These relations have simple limits at $\xi \to \infty$,

$$r \to \frac{R}{2}\,\xi, \quad \cos\theta \to \eta, \tag{2.7}$$

giving rise for referring to ξ as the radial coordinate and to η as the angular coordinate. As shown on Fig. 2.1, the relations (2.7) can be used to rather accurately visualize ξ and η already for $\xi = 4$.

As follows from the definition (2.1), the expressions for r_A, r_B are very simple in prolate spheroidal coordinates

$$r_A = \frac{R}{2}\,(\xi+\eta), \qquad r_B = \frac{R}{2}\,(\xi-\eta). \tag{2.8}$$

Another great advantage of prolate spheroidal coordinates consists in its convenience for describing the Coulomb interaction between an electron and the nuclei. Tackling the problem one has to deal with the Coulomb terms $1/r_{A,B}$ multiplied by volume element $\mathrm{d}v$. Making use of the expression for volume element

$$\mathrm{d}v = w\,\mathrm{d}\xi\,\mathrm{d}\eta\,\mathrm{d}\phi, \qquad w = \frac{R^3}{8}\,(\xi^2-\eta^2), \tag{2.9}$$

one obtains the extremely simple (compared to Cartesian or spherical coordinates) expressions

$$\frac{\mathrm{d}v}{r_A} = \frac{R}{2}\,(\xi-\eta)\,\mathrm{d}\xi\,\mathrm{d}\eta\,\mathrm{d}\phi, \quad \text{and} \quad \frac{\mathrm{d}v}{r_B} = \frac{R}{2}\,(\xi+\eta)\,\mathrm{d}\xi\,\mathrm{d}\eta\,\mathrm{d}\phi. \tag{2.10}$$

In the following, a brief list of identities is given which are important for applying prolate spheroidal coordinates for physical problems and used further in the present thesis. The Laplacian used to specify the kinetic energy operator reads in prolate spheroidal coordinates as

$$\begin{aligned}\nabla^2 = \frac{4}{R^2(\xi^2-\eta^2)}\left\{\frac{\partial}{\partial\xi}\left[(\xi^2-1)\frac{\partial}{\partial\xi}\right] + \frac{\partial}{\partial\eta}\left[(1-\eta^2)\frac{\partial}{\partial\eta}\right]\right. \\ \left. + \frac{\partial}{\partial\phi}\left[\frac{(\xi^2-\eta^2)}{(\xi^2-1)(1-\eta^2)}\frac{\partial}{\partial\phi}\right]\right\}.\end{aligned} \tag{2.11}$$

The inverse distance between two points, (ξ_1, η_1, ϕ_1) and (ξ_2, η_2, ϕ_2), used for the calculation of the two-electron integrals, can be expressed with the aid of the von Neumann expansion

$$\frac{1}{r_{12}} = \frac{4}{R} \sum_{\ell=0}^{\infty} \sum_{p=-\ell}^{\ell} S_\ell^{|p|} P_\ell^{|p|}(\xi_<) Q_\ell^{|p|}(\xi_>) P_\ell^{|p|}(\eta_1) P_\ell^{|p|}(\eta_2) e^{\mathrm{i}p(\phi_1 - \phi_2)} \tag{2.12}$$

where

$$S_\ell^p = \frac{2\ell+1}{2} (-1)^p \left[\frac{(\ell-p)!}{(\ell+p)!} \right]^2 , \tag{2.13}$$

and $\xi_>$, $\xi_<$ are the greater and the lesser values of ξ_1 and ξ_2, respectively. Besides, the associated Legendre functions of the first and second kind,

$$\begin{aligned} P_\ell^p(\xi) &= (\xi^2-1)^{\frac{p}{2}} \frac{d^p P_\ell(\xi)}{d\,\xi^p}, \qquad Q_\ell^p(\xi) = (\xi^2-1)^{\frac{p}{2}} \frac{d^p Q_\ell(\xi)}{d\,\xi^p}, \\ P_\ell^p(\eta) &= (1-\eta^2)^{\frac{p}{2}} \frac{d^p P_\ell(\eta)}{d\,\eta^p}, \end{aligned} \tag{2.14}$$

are used in Eq. (2.12). Partial derivatives used to specify the dipole operator in the velocity gauge take the form

$$\begin{aligned} \frac{R}{2}\frac{\partial}{\partial x} &= \cos\phi \frac{\sqrt{(\xi^2-1)(1-\eta^2)}}{(\xi^2-\eta^2)} \left\{ \xi \frac{\partial}{\partial \xi} - \eta \frac{\partial}{\partial \eta} \right\} - \frac{\sin\phi}{\sqrt{(\xi^2-1)(1-\eta^2)}} \frac{\partial}{\partial \phi} \\ \frac{R}{2}\frac{\partial}{\partial z} &= \eta \frac{(\xi^2-1)}{(\xi^2-\eta^2)} \frac{\partial}{\partial \xi} + \xi \frac{(1-\eta^2)}{(\xi^2-\eta^2)} \frac{\partial}{\partial \eta} . \end{aligned} \tag{2.15}$$

2.3. The one-electron Schrödinger equation in prolate spheroidal coordinates

Consider a diatomic molecule within the Born-Oppenheimer approximation. Assume that the one-electron Hamiltonian $\hat{\mathrm{h}}$ possesses rotational symmetry with respect to the internuclear axis and can therefore be written as

$$\hat{\mathrm{h}} = -\frac{1}{2}\nabla^2 + V(\xi, \eta) \, . \tag{2.16}$$

The explicit form of $V(\xi, \eta)$ which depends on the interaction between an electron and ionic cores is not further specified at this point. Solving the one-electron Schrödinger equation (OESE) $\hat{\mathrm{h}}\psi = \epsilon\psi$ yields the orbitals ψ. Due to rotational symmetry the orbitals

ψ can be specified by the quantum numbers $\lambda = 0, 1, \ldots$ and $m = \pm\lambda$. If the function $V(\xi, \eta)$ fulfills the condition $V(\xi, -\eta) = V(\xi, \eta)$ (for example, for a homonuclear molecule with equivalent cores), the Hamiltonian $\hat{\mathrm{h}}$ also possesses inversion symmetry with respect to the midpoint between the nuclei,

$$\xi \to \xi, \qquad \eta \to -\eta, \qquad \phi \to \phi + \pi. \tag{2.17}$$

The eigenvalue $\wp$ of the inversion operator is equal to 1 for *gerade* and to -1 for *ungerade* states. The complete set of orbital quantum numbers is specified by $\gamma \equiv \{\lambda, m, [\wp]\}$ (square brackets are used for optional quantum numbers). Since the energy does not depend on m, $|\gamma| \equiv \{\lambda, [\wp]\}$ is introduced. For example, in the case of H_2^+ orbitals with symmetry σ_g and π_u correspond to $|\gamma| = \{0, 1\}$ and $\{1, -1\}$, respectively.

Using the rotational symmetry of the OESE,

$$\hat{\mathrm{h}}\, \psi_\nu^\gamma = \epsilon_\nu^{|\gamma|}\, \psi_\nu^\gamma, \tag{2.18}$$

the orbitals ψ_ν^γ can be written as

$$\psi_\nu^\gamma(\xi, \eta, \phi) = \frac{1}{\sqrt{2\pi}}\, \psi_\nu^{|\gamma|}(\xi, \eta)\, e^{\mathrm{i}m\phi}. \tag{2.19}$$

If the potential $V(\xi, \eta)$ has the form

$$V(\xi, \eta) = -\frac{2}{R^2(\xi^2 - \eta^2)}\, \{Z_\xi(\xi) + Z_\eta(\eta)\} \tag{2.20}$$

with functions $Z_\xi(\xi)$ and $Z_\eta(\eta)$ depending on a single variable, the OESE is separable. As an example, consider the Hamiltonian $\hat{\mathrm{h}}$ that describes the motion of an electron in the Coulomb field of two nuclei with charge Z_A and Z_B,

$$V = -\frac{Z_A}{r_A} - \frac{Z_B}{r_B}. \tag{2.21}$$

Then, substituting (2.8) into (2.21) and transforming to the form (2.20), one obtains

$$Z_\xi(\xi) = (Z_B + Z_A)\, R\, \xi, \qquad Z_\eta(\eta) = (Z_B - Z_A)\, R\, \eta. \tag{2.22}$$

In case of separability of the OESE the orbitals can be written as

$$\psi_\nu^\gamma(\xi, \eta, \phi) \;=\; \mathcal{N}_\nu^{|\gamma|}\; \Xi_\nu^{|\gamma|}(\xi)\, \Pi_\nu^{|\gamma|}(\eta)\; e^{\mathrm{i}m\phi}, \tag{2.23}$$

where $\mathcal{N}_\nu^{|\gamma|}$ is a normalization factor. Substituting (2.11), (2.16), (2.20), and (2.23), the equation (2.18) can be transformed into the set of eigenvalue equations for $\Xi_\nu^{|\gamma|}(\xi)$ and $\Pi_\nu^{|\gamma|}(\eta)$

$$\begin{aligned}&\left(-\frac{\partial}{\partial\xi}\left[(\xi^2-1)\frac{\partial}{\partial\xi}\right] + \frac{\lambda^2}{\xi^2-1} - Z_\xi(\xi) - \frac{R^2}{2}\epsilon_\nu^{|\gamma|}\xi^2\right)\Xi_\nu^{|\gamma|}(\xi) = A^\xi(\epsilon_\nu^{|\gamma|})\Xi_\nu^{|\gamma|}(\xi)\\ &\left(-\frac{\partial}{\partial\eta}\left[(1-\eta^2)\frac{\partial}{\partial\eta}\right] + \frac{\lambda^2}{1-\eta^2} - Z_\eta(\eta) + \frac{R^2}{2}\epsilon_\nu^{|\gamma|}\eta^2\right)\Pi_\nu^{|\gamma|}(\eta) = A^\eta(\epsilon_\nu^{|\gamma|})\Pi_\nu^{|\gamma|}(\eta)\end{aligned} \tag{2.24}$$

where the eigenvalues $A^\xi(\epsilon_\nu^{|\gamma|})$ and $A^\eta(\epsilon_\nu^{|\gamma|})$ connect Eqs.(2.24) via the condition

$$A^\xi(\epsilon_\nu^{|\gamma|}) + A^\eta(\epsilon_\nu^{|\gamma|}) = 0. \tag{2.25}$$

In order to solve the OESE two sets of B splines are introduced. The first set comprises n_ξ B splines $B_r(\xi)(r = 1..n_\xi)$ of order k_ξ for variable ξ. The knot sequence $\{\xi_i^b\}$ is chosen according to

$$1 = \xi_1^b = ... = \xi_{k_\xi}^b < \xi_{k_\xi+1}^b < ... < \xi_{n_\xi+1}^b = ... = \xi_{n_\xi+k_\xi}^b = \xi_{\max}, \tag{2.26}$$

where the basis-set parameter $\xi_{\max}$ defines the size of the elliptical “box” in which the OESE is solved. Similarly, the second set comprises n_η B splines $B_r(\eta)(r = 1..n_\eta)$ of order k_η for variable η, but now using the knot sequence $\{\eta_i^b\}$ according to

$$-1 = \eta_1^b = ... = \eta_{k_\eta}^b < \eta_{k_\eta+1}^b < ... < \eta_{n_\eta+1}^b = ... = \eta_{n_\eta+k_\eta}^b = 1. \tag{2.27}$$

Instead of using the B splines directly, the (symmetry dependent) functions

$$X_\alpha^{|\gamma|}(\xi) = (\xi^2-1)^{\frac{\lambda}{2}}\, B_\alpha(\xi) \qquad \text{and} \qquad Y_\beta^{|\gamma|}(\eta) = (1-\eta^2)^{\frac{\lambda}{2}}\, B_\beta(\eta) \tag{2.28}$$

are introduced to correctly describe the square-root singularities at $\xi = 1$ and $\eta = \pm 1$. With the aid of all possible products of $X_\alpha^{|\gamma|}$ and $Y_\beta^{|\gamma|}$, the three-dimensional basis functions

$$U_{\alpha\beta}^\gamma(\xi,\eta,\phi) = \frac{1}{\sqrt{2\pi}}\, X_\alpha^{|\gamma|}(\xi)\, Y_\beta^{|\gamma|}(\eta)\, e^{\mathrm{i}m\phi}. \tag{2.29}$$

are constructed. Similar to Sec. 1.3, the wave functions are enforced to vanish at the box boundary $\xi_{\max}$. Since only $B_{n_\xi}(\xi)$ is nonzero at $\xi_{\max}$, its coefficients should be zero. This is equivalent to the simple omission of $X_{n_\xi}^{|\gamma|}(\xi)$ and the use of only $\tilde{n}_\xi = n_\xi - 1$ functions $X_\alpha^{|\gamma|}(\xi), \alpha = 1..\tilde{n}_\xi$.

While it is in general required to use $\tilde{n}_\eta = n_\eta$ basis functions $Y_\beta^{|\gamma|}(\eta)$, Hamiltonians with inversion symmetry allow the reduction of the number of basis functions to $\tilde{n}_\eta = n_\eta/2$. With the choice of the knot sequence $\{\eta_i^b\}$ according to

$$\eta_r^b = -\eta^b_{n_\eta+k_\eta+1-r} \quad \text{for} \quad r = 1\,..\,n_\eta+k_\eta \tag{2.30}$$

with even value of n_η, the identity $B_\beta(\eta) = B_{n_\eta+1-\beta}(-\eta)$ is fulfilled. Instead of the definition given in Eq. (2.28) the symmetry-adapted functions are defined as

$$Y_\beta^{|\gamma|}(\eta) = (1-\eta^2)^{\frac{\lambda}{2}}\{B_\beta(\eta) + (-1)^\lambda \wp B_{n_\eta+1-\beta}(\eta)\}. \tag{2.31}$$

This leads to correct inversion symmetry of $U^\gamma_{\alpha\beta}$ in Eq.(2.29).

After replacement of the two indices $\alpha = 1..\tilde{n}_\xi$ and $\beta = 1..\tilde{n}_\eta$ by the single index $i = (\alpha-1)\tilde{n}_\eta + \beta$, the OESE is projected onto a set of $\tilde{N} = \tilde{n}_\xi\tilde{n}_\eta$ linear independent basis functions $\{U_i^\gamma\}$. This yields the generalized matrix eigenvalue problem

$$\underline{\mathbf{h}}^{|\gamma|}\vec{C}^{|\gamma|} = \epsilon^{|\gamma|}\,\underline{\mathbf{S}}^{|\gamma|}\vec{C}^{|\gamma|} \tag{2.32}$$

with

$$\underline{\mathbf{h}}_{ij}^{|\gamma|} = \iiint\limits_{\mathrm{V}} \mathrm{d}v\; U_i^{\gamma *}\hat{\mathrm{h}}\,U_j^\gamma \;\; \text{and} \;\; \underline{\mathbf{S}}_{ij}^{|\gamma|} = \iiint\limits_{\mathrm{V}} \mathrm{d}v\; U_i^{\gamma *}U_j^\gamma \tag{2.33}$$

where dv is given by Eq. (2.9) and V is the integration volume corresponding to the ellipsoid bounded by $\xi_{\max}$. Due to the local support of B splines the matrices $\underline{\mathbf{h}}_{ij}^{|\gamma|}$ and $\underline{\mathbf{S}}_{ij}^{|\gamma|}$ are banded. This property is efficiently considered when the diagonalization is performed e.g. with LAPACK subroutine DSBGVX that also accounts for the symmetry of the matrices. The integration over angle ϕ in Eq. (2.33) can easily be performed. The remaining two-dimensional integrals have to be solved numerically (for example, by Gaussian quadrature). If the potential $V(\xi,\eta)$ is of the form (2.20), it is, however, possible to write the integrals as linear combinations of products of one-dimensional integrals. Each of them is a sum of integrals over intervals between neighbor knot points. In the case of a Coulomb field (2.22) the integrands are polynomials at most of order $2(k_\xi+\lambda)$ or $2(k_\eta+\lambda)$ and Gaussian quadrature of order $k_\xi+\lambda$ or $k_\eta+\lambda$ yields exact results.

The diagonalization subroutine provides a set of eigenvalues $\epsilon_\nu^{|\gamma|}$, sorted in ascending order ($\nu = 1..\tilde{N}$), and (optionally) the corresponding coefficients $C_{\nu,i}^{|\gamma|}$. The orbitals

(2.18) are thus given as

$$\psi_\nu^\gamma(\xi,\eta,\phi) = \sum_{i=1}^{\tilde{N}} C_{\nu,i}^{|\gamma|}\, U_i^\gamma(\xi,\eta,\phi). \tag{2.34}$$

Even if the potential $V(\xi,\eta)$ allows separability, the described procedure does not provide orbitals of the form given in Eq.(2.23), because every coefficient in Eq.(2.34) belongs to a pair of basis functions with respect to ξ and η. This does not only lead to a longer expansion than necessary ($\tilde{n}_\xi \tilde{n}_\eta$ instead of $\tilde{n}_\xi + \tilde{n}_\eta$), but, even more importantly, does not allow the significant simplification in the evaluation of one- and two-electron integrals that is discussed for the latter ones below (see Eq.(2.51)). Therefore, the following procedure for obtaining the eigenvectors is implemented for the case of separable Hamiltonians. Only the eigenvalues $\epsilon_\nu^{|\gamma|}$ of Eq.(2.32) are calculated as described above. Then for every eigenvalue $\epsilon_\nu^{|\gamma|}$ the Eqs.(2.24) are projected onto the sets of basis functions $\{X_\alpha^{|\gamma|}\}$ and $\{Y_\beta^{|\gamma|}\}$. The resulting two generalized matrix eigenvalue problems are again solved (including calculation of the eigenvectors) using subroutine DSBGVX. Out of the obtained eigenvalue sets $\{A^\xi(\epsilon_\nu^{|\gamma|})\}$ and $\{A^\eta(\epsilon_\nu^{|\gamma|})\}$ that pair $A^\xi_{\alpha_\nu}(\epsilon_\nu^{|\gamma|})$ and $A^\eta_{\beta_\nu}(\epsilon_\nu^{|\gamma|})$ is chosen, whose sum is close to zero (see Eq.(2.25). The eigenvectors $\{C_{\nu,\alpha}^{|\gamma|}\}$ and $\{C_{\nu,\beta}^{|\gamma|}\}$ belonging to this pair of eigenvalues define the orbital with energy $\epsilon_\nu^{|\gamma|}$ in the form of Eq.(2.23) with

$$\Xi_\nu^{|\gamma|}(\xi) = \sum_{\alpha=1}^{\tilde{n}_\xi} C_{\nu\alpha}^{|\gamma|}\, X_\alpha^{|\gamma|}(\xi) \quad \text{and} \quad \Pi_\nu^{|\gamma|}(\eta) = \sum_{\beta=1}^{\tilde{n}_\eta} C_{\nu\beta}^{|\gamma|}\, Y_\beta^{|\gamma|}(\eta). \tag{2.35}$$

Note, that if the functions $Y_\beta^{|\gamma|}(\eta)$ are defined according to Eq. (2.31) the function $\Pi_\nu^{|\gamma|}(\eta)$ satisfies

$$\Pi_\nu^{|\gamma|}(-\eta) = (-1)^\lambda \wp \Pi_\nu^{|\gamma|}(\eta). \tag{2.36}$$

It is useful to specify the orbitals ψ_ν^γ in Eq. (2.23) by the numbers N_ξ and N_η of nodes of the functions $\Xi_\nu^{|\gamma|}(\xi)$ and $\Pi_\nu^{|\gamma|}(\eta)$. In fact, the set $\{N_\xi, N_\eta, m\}$ can be used to uniquely identify an orbital, alternative to the set $\{\nu,\gamma\}$, and can be also treated as the set of quantum numbers (see Fig. 2.2 for an example). The physical meaning of N_ξ and N_η can be well understood in the united-atom-limit case. Consider the nuclei with changes $Z_A = Z_B = Z/2$ and $R \to 0$. Applying Eq. (2.7) to Eq. (2.24) it can be derived that

$$\begin{array}{lcllcl} \Xi_\nu^{|\gamma|}(\xi) & \approx & R_{nl}(r), & n & = & N_\xi + N_\eta + \lambda + 1, \\ \Pi_\nu^{|\gamma|}(\eta) e^{im\phi} & \approx & Y_{lm}(\hat{\mathbf{r}}), & l & = & N_\eta + \lambda, \end{array} \tag{2.37}$$

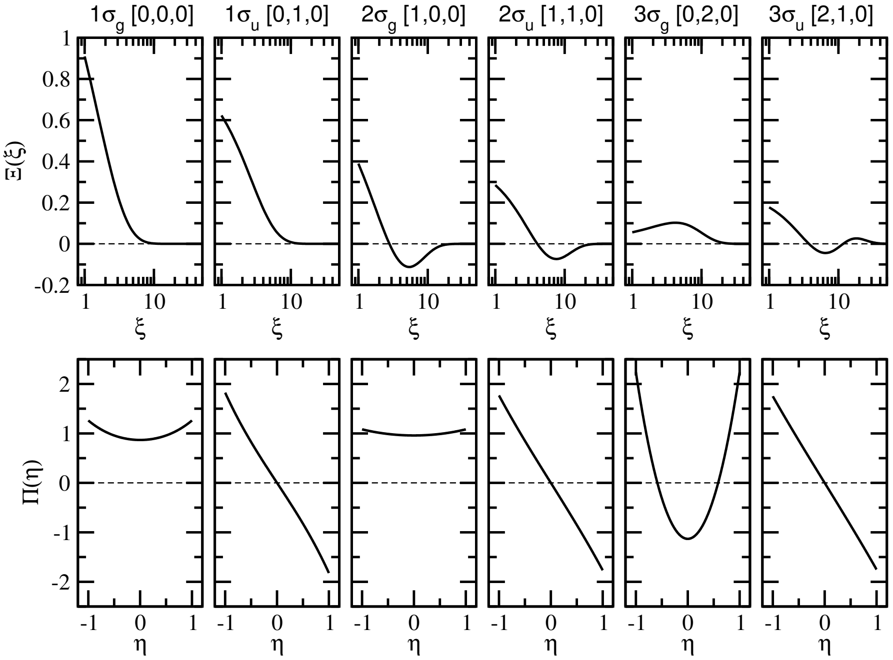

Figure 2.2.: Functions $\Xi_\nu^{|\gamma|}(\xi)$ and $\Pi_\nu^{|\gamma|}(\eta)$ for low-lying bound states of H_2^+ at $R = 2.0\,a_0$. Both $\nu\gamma$ and $\{N_\xi, N_\eta, m\}$ are used to specify the orbitals.

provided both $\Xi_\nu^{|\gamma|}$ and $\Pi_\nu^{|\gamma|}$ are properly normalized. Here $R_{nl}(r)$ is the radial wavefunction of hydrogenic atom with the charge Z, with the principal quantum number n and the angular momentum l, while $Y_{lm}(\hat{\mathbf{r}})$ is a spherical harmonic. Thus, for $R \to 0$ the orbital (2.23) with the set $\{N_\xi, N_\eta, m\}$ is equivalent to the hydrogenic orbital with the quantum numbers $\{n, l, m\}$. (Because of the box boundary condition this is not always the case for numerically calculated orbitals).

Using these relations it is possible to select configurations for the subsequent CI calculations in a more intuitive way (as is discussed below in Sec. 3.1). Even in the case of non-separability (as long as it is weak) it is possible to characterize the orbitals by two numbers that are related to the nodal structure. Since Eqs.(2.24) are the Sturm-Liouville problem, the number of nodes can be determined from the indices α_ν and β_ν. For $\Xi_\nu^{|\gamma|}(\xi)$ one finds $N_\nu^\xi = \alpha_\nu - 1$. For $\Pi_\nu^{|\gamma|}(\eta)$ one finds $N_\nu^\eta = \beta_\nu - 1$, if the basis functions $Y_\beta^{|\gamma|}(\eta)$ are chosen according to Eq.(2.28), and $N_\nu^\eta = 2\beta_\nu - (3 + (-1)^\lambda \wp)/2$, if the $Y_\beta^{|\gamma|}(\eta)$ are chosen according to Eq.(2.31).

For the purpose of illustration, Fig. 2.3 shows electronic potential energies $E(R)$ of the H_2^+ and HeH^{++} molecules obtained with the present method. In order to present the

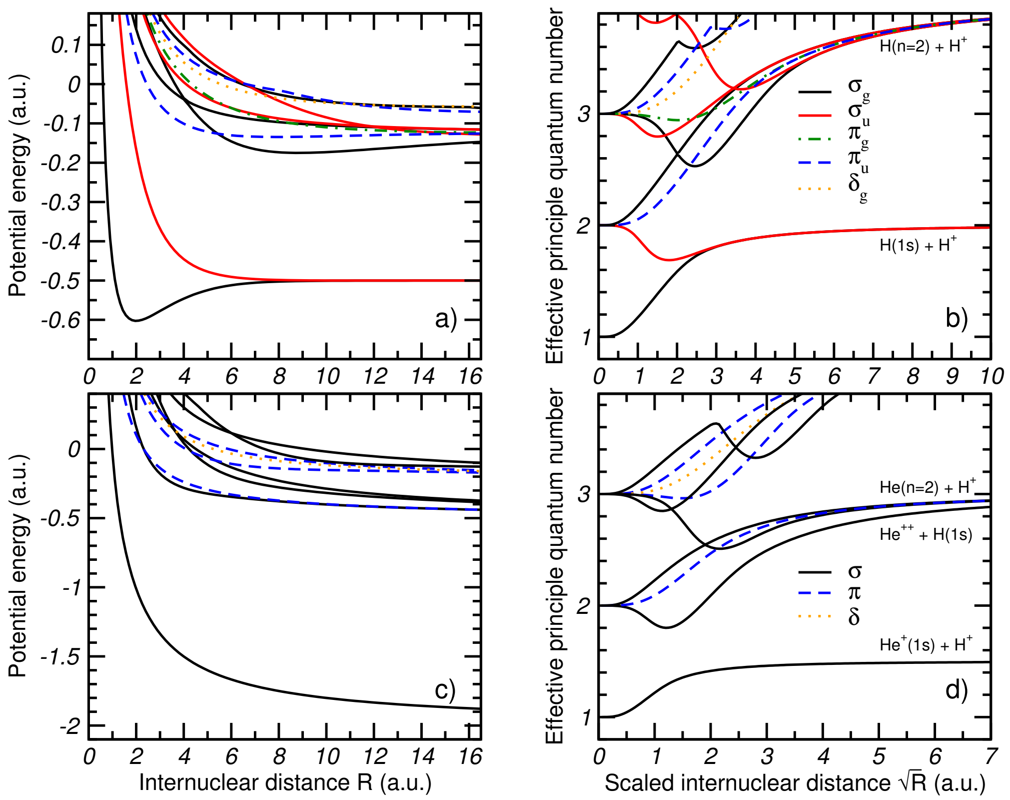

Figure 2.3.: Low-lying bound states of H_2^+ (a,b) and HeH^{++} (c,d) molecules. **a,c**) Molecular potential energy $E(R)$ as a function of the internuclear distance R. **b,d**) Effective principle quantum number $n^* = (Z_A + Z_B)/\sqrt{2E_{\text{bind}}}$, where E_{bind} being the binding energy, versus the square root of the internuclear distance R.

obtained energies in a wide region of internuclear separations, Figs. 2.3 b and 2.3 d show the effective principle quantum number $n^* = (Z_A + Z_B)/\sqrt{2E_{\text{bind}}}$ which depends on the binding energy $E_{\text{bind}} = E(R) - (Z_A Z_B)/R$ of the molecular ion. In addition, a scaled abscissa axis is used. Such a representation allows one to demonstrate how the molecular energies converge to both the united-atom limit (where the system reduces to a one-electron atom with the nuclear charge $Z_A + Z_B$) and the dissociation limit (where the system reduces to two non-interacting atoms).

Since all orbitals are enforced to be zero at $\xi_{\max}$, box discretization is employed in the present approach. Consequently, all orbitals are normalized to one, independently on whether they represent bound or continuum solutions. In one-electron calculations involving the continuum (for example, photoionization of H_2^+) it is, however, necessary to adopt energy normalization for the continuum orbitals. This can be achieved either

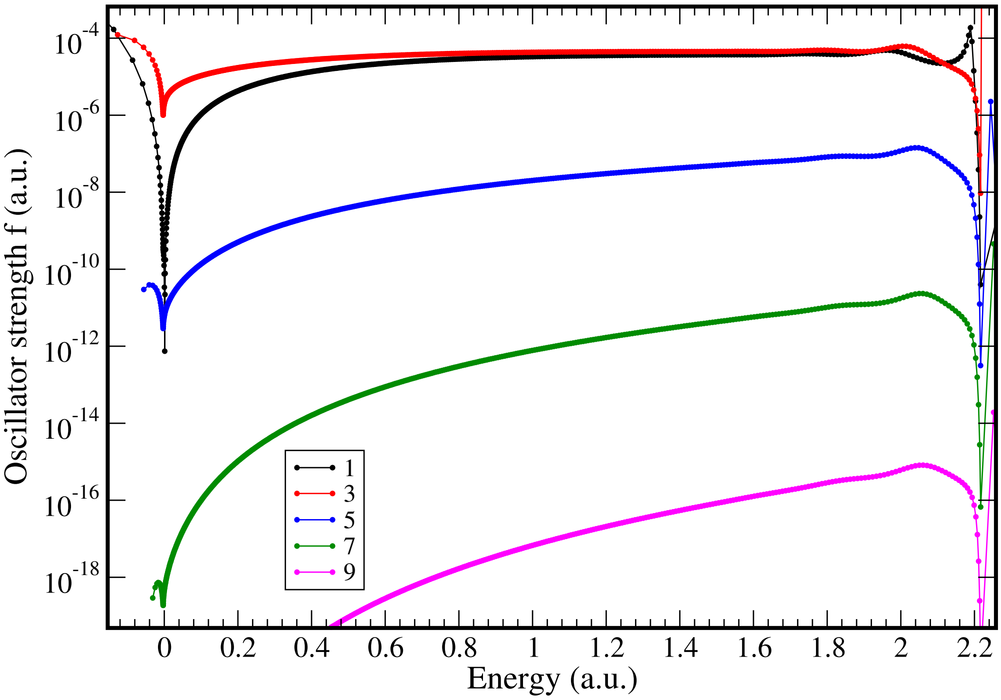

Figure 2.4.: Oscillator strengths from the ground state $1\sigma_g$ of H_2^+ to computed σ_u orbitals with different N_η.

by fitting the orbitals (close to the box boundary) to the known asymptotic behavior or using the density of states.

Since N_η is a good quantum number, it can be used to distinguish between different continuum channels, instead of the angular momentum l in the case of a single-electron atom. This possibility is demonstrated in Fig. 2.4 where the oscillator strengths f,

$$f_{ij} = 2(E_j - E_i)\, |\langle i\, |z|\, j\rangle|^2 \, , \tag{2.38}$$

for transitions from the ground state $1\sigma_g$ of H_2^+ to computed σ_u orbitals with different N_η are shown. The electronic-structure calculation was performed for the internuclear distance $R = 2.0\, a_0$ using the box size $\xi_{\max} = 700$ and 500 B splines for variable η. Due to symmetry, N_η may possess only an odd value, and the oscillator strengths f to orbitals with $N_\eta = 1$ and 3 are evidently stronger (Fig. 2.4) compared to those with higher N_η. As one can see, the oscillator strengths f belonging to the same N_η can be joined by a smooth line (in fact, the density of points is so high that individual points are often indistinguishable), and thus the interpolation procedure can be efficiently performed to calculate the contribution of continuum channels at an arbitrary energy $0 < E < E_{\mathrm{cr}}$ where the value of the critical energy $E_{\mathrm{cr}} = 2\,\mathrm{a.u.}$ can be inferred from the figure. Substituting relation (2.7) in Eq. (1.29) yields the following expression for an estimation of the critical energy

$$E_{\mathrm{cr}} \approx 3 \left(\frac{2s}{R\xi_{\mathrm{max}}} \right)^2 \tag{2.39}$$

which yields $E_{\mathrm{cr}} = 1.5\,\mathrm{a.u.}$ for the discussed case. In order to calculate the density of states one has to consider separately orbitals belonging to different N_η. However, if the orbitals are used in a CI calculation, they should not be energy renormalized, even if one is interested in continuum properties of the two-electron system. In fact, the orbitals should in this case only be seen as basis functions. Therefore, even the non-physical pseudo-states necessarily obtained in a box-discretized calculation (due to the infinite Rydberg series represented by a finite basis) are important ingredients for a subsequent CI calculation.

2.4. Two-electron basis set and configuration-interaction approach

As a basis set for solving the two-electron Schrödinger equation,

$$\hat{\mathrm{H}}(1,2)\Psi(1,2) = \Big(\hat{\mathrm{h}}(1) + \hat{\mathrm{h}}(2) + \frac{1}{r_{12}} + V_{AB}(R)\Big)\Psi(1,2) = E\Psi(1,2), \tag{2.40}$$

linear combinations of the orbitals [given either in Eqs. (2.23) and (2.35) or in Eqs. (2.34) and (2.29)] are used. The potential $V_{AB}(R)$ is either the Coulomb interaction $Z_A Z_B/R$ between the nuclei or describes the interaction between two cores. Let Γ specify the full set of quantum numbers, $\Gamma \equiv \{\Lambda, M, S, [\mathcal{P}, \mathcal{P}^\Sigma]\}$, where $\Lambda = 0, 1, \ldots$ is the absolute value of the component of the total angular momentum along the internuclear axis $(\Sigma, \Pi, \ldots)$, $M = \pm\Lambda$ and the total spin $S = 0, 1$. The optional quantum numbers $\mathcal{P}$ and $\mathcal{P}^\Sigma$ specify the parity with respect to inversion symmetry (*gerade* or *ungerade*, cf. Eq. (2.17)) and, for Σ states only, with respect to a reflection at a plane through the nuclei,

$$\xi_i \to \xi_i, \qquad \eta_i \to \eta_i, \qquad \phi_i \to -\phi_i. \tag{2.41}$$

The last transformation is equivalent to a complex conjugation of the wave function, if the normalization of the latter is chosen in such a way, that only its angular part is complex.

Normalized and fully symmetry-adapted configurations Υ_i^Γ are used in the CI calculations. The configurations are build with the aid of products of two orbitals $|\nu\gamma\ \bar{\nu}\bar{\gamma}\rangle \equiv \psi_\nu^\gamma(\xi_1,\eta_1,\phi_1)\psi_{\bar{\nu}}^{\bar{\gamma}}(\xi_2,\eta_2,\phi_2)$ with $\bar{\gamma} \equiv \{\bar{\lambda},\bar{m},[\bar{\wp}]\}$. For a given configuration $\Upsilon_i^\Gamma \equiv [\nu\gamma\,\bar{\nu}\bar{\gamma}]$ the orbitals $\nu\gamma$ and $\bar{\nu}\bar{\gamma}$ satisfy the conditions $m+\bar{m}=M$ and $\wp\bar{\wp}=\mathcal{P}$. For non-Σ states ($\Lambda \neq 0$) particle-exchange symmetry is considered using

$$[\nu\gamma\,\bar{\nu}\bar{\gamma}]_{\Lambda\neq 0} = \frac{|\nu\gamma\ \bar{\nu}\bar{\gamma}\rangle + (-1)^S|\bar{\nu}\bar{\gamma}\ \nu\gamma\rangle}{\sqrt{2(1+\delta_{\nu\bar{\nu}}\delta_{\gamma\bar{\gamma}})}} \quad . \tag{2.42}$$

For Σ states ($\Lambda = 0$) inclusion of the additional reflection symmetry leads to (note the misprint in [61])

$$[\nu\gamma\,\bar{\nu}\bar{\gamma}]_{\Lambda=0} = \frac{\big(|\nu\gamma\ \bar{\nu}\bar{\gamma}\rangle + (-1)^S|\bar{\nu}\bar{\gamma}\ \nu\gamma\rangle\big) + \mathcal{P}^\Sigma\big(|\nu\gamma\ \bar{\nu}\bar{\gamma}\rangle + (-1)^S|\bar{\nu}\bar{\gamma}\ \nu\gamma\rangle\big)^*}{\sqrt{4(1+\delta_{\nu\bar{\nu}}\delta_{|\gamma||\bar{\gamma}|})(1+\delta_{0m}\delta_{0\bar{m}})}} \tag{2.43}$$

where it was used that two different orbitals with the same ν and $|\gamma|$ can be obtained from each other by complex conjugation. Using the relation

$$\begin{aligned} |\nu\gamma\ \bar{\nu}\bar{\gamma}\rangle^* &\equiv |\nu\{\lambda,m,[\wp]\}\ \bar{\nu}\{\bar{\lambda},\bar{m},[\bar{\wp}]\}\rangle^* \\ &= |\nu\{\lambda,-m,[\wp]\}\ \bar{\nu}\{\bar{\lambda},-\bar{m},[\bar{\wp}]\}\rangle \equiv ||\nu\gamma^*\ \bar{\nu}\bar{\gamma}^*\rangle, \end{aligned} \tag{2.44}$$

configuration (2.43) can finally be represented as a linear combination of products of two orbitals. Clearly, the choice of $\nu\gamma$ and $\bar{\nu}\bar{\gamma}$ has always to be done in such a way that a double occurrence of the same configuration is prevented. The two-electron problem

$$\hat{\mathrm{H}}(1,2)\Psi_\mu^\Gamma(1,2) = E_\mu^\Gamma\Psi_\mu^\Gamma(1,2) \tag{2.45}$$

is solved by an expansion of the wave functions as linear combinations of N_Γ configurations,

$$\Psi_\mu^\Gamma(1,2) = \sum_{i=1}^{N_\Gamma} C_{\mu i}^\Gamma \Upsilon_i^\Gamma(1,2). \tag{2.46}$$

Due to the orthonormality of the set $\{\Upsilon_i^\Gamma\}$ the ordinary matrix eigenvalue problem

$$\underline{\mathbf{H}}^\Gamma\mathbf{C}^\Gamma = E^\Gamma\,\mathbf{C}^\Gamma \quad \text{with} \quad \underline{\mathbf{H}}_{ij}^\Gamma = \int_{V_1}\int_{V_2} dv_1\,dv_2 \Upsilon_i^{\Gamma *}(1,2)\hat{\mathrm{H}}(1,2)\Upsilon_j^\Gamma(1,2) \tag{2.47}$$

is obtained. The coefficients $\{C_{\mu i}^\Gamma\}$ and energies E_μ^Γ are calculated using LAPACK subroutine DSPEVX. The CI matrix elements $\underline{\mathbf{H}}_{ij}^\Gamma$ comprise one- and two-electron integrals. The evaluation of the one-electron integrals is trivial, because the orbitals are solutions of the one-electron Hamiltonian. Thus one finds

$$\langle \nu\gamma\ \bar{\nu}\bar{\gamma} | \hat{\mathrm{h}}(1) + \hat{\mathrm{h}}(2) |\ \nu'\gamma'\bar{\nu}'\bar{\gamma}' \rangle = (\epsilon_{\nu}^{|\gamma|} + \epsilon_{\bar{\nu}}^{|\bar{\gamma}|})\, \delta_{\nu\nu'}\, \delta_{\gamma\gamma'}\, \delta_{\bar{\nu}\bar{\nu}'}\, \delta_{\bar{\gamma}\bar{\gamma}'}. \tag{2.48}$$

Using the von Neumann expansion (2.12) the two-electron integrals can be written after some further simplifications [62] as

$$\begin{aligned} \langle \nu\gamma\ \bar{\nu}\bar{\gamma} | \frac{1}{r_{12}} |\ \nu'\gamma'\bar{\nu}'\bar{\gamma}' \rangle = \frac{R^5}{16} \sum_{\ell=\rho}^{\infty} S_{\ell}^{\rho} \Bigg\{ & \frac{Q_{\ell}^{\rho}(\xi_{\max})}{P_{\ell}^{\rho}(\xi_{\max})} F_{\nu\nu'\ell}^{|\gamma||\gamma'|\rho}(\xi_{\max}) F_{\bar{\nu}\bar{\nu}'\ell}^{|\bar{\gamma}||\bar{\gamma}'|\rho}(\xi_{\max}) \\ & + (-1)^{\rho} \frac{(\ell+\rho)!}{(\ell-\rho)!} \int_1^{\xi_{\max}} d\,\xi \frac{F_{\nu\nu'\ell}^{|\gamma||\gamma'|\rho}(\xi) F_{\bar{\nu}\bar{\nu}'\ell}^{|\bar{\gamma}||\bar{\gamma}'|\rho}(\xi)}{(\xi^2-1)[P_{\ell}^{\rho}(\xi)]^2} \Bigg\} \end{aligned} \tag{2.49}$$

where $\rho = |m' - m| = |\bar{m}' - \bar{m}|$, and

$$F_{\nu\nu'\ell}^{|\gamma||\gamma'|\rho}(\xi) = \int_1^{\xi} d\,\zeta P_{\ell}^{\rho}(\zeta) \int_{-1}^{1} d\,\eta P_{\ell}^{\rho}(\eta) \psi_{\nu}^{|\gamma|}(\zeta,\eta) \psi_{\nu'}^{|\gamma'|}(\zeta,\eta)(\zeta^2 - \eta^2). \tag{2.50}$$

In case of separability of the OESE the integral function $F_{\nu\nu'\ell}^{|\gamma||\gamma'|\rho}(\xi)$ reduces to a product of one-dimensional integrals,

$$\begin{aligned} F_{\nu\nu'\ell}^{|\gamma||\gamma'|\rho}(\xi) = \mathcal{N}_{\nu}^{|\gamma|} \mathcal{N}_{\nu'}^{|\gamma'|} & \int_1^{\xi} d\,\zeta P_{\ell}^{\rho}(\zeta) \Xi_{\nu}^{|\gamma|}(\zeta) \Xi_{\nu'}^{|\gamma'|}(\zeta) \\ & \times \int_{-1}^{1} d\,\eta P_{\ell}^{\rho}(\eta) \Pi_{\nu}^{|\gamma|}(\eta) \Pi_{\nu'}^{|\gamma'|}(\eta)(\zeta^2 - \eta^2). \end{aligned} \tag{2.51}$$

For Hamiltonians with inversion symmetry the functions $F_{\nu\nu'\ell}^{|\gamma||\gamma'|\rho}(\xi)$ are equal to zero, if the condition $\wp\wp' = (-1)^{\ell+1}$ is fulfilled. Indeed, from $P_{\ell}^{\rho}(-\eta) = (-1)^{\ell+\rho} P_{\ell}^{\rho}(\eta)$ and (2.36) follows

$$P_{\ell}^{\rho}(-\eta) \Pi_{\nu}^{|\gamma|}(-\eta) \Pi_{\nu'}^{|\gamma'|}(-\eta) = (-1)^{\ell+\lambda+\lambda'+\rho} \wp\wp' P_{\ell}^{\rho}(\eta) \Pi_{\nu}^{|\gamma|}(\eta) \Pi_{\nu'}^{|\gamma'|}(\eta), \tag{2.52}$$

where $(-1)^{\lambda+\lambda'+\rho} = 1$ for any m and m', as can be easily shown from the definition of ρ. Thus, in (2.51) the integrals with respect to η are equal to zero for $\wp\wp' = (-1)^{\ell+1}$, since in this case their integrands are odd functions with respect to η. If function $F_{\nu\nu'\ell}^{|\gamma||\gamma'|\rho}(\xi)$ is non-zero, the ratio $F_{\nu\nu'\ell}^{|\gamma||\gamma'|\rho}(\xi)/(\xi - 1)^t$ with $t = (\rho + \lambda + \lambda')/2 + 1$ remains finite even in the limit $\xi \to 1$. Since $(\xi^2 - 1)[\hat{P}_{\ell}^{\rho}(\xi)]^2 \xrightarrow{\xi \to 1} B(\xi - 1)^{\rho+1}$ where B is a non-zero constant, one obtains

$$\frac{F^{|\gamma||\gamma'|\rho}_{\nu\nu'\ell}(\xi)F^{|\bar{\gamma}||\bar{\gamma}'|\rho}_{\bar{\nu}\bar{\nu}'\ell}(\xi)}{(\xi^2-1)[\hat{P}^{\rho}_{\ell}(\xi)]^2} \xrightarrow{\xi\to 1} D(\xi-1)^{\lambda+\lambda'+\bar{\lambda}+\bar{\lambda}'+1}, \qquad \text{with} \qquad D = \text{const.} \tag{2.53}$$

Since $(\xi^2-1)[\hat{P}^{\rho}_{\ell}(\xi)]^2 \neq 0$ at any point $\xi \in (1, \xi_{\max}]$, the integrand has no singularities within $\xi \in [1, \xi_{\max}]$ and Gaussian quadrature can be used to calculate this integral. It is important to mention that the variety of $F^{|\gamma||\gamma'|\rho}_{\nu\nu'\ell}(\xi)$ functions is much smaller than the number of two-electron integrals. The storage of the values of the functions $F^{|\gamma||\gamma'|\rho}_{\nu\nu'\ell}(\xi)$ at Gaussian quadrature roots allows the simultaneous calculation of all two-electron integrals. This speeds up the calculations significantly.

2.5. Description of alkali dimers

Alkali metals (Li, Na, K, Rb, Cs, Fr) consist of a 'noble gas' core with effective charge equal to unity and a single weakly bound s electron outside the core. Therefore, it is similar to a hydrogen atom, with the only difference that the core is not a point charge and, therefore, one has to account for screening and polarization effects. The simple valence structure has stimulated the development of many approaches, such as model potential methods, frozen-core all-electron methods (MCSCF or valence CI), and non-empirical effective and pseudopotential methods, which were first formulated for alkali atoms and were later generalized to describe also alkali dimers (cations and neutrals) [63–69]. These different methods have in common that they attempt to accurately describe the correlated motions of the valence electrons and reduce the dimensionality of the original many-electron problem by simplifying the treatment of the interaction between valence and core electrons.

Asymptotically, the leading terms of the valence-core interaction have a simple analytical form and usually can be modeled reliably. At short range, on the other hand, the valence-core interaction is extremely complicated and its nonlocal and energy-dependent nature makes it difficult to approximate in terms of local operators. Nevertheless, it appears that many properties of the system do not depend sensitively on the detailed form of the short-range part of the valence-core interaction, and thus it can be replaced effectively by a local potential. Semi-local (e.g. angular-momentum dependent) and nonlocal potentials may be employed to improve accuracy. However, the use of nonlocal terms will increase the complexity of the calculation.

Different methods use different ways to simplify the valence-core interaction. Despite the often inconsistently used and thus quite confusing terminology, one can distinguish terms 'effective', 'pseudo-', and 'model' potentials in the following way[1]. Whereas an effective potential is obtained by projections of some exact wavefunctions onto a finite model space, a pseudopotential is obtain through simulation techniques, i.e. minimization of the distance between the exact and pseudo-operators in a reduced subspace. In contrast to effective and pseudopotentials that are obtained by means of well defined mathematical procedures, a model potential is generally parameterized from experiment and has, therefore, a much simpler form. Usually, the model potential is represented by an analytical function depending on a set of parameters, determined by minimizing the root-mean-square deviation between observed and calculated energies.

Being the simplest of all discussed methods, the model potential method is the most appropriate for an extension of the B-spline based CI method described above. Various implementations of the model potential method have been developed by several authors that differ by either the form of the atomic model potential or the treatment of two-body and three-body polarization effects. One can roughly distinguish between two approaches. In the first, developed by Dalgarno and coworkers [70–72], the atomic potential includes the Hartree-Fock potential, the correct asymptotic description of core polarization, and a short-range parametric function. Due to the number of parameters used, it was however impossible to unambiguously determine parameters from a fitting to experimental energies. In the second approach, developed by Klapish and Aymar [73, 74], only three parameters are used to describe the atomic potential, which has however no explicit polarization term. Both approaches yield comparably good results both for atomic energies and wavefunctions. In accordance with recent literature performing model potential calculations for alkali dimers [75–78], the present work employs the Klapish model potential.

Consider one or two electrons moving in the field of two ionic cores, A and B. The interaction of an active electron labeled i (for a neutral alkali dimer $i = 1, 2$, for a cation the label can be omitted) with the ionic cores is given by

$$V_i = V_{\mathrm{Kl}}^{(A)}(r_{iA}) + V_{\mathrm{Kl}}^{(B)}(r_{iB}) + V_{\mathrm{pol}}^{(A)}(\mathbf{r}_{iA}, R) + V_{\mathrm{pol}}^{(B)}(\mathbf{r}_{iB}, R) \tag{2.54}$$

where $\mathbf{r}_{ic}$ is the vector pointing from the core c ($c =$ A, B) to the active electron i. Here,

---

[1] This terminology has been proposed in [68]

the function $V_{\mathrm{Kl}}^{(c)}(r)$ represents the Klapish model potential [73]

$$V_{\mathrm{Kl}}^{(c)}(r) = -\frac{1}{r} - \frac{Z^{(c)} - 1}{r}[e^{-\gamma_1^{(c)} r} + \gamma_2^{(c)}\, r\, e^{-\gamma_3^{(c)} r}] \tag{2.55}$$

where $Z^{(c)}$ is the nuclear charge, $\gamma_j^{(c)}$ are the Klapish parameters as reported in [79] (due to the difference in the way the potential is written, the value of $\gamma_2^{(c)}$ from [79] is divided by $(Z^{(c)} - 1)$ before being employed in the actual calculation). The polarization term $V_{\mathrm{pol}}^{(c)}(\mathbf{r}, R)$ describes two-body electron-core polarization and three-body electron-core-core polarization

$$V_{\mathrm{pol}}^{(c)}(\mathbf{r}, R) = -\frac{\alpha_{\mathrm{d}}^{(c)}}{2r^4} f_6\left(\frac{r}{\rho^{(c)}}\right) + s_c \frac{\alpha_{\mathrm{d}}^{(c)}(\mathbf{r} \cdot \vec{R})}{r^3 R^3} f_3\left(\frac{r}{\rho^{(c)}}\right) \tag{2.56}$$

where $f_n(x) = 1 - \exp(-x^n)$ is a cut-off function, $\alpha_{\mathrm{d}}^{(c)}$ $(\rho^{(c)})$ is the static dipole polarizability (cut-off parameter) of the ionic core c [79], and s_c is equal to 1 (-1) for $c =$ A (B). Finally, the so-called core-core interaction is described as a sum of Coulombic and polarization terms:

$$V_{\mathrm{AB}}(R) = \frac{1}{R} - \frac{\alpha_{\mathrm{d}}^{(A)} + \alpha_{\mathrm{d}}^{(B)}}{2R^4} - \frac{\alpha_{\mathrm{q}}^{(A)} + \alpha_{\mathrm{q}}^{(B)}}{2R^6} \tag{2.57}$$

where $\alpha_{\mathrm{q}}^{(c)}$ is the static quadrupole polarizability of the ionic core c.

Substituting Eqs. (2.8) and (2.4) into Eq. (2.54), V_i can be expressed as a function of ξ_i, η_i and used to define $\hat{\mathrm{h}}(i)$ in Eq. (2.16). Note that V_i cannot be transformed to the form given by Eq. (2.20), and therefore no variable separation can be employed when solving the one-electron problem. Since the three-body electron-electron-core polarization effect is neglected in the present treatment, nothing should be changed solving the two-electron problem, except for a substitution of the pure Coulomb interaction between the cores with expression (2.57).

3. Applications of the two-center B-spline based CI method

This chapter gives a few examples for the proper implementation, accuracy, and convergence studies of the two-center B-spline based CI method implemented in this work. Thus, the application of the method to the calculation of energies of the ground and excited states of hydrogen molecule at small internuclear separations is discussed in Sec. 3.1. The discussion includes a careful convergence analysis performed in order to find a recipe for the optimal choice of configuration series. The ability of the present method to numerically treat the electronic continuum for a two-electron molecule is demonstrated in Sec. 3.2 with the example of the HeH^+ molecule. Section 3.3 proves the high accuracy which can be reached with the present method in describing autoionizing doubly-excited states at large internuclear separations. Finally, the applications to alkali dimers is briefly discussed in Sec. 3.4.

3.1. Convergence at small internuclear separations

Since the orbitals used in the CI calculations are solutions of the OESE and thus do not include any electron-electron interaction, they are not suitable for getting very high accuracy with a small number of configurations except for asymmetric excited states[1] [58]. The alternative use of Hartree-Fock orbitals is known to provide more accurate ground-state energies with smaller CI expansions, but those orbitals are not a good starting point for the description of highly lying excited states. On the other hand, the absence of linear dependencies in the present approach allows the use of rather large basis sets. It turns out that instead of simply increasing the number of configurations, a judicious selection of them can lead to significantly improved results. After some tests the following recipe has been developed for small internuclear distances where electronic correlation

---

[1] For example, states where one electron is left in the lowest lying orbital while the other one is highly excited or ionized

Table 3.1.: Convergence analysis of the ground-state energy[a] for a H_2 molecule at $R = 1.4\,a_0$. The fixed basis-set parameters are $\xi_{\max} = 12.0, \tilde{n}_\eta = 10, k_\eta = 6$. (Published in [61].)

	$\tilde{n}_\xi = 9, k_\xi = 7$		$\tilde{n}_\xi = 12, k_\xi = 8$		$\tilde{n}_\xi = 15, k_\xi = 9$		$\tilde{n}_\xi = 18, k_\xi = 10$	
$l_{\max}$	N_Γ	$-E$ [a.u.]	N_Γ	$-E$ [a.u.][b]	N_Γ	$-E$ [a.u.][b]	N_Γ	$-E$ [a.u.][b]
0	45	1.142 225	78	1.142 266(41)	120	1.142 271(05)	171	1.142 273(02)
1	135	1.171 264	234	1.171 340(76)	360	1.171 350(10)	513	1.171 353(03)
2	351	1.173 510	612	1.173 612(102)	945	1.173 628(16)	1350	1.173 633(05)
3	693	1.173 973	1212	1.174 094(121)	1875	1.174 115(21)	2682	1.174 121(07)
4	1242	1.174 126	2178	1.174 258(132)	3375	1.174 283(25)	4833	1.174 291(08)
5	1998	1.174 187	3510	1.174 327(140)	5445	1.174 355(28)	7803	1.174 364(09)
6	3042	1.174 215	5352	1.174 360(145)	8310	1.174 390(30)	11916	1.174 400(10)
7	4374	1.174 230	7704	1.174 378(148)	11970	1.174 409(31)	17172	1.174 420(11)
8	6075	1.174 238	10710	1.174 388(150)	16650	1.174 420(32)		
9	8145	1.174 242	14370	1.174 393(151)				
10	10665	1.174 245						

[a] Literature [54]: $E = -1.174\,475671$ a.u.

[b] In parenthesis the change of energy (in 10^{-6} a.u.) compared to the preceding column is given.

is important. In order to obtain good results it is more important to achieve the largest degree of completeness of the configuration set for some orbital basis than to strive for a high accuracy of the orbitals themselves. A complete configuration set is obtained, if all possible configurations are included that can be formed from all orbitals. Fortunately, those orbitals which in the united-atom limit would have a large angular momentum $l(= N_\eta + \lambda)$ give a small contribution to the energy. Introducing $l_{\max}$ and using only orbitals with $l \leqslant l_{\max}$ (instead of all possible orbitals) allows an efficient reduction of the configuration set.

In order to demonstrate this effect, the ground and some low-lying excited states of H_2 as well as electronic dipole transition moments between them have been calculated using different values of $l_{\max}$. Results of calculations for the ground-state energy of H_2 at $R = 1.4$ a.u. are given in Table 3.1 where they are compared with the best available literature value [54]. (That value was obtained with explicitly correlated basis functions and is supposed to be accurate within about $2 \cdot 10^{-8}$ a. u.) The convergence behavior and the change of the dimension of the CI matrix with respect to an increase of $l_{\max}$ is shown for a fixed box size and different sets of ξ-dependent B-spline parameters. With respect to the η-dependent B-spline parameters $\tilde{n}_\eta, k_\eta$ convergence is already achieved. The box size ($\xi_{\max}$) is chosen in such a way that the ground-state wave function has sufficiently decayed at the box boundary. Therefore, the eigenfunction and thus the energy is not influenced by the infinite wall implied by the box.

The rows in Table 3.1 show the convergence behavior with respect to the radial parameters; namely, with respect to the B-spline basis. The columns demonstrate the

Table 3.2.: Convergence analysis for the 6 lowest-lying $^1\Sigma_u$ states of H_2 at $R = 2.0\,a_0$. The fixed basis-set parameters are $\tilde{n}_\xi = 24, k_\xi = 12, g_\xi = 1.15, \tilde{n}_\eta = 10, k_\eta = 6$. (Published in [61].)

$\xi_{\max}$	$l_{\max}$	$-E_1$ [a.u.]	$-E_2$ [a.u.]	$-E_3$ [a.u.]	$-E_4$ [a.u.]	$-E_5$ [a.u.]	$-E_6$ [a.u.]
40.0	4	0.751 8547	0.665 4215	0.636 6922	0.634 0141	0.619 4238	0.618 6471
40.0	5	0.751 9614	0.665 4492	0.636 7038	0.634 0146	0.619 4244	0.618 6489
60.0	4	0.751 8511	0.665 4206	0.636 9360	0.634 1010	0.624 0293	0.622 6471
60.0	5	0.751 9568	0.665 4480	0.636 9468	0.634 1015	0.624 0350	0.622 6474
80.0	4	0.751 8451	0.665 4188	0.636 9356	0.634 1011	0.624 1910	0.622 7480
80.0	5	0.751 9496	0.665 4458	0.636 9462	0.634 1016	0.624 1962	0.622 7483
100.0	4	0.751 8360	0.665 4159	0.636 9343	0.634 1009	0.624 1916	0.622 7487
100.0	5	0.751 9390	0.665 4426	0.636 9447	0.634 1013	0.624 1967	0.622 7490
Lit. [80]		0.752 0825	0.665 4811	0.636 9602	0.634 1016	0.624 2044	0.622 7488

importance of the angular parameter $l_{\max}$. In order to clarify the idea of completeness the following calculation is instructive. Using the basis set parameters of the last column, a CI calculation with a reduced number of configurations was performed. With the help of the 180 $\sigma_g, \sigma_u, \ldots$ orbitals configuration series $[1\sigma_g : 1..100\sigma_g]$, $[2\sigma_g : 2..25\sigma_g]$, $[3\sigma_g : 3..25\sigma_g]$, $\ldots$, $[25\sigma_g : 25\sigma_g]$ and the analogous ones for σ_u, π_g and π_u were constructed, yielding 1600 configurations and $E = -1.170\,943$ a.u. Comparing to the result obtained with a more than 10 times smaller but complete configuration set (see 2nd row and 1st column of Table 3.1), one notices that the larger basis gives a worse result, even though an apparently better B-spline basis is adopted. While completeness is crucial for small internuclear distances, it is found that for large internuclear distances a different procedure for configuration selection has to be used. In this case it is more important to choose configurations by energy arguments, as will be discussed in Sec. 3.3

If a number of states should simultaneously be calculated, a small box as was used for the ground state is insufficient. An increase of the box size requires the use of an increased number of B splines ($\tilde{n}_\xi$), if a linear knot sequence $\{\xi_i^b\}$ is adopted and the same level of accuracy should be achieved. Alternatively, a non-uniform knot sequence can be used. A geometrically progressive distribution ($\xi_{i+1}^b - \xi_i^b = g_\xi\,(\xi_i^b - \xi_{i-1}^b)$ with $g_\xi > 1$) was found to give satisfactory results with a reasonable number of B splines. As an example, Table 3.2 shows the results for a number of $^1\Sigma_u$ states of H_2 calculated with the same basis set (in fact, obtained within the same calculation) and $g_\xi = 1.15$. Again the values are compared with energies that were obtained with explicitly correlated basis functions [80] but are supposedly less accurate than the ground-state calculation in [54]. Clearly, a too small choice of the box size $\xi_{\max}$ does not give very accurate results, because the boundary condition imposed at $\xi_{\max}$ leads effectively to an artificial

Table 3.3.: Electronic dipole transition moments for H_2 at $R = 2.0\,a_0$. The fixed basis-set parameters are $\xi_{\max} = 40.0, \tilde{n}_\xi = 20, k_\xi = 10, g_\xi = 1.1, \tilde{n}_\eta = 10, k_\eta = 6$. (Published in [61].)

$l_{\max}$	Gauge	$1^1\Sigma_g - 1^1\Sigma_u$	$2^1\Sigma_g - 1^1\Sigma_u$	$3^1\Sigma_g - 1^1\Sigma_u$	$4^1\Sigma_g - 1^1\Sigma_u$
2	l	1.3036	2.4083	1.8113	0.1634
3	l	1.3114	2.3819	1.8104	0.1708
4	l	1.3134	2.3753	1.8047	0.1730
4	v	1.3116	2.3737	1.8039	0.1728
Lit.	l	1.3133[a]	2.3709[c]	1.8003[c]	0.1748[c]
$l_{\max}$	Gauge	$1^1\Sigma_g - 2^1\Sigma_u$	$2^1\Sigma_g - 2^1\Sigma_u$	$3^1\Sigma_g - 2^1\Sigma_u$	$4^1\Sigma_g - 2^1\Sigma_u$
2	l	0.4396	3.0966	5.2911	5.8647
3	l	0.4368	3.1206	5.2248	5.8268
4	l	0.4361	3.1264	5.2213	5.8155
4	v	0.4356	3.1252	5.2315	5.8136
Lit.	l	0.4352[a]	3.1300[c]	5.2191[c]	5.8066[c]
$l_{\max}$	Gauge	$1^1\Sigma_g - 1^1\Pi_u$	$2^1\Sigma_g - 1^1\Pi_u$	$3^1\Sigma_g - 1^1\Pi_u$	$4^1\Sigma_g - 1^1\Pi_u$
2	l	0.8659	3.2515	1.4187	0.6324
3	l	0.8681	3.2440	1.4168	0.6206
4	l	0.8687	3.2442	1.4116	0.6185
4	v	0.8471	0.9476	1.4213	0.6342
Lit.	l	0.8634[b]			
$l_{\max}$	Gauge	$1^1\Sigma_g - 2^1\Pi_u$	$2^1\Sigma_g - 2^1\Pi_u$	$3^1\Sigma_g - 2^1\Pi_u$	$4^1\Sigma_g - 2^1\Pi_u$
2	l	0.3877	1.9037	2.0561	7.8762
3	l	0.3878	1.9134	2.0552	7.8599
4	l	0.3879	1.9154	2.0562	7.8566
4	v	0.3781	1.8884	2.0471	6.5457
Lit.	l	0.3855[b]			

[a] Theoretical data from [81]
[b] Theoretical data from [82]
[c] Theoretical data from [83]

confinement of the wave function and thus to an increased energy. On the other hand, if the box is too large, the B-spline basis (with a fixed number of B splines $\tilde{n}_\xi$) is not able to properly represent the radial behavior of the wave function. As can be seen from Table 3.2, different box sizes are optimal for different states. Therefore, the accurate simultaneous description of a number of states requires a careful choice of the box size. One can also see that convergence with respect to $l_{\max}$ is different for different states. For example, the states $4\,{}^1\Sigma_u$ and $6\,{}^1\Sigma_u$ are almost converged for $l_{\max} = 4$, while convergence for the other states is not yet achieved.

Since electronic dipole transition moments are known to be much more sensitive to the accuracy of the wave functions than the energy, such transition moments have been calculated for H_2 and compared to literature values (where available). Examples together with a convergence analysis with respect to $l_{\max}$ are given in Table 3.3. While most results are calculated in length gauge, the corresponding velocity-gauge results are also given, but only for $l_{\max} = 4$. In general, good agreement is found with literature values. Also, the dipole moments calculated in the two gauges agree well, except for those transitions where the transition energy is extremely small (for example, $2^1\Sigma_g - 1^1\Pi_u$). In these cases a small error in the transition energy leads to large errors in the final result, since a division by the energy difference has to be performed when comparing results in length and velocity gauges.

3.2. Photoionization cross section

As an example of the numerical treatment of the electronic continuum for a two-electron molecule, consider a calculation of the photoionization spectrum of HeH^+. The system is chosen to demonstrate the applicability of the present approach also to heteronuclear systems. The purpose of this section is to demonstrate how the box discretization leads to the ability to calculate transitions into the electronic continuum of states. For the sake of simplicity, the investigation is limited to the case of a parallel orientation of the molecular axis with respect to the field as well as to a consideration of only single internuclear distance $R = 1.45\,a_0$.

The partial ($X^1\Sigma \to {}^1\Sigma$) photoionization cross section (for single electron ejection) is given by

$$\sigma(E) = \frac{4\pi^2(E - E_0)}{3c} \sum_{\mu} |D_\mu(E)|^2 \tag{3.1}$$

where E_0 is the ground-state energy and μ specifies all possible degenerate final states with energy E. For the calculation of the electronic dipole transition moment

$$D_\mu(E) = \langle \Psi_{E\mu} | \hat{\mathrm{D}} | \Psi_0 \rangle \tag{3.2}$$

with the dipole operator $\hat{\mathrm{D}}$ in length gauge the ground and final state wave functions Ψ_0 and $\Psi_{E\mu}$ are required. The latter has to be properly energy normalized. Since the box-discretized calculation yields wave functions with bound-state normalization, it is necessary to perform a renormalization [47]. In the present case of the two-electron diatomic problem, a further complication arises from the occurrence of a multiply degenerate electronic continuum even between the first and second ionization thresholds [84, 85]. In [84]

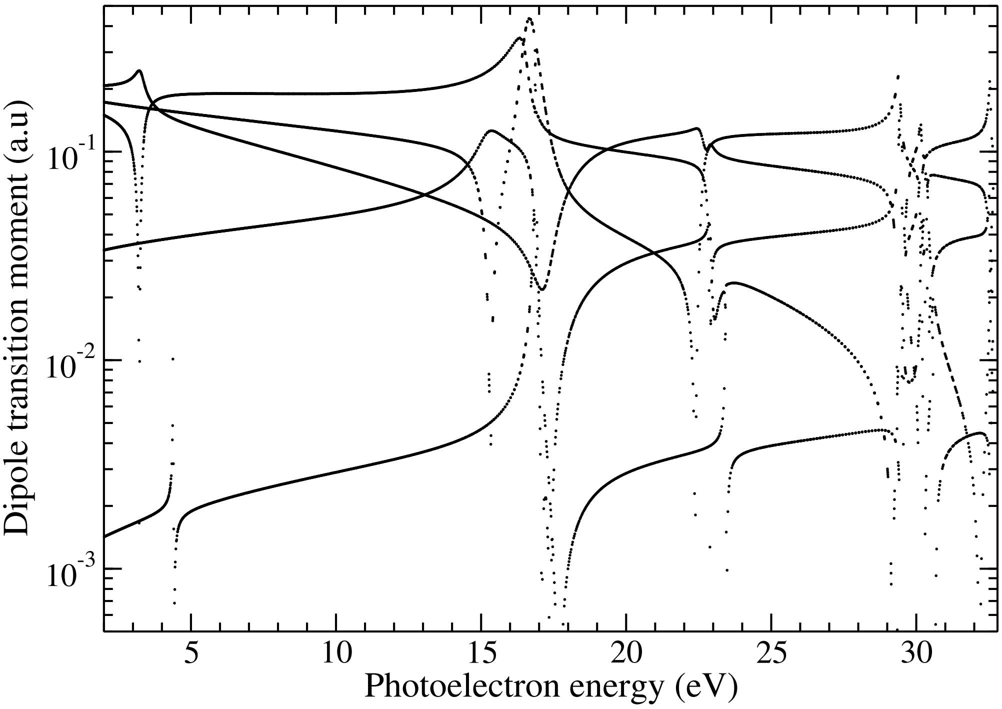

Figure 3.1.: Electronic dipole transition moments between the ground state of HeH$^+$ and $^1\Sigma$ continuum states (at $R = 1.45\,a_0$). Every point represents the transition to a single discretized continuum state. The shown results were obtained using different box sizes in order to achieve a denser spectrum. In this way an almost continuous spectrum is yielded. (Published in [61].)

a one-center approach was used and renormalization was performed by characterizing the states, i. e. attributing to every state a channel index μ, according to their leading l quantum number at the asymptotic limit. Within every channel the renormalization factors were obtained from the (partial) density of states. A detailed investigation reveals, however, that in some cases it is possible that two degenerate states are both simultaneously dominated by two different l quantum numbers. In order to be able to handle also this situation the following procedure was developed.

If the photoelectron is far away from the remaining ion left in its 1σ ground state, an energy-normalized molecular wave function with singlet spin symmetry behaves asymptotically as

$$\Psi_{E\mu}(1,2) \to \frac{1}{\sqrt{2}}(\psi_{1\sigma}(1)\psi_{\epsilon\mu}(2) + \psi_{\epsilon\mu}(1)\psi_{1\sigma}(2)). \tag{3.3}$$

Since for large distances $R\xi/2 \to r$ and $\eta \to \cos\theta$, the one-electron continuum wave function $\psi_{\epsilon\mu}$ with energy $\epsilon = E - \epsilon_{1\sigma}$ is asymptotically given by

$$\psi_{\epsilon\mu}(\xi,\eta,\phi) \rightarrow \frac{1}{\sqrt{2\pi k}}\frac{2}{r}\sin\{kr + \frac{2}{k}\ln 2kr + \delta_\mu(\epsilon)\}\Omega_\mu(\theta,\epsilon)\exp(\imath m\phi) \tag{3.4}$$

due to the standing-wave boundary conditions imposed by the box. In Eq. (3.4) the wavenumber $k = \sqrt{2\epsilon}$, the phase shift $\delta_\mu(\epsilon)$, and the angular functions $\Omega_\mu(\theta,\epsilon)$ are introduced. The latter functions fulfill the normalization condition

$$2\pi \int_0^\pi \Omega_\mu^2(\theta,\epsilon)\,\sin\theta\,\mathrm{d}\theta = 1. \tag{3.5}$$

Matching the calculated bound-state-normalized molecular wave function to the form given in Eqs. (3.3) and (3.4) gives the desired normalization factor. In the atomic case the angular part is simply given by a single spherical harmonic, $\Omega_\mu(\theta,\epsilon)\exp(\imath m\phi) = Y_{lm}(\theta,\phi)$. Different channels μ are then uniquely characterized by the angular quantum number l. In a diatomic molecule, l is no longer a good quantum number, and thus $\Omega_\mu(\theta,\epsilon)\exp(\imath m\phi)$ is analyzed in terms of linear combinations of spherical harmonics with a common value of m,

$$\Omega_\mu(\theta,\epsilon)\exp(\imath m\phi) = \sum_l C_{\mu l}(\epsilon)Y_{lm}(\theta,\phi). \tag{3.6}$$

Note, the coefficients $C_{\mu l}(\epsilon)$ are continuous functions with respect to energy ϵ.

Using box discretization and thus imposing the boundary condition that the wave functions are zero at $\xi_{\max}$ leads to a selection of the continuum solutions obtained for a given box size. If the box is sufficiently large, the continuum wave functions have reached their correct asymptotic behavior at $\xi_{\max}$. In this case, they are satisfying the equation $\sin(kr_{\max} + \frac{2}{k}\ln 2kr_{\max} + \delta_\mu(\epsilon)) = 0$ with $r_{\max} = R\xi_{\max}/2$ and thus Eq. (3.4) reduces to

$$\psi_{\epsilon\mu}(\xi,\eta,\phi) \rightarrow \frac{1}{\sqrt{2\pi k}}\frac{2}{r}\sin\{k(r - r_{\max}) + \frac{2}{k}\ln(r/r_{\max})\}\,\Omega_\mu(\theta,\epsilon)\exp(\imath m\phi) \tag{3.7}$$

The normalization can now be performed without knowledge of $\delta_\mu(\epsilon)$. The correctly renormalized electronic transition dipole moments $D_\mu(E)$ for different but still unknown channels μ are given in Fig. 3.1. In the calculation the following basis set parameters were used. In ξ direction $\tilde{n}_\xi = 300$ and $k_\xi = 8$ with a knot sequence $\{\xi_i^b\}$ that is slightly denser for small values of ξ. This is done using a geometric progression with $g_\xi = 1.1$ for the first 30 intervals and a linear knot sequence afterwards. A linear knot sequence $\{\eta_i^b\}$ with $\tilde{n}_\eta = 30, k_\eta = 6$ was used in η direction. The configuration set includes about 3000

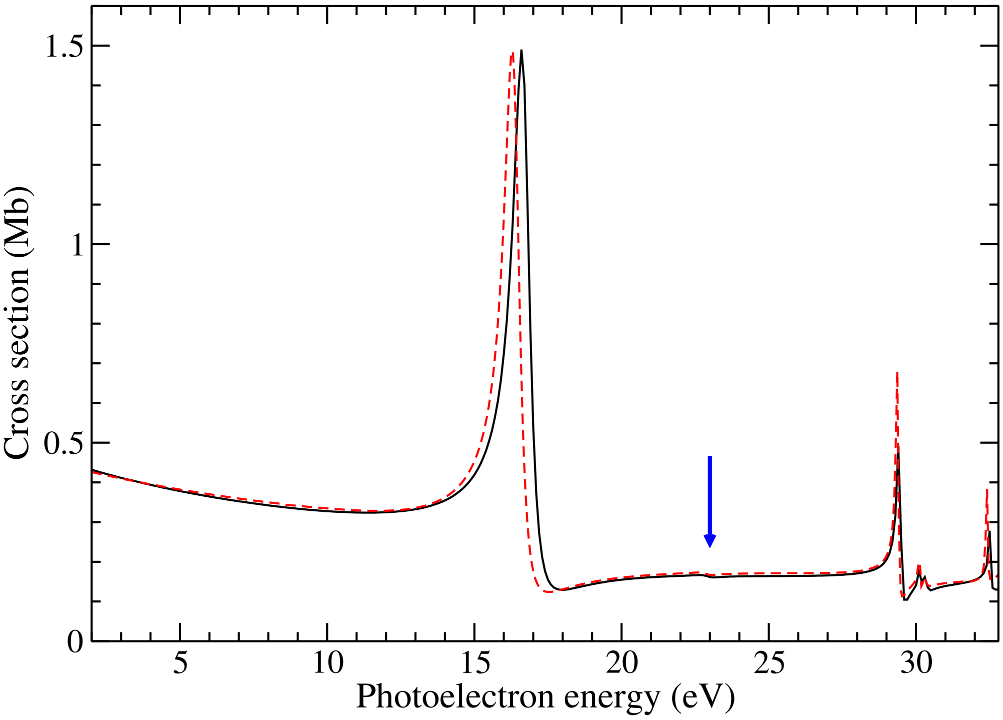

Figure 3.2.: Partial ($X^1\Sigma \rightarrow {}^1\Sigma$) photoionization cross-section of HeH$^+$ in the fixed-nuclei approximation at $R = 1.45\,a_0$. The result obtained in the present method (solid line) is compared to the result given in [86] (red dashed line). The blue arrow indicates the position of the second (almost invisible) resonance. (Published in [61].)

configurations with both electrons in low energy orbitals to describe electron correlation. In addition, five configuration series are used to describe the continuum. In those one electron occupies one of the $1\sigma - 5\sigma$ orbitals and the other is put into one of the possible 1500 orbitals with $N_\eta \leqslant 4$.

Since the density of states obtained with a single box is insufficient for both the determination of the coefficients $C_{\mu l}(\epsilon)$ and a resolution of narrow resonant structures in the dipole moments, a variation of the box size $\xi_{\max}$ in between 500 and 510 with step size 1 was performed. In Fig. 3.1, 5 different μ channels are easily recognized. The occurrence of the five channels is due to the limitation of the calculation to $0 \leqslant N_\eta \leqslant 4$. The knowledge of the expansion coefficients allows the attribution of every state (and its dipole moment) to one channel. For a given channel μ the continuous dipole function $D_\mu(E)$ is obtained from its values at discrete energies via interpolation. Using Eq. (3.1) the photoionization cross section can be calculated. In Fig. 3.2 the result is compared to the calculation in [86] where explicitly correlated basis functions and the complex-scaling method were used. The agreement is very good, even on the absolute scale. The main difference occurs at the first resonance at about 16 eV where a small shift is observed. The probable reason for the difference is the more accurate inclusion of correlation in [86] that leads to a lower energy for the doubly excited state responsible for the resonant structure in the spectrum. As was discussed in [86] and is confirmed by the present calculations, the second resonance is practically invisible due to the contributions of different channels canceling each other.

3.3. Doubly excited autoionizing states of H_2

The present B-spline based method is especially suitable for a numerical investigation of doubly excited states. Since accurate molecular orbitals for the whole R range can be obtained due to the use of the prolate spheroidal coordinate system, a calculation of doubly excited states can be efficiently performed by means of the Feshbach projection technique. In this section the high accuracy is demonstrated that can be achieved with the present method for both highly-excited states and large internuclear distances. As an example, the so-called Q(2) states are considered which separate at large internuclear distances R into a product of two hydrogen atoms each in a state with principal quantum number $n = 2$. These states are of interest for theoretical study of H(2s)+ H(2s) cold collisions [60, 87] and their study was previously performed by means of the R-matrix method [88], the complex scaling method [89], or the Feshbach projection technique, with Gaussian functions centered at the two nuclei [90] or with single-centered B-spline basis sets [85]. However, only with the present method the results were sufficiently accurate to achieve a direct connection between the short range and the asymptotic van der Waals regime. This obviates the need for an interpolation that bridges these two extreme regimes and is very important for scattering calculations, especially in the case of low collision energies.

For sufficiently large internuclear distances electron-electron exchange becomes negligible and the remaining electrostatic atom-atom interaction may be treated by perturbation theory. The application of perturbation theory to $\mathrm{H}(n{=}2) + \mathrm{H}(n'{=}2)$ collisions was discussed previously [60, 89, 91]. The comparison of the present CI results with the earlier perturbative results showed a significant disagreement for some states. Owing to the high accuracy of the here implemented CI method, this disagreement could not be explained by numerical inaccuracies. This finding motivated the author to reanalyze in detail the application of perturbation theory to the problem. This study revealed an unjustified neglect of dipole-quadrupole terms due to wrong symmetry arguments [91] which led to erroneous C_5 coefficients.

A thorough numerical investigation including a careful reanalysis of first-order perturbation theory as well as the evaluation of the leading term (C_6) of second-order perturbation theory can be found in [32]. Projection coefficients and potential curves obtained in this work were used for the subsequent calculation of low-temperature cross sections for collisions between spin-polarized metastable hydrogen atoms [33]. Since this investigation is beyond the scope of the present thesis, only a brief description of some of the results is given. One of the main purposes of this section is to show how B-spline parameters and configurations for the CI calculation have to be selected in an optimal way, if large internuclear distances are of interest.

The Feshbach projection-operator approach is especially convenient for dealing with autoionizing states. In Feshbach theory the Hilbert space is divided into two orthogonal Q and P subspaces. Their mutual interaction results in the autoionization width and an energy shift. According to [90] the energy shift is expected to be minimal, if the P subspace is constructed using the n lowest-lying solutions of the one-electron Schrödinger equation. The corresponding orthogonal Q subspace can directly be obtained by simply excluding these orbitals from the configuration space of the CI calculation. The Q(2) states are obtained by omitting the two lowest lying orbitals ($1\sigma_g$ and $1\sigma_u$) from the configuration list. (This is actually the motivation for calling these states Q(2) states.) Clearly, the accuracy of this procedure depends crucially on the precision of the calculated P-subspace wave functions. The present approach allows the very highly accurate evaluation of these orbitals for arbitrary internuclear distances due to the use of B splines and prolate spheroidal coordinates. While the one-center calculations (using B splines) of Martín and co-workers [85] run into numerical problems (due to slow convergence) for internuclear distances larger than 4-5 a_0, the traditional approaches with global atom-centered basis functions (like Gaussians) or explicitly correlated basis functions (geminals) are typically hampered by numerically caused linear dependencies that often prevent systematic basis-set-convergence investigations.

The Q(2) states converge in the separated-atom limit to two hydrogen atoms with principal quantum number $n = 2$, if they are adiabatically continued from small to infinite internuclear distances R. All possible combinations of H($n = 2$) (with spin up and down) result in 32 singlet and triplet states. In the absence of external fields and ignoring relativistic effects there occur 22 different molecular Q(2) states out of which 10 are doubly degenerate Π and Δ states. All these 22 states (converging for $R \to \infty$

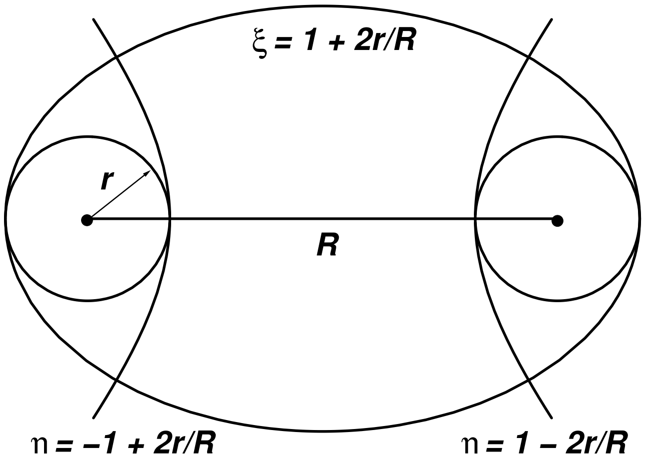

Figure 3.3.: Visualization of the used prolate spheroidal coordinates (ξ, η) and their relations to the distance r from the focal points.

to $E = -0.25\,\mathrm{a.\,u.}$) have been reevaluated with the present method, the calculations extending from $R = 1.0\,a_0$ (where accurate potential curves existed before) to at least $R = 100\,a_0$ and thus far beyond previously existing *ab initio* data. For this purpose, a careful basis-set optimization has been performed. The efficient calculation of the potential curves requires a judicious choice of the basis-set parameters depending on the internuclear distance in order to keep the number of configurations in the CI calculation reasonably small.

The electronic density of two non-interacting H($n = 2$) atoms is almost exclusively located within two spheres of radius $r_{\mathrm{n=2}} = 35\,a_0$ centered at the two nuclei. At very large internuclear separations ($R > 70\,a_0$) the electron densities of the Q(2) states of H_2 are thus very similar to the ones of two non-interacting H($n = 2$) atoms and are only slightly distorted by the interatomic interaction. Translating this geometry into the prolate spheroidal coordinate system, the box size $\xi_{\mathrm{max}} = 1 + 2r_{\mathrm{n=2}}/R$ is chosen (see Fig. 3.3). Convergence with respect to ξ was achieved using $\tilde{n}_\xi = 25$ and a geometrically progressive distribution characterized by $g_\xi = 1.1$. For $R = 70\,a_0$ convergence with respect to η was obtained with a uniform knot sequence and $\tilde{n}_\eta = 40$. For a uniform knot sequence an increase of R leads to an increase of the length of non-zero knot intervals and, therefore, to a decrease of the number of such intervals inside $1 - 2r_{\mathrm{n=2}}/R < |\eta| < 1$ (see Fig. 3.3). Such a decrease can be compensated by an increase of $\tilde{n}_\eta$. Since the calculation of the orbitals with large $\tilde{n}_\eta$ is time-consuming, for $R > 140\,a_0$ the value of $\tilde{n}_\eta$ was fixed at 80 and a geometrically progressive distribution was used that assures that the ratio of knot points inside the interval $|\eta| < 1 - 2r_{\mathrm{n=2}}/R$ does not exceed 50%. With these basis-

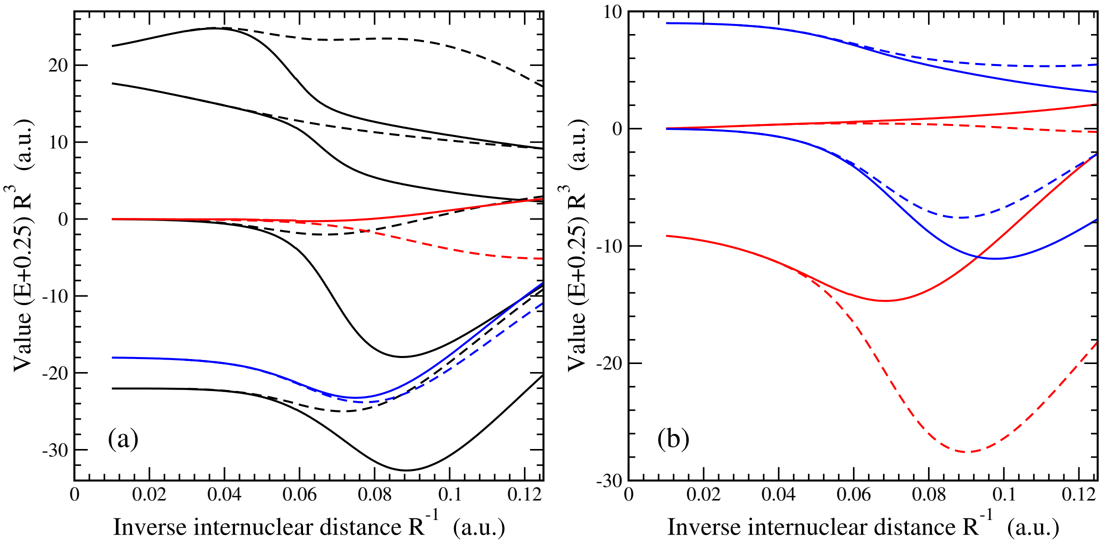

Figure 3.4.: Energies of some Q(2) states of H_2. In order to connect the results with the long-range behavior predicted by perturbation theory the energies are plotted vs. the inverse internuclear distance R, shifted by 0.25 a. u., and multiplied by R^3. Plotted this way, the curves converge to the van der Waals C_3 coefficients for $R^{-1} \longrightarrow 0$ equal to $0, \pm 9, \pm 18$, and $\pm 9\sqrt{6}$ (see Table I of [32] for more details). (**a**) ${}^1\Sigma_g^+$ (black solid), ${}^3\Sigma_u^+$ (black dashed), ${}^1\Sigma_u^+$ (blue solid), ${}^3\Sigma_g^+$ (blue dashed), ${}^1\Sigma_u^-$ (red solid) and ${}^3\Sigma_g^-$ (red dashed) symmetry. (**b**) ${}^1\Pi_u$ (blue solid), ${}^3\Pi_g$ (blue dashed), ${}^1\Pi_g$ (red solid) and ${}^3\Pi_u$ (red dashes) symmetry.

set parameters all possible orbitals ($\tilde{N} = \tilde{n}_\xi \tilde{n}_\eta$) for $\sigma_{g,u}, \pi_{g,u}$, $\delta_{g,u}$ (additionally $\phi_{g,u}$ for $R = 70 - 100\,a_0$) were calculated. As for all other R values, the $1\,\sigma_{g,u}$ orbitals are then removed from the orbital list, if the Q(2) states should be calculated. The remaining orbitals are classified according to two properties. First, they are sorted with respect to the energy value to which they converge asymptotically for $R \to \infty$. In this way the label n is introduced using the relation $E(R \to \infty) = -\frac{1}{2n^2}$. Due to the discretization (implied by the finite box size) this sorting has a physical meaning only for small n. This is, however, adequate in the present calculation of the states converging to $n = 2$. The second important criterion for the configuration selection is the number of nodes N_η. Limiting N_η leads to a removal of strongly oscillating orbitals in the η coordinate.

The configurations for the CI calculation are now constructed in the following way. One electron occupies one of the n orbitals and the other one all orbitals from the list that fulfill the symmetry requirements (correct m and inversion quantum numbers) and the condition $N_\eta \leqslant 2\kappa_n - 1$ where $\{\kappa_n\}$ is an R-dependent set of natural numbers. The choice of $\{\kappa_n\}$ at some R is directly related to the choice of the configuration set used for the CI calculations at this R. In the case of the Q(2) states the configurations containing two

Table 3.4.: Energies of Q(2) states for large internuclear distances R.

R, a_0	$1^1\Sigma_g^+$	$2^1\Sigma_g^+$	$3^1\Sigma_g^+$	$4^1\Sigma_g^+$
80.0	-0.250 043 043 908[a]	-0.250 000 050 608[a]	-0.249 965 917 821[a]	-0.249 955 663 782[a]
	-0.250 043 018 873[b]	-0.250 000 025 627[b]	-0.249 965 891 914[b]	-0.249 955 622 359[b]
90.0	-0.250 030 233 004[a]	-0.250 000 028 049[a]	-0.249 975 922 156[a]	-0.249 969 031 692[a]
	-0.250 030 217 611[b]	-0.250 000 012 641[b]	-0.249 975 904 390[b]	-0.249 969 009 043[b]
100.0	-0.250 022 041 050[a]	-0.250 000 016 746[a]	-0.249 982 370 561[a]	-0.249 977 516 867[a]
	-0.250 022 031 068[b]	-0.250 000 006 718[b]	-0.249 982 358 228[b]	-0.249 977 503 361[b]
150.0	-0.250 006 531 530[a]	-0.250 000 002 472[a]	-0.249 994 718 647[a]	-0.249 993 407 618[a]
	-0.250 006 529 786[b]	-0.250 000 000 590[b]	-0.249 994 716 095[b]	-0.249 993 405 673[b]
200.0	-0.250 002 755 502[a]	-0.250 000 000 615[a]	-0.249 997 762 598[a]	-0.249 997 229 626[a]
	-0.250 002 755 122[b]	-0.250 000 000 105[b]	-0.249 997 761 935[b]	-0.249 997 229 241[b]
R, a_0	$1^1\Pi_g$	$2^1\Pi_g$	$1^1\Pi_u$	$2^1\Pi_u$
88.0	-0.250 013 463 614[a]	-0.249 999 949 925[a]	-0.250 000 040 912[a]	-0.249 986 806 031[a]
	-0.250 013 464 074[b]	-0.249 999 926 219[b]	-0.250 000 016 152[b]	-0.249 986 806 570[b]
96.0	-0.250 010 337 535[a]	-0.249 999 968 227[a]	-0.250 000 026 572[a]	-0.249 989 834 374[a]
	-0.250 010 338 537[b]	-0.249 999 951 741[b]	-0.250 000 009 583[b]	-0.249 989 835 350[b]
100.0	-0.250 009 133 834[a]	-0.249 999 974 242[a]	-0.250 000 021 583[a]	-0.249 991 004 931[a]
	-0.250 009 135 155[b]	-0.249 999 960 472[b]	-0.250 000 007 501[b]	-0.249 991 006 165[b]

[a] Present calculation

[b] Prediction of perturbation theory (first-order term plus the leading second order term varying as R^{-6})

$n = 2$ orbitals may be called *basic* configurations. For very large R these configurations give the main contribution to the energy but require a rather large value of κ_2 (around $20 - 25$) to achieve convergence. Since the configurations belonging to $n = 3$ add only a small correction, κ_3 is chosen around $5 - 10$, while all $\kappa_{n>3}$ are set to 0 for $R > 100\,a_0$. With decreasing internuclear distance R the importance of the configurations that do not belong to the basic ones grows. Therefore, κ_2 was decreased in order to allow larger κ_n for $n > 2$ while retaining a reasonable size of the total number of configurations (typically, $5000 - 10000$ configuration for each symmetry). For $R < 100\,a_0$ $\kappa_4 \neq 0$ has to be used. Because of the different structures of the various Q(2) states it is difficult to provide a general recipe for the change of $\{\kappa_n\}$ with R. Moreover, for $R = 70 - 80\,a_0$ the configurations with one electron occupying an orbital with $n > 4$ and the other one occupying a symmetry-allowed low-energy orbital are more important than is reflected by the selection rule based on $\{\kappa_n\}$.

The potential curves of the Q(2) states for large internuclear distances are presented in Fig. 3.4. In order to emphasize the asymptotic long-range behavior the potential curves

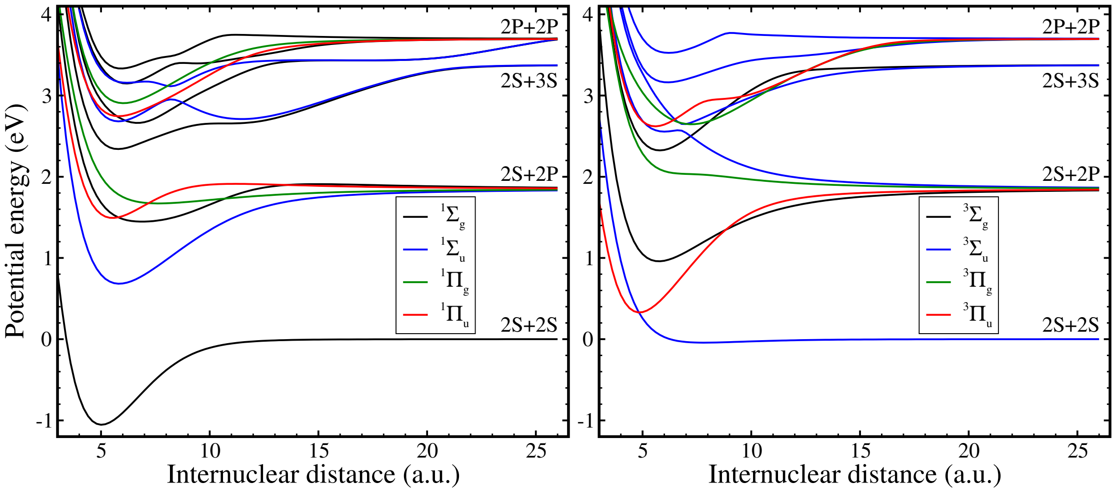

Figure 3.5.: Electronic potential curves of some low-lying singlet (left) and triplet (right) states of Li_2 obtained with the present method. Energies are given relative to the ground-state asymptote. The corresponding states of the Li atoms in the dissociation limit are indicated in the right part on the plots.

are plotted as a function of $(E + 0.25)\,R^3$ vs. the inverse internuclear distance R^{-1}. Plotted this way the energy curves should converge for $R^{-1} \to 0$ to the value of the corresponding C_3 van der Waals coefficient. As can be seen from Fig. 3.4, the CI results are in very good agreement with the C_3 coefficients obtained from perturbation theory. Note that singlet and triplet curves merge together before $R = 30\,a_0$ and, therefore, for larger R values exchange interaction is negligible. This means that a perturbative approach that ignores exchange is in principle applicable beyond this internuclear distance. A quantitative comparison of the present calculation with the prediction of the perturbation theory is presented in Table 3.4. An agreement within 8 to 9 significant digits is found. Note, that the energies obtained with the present approach are mostly lower than the ones predicted by the perturbation theory. Extensive tests were performed to check the numerical stability of the non-perturbative calculations and their convergence with respect to the expansion length of the basis set. Since these tests indicate a numerical stability of 13 digits and basis-set convergence within at least 9 significant digits for $R = 80\,a_0$ and 11 digits for $200\,a_0$, the observed small remaining discrepancies are very likely to be caused by the higher-order terms omitted in the perturbative expansion.

3.4. Application to alkali dimers

The method has been successfully applied in the calculation of the photoionization cross sections of the three alkali dimer cations (Li_2^+, Na_2^+ and $LiNa^+$) for both parallel and perpendicular orientations of the molecular axis with respect to the field [92]. Two-active electron calculations have been performed for lighter alkali dimers (e.g. Li_2) and the obtained electronic potential curves (Fig. 3.5) and dipole transition matrix elements were found to be in a good agreement with literature data. These calculations are beyond the scope of the present thesis and will not be discussed further.

Part II.

Investigation of ionization process

4. Atoms and molecules in a laser field

Ongoing progress in the understanding of different aspects of the ionization process of atoms and molecules exposed to intense laser fields is accompanied by the emergence of new concepts and models. Section 4.1 provides a retrospective view of the development of these concepts and briefly highlights the main achievements attained in the past. The interaction of a quantum system with an externally applied electromagnetic field can be treated in the dipole approximation by means of different gauges. These different formulations lead to identical and unambiguous predictions for physical quantities. If, however, physical quantities are calculated using some approximations, the different formulations can lead to disagreeing results. This problem, which is known as the gauge problem, led to a considerable confusion and long-lasting debates on the choice of the appropriate gauge. Therefore, a detailed discussion of the gauge invariance is given in Sec. 4.2. Besides the description of traditional gauges, the concept of a generalized gauge is introduced for a deeper understanding of the gauge problem. Section 4.3 presents gauge-dependent wavefunctions of a free electron in the presence of a laser field. Section 4.4 aims to demonstrate that the TDSE formulated in different gauges can be reduced to an identical system of ordinary differential equations, if the Hamiltonian is correspondingly partitioned. For this purpose, the concept of the generalized field-free Hamiltonian is introduced and the time-dependent wavefunction is expanded in the basis of solutions of the TDSE with the generalized field-free Hamiltonian. In a similar way, these new concepts are used also in the following chapter in order to introduce generalized SFA formulations.

4.1. Ionization in an electromagnetic field and its mechanisms

A quantum system (atom, ion or molecule) being exposed to an intense electromagnetic field has a certain probability to ionize, that is, to lose one or more electrons due to the interaction with the field. (Only ionization due to the electric component of the electromagnetic field will be considered in the following.) One can distinguish between two basic mechanisms of ionization according to whether a ’field’ or a ’photon’ picture is adopted for the description of the electromagnetic field. Considering a static or slowly varying electric field, the field picture is adequate. In this picture the occurrence of ionization of an atom in very intense fields can be understood even classically. Indeed, in this case the field drastically distorts the potential well formed by a positively charged nucleus in such a way that the potential barrier is suppressed in one direction and the electron has enough energy to escape over the barrier (see Fig. 4.1 a). The field picture can even be used for a laser with optical frequencies, where the ionization mechanism is often referred to as *optical field ionization.* An intuitive condition for the validity of the ’field’ picture is that the ionization process occurs considerably faster than a field period. On the other hand, if ionization lasts longer than the oscillating period of the field, the photon picture becomes more adequate. In this case one can speak about absorption of a quantum of the electromagnetic field by the quantum system. The process in which one or more absorbed photons eject one or several electrons is called *photoionization.* Depending on the system, intensity, and frequency of the electromagnetic field, the photoionization process can be described by different mechanisms. The simplest one is the so-called *photoelectric effect*, a single ionization via one-photon absorption (see Fig. 4.1 b). Discovered in 1887 and explained by Einstein in 1905, this phenomenon was one of the non-classical effects leading to the establishment of the quantum theory. It occurs, if the photon energy of radiation, $\hbar\omega$, is larger than the binding energy E_{b} of the outermost electron in the system. Such process is also referred to as linear photoionization, since the ionization rate Γ is proportional to the intensity I of the field, $\Gamma = \sigma(I/\hbar\omega)$, where σ is the total photoionization cross section and the intensity I is sufficiently low.

After the quantum theory was established, other variations of these two basic ionization mechanisms have been discussed. First, ionization of the hydrogen atom in a weak static electric field was considered by Oppenheimer [93], who gave a formula of the ionization rate for the 1S state. According to quantum mechanics, the electron in this case gains the ability to leave the system by tunneling through the barrier and such a mechanism is referred to as *tunneling ionization* (see Fig. 4.1 c). Although the pre-exponential factor in Oppenheimer’s formula turned out to be wrong (partly due to the fact that the Coulomb interaction has been completely neglected in the description of the ejected electron) the most important exponential term $\exp[-2/(3F)]$ was correct showing that the probability of an electron tunneling through the barrier drops off exponentially with the field strength F. The correct formula was derived by Landau and Lifshitz [94]

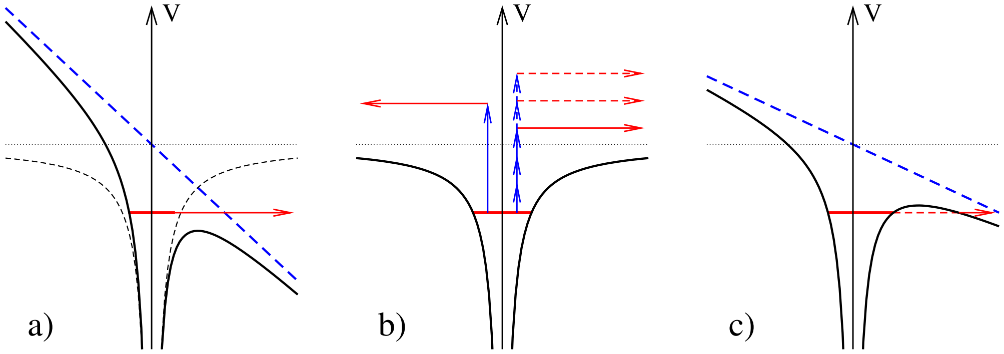

Figure 4.1.: Different mechanisms of ionization: (**a**) Over-the-barrier ionization. A potential well formed by a positively charged nucleus (black dashed curve) is distorted by the intense electric field (its potential is shown by a blue dashed curve) so that the electron has enough energy to escape. (**b**) Various mechanisms of photoionization: one-photon ionization (left part) and multi-photon ionization (right part). Blue arrows designate absorption of one photon, formation of above-threshold-ionization photoelectron spectra is shown by dashed arrows. (**c**) Tunneling ionization. The tunneling path is shown by the red dashed line.

yielding the ionization rate of the ground state of a hydrogen atom

$$\Gamma = \frac{4}{F} \exp\left(-\frac{2}{3F}\right). \tag{4.1}$$

General expressions for the static and the quasi-static (for a low-frequency alternating electric field) ionization rates for arbitrary bound states of hydrogen were obtained by Perelomov, Popov, and Terent'ev [95] (PPT formula) and later generalized (by means of some further approximations) to arbitrary atoms by Ammosov, Delone, and Krainov [96] (ADK formula). These theories and their extensions to molecules are frequently used nowadays for a theoretical description of the field ionization.

The invention of the laser has led to abundant experimental verification [97, 98] of Göppert-Mayer's theory [99] of the simultaneous absorption of two photons by an atomic system. This new experimental capability has in turn motivated the study [100, 101] of the photoionization by simultaneous absorption of several photons, the so-called *multiphoton ionization* (MPI) (see Fig. 4.1 c). Voronov and Delone measured the rate of ionization of Xe atoms by ruby-laser light [102], where seven photons are required for ionization.

Before experiments were carried out on the energy distribution of electrons produced in MPI of atoms, it had been assumed that the electron kinetic energy would be given by $N\omega - E_\mathrm{b}$. This is a simple extrapolation of the Einstein picture of the photoelectric effect.

In accordance with this concept, the MPI was modeled by the lowest-order perturbation theory (LOPT) [103, 104] in early experiments. Therein, the N-photon ionization rate is given by

$$\Gamma_N = \sigma_N \left(\frac{I}{\hbar} \right)^N \tag{4.2}$$

where N is the minimum number of photons needed for ionization. Generalized N-photon ionization cross sections were accurately measured and found to be in good agreement with the corresponding ionization cross sections calculated within LOPT, although some complications occurred, if MPI happened to go through an intermediate bound state. This process, called *resonant enhanced multiphoton ionization* (REMPI), causes divergencies in LOPT, but the latter has been successfully modified to handle these difficulties.

A crucial breakthrough was made when experiments detecting the energy-resolved photoelectrons were performed and several papers [105–108] reported the observation of MPI with the production of electrons with energies exceeding the photon energy. The interpretation was not clear because a free electron cannot absorb photons. Two possible mechanisms were proposed to explain this effect as a two-step process. One of them supposed that electrons are accelerated by the action of ponderomotive forces [106], the other [107, 108] assumed that the free electrons absorb the photons in the field of neighboring atoms or ions through the *inverse bremsstrahlung* process (IBS).

Alternatively, a one-step process named *above-threshold ionization* (ATI) was proposed by Gontier *et al.* [109] (see Fig. 4.1 b). It turned out to be more suitable in describing experiments like the one by Agostini *et al.* [107], where the energy spectrum of electrons produced in a 6-photon ionization of xenon atoms consists of two peaks corresponding to the absorption of either 6 or 7 photons. Further experiments supported the ATI model showing that the electron energy spectrum may consist of a series of evenly spaced peaks with the spacing corresponding to the energy of a photon. The amplitude of these peaks was shown to vary linearly with the initial atomic density, which contradicts to the IBS predicting a quadratic dependence on the atomic density.

Despite the difficulties, perturbation theory has been applied to ATI [110] and its results were verified experimentally [111]. The non-perturbative character of ATI became evident at higher laser intensities, where the energy spectrum is dominated by higher-energy peaks and not by the first one [112]. Another interesting feature of ATI spectra has been observed in low-frequency short laser pulses, where a certain number of first ATI peaks disappear with the increase of the laser intensity [113] showing intensity dependence of the ionization potential. This effect is a clear experimental evidence that the electron must acquire energy additional to the field-free ionization potential in order to escape. This energy is essentially given by the ponderomotive energy U_p of the electron, which is the cycle-averaged kinetic energy of a quivering electron in a laser field. For non-relativistic velocities the ponderomotive energy is given by

$$U_p = \frac{I}{4\omega^2}, \tag{4.3}$$

and must be taken into account to correctly predict ATI peaks. It is worth to mention that this effect was not seen in the earlier long-pulse experiments because in that case the photoelectrons regain their ponderomotive energy deficit from the laser field as they escape from the focal volume.

For low laser frequencies and for the electric fields of laser radiation comparable to the Coulomb field, the sharp ATI peaks of the photoelectron spectrum gradually blur into a continuous distribution. This indicates that such mechanism as the field ionization starts to dominate over the multiphoton ionization, so that ionization can be understood by using a model in which the electron is liberated from its parent atom either by tunneling ionization or, at higher intensities, by *over-the-barrier* ionization (OTBI). The possibility of merging such different ionization mechanisms as field ionization and photoionization within a common non-perturbative theory has been demonstrated by Keldysh [114]. In his pioneering work, Keldysh has shown that the dominant ionization mechanism can be indicated by the so-called *Keldysh (adiabaticity) parameter*,

$$\gamma = \sqrt{\frac{E_\mathrm{b}}{2U_p}} = \frac{\kappa\omega}{F} \tag{4.4}$$

where $\kappa = \sqrt{2E_\mathrm{b}}$. The parameter represents a ratio of the "tunneling time" to the period of the laser wave. Photoionization is expected to dominate for $\gamma > 1$ and vice versa. In [114], the transition amplitude from the initial bound state to the continuum was approximated by treating the effect of the binding potential on the detached electron as a small influence with respect to the external field effects whereas the initial state remains unperturbed by the field. The laser-dressed continuum state was thus expressed by a Volkov state [115] which has the virtue of automatically incorporating all orders of the radiative interaction. The same idea was used in the works of Faisal [116] and Reiss [117], though they employed velocity (or radiation) gauge instead of length gauge used by Keldysh. Whereas the direct-time S matrix formulation was used in [116], much simpler expressions were obtained by Reiss using the time-reversed S matrix. These different, but unquestionably related, non-perturbative methods are collectively referred to as either the KFR method or *strong-field approximation* (SFA).

When an atom is exposed to an intense laser field, it develops a time-dependent dipole moment and radiates at odd multiples (harmonics) of the incident laser frequency. This process, known as optical harmonic generation, has been thoroughly studied experimentally starting from the 1960s. However, it was only in the late 1980s that the availability of intense, short laser pulses allowed the *high-order harmonic generation* (HHG), i.e. generation of harmonics with the order of 11 and larger. Using low-frequency laser L'Huillier and Balcou [118] observed the existence of a *plateau* of nearly constant conversion efficiency, which was particularly long for helium and neon. Another interesting effect was found considering the angular distributions of electrons in the ATI spectrum produced by very intense laser fields. Although they are usually aligned along the polarization axis of the applied laser field, it has been shown by Yang *et al.* [119] that for noble gases a few high energy peaks may be highly structured, and in some cases feature rings 45° off the polarization axis. The existence of a *plateau* in the ATI photoelectron energy spectra for linear polarization has been also revealed in later experiments [120]. Theoretical investigations have shown that these effects appear due to the rescattering of the detached electron by the parent ion and thus cannot be described with conventional KFR theory. Based on the earlier 'Simpleman' picture [121, 122] of a quivering electron Corkum [123] and Schafer *et al.* [124] developed the 'recollision picture' explaining the main features of HHG. In this model, electrons first tunnel through the barrier formed by the atomic potential and the laser field and appear in the continuum with zero velocity. Their subsequent motion in the field is treated classically. Only those electrons that return to the nucleus can emit harmonics by recombining to the ground state. In addition, a quantum version of Simpleman's picture has been proposed by Lewenstein *et al.* [125] in order to treat HHG by a low-frequency laser field.

Unfortunately, in the literature the limit $\gamma \ll 1$ is often referred to as 'tunneling ionization' limit, instead of 'field ionization' limit. As mentioned above, at high intensities the ionization mechanism is over-the-barrier ionization, rather than tunneling ionization. For some systems and laser frequencies, the dominant ionization mechanism with an increase of the field strength may change directly from MPI to OTBI. This must be taken into account, since the application of a tunneling theory, e.g. the ADK theory, may lead to a significant error in this regime. For a hydrogenic system with the charge Z the minimum field strength required to allow OTBI is $F_{\text{cr}} = E_{\text{b}}^2/(4Z)$. Another argument against the terminology "tunneling ionization limit" is that the tunneling view of ionization is specific to the dipole-approximation length gauge, whereas in the velocity gauge a depressed-barrier model of the type shown in Fig. 4.1 c is never employed. Since, the validity of the dipole-approximation length gauge at high laser intensities or low frequencies of electromagnetic field is questionable and thus the physical interpretation of ionization as a tunneling process may be inappropriate [126, 127].

There exist two main mechanisms of *multiple ionization*, i.e. the removal of several electrons from a many-electron system. Usually the *sequential ionization* is the dominant mechanism. However, it has been experimentally shown [128] that at low intensities the double ionization of He is mainly simultaneous, and a *non-sequential* (NS) mechanism results in a large enhancement of ionization. For the theoretical description of NS ionization electron-correlation effects must be incorporated into the theory [129].

The additional nuclear degrees of freedom in molecules lead to a number of laser-induced effects that are necessarily absent in atoms. This includes phenomena like, e.g. bond softening, bond hardening, enhanced ionization at some critical internuclear separation, and above-threshold dissociation [130, 131]. It was found in earlier experiments [132–134] that in intense laser fields ionization signals of molecules and noble gas atoms with comparable ionization energies look similarly. This has often been assumed to be understood in terms of the ADK theory, where the probability of ionization depends primarily on the ionization energy of the system. Thus, for example, the ionization signals of the pair N_2 and Ar with comparable ionization energies (15.58 eV and 15.76 eV, correspondingly) showed very similar ion yields as a function of intensity. Later, however, a strong deviation from this general expectation was discovered in two independent experiments using femtosecond Ti:sapphire laser pulses. Talebpour *et al.* [135] and Guo *et al.* [136] found that although as before the ionization signal for N_2 remains comparable to that of its companion Ar atom, the signal for the O_2 molecule is greatly suppressed compared to that of its companion noble gas amon Xe (the ionization energies are equal to 12.07 eV and 12.13 eV, correspondingly). The ionization suppression for O_2 turns out to be more than an order of magnitude. This finding has generated considerable interest in symmetry-dependent dynamical effects on the laser induced ionization process, especially for diatomic molecules. Another example of experimentally observed characteristic features of molecular ionization is the orientation dependence of the strong-field ionization of N_2 [137]. The experiment shows that the total ionization rate as a function of the angle between the internuclear axis and the laser-field polarization axis has maxima for parallel orientation.

4.2. Gauge invariance

Gauge-invariance is one of the fundamental concepts of electrodynamics. As a consequence it is, e. g., possible to formulate the interaction of charged particles with electromagnetic fields in different gauges. Although the choice of the gauge clearly influences parameters like the scalar or the vector potential, all physical quantities (observables) are independent of the gauge, if an exact treatment is performed. On the other hand, an approximate treatment often leads to gauge-dependent predictions for physical observables. For example, the use of a truncated series expansion may result in a gauge-dependence for the prediction of physical observables. This is valid both for theories based on an S-matrix expansion (like different versions of SFA) and numerical methods for solving the TDSE in which the Hilbert space is restricted in some way. Moreover, the physical interpretations of processes occurring in the strong field may differ rather drastically in different gauges. For example, there is no tunneling in the velocity gauge. This promotes the long-lasting debates on the choice of the "fundamental" (or physical) gauge which appear to go on for ever.

In this section local gauge invariance and different gauges are briefly discussed. Also, a generalized gauge is introduced for later purposes.

In the case of intense laser fields the photon density is very high. Under these circumstances the number of photons can be treated as a continuous variable and the field can be described classically by using Maxwell's equations. Therefore, in the following a *semi-classical* theory will be used in which the radiation field is treated classically, but the atomic or molecular system is described using quantum mechanics. The influence of the quantum system on the external field is also neglected.

4.2.1. Local gauge invariance

A classical electromagnetic field is described by the electric and magnetic field vectors, $\mathbf{F}(\mathbf{r}, t)$ and $\mathbf{B}(\mathbf{r}, t)$ or, alternatively, by the scalar and vector potentials $\Phi(\mathbf{r}, t)$ and $\mathbf{A}(\mathbf{r}, t)$. Consider a system consisting of an electron in an electrostatic potential $U(\mathbf{r})$ created by a nucleus (or some nuclei) which interacts with an external electromagnetic field. In the semi-classical theory, the evolution of the system is governed by the time-dependent Schrödinger equation that satisfies *local gauge invariance* and is given in the coordinate representation with the minimal-coupling Hamiltonian by

$$\mathrm{i}\frac{\partial}{\partial t}\Psi_\chi(\mathbf{r},t) = \left\{\frac{1}{2}\Big[\mathbf{p}_\mathrm{c} + \mathbf{A}_\chi(\mathbf{r},t)\Big]^2 - \Phi_\chi(\mathbf{r},t) + U(\mathbf{r})\right\}\Psi_\chi(\mathbf{r},t) \tag{4.5}$$

where the subscript denotes the used gauge χ and the operator of canonical momentum is given independently of the gauge as $\mathbf{p}_\mathrm{c} \equiv -\mathrm{i}\nabla$; a consequence of the definition of the minimal-coupling Hamiltonian. The word *invariance* means that if the wavefunction Ψ_χ and both potentials $\mathbf{A}_\chi$ and Φ_χ are simultaneously transformed into a new gauge χ' using the transformation recipes

$$\begin{aligned}
\Psi_{\chi'}(\mathbf{r},t) &= \Psi_\chi(\mathbf{r},t)e^{\left[\mathrm{i}T_{\chi\to\chi'}(\mathbf{r},t)\right]} & \Psi_\chi(\mathbf{r},t) &= \Psi_{\chi'}(\mathbf{r},t)e^{\left[\mathrm{i}T_{\chi'\to\chi}(\mathbf{r},t)\right]}\\
\mathbf{A}_{\chi'}(\mathbf{r},t) &= \mathbf{A}_\chi(\mathbf{r},t) - \nabla T_{\chi\to\chi'}(\mathbf{r},t) & \mathbf{A}_\chi(\mathbf{r},t) &= \mathbf{A}_{\chi'}(\mathbf{r},t) - \nabla T_{\chi'\to\chi}(\mathbf{r},t)\\
\Phi_{\chi'}(\mathbf{r},t) &= \Phi_\chi(\mathbf{r},t) + \frac{\partial}{\partial t}T_{\chi\to\chi'}(\mathbf{r},t) & \Phi_\chi(\mathbf{r},t) &= \Phi_{\chi'}(\mathbf{r},t) + \frac{\partial}{\partial t}T_{\chi'\to\chi}(\mathbf{r},t)
\end{aligned} \tag{4.6}$$

equation (4.5) is transformed into itself, but with $\Psi_\chi \to \Psi_{\chi'}$, $\mathbf{A}_\chi \to \mathbf{A}_{\chi'}$, and $\Phi_\chi \to \Phi_{\chi'}$. The transformation functions $T_{\chi\to\chi'}(\mathbf{r},t)$ satisfy the relations

$$T_{\chi\to\chi'} = -T_{\chi'\to\chi}, \quad T_{\chi\to\chi'} + T_{\chi'\to\chi''} = T_{\chi\to\chi''} \quad . \tag{4.7}$$

Of course, physical quantities as the probability $P(\mathbf{r},t)$ or the electric and magnetic fields ($\mathbf{F}(\mathbf{r},t)$ and $\mathbf{B}(\mathbf{r},t)$) are gauge independent, i. e.

$$P(\mathbf{r},t) = |\Psi_\chi(\mathbf{r},t)|^2 = |\Psi_{\chi'}(\mathbf{r},t)|^2 \tag{4.8}$$

$$\mathbf{F}(\mathbf{r},t) = -\nabla\Phi_\chi(\mathbf{r},t) - \frac{\partial}{\partial t}\mathbf{A}_\chi(\mathbf{r},t) = -\nabla\Phi_{\chi'}(\mathbf{r},t) - \frac{\partial}{\partial t}\mathbf{A}_{\chi'}(\mathbf{r},t) \tag{4.9}$$

$$\mathbf{B}(\mathbf{r},t) = \nabla\times\mathbf{A}_\chi(\mathbf{r},t) = \nabla\times\mathbf{A}_{\chi'}(\mathbf{r},t). \tag{4.10}$$

4.2.2. Form-invariant physical quantities

A form-invariant quantity is defined as a quantity whose corresponding operator $G_\chi = G(\mathbf{A}_\chi, \Phi_\chi)$ is form invariant under a unitary transformation $\hat{\mathrm{T}}_{\chi\to\chi'} = \exp\left[\mathrm{i}T_{\chi\to\chi'}(\mathbf{r},t)\right]$, i. e.,

$$G_{\chi'} \equiv \hat{\mathrm{T}}_{\chi\to\chi'}G_\chi\hat{\mathrm{T}}^\dagger_{\chi\to\chi'} = G(\mathbf{A}_{\chi'}, \Phi_{\chi'}) \tag{4.11}$$

The important difference between physical and non-physical quantities lies in the gauge invariance of their eigenvalues. The eigenvalues of a physical quantity (an observable) are identical in all gauges, whereas the eigenvalues of non-physical quantities may depend on the chosen gauge. It can be shown that the eigenvalues of a form-invariant quantity are gauge-invariant, i. e. a physical quantity must be form-invariant. Consider the operator G_χ with the eigenvalues g_n and the corresponding eigenstates $|\chi, n\rangle$,

$$G_\chi|\chi, n\rangle = g_n|\chi, n\rangle \tag{4.12}$$

The operator $G_{\chi'}$ obtained by the unitary transformation (4.11) has the eigenstates $|\chi', n\rangle = \hat{\mathrm{T}}_{\chi\to\chi'}|\chi, n\rangle$ and the same eigenvalues g_n

$$G_{\chi'}|\chi', n\rangle = (\hat{\mathrm{T}}_{\chi\to\chi'}G_\chi\hat{\mathrm{T}}^\dagger_{\chi\to\chi'})(\hat{\mathrm{T}}_{\chi\to\chi'}|\chi, n\rangle) = \hat{\mathrm{T}}_{\chi\to\chi'}g_n|\chi, n\rangle = g_n|\chi', n\rangle \tag{4.13}$$

Both $\mathbf{A}_\chi$ and Φ_χ are not operators that correspond to physical quantities. The canonical momentum is also not form-invariant,

$$\hat{\mathrm{T}}_{\chi\to\chi'}\mathbf{p}_\mathrm{c} = \hat{\mathrm{T}}^\dagger_{\chi\to\chi'}\mathbf{p}_\mathrm{c} - \nabla T_{\chi\to\chi'}(\mathbf{r}, t)\ , \tag{4.14}$$

and, therefore, does not represent a physical measurable quantity, whereas the mechanical momentum

$$\boldsymbol{\pi}_\chi \equiv \mathbf{p}_\mathrm{c} + \mathbf{A}_\chi(\mathbf{r}, t) \tag{4.15}$$

is form-invariant,

$$\hat{\mathrm{T}}_{\chi\to\chi'}\boldsymbol{\pi}_\chi\hat{\mathrm{T}}^\dagger_{\chi\to\chi'} = \mathbf{p}_\mathrm{c} - \nabla T_{\chi\to\chi'}(\mathbf{r}, t) + \mathbf{A}_\chi = \mathbf{p}_\mathrm{c} + \mathbf{A}_{\chi'} = \boldsymbol{\pi}_{\chi'}, \tag{4.16}$$

and represents an observable. The electrostatic potential $U(\mathbf{r})$ also represents a physical quantity. The instantaneous energy operator of the system, $\mathcal{E}_\chi$,

$$\mathcal{E}_\chi \equiv \frac{1}{2}\Big[\mathbf{p}_\mathrm{c} + \mathbf{A}_\chi(\mathbf{r}, t)\Big]^2 + U(\mathbf{r}) \ = \ \frac{\boldsymbol{\pi}_\chi^2}{2} + U(\mathbf{r})\ , \tag{4.17}$$

represents a physical quantity, since it is a function of only physical quantities: $\boldsymbol{\pi}_\chi$ and $U(\mathbf{r})$.

It is essential that both the total Hamiltonian of the system,

$$\hat{\mathrm{H}}_\chi \equiv \frac{1}{2}\Big[\mathbf{p}_\mathrm{c} + \mathbf{A}_\chi(\mathbf{r}, t)\Big]^2 - \Phi_\chi(\mathbf{r}, t) + U(\mathbf{r}) = \mathcal{E}_\chi - \Phi_\chi(\mathbf{r}, t), \tag{4.18}$$

and the field-free Hamiltonian,

$$\hat{\mathrm{H}}_0 \equiv \frac{\mathbf{p}_\mathrm{c}^2}{2} + U(\mathbf{r}), \tag{4.19}$$

are not form-invariant, although they determine the evolution of a physical system.

4.2.3. Different gauges

The *radiation gauge* (labeled in the following by the subscript R) is convenient, if no sources are presented. It is defined by the relations

$$\nabla \cdot \mathbf{A}_{\mathrm{R}} = 0, \quad \Phi_{\mathrm{R}} = 0 \quad . \tag{4.20}$$

Therefore, one has $\nabla \cdot (\mathbf{A}_{\mathrm{R}}\Psi) = \mathbf{A}_{\mathrm{R}}(\nabla\Psi) + (\nabla \cdot \mathbf{A}_{\mathrm{R}})\Psi = \mathbf{A}_{\mathrm{R}}(\nabla\Psi)$ and the total Hamiltonian of the system possesses the form

$$\hat{\mathrm{H}}_{\mathrm{R}} = \mathbf{p}_{\mathrm{c}}^2/2 + \mathbf{A}_{\mathrm{R}} \cdot \mathbf{p}_{\mathrm{c}} + \mathbf{A}_{\mathrm{R}}^2/2 + U \quad . \tag{4.21}$$

The vector potential in this gauge satisfies the wave equation and can be given by a superposition of monochromatic plane wave solutions. In the following, the vector function $\mathbf{A}(\mathbf{r}, t)$ specifies the vector potential $\mathbf{A}_{\mathrm{R}}(\mathbf{r}, t)$ in radiation gauge, so that

$$\mathbf{F}(\mathbf{r}, t) = -\frac{\partial}{\partial t}\mathbf{A}(\mathbf{r}, t), \quad \mathbf{B}(\mathbf{r}, t) = \nabla \times \mathbf{A}(\mathbf{r}, t). \tag{4.22}$$

If the wavelength of the considered radiation is sufficiently long, the spatial variation of the radiation field across the system can be neglected. Assuming $\mathbf{A}(\mathbf{r}, t) \approx \mathbf{A}(t)$ one obtains

$$\mathbf{F} = \mathbf{F}(t) = -\frac{\mathrm{d}\mathbf{A}(t)}{\mathrm{d}t}, \qquad \mathbf{B} = 0. \tag{4.23}$$

There exist two gauges, length and velocity gauge, which are extensively used in the context of the dipole approximation. It is, however, known that the conditions for a breakdown of the dipole approximation differ in different gauges. In order to explicitly highlight the terms which are neglected in the subsequent use of the dipole approximation, the general definitions of length and velocity gauges are given in the following paragraphs.

The *velocity gauge* (labeled in the following by the subscript V) is often used to remove the square of the vector potential from the total Hamiltonian. Note, the name "velocity gauger" is frequently used, if in fact the radiation gauge is meant. The reason is the equivalence of these two gauges in the weak-field limit in which the A^2 term can be neglected (with respect to the remaining terms). For strong fields this term is, however, not negligible and it is thus important to distinguish between these two gauges. The velocity gauge can in fact be obtained from the radiation gauge by means of the transformation function

$$T_{\mathrm{R}\to\mathrm{V}}(\mathbf{r},t) = \frac{1}{2}\int^{t} \mathbf{A}^2(\mathbf{r},t')\,\mathrm{d}t' \equiv \beta(\mathbf{r},t) \quad . \tag{4.24}$$

The vector and scalar potentials are given in the velocity gauge by

$$\mathbf{A}_{\mathrm{V}} = \mathbf{A} - \nabla\beta, \qquad \Phi_{\mathrm{V}} = \mathbf{A}^2/2 \tag{4.25}$$

and the total Hamiltonian can be rewritten as

$$\hat{\mathrm{H}}_{\mathrm{V}} = \mathbf{p}_{\mathrm{c}}^2/2 + \mathbf{A}_{\mathrm{V}}\cdot\mathbf{p}_{\mathrm{c}} + \mathrm{i}\Delta\beta + U \tag{4.26}$$

where the identity $\nabla\cdot\mathbf{A}_{\mathrm{V}} = -\Delta\beta$ has been used.

Within the dipole approximation, the vector potential has the simpler form $\mathbf{A}_{\mathrm{V}} = \mathbf{A}(t)$ and Eq. (4.26) reduces to

$$\hat{\mathrm{H}}_{\mathrm{V}} = \mathbf{p}_{\mathrm{c}}^2/2 + U + \mathbf{A}(t)\cdot\mathbf{p}_{\mathrm{c}} \quad . \tag{4.27}$$

Another useful and popular gauge is the *length gauge* (labeled in the following by the subscript L). It is obtained from the radiation gauge, if the transformation function

$$T_{\mathrm{R}\to\mathrm{L}}(\mathbf{r},t) = \mathbf{A}(\mathbf{r},t)\cdot\mathbf{r} \tag{4.28}$$

is applied. This leads to the length-gauge vector and scalar potentials

$$\mathbf{A}_{\mathrm{L}} = \mathbf{A} - \nabla(\mathbf{A}\cdot\mathbf{r}) = -\mathrm{i}\mathbf{L}\times\mathbf{A}, \quad \Phi_{\mathrm{L}} = -\mathbf{F}\cdot\mathbf{r} \tag{4.29}$$

where $\mathbf{L}\equiv\mathbf{r}\times\mathbf{p}_{\mathrm{c}}$ is the canonical angular momentum. Within the dipole approximation, the vector potential in length gauge is simply zero. This leads to a simple form of the total Hamiltonian that is given in length gauge by

$$\hat{\mathrm{H}}_{\mathrm{L}} = \mathbf{p}_{\mathrm{c}}^2/2 + U + \mathbf{F}(t)\cdot\mathbf{r}. \tag{4.30}$$

Note, in this case the operators of the mechanical and canonical momentum coincide, $\boldsymbol{\pi}_{\mathrm{L}} = \mathbf{p}_{\mathrm{c}}$.

It can be shown that both the length and velocity gauges are only particular cases of a generalized gauge defined by an arbitrary set of parameters, $X = \{x_1, x_2\}$. This gauge, which will be referred to as X *gauge*, is obtained via the transformation

$$T_{\mathrm{R}\to X}(\mathbf{r}, t) = x_1\mathbf{A}(t)\cdot\mathbf{r} + x_2\beta(t) \tag{4.31}$$

In the X gauge the vector and scalar potentials are given as

$$\mathbf{A}_X(t) = (1-x_1)\mathbf{A}(t), \quad \Phi_X = -x_1\mathbf{F}(t)\cdot\mathbf{r} + x_2\mathbf{A}^2(t)/2 \quad . \tag{4.32}$$

This leads to the total Hamiltonian

$$\begin{aligned}\hat{\mathrm{H}}_X = \;& \mathbf{p}_{\mathrm{c}}^2/2 + U + (1-x_1)\mathbf{A}(t)\cdot\mathbf{p}_{\mathrm{c}} + x_1\,\mathbf{F}(t)\cdot\mathbf{r} \\ & + \left[(1-x_1)^2 - x_2\right]\mathbf{A}^2(t)/2.\end{aligned} \tag{4.33}$$

In particular, $X = \{0, 0\}$, $X = \{0, 1\}$, and $X = \{1, 0\}$ correspond to the total Hamiltonians in radiation gauge (4.21), velocity gauge (4.27), and length gauge (4.30), respectively.

In fact, even the X gauge is only a particular case of a more generalized gauge defined by an arbitrary set of functions $\{\mathbf{X}(t), X_0(t)\}$. This gauge, which will be referred to as **X** *gauge*, is obtained via the transformation

$$T_{\mathrm{R}\to X}(\mathbf{r}, t) = \mathbf{X}(t)\cdot\mathbf{r} + X_0(t). \tag{4.34}$$

The vector and scalar potentials are thus given in the **X** gauge as

$$\mathbf{A}_{\mathbf{X}}(t) = \mathbf{A}(t) - \mathbf{X}(t), \quad \Phi_{\mathbf{X}} = \dot{\mathbf{X}}(t)\cdot\mathbf{r} + \dot{X}_0(t), \tag{4.35}$$

and the total Hamiltonian $\hat{\mathrm{H}}_{\mathbf{X}}$ reads

$$\hat{\mathrm{H}}_{\mathbf{X}} = \mathbf{p}_{\mathrm{c}}^2/2 + U + \mathbf{A}_{\mathbf{X}}(t)\cdot\mathbf{p}_c - \Phi_{\mathbf{X}}(\mathbf{r}, t) + \mathbf{A}_{\mathbf{X}}^2(t)/2 \tag{4.36}$$

As is clear from the definitions, the **X** gauge reduces to the X gauge with the following choice of functions

$$\mathbf{X}(t) = x_1\mathbf{A}(t), \qquad X_0(t) = x_2\beta(t) \tag{4.37}$$

Generalized gauges provide the additional flexibility which can be employed in the numerical solution of the TDSE or in the formulation of the S-matrix theory describing atomic and molecular systems in intense laser fields, as will be discussed in Sec. 5.1.

4.3. Free electron in a laser field

Consider now a free electron in the presence of a laser field described by $\mathbf{A}(t)$. In the velocity gauge the TDSE reads

$$\mathrm{i}\frac{\partial}{\partial t}\Psi_{\mathrm{V}}(\mathbf{r},t) = \Big[\mathbf{p}_{\mathrm{c}}^2/2 + \mathbf{A}(t)\cdot\mathbf{p}_{\mathrm{c}}\Big]\Psi_V(\mathbf{r},t). \tag{4.38}$$

The solution of Eq. (4.38) is the (non-relativistic) *Volkov wavefunction* [115]

$$\Psi^{\mathrm{Vv}}_{\mathrm{V},\mathbf{p}}(\mathbf{r},t) = \exp\Big[\mathrm{i}\,\mathbf{p}\cdot\big\{\mathbf{r}-\boldsymbol{\alpha}(t)\big\} - \mathrm{i}E_p t\Big], \quad E_p = p^2/2. \tag{4.39}$$

where $\boldsymbol{\alpha}(t) = \int^t \mathbf{A}(t')\,\mathrm{d}t'$ and the δ-function normalization is used. It is important to emphasize the physical meaning of the vector $\mathbf{p}$ and the scalar E_p that are usually referred to as electron momentum and electron energy, respectively. In fact, $\mathbf{p}$ is the mean value of canonical momentum in velocity gauge, $\langle\mathbf{p}_{\mathrm{c}}\rangle_{\mathrm{V}} \equiv \mathbf{p}$. The mean value of mechanical momentum is on the other hand time-dependent and equal to $\mathbf{p}+\mathbf{A}(t)$. As was discussed above, this latter value is gauge-independent and will be denoted in the following by $\boldsymbol{\pi}$; thus one has $\boldsymbol{\pi} = \boldsymbol{\pi}(\mathbf{p},t) = \mathbf{p}+\mathbf{A}(t)$. To stress the independence on a gauge, the vector function $\boldsymbol{\pi}$ has no subscript, in contrast to the operators $\boldsymbol{\pi}_{\mathrm{R}}$, $\boldsymbol{\pi}_{\mathrm{V}}$, or $\boldsymbol{\pi}_{\mathrm{L}}$. The mean value $\mathcal{E}(\mathbf{p},t) = \boldsymbol{\pi}^2(\mathbf{p},t)/2$ of the instantaneous energy operator (4.17) is thus also time-dependent.

Using the identity

$$\frac{1}{2}\int^t \mathcal{E}(\mathbf{p},t')\,\mathrm{d}t' = E_p t + \mathbf{p}\cdot\boldsymbol{\alpha}(t) + \beta(t) \tag{4.40}$$

the Volkov wavefunction can be written as either

$$\Psi^{\mathrm{Vv}}_{\mathrm{R},\mathbf{p}}(\mathbf{r},t) = \exp\Big[\mathrm{i}\mathbf{p}\cdot\mathbf{r} - \mathrm{i}\int^t \mathcal{E}(\mathbf{p},t')\,\mathrm{d}t'\Big] \tag{4.41}$$

or

$$\Psi^{\mathrm{Vv}}_{\mathrm{L},\mathbf{p}}(\mathbf{r},t) = \exp\Big[\mathrm{i}\boldsymbol{\pi}(\mathbf{p},t)\cdot\mathbf{r} - \mathrm{i}\int^t \mathcal{E}(\mathbf{p},t')\,\mathrm{d}t'\Big] \tag{4.42}$$

in radiation and length gauge, respectively.

In X gauge one finds

$$\Psi^{\mathrm{Vv}}_{X,\mathbf{p}}(\mathbf{r},t) = \exp\Big[\mathrm{i}x_1\mathbf{A}(t)\cdot\mathbf{r} + \mathrm{i}x_2\beta(t)\Big]\Psi^{\mathrm{Vv}}_{\mathrm{R},\mathbf{p}}(\mathbf{r},t) = e^{-\mathrm{i}\Theta_X(t)}e^{\mathrm{i}\mathbf{p}\cdot\mathbf{r}} \tag{4.43}$$

with

$$\Theta_X(t) = E_p t + \mathbf{p} \cdot \boldsymbol{\alpha}(t) - x_1 \mathbf{A}(t) \cdot \mathbf{r} - (x_2 - 1)\beta(t) \quad . \tag{4.44}$$

Note, in length gauge $\mathbf{p}$ can be seen purely as a parameter, since also the mean value of the canonical momentum $\langle \mathbf{p}_{\mathrm{c}} \rangle_{\mathrm{L}}$ is equal to $\boldsymbol{\pi}$. Nevertheless, the physical meaning of $\mathbf{p}$ becomes evident in the case of a linear-polarized monochromatic electromagnetic field.

For a vector potential given by $\mathbf{A}(t) = -\mathbf{A} \sin \omega t$ the corresponding electric field is $\mathbf{F}(t) = \mathbf{F} \cos \omega t$ with $\mathbf{F} = \omega \mathbf{A}$. In this case the mean value of the mechanical momentum is equal to $\boldsymbol{\pi}(\mathbf{p}, t) = \mathbf{p} - \mathbf{F}/\omega \sin \omega t$. Therefore, $\mathbf{p}$ is the value of the cycle-averaged $\boldsymbol{\pi}$. An electron with $\mathbf{p} = 0$ quivers in the field around a single point in space.

The mean value $\mathcal{E}(\mathbf{p}, t)$ of the instantaneous energy operator (4.17) is time-dependent and given by

$$\mathcal{E}(\mathbf{p}, t) = \frac{1}{2}\left(\mathbf{p} - \frac{\mathbf{F}_0}{\omega} \sin \omega t\right)^2 = E_p - \mathbf{p} \cdot \frac{\mathbf{F}_0}{\omega} \sin \omega t - U_p \cos 2\omega t + U_p. \tag{4.45}$$

Therefore, its cycle-averaged value is equal to $E_p + U_p$. The ponderomotive energy $U_p = F^2/(4\omega^2)$ is thus the cycle-averaged instantaneous energy of a quivering electron ($\mathbf{p} = 0$).

4.4. Generalized field-free Hamiltonian

Consider an N-electron system that in the absence of an electromagnetic field is described by the field-free Hamiltonian

$$\hat{\mathrm{H}}^0(\mathbf{r}_1, \ldots, \mathbf{r}_N) = \sum_i^N \frac{\mathbf{p}_{\mathrm{c}}^2(i)}{2} + U(\mathbf{r}_1, \ldots, \mathbf{r}_N) \tag{4.46}$$

where U incorporates all possible electron-nucleus and electron-electron interactions. A solution of the TDSE with $\hat{\mathrm{H}}^0$ can be given as a linear superposition of vectors $|\Psi_\alpha(t)\rangle$ defined as

$$|\Psi_\alpha(t)\rangle = e^{-\mathrm{i}E_\alpha t} |\psi_\alpha\rangle \tag{4.47}$$

where E_α and $|\psi_\alpha\rangle$ are eigenvalues and eigenvectors of the operator $\hat{\mathrm{H}}^0$, correspondingly. (The composed index α denotes discrete as well as continuum states and is itself either discrete or continuous.)

If the system is exposed to an intense laser pulse, the TDSE formulated in the **X** gauge,

$$\left(\mathrm{i}\frac{\partial}{\partial t} - \hat{\mathrm{H}}_{\mathbf{X}}(t)\right)|\Psi_{\mathbf{X}}(t)\rangle = 0, \tag{4.48}$$

where Hamiltonian $\hat{\mathrm{H}}_{\mathbf{X}}$ is given by

$$\hat{\mathrm{H}}_{\mathbf{X}} = \hat{\mathrm{H}}^0 + \sum\nolimits_i \left\{\mathbf{A}_{\mathbf{X}}(t)\cdot\mathbf{p}_c(i) - \Phi_{\mathbf{X}}(\mathbf{r}_i,t) + \mathbf{A}^2_{\mathbf{X}}(t)/2\right\}, \tag{4.49}$$

can be solved by expanding the time-dependent vector $|\Psi_{\mathbf{X}}(t)\rangle$ in the basis of vectors $|\Psi_\alpha(t)\rangle$. This is, however, not the only choice. More generally, the time-dependent vector $|\Psi_{\mathbf{X}}(t)\rangle$ can be expanded as

$$|\Psi_{\mathbf{X}}(t)\rangle = \sum_\alpha C_\alpha(t)|\Psi_{\gamma,\alpha}(t)\rangle \tag{4.50}$$

where the $|\Psi_{\gamma,\alpha}(t)\rangle$ are solutions of the TDSE with the generalized field-free Hamiltonian $\hat{\mathrm{H}}^0_\gamma(\mathbf{r}_1,\ldots,\mathbf{r}_N,t)$,

$$\begin{aligned}\hat{\mathrm{H}}^0_\gamma &= e^{\mathrm{i}\gamma}\hat{\mathrm{H}}^0 e^{-\mathrm{i}\gamma} - \frac{\partial\gamma}{\partial t}\\ &= \hat{\mathrm{H}}^0 + \sum_i^N \left\{\mathrm{i}\frac{\Delta\gamma}{2} - (\nabla\gamma)\cdot\mathbf{p}_c(i) + \frac{1}{2}(\nabla\gamma)^2\right\} - \frac{\partial\gamma}{\partial t},\end{aligned} \tag{4.51}$$

which is defined with the aid of an arbitrary function

$$\gamma(\mathbf{r}_1,\ldots,\mathbf{r}_N,t) = \sum_i^N \mathbf{L}_i(t)\cdot\mathbf{r}_i + L_0(t). \tag{4.52}$$

in such a way that it reduces for $\gamma = 0$ to the field-free Hamiltonian $\hat{\mathrm{H}}^0$. The function γ is in turn defined with the aid of the arbitrary time-dependent functions $\mathbf{L}_i(t)$ and $L_0(t)$. As follows from the definition (4.51), solutions of the TDSE with $\hat{\mathrm{H}}^0_\gamma$ can be simply written as

$$|\Psi_{\gamma,\alpha}(t)\rangle = e^{\mathrm{i}\gamma}|\Psi_\alpha(t)\rangle \tag{4.53}$$

Making the partitioning $\hat{\mathrm{H}}_{\mathbf{X}} = \hat{\mathrm{H}}^0_\gamma + V_{\mathbf{X},\gamma}$ and using Eqs. (4.23), (4.35), (4.49), (4.51) and (4.52) one obtains

$$V_{\mathbf{X},\gamma} = \sum_i^N \Big\{ \mathbf{G}_i(t)\cdot\mathbf{p}_{\mathrm{c}}(i) + [\mathbf{F}(t) + \dot{\mathbf{G}}_i(t)]\cdot\mathbf{r}_i \\ + \mathbf{G}_i^2(t)/2 - \mathbf{G}_i(t)\cdot\mathbf{L}_i(t)\Big\} + \dot{G}_0(t), \tag{4.54}$$

where some new functions were introduced that are defined as

$$\mathbf{G}_i(t) = \mathbf{A}(t) + \mathbf{L}_i(t) - \mathbf{X}(t), \qquad G_0(t) = L_0(t) - NX_0(t) \tag{4.55}$$

One can show that matrix elements of the operator $V_{\mathbf{X},\gamma}$ expressed in the basis of the vectors $|\Psi_{\gamma,\alpha}(t)\rangle$,

$$\begin{aligned}\left\langle \Psi_{\gamma,\alpha'}(t)\left|V_{\mathbf{X},\gamma}(t)\right|\Psi_{\gamma,\alpha}(t)\right\rangle &= \left\langle \Psi_{\alpha'}(t)\left|V_{\mathbf{X},\gamma}(t) + \sum_i^N \mathbf{G}_i(t)\cdot\mathbf{L}_i(t)\right|\Psi_\alpha(t)\right\rangle \\ &= \left\langle \Psi_{\alpha'}(t)\left|\bar{V}_G(t)\right|\Psi_\alpha(t)\right\rangle \ ,\end{aligned} \tag{4.56}$$

depends only on these new functions $\mathbf{G}_i(t)$ and $G_0(t)$, since

$$\bar{V}_G(t) = \bar{V}_0(t) + \sum_i^N \bar{V}_i(t) \tag{4.57}$$

where

$$\bar{V}_i(t) = \mathbf{G}_i(t)\cdot\mathbf{p}_{\mathrm{c}}(i) + [\mathbf{F}(t) + \dot{\mathbf{G}}_i(t)]\cdot\mathbf{r}_i, \quad \bar{V}_0(t) = \dot{G}_0(t) + \sum_i^N \mathbf{G}_i^2(t)/2. \tag{4.58}$$

Multiplication of Eq. (4.48) with $\langle\Psi_{\gamma,\alpha'}(t)|$ for all α' and integration over the electronic coordinates yields a system of ordinary differential equations (ODE)

$$\begin{aligned}0 &= \left\langle \Psi_{\gamma,\alpha'}(t)\left|\mathrm{i}\frac{\partial}{\partial t} - \hat{\mathrm{H}}_{\mathbf{X}}\right|\Psi_{\mathbf{X}}(t)\right\rangle = \sum_\alpha \left\langle \Psi_{\gamma,\alpha'}(t)\left|\mathrm{i}\dot{C}_\alpha(t) + C_\alpha(t)\hat{\mathrm{H}}^0_\gamma\right|\Psi_{\gamma,\alpha}(t)\right\rangle \\ &\quad - \sum_\alpha C_\alpha(t)\left\langle \Psi_{\gamma,\alpha'}(t)\left|\hat{\mathrm{H}}^0_\gamma + V_{\mathbf{X},\gamma}(t)\right|\Psi_{\gamma,\alpha}(t)\right\rangle \\ &= \mathrm{i}\sum_\alpha \dot{C}_\alpha(t)\langle\Psi_{\gamma,\alpha'}(t)|\Psi_{\gamma,\alpha}(t)\rangle - \sum_\alpha C_\alpha(t)\left\langle \Psi_{\gamma,\alpha'}(t)\left|V_{\mathbf{X},\gamma}(t)\right|\Psi_{\gamma,\alpha}(t)\right\rangle\end{aligned} \tag{4.59}$$

Assuming that γ is a real function and applying Eq. (4.56) to the system of equations (4.59), the latter can be rewritten as

$$\mathrm{i}\sum_{\alpha}\dot{C}_{\alpha}(t)\langle\Psi_{\alpha'}(t)|\Psi_{\alpha}(t)\rangle=\sum_{\alpha}C_{\alpha}(t)\left\langle\Psi_{\alpha'}(t)\left|\bar{V}_G(t)\right|\Psi_{\alpha}(t)\right\rangle\ . \tag{4.60}$$

If a discretization of the continuum is used and the vectors $|\psi_\alpha\rangle$ fulfill the ortho-normality condition $\langle\psi_{\alpha'}|\psi_\alpha\rangle=\delta_{\alpha'\alpha}$, the system of equations (4.60) can be further simplified as

$$\mathrm{i}\dot{C}_{\alpha'}(t)=\sum_{\alpha}C_{\alpha}(t)\left\langle\Psi_{\alpha'}(t)\left|\bar{V}^0_G(t)\right|\Psi_{\alpha}(t)\right\rangle\ . \tag{4.61}$$

From this discussion follows that an identical system of ODEs can be obtained solving the TDSE in different gauges. It can be realized by the appropriate choice of the generalized field-free Hamiltonian, i.e. so that the functions $\mathbf{G}_i(t)$ and $G_0(t)$ remain unchanged. Since the functions $\mathbf{G}_i(t)$ are arbitrary, one can write down the system of ODEs in infinitely many ways. For example, the traditional L-gauge form with $\bar{V}_i(t)=\mathbf{F}(t)\cdot\mathbf{r}_i$ is obtained using $\mathbf{G}_i(t)=0$, whereas using $\mathbf{G}_i(t)=\mathbf{A}(t)$ the traditional V-gauge form $\bar{V}_i(t)=\mathbf{A}(t)\cdot\mathbf{p}_{\mathrm{c}}(i)$ is yielded. For any choice of functions $\mathbf{G}_i(t)$ the term $\bar{V}_0(t)$ can be turned to zero using $G_0(t)=-\sum_i\int\mathrm{d}t\,\mathbf{G}_i^2(t)/2$. If both $\mathbf{X}(t)$ and $\mathbf{G}_i(t)$ are zero before and after the pulse, the final probabilities $|C_\alpha(\infty)|^2$ will not depend on their specific choice. However, one of the various forms may be preferable to the others from the numerical point of view or for the analysis of dynamics during the pulse (see Sec. 6.6)

To conclude, one has to be very careful not to consider solely the gauge, since a suitable choice of the partitioning may lead to an expansion that is identical to the one obtained in some other gauge. Thus, the question of a "proper" choice of the gauge is in fact the question of a "proper" choice of the expansion, since truncation of an infinite series may result in different errors for different expansions.

Furthermore, the present formulation leads to an additional flexibility compared to traditional formulations. For example, for many-electron systems one can construct an expansion using different $\mathbf{G}_i(t)$ functions for different electron indices i. In the traditional formulation this corresponds to the case, where different electrons of the system are described in different gauges.

5. Strong-field approximation

The strong-field approximation is very popular to describe nonresonant multiphoton ionization of atoms and molecules in intense laser fields. While the principle concept of ignoring the effect of the interaction of the ionized electron with the remaining atomic or molecular system in the final state is common to all variants of the strong-field approximation, the approaches differ in the details of their formulations. Thus, formulations in length and velocity gauges result in different expressions for the transition amplitudes and there is no *a priori* reason that one of the two SFA formulations is superior to the other (the gauge problem of SFA). Based on the concepts of a generalized gauge and a generalized field-free Hamiltonian, a deeper insight into the gauge problem of SFA is provided in Sec. 5.1 by introducing the concept of generalized SFA formulations. It is demonstrated, that one has to be very careful not to consider solely the gauge, since identical expression can be obtained in different gauges if the Hamiltonian is correspondingly partitioned.

Even if the same formulation is used, different approximations can further be employed by various SFA implementations. For example, the method of steepest descent (also known as saddle-point approximation) is very frequently used in length-gauge SFA calculations. Recently, a new method [138] has been proposed to avoid this approximation. Shortcomings of these two approaches are discussed in Sec. 5.2.

SFA rates in the length and velocity gauges may differ even qualitatively. This is demonstrated in Sec. 5.3 where the quasistatic limit of the velocity-gauge SFA is derived. It is shown that in the low-frequency limit the ionization rate is proportional to the laser frequency, if a Coulombic long-range interaction is present. Therefore, unlike the length-gauge SFA, the velocity-gauge SFA ionization rates do not converge to the limit predicted by quasistatic theories.

The chapter closes with a brief discussion of how the SFA theory is generalized to describe molecules. Furthermore, it is shown that for molecular hydrogen the velocity formulation of SFA predicts a simple interference pattern for the ratio of the energy-resolved electron spectra obtained for a parallel and a perpendicular orientations of the molecular axis with respect to the polarization axis of linear polarized laser pulses. Thus, an experimental investigation of the interference prediction of SFA in velocity gauge is proposed.

5.1. Generalized SFA formulations

The strong-field approximation is based on an (infinite) series expansion of the exact S matrix describing the interaction of an atomic (molecular) system with a laser pulse. Besides a phase factor, the S matrix obtained from a calculation of the complete expansion should thus be independent on the chosen gauge, provided the series converges. Consequently, the corresponding observable transition probabilities (obtained from the squared absolute values of the S-matrix elements) should be gauge independent.

This gauge-independence of physical observables is usually lost, if only a truncated series is considered. This is the case for the SFA which is defined as the first term of the S-matrix expansion. In a number of investigations it has been shown that transition probabilities or rates predicted by either the length- or the velocity-gauge formulation of the SFA differ easily by one or two orders of magnitude for experimentally relevant laser parameters [139]. Recently, it was also demonstrated that there are pronounced qualitative differences between the energy distributions of the electrons ejected from, e. g., the 2p state of hydrogen atoms exposed to intense laser fields, if they are calculated within the SFA and either the length or the velocity gauge [140]. The recent extensions of the SFA to molecular systems in velocity gauge [141], length gauge [142], or dressed length gauge [19] indicate similar or even more pronounced gauge dependencies for molecules. These findings have intensified the discussions whether the formulation of the SFA in one of the two gauges may be "superior" to the other. One approach to answer this question is rather pragmatic and based on a direct comparison of the SFA predictions in both gauges to either exact (numerical) solutions of the full time-dependent Schrödinger equation [40, 140] or to experimental results [143, 144]. Clearly, if there is no *a priori* reason that one of the two SFA formulations is superior to the other, the conclusions may vary depending on the considered atomic or molecular system (even its quantum state) as well as on laser-pulse parameters.

A second line of argumentation in favor of one of the two gauges is based on the question of "universality". For example, it has been argued that an evident limitation of the length-gauge formulation is the fact that in this case the predicted observables depend only on the scalar potential and thus a one-dimensional parameter, while the full description of an electromagnetic field requires in principle more than one dimension [145]. Very recently, Faisal proposes a "gauge-invariant" intense-field S-matrix theory that yields equal transition probabilities in length or velocity gauge; independent of the order of the expansion [146]. Consequently, Faisal claims that his theory overcomes the above-mentioned long-standing discrepancy between the SFA in the two gauges. According to the findings in [146] the "gauge-invariant" and thus universal S-matrix theory appears to be equivalent to the traditional length-gauge formulation. Specifically, the first-order term reproduces exactly the Keldysh result [114] which was obtained in length gauge. In view of the popularity of the SFA for describing atomic and molecular ionization in intense laser fields (see, e. g., [147] or [6] and references therein), this is an important result.

Besides the evident appeal of a universal S-matrix formulation which would provide an end to the long-lasting debates on the choice of the appropriate gauge (for a very recent example, see [148–150]), it appears, however, quite surprising that such a formulation should exist. In fact, Faisal derives in [151] an alternative S-matrix expansion that reproduces in length and velocity gauge the traditional velocity-gauge result. Inspired by the results in [146] and [151] it is shown in the present work that it is possible to achieve an S-matrix expansion in agreement to any traditional SFA formulation in either length, velocity, or radiation gauge for an arbitrary choice of the gauge, if the Hamiltonian is correspondingly partitioned. In fact, introducing a generalized gauge transformation that includes the mentioned particular gauges as special cases, an in principle infinite set of different S-matrix expansions can be formulated. All of them can be shown to be achievable within any gauge as long as a proper partitioning of the Hamiltonian is performed. Furthermore, the introduction of the generalized gauge allows to clearly demonstrate how the choice of the gauge and the partitioning of the Hamiltonian describing the atomic or molecular system exposed to a laser field are connected with each other. This provides a much deeper insight in the gauge-problem of the SFA that in fact turns out to be more properly described as an expansion problem.

5.1.1. Formal *S*-matrix formulation of the SFA

The following formulation of the S-matrix theory describing atomic and molecular systems in intense laser fields considers the case of a one-electron system for the sake of simplicity. The generalization to an arbitrary number of electrons is, however, straightforward. As a starting point the TDSE is formulated in the X gauge (see Sec. 4.2.3),

$$\left(\mathrm{i}\frac{\partial}{\partial t} - \hat{\mathrm{H}}_X(t)\right)|\Psi_X(t)\rangle = 0, \tag{5.1}$$

where Hamiltonian $\hat{\mathrm{H}}_X$ is given by Eq. (4.33). The electromagnetic field is absent before and after the pulse, i. e.

$$\mathbf{A}(t) = \mathbf{A}_0, \qquad \mathbf{F}(t) = 0, \qquad \hat{\mathrm{H}}_X(t) = \hat{\mathrm{H}}^0 \qquad \text{for } t < t_i \text{ and } t > t_f \tag{5.2}$$

where the constant $\mathbf{A}_0$ has no physical meaning (since both the electric and magnetic fields are obtained as derivatives of the vector potential) and will be set to zero for the sake of simplicity. (Note, that using $\mathbf{A}_0 \neq 0$ requires a considerable modification of the following formulations). The operator $\hat{\mathrm{H}}^0$ is the field-free Hamiltonian with eigenvalues E_α and eigenvectors $|\psi_\alpha\rangle$,

$$\hat{\mathrm{H}}^0 = \mathbf{p}_\mathrm{c}^2/2 + U, \qquad \hat{\mathrm{H}}^0|\psi_\alpha\rangle = E_\alpha|\psi_\alpha\rangle. \tag{5.3}$$

(The index α denotes discrete as well as continuum states and is thus itself either discrete or continuous.)

To describe the action of the pulse on the system, complete and orthonormal initial- and final-state basis sets are introduced. The initial-state basis set is given by $|\psi_\alpha(t_i)\rangle = e^{-\mathrm{i}E_\alpha t_i}|\psi_\alpha\rangle$ where the phase factor is introduced for convenience. The final-state basis set is given by plane waves with momentum $\mathbf{p}$, again for convenience multiplied by a phase factor, and depends both on the adopted gauge and on $\mathbf{p}$,

$$|\Psi_{X,\mathbf{p}}(t_f)\rangle = e^{-\mathrm{i}\Theta_X(t_f)}|\mathbf{p}\rangle. \tag{5.4}$$

The phase (see Eqs. (4.44) and (5.2))

$$\Theta_X(t_f) = E_k t_f + \mathbf{p}\cdot\boldsymbol{\alpha}(t_f) - (x_2 - 1)\beta(t_f) \tag{5.5}$$

is $\mathbf{r}$ independent but depends on the used gauge, $\mathbf{p}$, and the pulse. Note, that the for reasons of convenience introduced phase factors add only constant phases in the transition amplitudes and do not alter transition probabilities.

The probability amplitude of a transition from an initial state $|\psi_\alpha(t_i)\rangle$ to a final state $|\Psi_{X,\mathbf{p}}(t_f)\rangle$ is given by

$$S_{\mathbf{p}\alpha} = \mathrm{i}\left\langle \Psi_{X,\mathbf{p}}(t_f)\left|\hat{\mathrm{G}}_X(t_f,t_i)\right|\psi_\alpha(t_i)\right\rangle \tag{5.6}$$

where the propagator $\hat{\mathrm{G}}_X(t,t')$ is associated with $\hat{\mathrm{H}}_X(t)$ by the inhomogeneous equation

$$\left(\mathrm{i}\frac{\partial}{\partial t} - \hat{\mathrm{H}}_X(t)\right)\hat{\mathrm{G}}_X(t,t') = \delta(t-t'). \tag{5.7}$$

To obtain a systematic expansion of the transition amplitudes of interest it is convenient to express the total propagator $\hat{\mathrm{G}}_X$ of the system in terms of a partial propagator, defined by the *partitioning* of the total Hamiltonian. The choice of the partitioning is made in such a way that the partial propagator can be expressed analytically, i. e. the Schrödinger equation with the corresponding partial Hamiltonian is solvable.

One class of Hamiltonians that leads to analytical solutions is the one describing a free electron in the field. As was discussed in Sec. 4.3, such Hamiltonians are gauge-dependent and their solutions are given by Volkov states. The partitioning of $\hat{\mathrm{H}}_X$ using the free-electron Hamiltonian in X gauge, $\hat{\mathrm{H}}^{\mathrm{f}}_X$, is given by

$$\hat{\mathrm{H}}_X = \hat{\mathrm{H}}^{\mathrm{f}}_X + U \tag{5.8}$$

The corresponding propagator can be written analytically using the solutions $|\Psi^{\mathrm{Vv}}_{X,\mathbf{p}}(t)\rangle$,

$$\hat{\mathrm{G}}^{\mathrm{f}}_X(t,t') = -i\theta(t-t')\sum_{\mathbf{p}}|\Psi^{\mathrm{Vv}}_{X,\mathbf{p}}(t)\rangle\langle\Psi^{\mathrm{Vv}}_{X,\mathbf{p}}(t')|, \tag{5.9}$$

where $\theta(x)$ is the step function. From Eq. (5.9) follows

$$-i\langle\Psi^{\mathrm{Vv}}_{X,\mathbf{p}}(t_f)|\hat{\mathrm{G}}^{\mathrm{f}}_X(t_f,t) = \langle\Psi^{\mathrm{Vv}}_{X,\mathbf{p}}(t)| \quad \text{for } t < t_f. \tag{5.10}$$

Another Hamiltonian that can be used for the partitioning is the field-free Hamiltonian $\hat{\mathrm{H}}^0$. It is, however, only a special case of the generalized field-free Hamiltonians, which were introduced in Sec. 4.4 for the **X** gauge (the reader is reminded that the X gauge is a particular case of a more general **X** gauge). Consider a particular choice of $\gamma(\mathbf{r},t)$ parameterized by a set of parameters, $\lambda = \{\lambda_1,\lambda_2\}$,

$$\gamma_\lambda(\mathbf{r},t) = \lambda_1\mathbf{A}(t)\cdot\mathbf{r} + \lambda_2\beta(t) \quad . \tag{5.11}$$

The corresponding generalized field-free Hamiltonian defined in Eq. (4.51) is then given by

$$\hat{\mathrm{H}}^0_\lambda = \hat{\mathrm{H}}^0 - \lambda_1\,\mathbf{A}(t)\cdot\mathbf{p}_{\mathrm{c}} + \lambda_1\,\mathbf{F}(t)\cdot\mathbf{r} + (\lambda_1^2-\lambda_2)\mathbf{A}^2(t)/2. \tag{5.12}$$

where here and in the following the subscript λ is adopted instead of γ_λ for the sake of notational simplicity. Note, for all choices of λ the Hamiltonian $\hat{\mathrm{H}}^0_\lambda$ gives an equivalent description of the evolution before and after the pulse, since for those times both $\mathbf{A}(t)$ and $\mathbf{F}(t)$ are equal to zero. Different choices of λ yield, however, different partial propagators $\hat{\mathrm{H}}^0_\lambda$ during the pulse that can be written analytically as

$$\hat{\mathrm{G}}^0_\lambda(t,t') = -i\theta(t-t')\sum_\alpha |\Psi_{\lambda,\alpha}(t)\rangle\langle\Psi_{\lambda,\alpha}(t')|. \tag{5.13}$$

In order to express the total propagator $\hat{\mathrm{G}}_X$ in terms of $\hat{\mathrm{G}}^0_\lambda$, the total Hamiltonian is partitioned in two parts,

$$\hat{\mathrm{H}}_X = \hat{\mathrm{H}}^0_\lambda + V_{X,\lambda} \tag{5.14}$$

with the interaction operator $V_{X,\lambda}$ given by

$$\begin{aligned} V_{X,\lambda}(t) = (1-x_1+\lambda_1)\mathbf{A}(t)\cdot\mathbf{p}_\mathrm{c} + (x_1-\lambda_1)\,\mathbf{F}(t)\cdot\mathbf{r} \\ + \left[(1-x_1)^2 - x_2 - \lambda_1^2 + \lambda_2\right]\mathbf{A}^2(t)/2\ . \end{aligned} \tag{5.15}$$

It is worth reminding that both sets of parameters, $X = \{x_1, x_2\}$ and $\lambda = \{\lambda_1, \lambda_2\}$, are independent of each other. Therefore, the same interaction operator can be obtained for different X gauges, if the λ parameters are appropriately chosen. It can be shown, for example, that

$$V_{\mathrm{R},\{-1,0\}} = V_{\mathrm{V},\{-1,1\}} = V_{\mathrm{L},\{0,0\}} = \mathbf{F}(t)\cdot\mathbf{r} \tag{5.16}$$

$$V_{\mathrm{R},\{0,-1\}} = V_{\mathrm{V},\{0,0\}} = V_{\mathrm{L},\{1,1\}} = \mathbf{A}(t)\cdot\mathbf{p}_\mathrm{c} \tag{5.17}$$

$$V_{\mathrm{R},\{0,0\}} = V_{\mathrm{V},\{0,1\}} = V_{\mathrm{L},\{1,2\}} = \mathbf{A}(t)\cdot\mathbf{p}_\mathrm{c} + \mathbf{A}^2(t)/2 \tag{5.18}$$

Since $|\Psi_{\lambda,\alpha}(t_i)\rangle = |\psi_\alpha(t_i)\rangle$, Eq. (5.13) yields

$$i\hat{\mathrm{G}}^0_\lambda(t,t_i)|\psi_\alpha(t_i)\rangle = |\Psi_{\lambda,\alpha}(t)\rangle, \quad \text{for } t > t_i. \tag{5.19}$$

5.1.2. Matrix elements

It will now be shown that most of the matrix elements of interest depend at most on the two parameters $v = \{v_1, v_2\}$ with $v_1 = 1 + \lambda_1 - x_1$ and $v_2 = \lambda_2 - x_2$.

Indeed, one finds for different matrix elements the relations

$$\langle\Psi^{\mathrm{Vv}}_{X,\mathbf{p}}(t)|\Psi_{\lambda,\alpha}(t)\rangle = \left\langle\mathbf{p}\left|e^{\mathrm{i}\Omega_{v\mathbf{p}\alpha}(t)}\right|\psi_\alpha\right\rangle, \tag{5.20}$$

$$\left\langle \Psi^{\mathrm{Vv}}_{X,\mathbf{p}}(t) \left| U \right| \Psi_{\lambda,\alpha}(t) \right\rangle = \left\langle \mathbf{p} \left| e^{\mathrm{i}\Omega_{v\mathbf{p}\alpha}(t)} U \right| \psi_\alpha \right\rangle, \tag{5.21}$$

$$\left\langle \Psi_{\lambda,\alpha'}(t) \left| V_{X,\lambda}(t) \right| \Psi_{\lambda,\alpha}(t) \right\rangle = e^{\mathrm{i}(E_{\alpha'}-E_\alpha)t} \left\langle \psi_{\alpha'} \left| \bar{V}_v(t) \right| \psi_\alpha \right\rangle, \tag{5.22}$$

and

$$\left\langle \Psi^{\mathrm{Vv}}_{X,\mathbf{p}}(t) \left| V_{X,\lambda}(t) \right| \Psi_{\lambda,\alpha}(t) \right\rangle = \left\langle \mathbf{p} \left| e^{\mathrm{i}\Omega_{v\mathbf{p}\alpha}(t)} \bar{V}_v(t) \right| \psi_\alpha \right\rangle \tag{5.23}$$

where

$$\begin{aligned} \bar{V}_v(t) &= V_{X,\lambda}(t) + \lambda_1(1 - x_1 + \lambda_1)\mathbf{A}^2(t) \\ &= v_1\mathbf{A}(t)\cdot\mathbf{p}_{\mathrm{c}} + (1-v_1)\mathbf{F}(t)\cdot\mathbf{r} + (v_1^2 + v_2)\mathbf{A}^2(t)/2 \end{aligned} \tag{5.24}$$

and

$$\begin{aligned} \Omega_{v\mathbf{p}\alpha}(t) &= \Theta_X(t) + \gamma_\lambda(\mathbf{r},t) - E_\alpha t \\ &= (E_p - E_\alpha)t + \mathbf{p}\cdot\boldsymbol{\alpha}(t) + (v_1 - 1)\mathbf{A}(t)\cdot\mathbf{r} + (v_2+1)\beta(t) \end{aligned} \tag{5.25}$$

Finally, the matrix element

$$\left\langle \Psi^{\mathrm{Vv}}_{X,\mathbf{p}'}(t) \left| U \right| \Psi^{\mathrm{Vv}}_{X,\mathbf{p}}(t) \right\rangle = e^{\mathrm{i}(E_{p'}-E_p)t + \mathrm{i}(\mathbf{p}'-\mathbf{p})\cdot\boldsymbol{\alpha}(t)} \left\langle \mathbf{p}' \left| U \right| \mathbf{p} \right\rangle \tag{5.26}$$

is independent both on gauge and partitioning.

As a consequence of these properties of the matrix elements the transition amplitude depends only on v, as is shown below.

5.1.3. S-matrix series

The operator $\hat{\mathrm{G}}_X(t,t')$ can be expanded either in terms of the operator $\hat{\mathrm{G}}^0_\lambda(t,t')$,

$$\hat{\mathrm{G}}_X(t,t') = \hat{\mathrm{G}}^0_\lambda(t,t') + \int \mathrm{d}t_1 \hat{\mathrm{G}}_X(t,t_1) V_{X,\lambda}(t_1) \hat{\mathrm{G}}^0_\lambda(t_1,t'), \tag{5.27}$$

or in terms of the operator $\hat{\mathrm{G}}^{\mathrm{f}}_X(t,t')$,

$$\hat{\mathrm{G}}_X(t,t') = \hat{\mathrm{G}}^{\mathrm{f}}_X(t,t') + \int \mathrm{d}t_1 \hat{\mathrm{G}}^{\mathrm{f}}_X(t,t_1) U \hat{\mathrm{G}}_X(t_1,t'). \tag{5.28}$$

Substitution of Eq. (5.28) in (5.27) yields

$$\begin{aligned}\hat{\mathrm{G}}_X(t,t') = \hat{\mathrm{G}}^0_\lambda(t,t') + \int \mathrm{d}t_1 \hat{\mathrm{G}}^{\mathrm{f}}_X(t,t_1) V_{X,\lambda}(t_1) \hat{\mathrm{G}}^0_\lambda(t_1,t') \\ + \iint \mathrm{d}t_2\, \mathrm{d}t_1 \hat{\mathrm{G}}^{\mathrm{f}}_X(t,t_2) U \hat{\mathrm{G}}_X(t_2,t_1) V_{X,\lambda}(t_1) \hat{\mathrm{G}}^0_\lambda(t_1,t').\end{aligned} \tag{5.29}$$

A further substitution of either (5.27) or (5.28) in Eq. (5.29) results in a series expansion of $\hat{\mathrm{G}}_X(t,t')$. Inserting this expansion in Eq. (5.6) generates the S-matrix series for the transition amplitude between the initial state and the final state to any desired order,

$$S_{\mathbf{p}\alpha} = \sum_{n=0}^{\infty} S^{(n)}_{\mathbf{p}\alpha}, \tag{5.30}$$

with

$$S^{(0)}_{\mathbf{p}\alpha} = \mathrm{i} \left\langle \Psi^{\mathrm{Vv}}_{X,\mathbf{p}}(t_f) \left| \hat{\mathrm{G}}^0_\lambda(t_f,t_i) \right| \psi_\alpha(t_i) \right\rangle, \tag{5.31}$$

$$S^{(1)}_{\mathbf{p}\alpha} = \mathrm{i} \int \mathrm{d}t_1 \left\langle \Psi^{\mathrm{Vv}}_{X,\mathbf{p}}(t_f) \left| \hat{\mathrm{G}}^{\mathrm{f}}_X(t_f,t_1) V_{X,\lambda}(t_1) \hat{\mathrm{G}}^0_\lambda(t_1,t_i) \right| \psi_\alpha(t_i) \right\rangle. \tag{5.32}$$

Depending on whether (5.27) or (5.28) is substituted in (5.29) one obtains either

$$S^{(2)}_{\mathbf{p}\alpha} = \mathrm{i} \iint \mathrm{d}t_1\, \mathrm{d}t_2 \left\langle \Psi^{\mathrm{Vv}}_{X,\mathbf{p}}(t_f) \left| \hat{\mathrm{G}}^{\mathrm{f}}_X(t_f,t_2) U \hat{\mathrm{G}}^0_\lambda(t_2,t_1) V_{X,\lambda}(t_1) \hat{\mathrm{G}}^0_\lambda(t_1,t_i) \right| \psi_\alpha(t_i) \right\rangle \tag{5.33}$$

or

$$S^{(2)}_{\mathbf{p}\alpha} = \mathrm{i} \iint \mathrm{d}t_1\, \mathrm{d}t_2 \left\langle \Psi^{\mathrm{Vv}}_{X,\mathbf{p}}(t_f) \left| \hat{\mathrm{G}}^{\mathrm{f}}_X(t_f,t_2) U \hat{\mathrm{G}}^{\mathrm{f}}_X(t_2,t_1) V_{X,\lambda}(t_1) \hat{\mathrm{G}}^0_\lambda(t_1,t_i) \right| \psi_\alpha(t_i) \right\rangle \tag{5.34}$$

and so on, where the integration is performed in the interval t_i to t_f.

From Eqs. (5.19) and (5.20) follows

$$S^{(0)}_{\mathbf{p}\alpha} = \langle \Psi^{\mathrm{Vv}}_{X,\mathbf{p}}(t_f) | \Psi_{\lambda,\alpha}(t_f) \rangle = e^{\mathrm{i}\Omega_{v\mathbf{p}\alpha}(t_f)} \tilde{\psi}_\alpha(\mathbf{p}) \tag{5.35}$$

where $\tilde{\psi}_\alpha(\mathbf{p}) = \langle \mathbf{p} | \psi_\alpha \rangle$ is the Fourier transform of ψ_α.

From Eqs. (5.19) and (5.10) follows on the other hand

$$S^{(1)}_{\mathbf{p}\alpha} = \mathrm{i} \int_{t_i}^{t_f} \mathrm{d}t \left\langle \Psi^{\mathrm{Vv}}_{X,\mathbf{p}}(t) \left| V_{X,\lambda}(t) \right| \Psi_{\lambda,\alpha}(t) \right\rangle \tag{5.36}$$

which — using the identity (5.23) — can be reduced to

$$S^{(1)}_{\mathbf{p}\alpha} = \mathrm{i}\int_{t_i}^{t_f} \mathrm{d}t \left\langle \mathbf{p} \left| e^{\mathrm{i}\Omega_{v\mathbf{p}\alpha}(t)} \bar{V}_v(t) \right| \psi_\alpha \right\rangle . \tag{5.37}$$

In an analogous way, Eq. (5.33) can be transformed using (5.13) as

$$\begin{aligned}
S^{(2)}_{\mathbf{p}\alpha} &= \mathrm{i}\int_{t_i}^{t_f} \mathrm{d}t_2 \int_{t_i}^{t_f} \mathrm{d}t_1 \left\langle \Psi^{\mathrm{Vv}}_{X,\mathbf{p}}(t_2) \left| U \hat{\mathrm{G}}^0_\lambda(t_2,t_1) V_{X,\lambda}(t_1) \right| \psi_{\lambda,\alpha}(t_1) \right\rangle \\
&= \int_{t_i}^{t_f} \mathrm{d}t_2 \sum_{\alpha'} \left\langle \Psi^{\mathrm{Vv}}_{X,\mathbf{p}}(t_2) \left| U \right| \Psi_{\lambda,\alpha'}(t_2) \right\rangle \int_{t_i}^{t_2} \mathrm{d}t_1 \left\langle \Psi_{\lambda,\alpha'}(t_1) \left| V_{X,\lambda}(t_1) \right| \Psi_{\lambda,\alpha}(t_1) \right\rangle \\
&= \int_{t_i}^{t_f} \mathrm{d}t_2 \sum_{\alpha'} \left\langle \mathbf{p} \left| e^{\mathrm{i}\Omega_{v\mathbf{p}\alpha'}(t_2)} U \right| \psi_{\alpha'} \right\rangle \int_{t_i}^{t_2} \mathrm{d}t_1 e^{\mathrm{i}(E_{\alpha'}-E_\alpha)t_1} \left\langle \psi_{\alpha'} \left| \bar{V}_v(t_1) \right| \psi_\alpha \right\rangle
\end{aligned} \tag{5.38}$$

or Eq. (5.34) can be transformed using (5.9) as

$$\begin{aligned}
S^{(2)}_{\mathbf{p}\alpha} &= \mathrm{i}\int_{t_i}^{t_f} \mathrm{d}t_2 \int_{t_i}^{t_f} \mathrm{d}t_1 \left\langle \Psi^{\mathrm{Vv}}_{X,\mathbf{k}}(t_2) \left| U \hat{\mathrm{G}}^{\mathrm{f}}_X(t_2,t_1) V_{X,\lambda}(t_1) \right| \psi_{\lambda,\alpha}(t_1) \right\rangle \\
&= \int_{t_i}^{t_f} \mathrm{d}t_2 \sum_{\mathbf{k}'} \left\langle \Psi^{\mathrm{Vv}}_{X,\mathbf{p}}(t_2) \left| U \right| \Psi_{X,\mathbf{p}'}(t_2) \right\rangle \int_{t_i}^{t_2} \mathrm{d}t_1 \left\langle \Psi^{\mathrm{Vv}}_{X,\mathbf{p}'}(t_1) \left| V_{X,\lambda}(t_1) \right| \Psi_{\lambda,\alpha}(t_1) \right\rangle \\
&= \int_{t_i}^{t_f} \mathrm{d}t_2 \sum_{\mathbf{p}'} e^{\mathrm{i}(E_p - E_{p'})t_2 + \mathrm{i}(\mathbf{p}-\mathbf{p}')\cdot\boldsymbol{\alpha}(t_2)} \left\langle \mathbf{p} \left| U \right| \mathbf{p}' \right\rangle \int_{t_i}^{t_2} \mathrm{d}t_1 \left\langle \mathbf{p}' \left| e^{\mathrm{i}\Omega_{v\mathbf{p}'\alpha}(t_1)} \bar{V}_v(t_1) \right| \psi_\alpha \right\rangle .
\end{aligned} \tag{5.39}$$

Continuing in an analogous manner, it can be shown that $S^{(n)}_{\mathbf{p}\alpha}$ for any order n depends only on v. Therefore, $S_{\mathbf{p}\alpha}$ itself depends only on v. In the next subsection some particular examples will be considered explicitly.

5.1.4. Particular examples

As a first example, consider the case $v = \{0,0\}$ where one has

$$\bar{V}_v(t) = \mathbf{F}(t)\cdot\mathbf{r} \tag{5.40}$$

$$\Omega_{v\mathbf{p}\alpha}(t) = (E_p - E_\alpha)t + \mathbf{p}\cdot\boldsymbol{\alpha}(t) - \mathbf{A}(t)\cdot\mathbf{r} + \beta(t). \tag{5.41}$$

This formulation is achieved using the following partitionings for different gauges:

$$\lambda = \{-1,0\} \text{ in R gauge}, \quad \lambda = \{-1,1\} \text{ in V gauge}, \quad \lambda = \{0,0\} \text{ in L gauge}. \tag{5.42}$$

Since in L-gauge the relation $\hat{\mathrm{H}}^0_\lambda = \hat{\mathrm{H}}^0$ holds, the gauge-invariant formulation with $v = \{0, 0\}$ reproduces the traditional SFA in the L gauge.

However, in an analogous way, the traditional V-gauge SFA is obtained with $v = \{1, -1\}$ (cf. [151]), where

$$\bar{V}_v(t) = \mathbf{A}(t) \cdot \mathbf{p}_\mathrm{c} \tag{5.43}$$

$$\Omega_{v\mathbf{p}\alpha}(t) = (E_p - E_\alpha)t + \mathbf{p} \cdot \boldsymbol{\alpha}(t)\ . \tag{5.44}$$

It can be achieved using the following partitionings for different gauges:

$$\lambda = \{0, -1\} \text{ in R gauge}, \quad \lambda = \{0, 0\} \text{ in V gauge}, \quad \lambda = \{1, -1\} \text{ in L gauge}. \tag{5.45}$$

In a similar way, the traditional R-gauge SFA is obtained with $v = \{1, 0\}$, where

$$\bar{V}_v(t) = \mathbf{A}(t) \cdot \mathbf{p}_\mathrm{c} + \mathbf{A}^2(t)/2 \tag{5.46}$$

$$\Omega_{v\mathbf{p}\alpha}(t) = (E_p - E_\alpha)t + \mathbf{p} \cdot \boldsymbol{\alpha}(t) + \beta(t). \tag{5.47}$$

It can be achieved using the following partitionings for different gauges:

$$\lambda = \{0, 0\} \text{ in R gauge}, \quad \lambda = \{0, 1\} \text{ in V gauge}, \quad \lambda = \{1, 0\} \text{ in L gauge}. \tag{5.48}$$

Clearly, every S-matrix expansion (SFA formulation) in one of the “conventional” (length, velocity, or radiation) gauges can be obtained by adopting any of the possible gauges, if the partitioning of the Hamiltonian is chosen accordingly.

Furthermore, the present result demonstrates that there remains an in principle infinite set of S-matrix expansions (characterized by different values of v_1, v_2) that are only shown to provide the same transition probabilities in the limit of an infinite series expansion, if the latter converges. Truncated series like, e. g., the 0th, 1st, or 2nd order expansions will, however, in general disagree. Thus the question of a “proper” choice of the expansion in the case of truncation remains and can only be clarified by a comparison to either experiment or gauge-independent theory (like full solutions of the time-dependent Schrödinger equation).

In author’s opinion, there is no *a priori* reason to believe that one expansion is necessarily advantageous to the others for all atomic or molecular systems as well as all possible laser parameters. Similar to various physical applications, where the choice of a suitable expansion is optimized in order to achieve faster convergence, there may exist an optimal parameter set v for a given problem. This set may, however, not necessarily agree to one of the traditional SFA expansions. A deeper understanding requires certainly further studies.

5.2. The length gauge SFA

Among the numerous approximations developed to treat the ionization process the Keldysh theory [114] possesses a prominent role. This theory was proposed by Keldysh more than 40 years ago and describes the ionization process as a transition between an initial electronic bound and a Volkov continuum state adopting the length-gauge formulation. Within this theory, the total ionization rate of a one-electron atomic system with the electron binding energy E_b in the harmonic laser field $\mathbf{F}(t) = \mathbf{F}\cos\omega t$, with the period $T = 2\pi/\omega$, can be expressed as the sum over N-photon processes

$$W = 2\pi \int \frac{d^3p}{(2\pi)^3} |A(\mathbf{p})|^2 \sum_{N=N_\mathrm{min}}^{\infty} \delta(E_\mathrm{b} + \frac{p^2}{2} + U_p - N\omega) \tag{5.49}$$

where $U_p = F^2/(4\omega^2)$ is the electron quiver (ponderomotive) energy due to the field. The transition amplitude $A(\mathbf{p})$ can be calculated using

$$A(\mathbf{p}) = \frac{1}{T}\int_0^T dt \int d^3r\, \Psi^*_\mathbf{p}(\mathbf{r},t)\big[\mathbf{r}\cdot\mathbf{F}(t)\big]\Psi_0(\mathbf{r},t) \tag{5.50}$$

where $\Psi_0(\mathbf{r},t) = e^{\mathrm{i}E_\mathrm{b}t}\Phi_0(\mathbf{r})$ is the wave function describing the initial electronic state in the atomic potential $U(\mathbf{r})$ and $\Psi_\mathbf{p}(\mathbf{r},t)$ is the Volkov wave function

$$\Psi_\mathbf{p}(\mathbf{r},t) = \exp\left[\mathrm{i}\mathbf{r}\cdot\boldsymbol{\pi}(t) - \frac{\mathrm{i}}{2}\int_0^t \boldsymbol{\pi}^2(t')dt'\right], \qquad \boldsymbol{\pi}(t) = \mathbf{p} - (\mathbf{F}/\omega)\sin\omega t \tag{5.51}$$

Introducing the auxiliary function

$$V_0(\mathbf{q}) = \int d^3r\, e^{-\mathrm{i}\mathbf{q}\cdot\mathbf{r}}(\mathbf{F}\cdot\mathbf{r})\Phi_0(\mathbf{r}) = \mathrm{i}\mathbf{F}\cdot\nabla_\mathbf{q}\tilde{\Phi}_0(\mathbf{q}) \tag{5.52}$$

(where $\tilde{\Phi}_0(\mathbf{q})$ is the Fourier transform of $\Phi_0(\mathbf{r})$) and using quasi-classical action

$$S_{\mathbf{p}}(t) = \int_0^t dt' \left[E_{\mathrm{b}} + \frac{1}{2}\boldsymbol{\pi}^2(t')\right] \tag{5.53}$$

the transition amplitude $A(\mathbf{p})$ can be rewritten as

$$A(\mathbf{p}) = \frac{1}{T}\int_0^T dt\, \cos(\omega t)\, V_0\left(\boldsymbol{\pi}(t)\right)\, e^{\mathrm{i}S(t)} \quad . \tag{5.54}$$

The function $S_{\mathbf{p}}(t)$ is a rapidly varying function of time t. Introduction of the new complex variable $u = \sin\omega t$ allows to transform the integration $\int_0^T dt$ in Eq. 5.54 to one on the closed contour C_{in} which encloses the interval $(-1, 1)$ in the complex plane u (see Sec. A.1 for more detail discussion), so that Eq. 5.54 can be rewritten as

$$A(\mathbf{p}) = \oint_{C_{\mathrm{in}}} du\, \tilde{V}_0\,(u)\, e^{\mathrm{i}S_{\mathbf{p}}(u)}, \qquad \tilde{V}_0(u) = \frac{1}{2\pi} V_0\left(\mathbf{p} - \frac{\mathbf{F}}{\omega}u\right) \tag{5.55}$$

Besides the main approximation of the Keldysh theory, the neglect of the interaction of the escaping electron with the long-range Coulomb potential (in the case of a neutral atom), two additional simplifications were made in [114]: (i) the method of steepest descent (MSD) [152] (also known as saddle-point approximation) for performing the contour integral in Eq. (5.55), and (ii) the assumption of a small kinetic momentum of the escaping electron. The simplification (ii) is justified only for obtaining the total ionization rate in the case of multiphoton ionization processes and should be avoided in the field ionization regime, where the contribution of the fast photoelectrons is non-negligible. This simplification (ii) has been done in [114] for obtaining a simple analytical expression for the total ionization rate and can easily be omitted in numerical calculations. In contrast, the simplification (i) is substantial since it provides a simple analytical expression for the integral whose numerical calculation is very expensive and may in practice face problems due to an accumulation of rounding errors. Within the simplification (i) the closed contour C_{in} is deformed to a path in the vicinity of the two special points $u_{\pm}$, which are for a hydrogen-like atom simultaneously the saddle points of the function $S_{\mathbf{p}}(u)$ (see Sec. A.2) and the poles of the function $\tilde{V}_0(u)$ (see Sec. C.1). As shown in Fig. 5.1, deforming the contour C_{in} to pass along the contour C_{-}^{+} in positive direction, along C_{+}^{-} in negative direction (see Sec. A.3 for the definition of C_{-}^{+} and C_{+}^{-}),

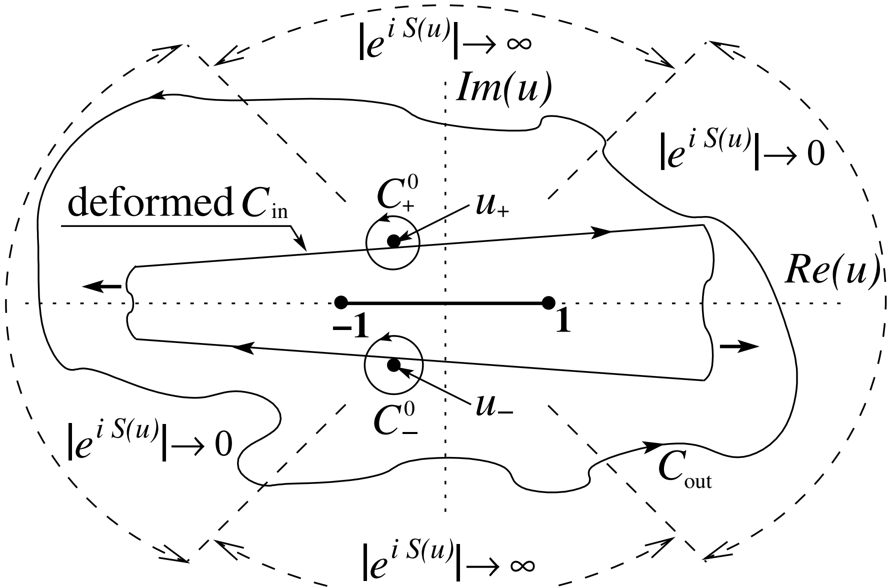

Figure 5.1.: The closed contour C_{in} can be deformed to path in the vicinity of the two special points $u_\pm$. The asymptotic behavior of $\exp[\mathrm{i}S(u)]$, contours $C_\pm^0$ around the points $u_\pm$, the closed contour C_{out}, and deformed C_{in} used within MSD. (Published in [41].)

and connecting the ends of these contours at infinity one obtains

$$A(\mathbf{p}) = I_+^- - I_-^+ \tag{5.56}$$

where I_-^+ (I_+^-) is the integral along the paths C_-^+ (C_+^-). Here is assumed that the contribution from the contours at infinity is equal to zero. This assumption is valid, since the function $\tilde{V}_0(u)$ vanishes at infinity [see Eq. (C.7)] and the function $e^{\mathrm{i}S(u)}$ exponentially vanishes at infinity for $|\mathrm{Re}\,u| > |\mathrm{Im}\,u|$ [see Eq. (A.29) and the previous discussion]. According to Eq. (A.30) the same inequality is valid for the ends of C_+^- and C_-^+, and thus for the contours connecting these ends (see Fig. 5.1). Therefore, the integrand in Eq. (5.55) is equal to zero for the contours at infinity. Within the MSD the integrals I_-^+, I_+^- are further approximated as described in Sec. B.1 yielding the approximate transition amplitude

$$A_{\text{MSD}} = I_{+,\text{MSD}}^- - I_{-,\text{MSD}}^+ \ . \tag{5.57}$$

Recently, a new method referred by the authors as *generalized Keldysh theory* (GKT) [138] has been proposed to avoid approximation (i) by solving the occurring contour integrals with the aid of the exact residue theorem (RT) instead of the MSD. Within the following five years the method has been extensively applied for the theoretical study of different atoms and molecules [153–163]. It was shown that the RT method yields a two times larger transition amplitude for the 1s state of a hydrogen-like atom and, as a consequence, a four times larger ionization rate. Furthermore, the ionization rate of the first excited (2s) state obtained in [155] when applying the GKT differs significantly from the MSD result. In view of the popularity of the MSD approximation for treating strong-field problems like ionization [6] or high-harmonic generation [164] this is of course a very important result. That sheds a lot of doubts on the popular SFA in the length gauge itself, as it is usually implemented using the MSD method.

Surprisingly, numerical tests performed by the author of the present thesis for the H atom has shown that the method employing the MSD yields results by about a factor of two smaller than the one obtained by numerical integration, whereas the supposedly exact method yields results by about a factor of two larger than the numerically obtained ones. This finding has stimulated a careful analysis of the derivation given in [138], which revealed an unjustified neglect of an important contribution occurring in the application of the GKT.

Within the GKT, the integral along the closed contour C_{in} is presented using Cauchy integration rules [152] as

$$\oint\limits_{C_{\text{in}}} = \oint\limits_{C_+^0} + \oint\limits_{C_-^0} - \oint\limits_{C_{\text{out}}} \tag{5.58}$$

where $C_\pm^0$ are contours around $u_\pm$ and C_{out} is a contour enclosing $(-1,1)$ and $u_\pm$ (see Fig. 5.1). The integrals $A_\pm$ along $C_\pm$ can be calculated using RT which yields

$$A_\pm = \frac{2\pi \mathrm{i}}{\nu!} \lim_{u\to u_\pm} \frac{d^\nu}{du^\nu} \left[\tilde{V}_0(u)(u-u_\pm)^\nu e^{\mathrm{i}S(u)} \right] \quad . \tag{5.59}$$

where ν is the order of poles of the function $\tilde{V}_0(u)$ at $u = u_\pm$. For hydrogen-like atoms $\nu = n + 3$, where n is the principle quantum number.

With the knowledge of the integral along C_{out},

$$I_{\text{out}} = \oint_{C_{\text{out}}} \mathrm{d}u\, \tilde{V}_0(u)\, e^{\mathrm{i}S(u)}, \tag{5.60}$$

the value of $A(\mathbf{p})$ can be calculated using (5.58) as

$$A(\mathbf{p}) = (A_+ + A_-) - I_{\text{out}}. \tag{5.61}$$

In [138] the value of I_{out} is implicitly assumed to be zero and a simple formula is proposed to calculate the transition amplitude within the GKT,

$$A_{\text{GKT}} = A_+ + A_- \ . \tag{5.62}$$

However, a simple analysis shows that there are no reasons for such an assumption. Indeed, according to Eq. (A.29) the function $e^{\mathrm{i}S(u)}$ grows exponentially at infinity for $|\mathrm{Re}\, u| < |\mathrm{Im}\, u|$, and thus it is impossible to select C_{out} in such a way that the integrand on the whole contour approaches zero. Moreover, numerical calculations have shown that I_{out} is often of the same order of magnitude as $A(\mathbf{p})$ or can even be larger. Thus, both the MSD and the GKT (as defined in [138]) yield only approximate Keldysh transition amplitudes.

It is instructive to obtain I_{out} within the MSD. Deforming the contour C_{in} to pass along the contour C_+^+ in negative direction, along C_-^- in positive direction (see Sec. A.3 for the definition of C_+^+ and C_-^-), and connecting the ends of these contours at infinity one obtains

$$I_{\text{out}} = I_-^- - I_+^+ \tag{5.63}$$

where I_+^+ (I_-^-) is the integral along the paths C_+^+ (C_-^-) and the contribution from the contours connecting the ends of C_+^+ and C_-^- at infinity is zero according to the discussion following Eq. (5.56). Applying the MSD to Eqs. (5.56), (5.63) and using the relation between $I_\pm^-$ and $I_\pm^+$ given in Eq. (B.7) one obtains

$$I_{\text{out}} = (-1)^{\nu-1} A(\mathbf{p}), \qquad\qquad [\text{within the MSD}]. \tag{5.64}$$

Substituting this simple relation to Eq. (5.61) the following relation between $A(\mathbf{p})$ and A_{GKT} can be obtained within the MSD

$$A(\mathbf{p}) \approx A_{\text{GKT}}/2 \qquad\qquad [\text{MSD, odd } \nu]. \tag{5.65}$$

$$A(\mathbf{p}) \gg A_{\text{GKT}}/2 \qquad\qquad [\text{MSD, even } \nu]. \tag{5.66}$$

Thus, for odd ν (and therefore for odd principle number n) the value of $A(\mathbf{p})$ is two times smaller than the one obtained with the assumption $I_{\text{out}} = 0$, whereas for even ν $A(\mathbf{p})$ should be much larger than the value A_{GKT} proposed in [138]. The fact that for the 1s state of hydrogen-like atoms one finds exactly a factor 2 difference between MSD and GKT should be seen as an accidental case that is due to the relative simplicity of $\tilde{V}_0(u)$ for the 1s state.

Table 5.1.: The exact value of the N-photon ionization probability $|A(\mathbf{p})|^2$ (the direction of $\mathbf{p}$ is fixed by the relation $\hat{\mathbf{F}} \cdot \hat{\mathbf{p}} = 0.8$) in the laser pulse with different intensities I and wavelengths λ calculated for the 1S state of the H atom ($n = 1$) and the 2S state of the He$^+$ atom ($n = 2$). The minimal number of photons $N_{\min}$ is given for each pulse. The ratios $R_{\mathrm{GKT}} = |A_{\mathrm{GKT}}/A(\mathbf{p})|^2$, $R_{\mathrm{MSD}} = |A_{\mathrm{MSD}}/A(\mathbf{p})|^2$, and $R_{\mathrm{cMSD}} = |A_{\mathrm{cMSD}}/A(\mathbf{p})|^2$ are presented in order to compare the exact value $|A(\mathbf{p})|^2$ with the predictions of the generalized Keldysh theory, the simple MSD formula, and the corrected MSD (cMSD) formula.

		$n=1$				$n=2$			
I, λ, $N_{\min}$	N	$\|A(\mathbf{p})\|^2$	R_{GKT}	R_{MSD}	R_{cMSD}	$\|A(\mathbf{p})\|^2$	R_{GKT}	R_{MSD}	R_{cMSD}
10^{13}W/cm^2, 248 nm, 3	3	4.273(-6)	2.020	0.505	1.010	7.119(-5)	0.351	0.379	0.946
	4	7.809(-9)	2.107	0.527	0.996	3.396(-8)	0.066	0.689	1.047
10^{14}W/cm^2, 248 nm, 3	3	3.438(-3)	2.024	0.506	1.008	6.219(-2)	0.362	0.374	0.947
	4	8.440(-5)	2.093	0.523	1.000	5.269(-4)	0.135	0.577	1.004
10^{15}W/cm^2, 248 nm, 4	4	9.746(-3)	1.948	0.487	0.978	6.442(-2)	0.260	0.392	0.943
	5	7.625(-2)	2.169	0.542	0.992	7.226(-1)	0.168	0.557	0.996
	6	2.145(-2)	2.172	0.543	0.998	1.380(-1)	0.103	0.639	0.981
	7	4.560(-3)	2.196	0.549	1.002	1.975(-2)	0.036	0.780	0.977
10^{14}W/cm^2, 800 nm, 13	13	4.641(-5)	2.712	0.678	0.997	1.578(-3)	0.088	0.687	1.010
	15	8.564(-6)	2.722	0.681	0.998	2.617(-4)	0.075	0.710	1.004
	20	9.36(-10)	3.227	0.807	0.998	9.586(-8)	0.078	0.732	0.999

After the lack of justification for assumption $I_{\mathrm{out}} = 0$ was pointed out to the authors of the generalized Keldysh theory, in their new publication [163] the method was corrected by including I_{out} which is calculated by means of the residue at $u = \infty$. Comparing photoionization rates for the 1s hydrogen atom exposed to a 248 nm laser field calculated with and without the assumption $I_{\mathrm{out}} = 0$, the authors concluded that the contribution from I_{out} is almost negligibly small.

Two comments can be made to the aforesaid. The calculation of $I_{\mathrm{out}} = 2\pi \mathrm{i} \operatorname*{Res}_{u=\infty}[\tilde{V}_0(u) e^{\mathrm{i}S(u)}]$ can indeed be performed according to Eq. (A.33) using an expansion of $\tilde{V}_0(u)$ in powers of u^{-1} [see Eq. (C.18) for $n = 1$ and the derivation above for higher n]. However, for large N the convergence of the sum in Eq. (A.33) is very slow and the rounding errors rapidly accumulate due to the oscillatory character of the sum. In fact, the numerical calculation of the residue at infinity may be much more involved than the numerical integration of the integrals I_+^- and I_-^+ which are required to obtain $A(\mathbf{p})$. Therefore, a practical benefit of using residues for the calculation of $A(\mathbf{p})$ is questionable. Second, the author has applied this approach in order to calculate I_{out} for 248 nm laser field and obtained results which are agreeing with those obtained when employing a numerical integration and Eq. (5.63). Nevertheless, the results do not support the statement about negligibility of I_{out}. As is demonstrated in Table 5.1, the assumption $I_{\mathrm{out}} = 0$ results in a transition probability that is for a wide range of intensities by about a factor of 2 larger. This remains valid for different angles between **F** and **p**, so that the photoionization rates for the 1s hydrogen atom obtained with and without the assumption $I_{\text{out}} = 0$ differ also by about a factor of 2.

Table 5.1 demonstrates also the validity of the prediction of the MSD about the smallness of $|A_{\text{GKT}}|$ compared to $|A(\mathbf{p})|$ for $n = 2$. Moreover, results for R_{GKT} show that for a 248 nm laser field the ratio tends to become smaller with an increase of the photon number N.

According to Table 5.1, the accuracy of the simple MSD formula is often of the same level as the accuracy of GKT. However, the accuracy of the MSD can be essentially improved using the corrected MSD formula

$$A_{\text{cMSD}} = I^{-}_{+,\text{cMSD}} - I^{+}_{-,\text{cMSD}} \tag{5.67}$$

where $I^{-}_{+,\text{cMSD}}$ and $I^{+}_{-,\text{cMSD}}$ are the approximations of the integrals I^{-}_{+} and I^{+}_{-} obtained using Eq. (B.10). As can be seen from Table 5.1, the corrected MSD formula yields a significant improvement both for $n = 1$ and $n = 2$. Superiority of the corrected MSD formula is especially prominent for large principle quantum numbers n, as was demonstrated in [41].

5.3. The velocity-gauge SFA in the quasistatic limit

A possible test of SFA theories is a comparison of their predictions in the tunneling limit with the corresponding one of quasistatic theories [95, 96]. Whereas the tunneling limit of the length-gauge SFA (SFA-LG) was considered already by Keldysh for the explicit example of a hydrogen atom, asymptotic expressions for the velocity-gauge SFA (SFA-VG) in the limit of vanishing laser frequency ($\omega \to 0$) have not been derived explicitly in the past. In his detailed work [117] about SFA-VG theory Reiss has used the MSD method to obtain an approximation for the generalized Bessel functions ('asymptotic approximation') that are required for the calculation of the transition amplitude. The algebraically cumbersome form of the in [117] derived 'asymptotic approximation' has motivated the development of a simpler form appropriate for the tunneling regime. This approximation [165] is again based on the MSD method and is referred to as 'tunneling 1 approximation'. It was, however, shown [166, 167] that the 'tunneling 1 approximation' is much worse than the 'asymptotic approximation' in the case of large kinetic momenta.

Since neither [117] nor [165] contain explicit asymptotic expressions in the limit of vanishing laser frequency ($\omega \to 0$), a systematic study of the quasistatic limit on their basis is almost impossible.

For a long time, it was believed that the SFA-VG behaves similar to SFA-LG in the limit $\omega \to 0$. For example, in the discussion given in [147], it was explicitly stressed that SFA-VG (corresponding to the first-order S-matrix theory in velocity gauge) approaches the correct tunneling limit for $\omega \to 0$ (and sufficiently weak fields). However, in [147] (and corresponding references therein) this conclusion is reached on the basis of a derivation valid for short-range potentials and is then adopted to the case of the long-range Coulomb potential. Since SFA neglects the long-range Coulomb interaction between the ionized electron and the remaining ion, the correct tunneling limit is obtained by rescaling the SFA-VG rate with a frequency-independent Coulomb correction factor. Such a factor was proposed by Becker and Faisal (see [147] and references therein) and is extensively used in their atomic and molecular SFA calculations[147, 168].

In order to verify this statement, SFA rates for the H atom exposed to low-frequency fields have been numerically calculated by the author of this thesis. Surprisingly, the results of the calculations have indicated that the SFA-VG rates continue to substantially decrease with decreasing ω, whereas for these frequencies the quasistatic limit for the SFA-LG rates is already reached. This finding has motivated a derivation of the analytical asymptotic expression for the quasistatic limit of the SFA-VG rates (denoted QSFA-VG rates). Besides its simple analytical form, the obtained expression has shown that in the presence of long-range Coulomb interactions and thus for the ionization of neutral or positively charged atoms or molecules the SFA-VG rate is proportional to the laser frequency in this limit. This section discusses the derivation of the expression for the QSFA-VG rates and its application to hydrogen-like atoms. Besides, it introduces a frequency-dependent Coulomb correction factor which can be used for correcting the SFA-VG rates in the low-frequency limit.

5.3.1. Derivation

The velocity-gauge SFA in its most popular form was proposed by Reiss [117]. After some algebra, the total ionization rate is given in the SFA-VG by

$$W = (2\pi)^{-2} \sum_{N \geqslant N_0} p_N \int d\hat{\mathbf{p}} \, |A(p_N \hat{\mathbf{p}})|^2 \tag{5.68}$$

where the transition amplitude $A(\mathbf{p})$ is

$$A(\mathbf{p}) = -\left(\frac{\mathbf{p}^2}{2} + E_\mathrm{b}\right) \tilde{\Psi}_0(\mathbf{p}) L(\mathbf{p}), \tag{5.69}$$

and E_b is the binding energy of the initial bound state Ψ_0 with its Fourier transform $\tilde{\Psi}_0$. The number of absorbed photons N satisfies $N \geqslant N_0 = (E_\mathrm{b}+U_p)/\omega$. Furthermore, $p_N = \sqrt{2(N\omega - E_\mathrm{b} - U_p)}$ is the momentum of ejected electron for an N photon transition. The function $L(\mathbf{p})$ is defined as

$$L(\mathbf{p}) = \frac{1}{T} \int\limits_0^T e^{\mathrm{i}S_\mathbf{p}(t)} dt \tag{5.70}$$

where $S_\mathbf{p}(t)$ is given by Eq. (5.53).

An analytic expression for the SFA-VG rate in the quasistatic limit is derived by the author as follows. First, the exact limit of $|L|^2$ for $\gamma \to 0$ is found (see Sec. A.5). Further, some asymptotically exact approximations are employed. Defining the azimuthal angle ϕ around the axis parallel to $\mathbf{F}$ and using

$$\int d\hat{\mathbf{p}} = \int\limits_{-1}^{1} d\zeta \int\limits_0^{2\pi} d\phi \tag{5.71}$$

where $\zeta = -\hat{\mathbf{p}} \cdot \hat{\mathbf{F}}$, Eq. (5.68) is rewritten as

$$W_\text{SFA-VG} = \frac{\kappa^5}{16\pi^2} \int\limits_{-1}^{1} d\zeta \sum_{N \geqslant N_0} q_N \left(1 + q_N^2\right)^2 |L|^2 \, \tilde{\Phi} \tag{5.72}$$

where $\kappa = \sqrt{2E_\mathrm{b}}$, $q_N = p_N/\kappa$, and

$$\tilde{\Phi} = \int\limits_0^{2\pi} d\phi |\tilde{\Psi}_0|^2. \tag{5.73}$$

Note, the argument of the cosine in Eq. (A.46) is proportional to γ^{-3} and leads to fast oscillations, if N and ζ are varied. Thus the contribution of this term to the final result is negligibly small and it is possible to substitute $|L|^2$ in Eq. (5.72) with $2\mathcal{L}^2$,

$$W^{\text{ap1}}_{\text{SFA-VG}} = \frac{\kappa^5}{8\pi^2} \int\limits_{-1}^{1} d\zeta \sum_{N \geqslant N_0} q_N \left(1 + q_N^2\right)^2 \mathcal{L}^2 \tilde{\Phi} \,. \tag{5.74}$$

The next step is to substitute the summation over N by an integral. A standard approach consists of a transformation of the sum into an integral over q_N. This allows to calculate differential rates, but due to the coupling of q_N and ζ it is impossible to obtain a simple analytical expression without the use of an expansion (e. g. the small kinetic momentum one, $q_N \ll 1$). Indeed, according to Eqs. (A.53) the function $\mathcal{L}$ depends on q_N and ζ through the variable $\rho = \sqrt{1 + q_N^2(1 - \zeta^2)}$, and thus q_N and ζ cannot be decoupled. Instead of the use of a double integral with respect to q_N and ζ, Eq. (5.74) is rewritten as a double integral with respect to ρ and the variable $\chi = q_N\zeta/\rho$. Transforming the sum into an integral over ρ with

$$\sum_{N \geqslant N_0} \to \int\limits_{1}^{\infty} d\rho \frac{\rho\tau}{\gamma(1 - \zeta^2)} \tag{5.75}$$

and using

$$1 + q_N^2 = \rho^2(1 + \chi^2), \quad \int\limits_{-1}^{1} d\zeta \, \frac{q_N}{(1 - \zeta^2)} = \int\limits_{-\infty}^{\infty} d\chi \, \rho \tag{5.76}$$

one obtains

$$W^{\text{ap2}}_{\text{SFA-VG}} = \frac{\kappa^5 \tau}{8\pi^2 \gamma} \int\limits_{1}^{\infty} d\rho \, \rho^6 \int\limits_{-\infty}^{\infty} d\chi (1 + \chi^2)^2 \mathcal{L}^2(\rho, \chi) \tilde{\Phi}(\rho, \chi) \,. \tag{5.77}$$

Substitution of Eq. (A.53) into Eq. (5.77) yields an analytical expression for the quasistatic limit of the SFA-VG

$$W_{\text{QSFA-VG}} = \omega \, R(\tau, \kappa) \tag{5.78}$$

with

$$R(\tau, \kappa) = \int\limits_{1}^{\infty} \frac{8\tau^2}{3\pi} B(\rho, \kappa) K^2_{1/3} \left(\frac{\tau\rho^3}{3}\right) d\rho \,, \tag{5.79}$$

$$B(\rho,\kappa) = \rho^8 \left(\frac{\kappa}{4\pi}\right)^3 \int\limits_{-\infty}^{\infty} d\chi \, (1+\chi^2)^2 \, \tilde{\Phi}(\rho,\chi) \, . \tag{5.80}$$

Equation (5.78) shows that the ionization rate calculated within SFA-VG is proportional to the frequency ω in the limit $\omega \to 0$. Thus the SFA-VG rate vanishes in the static limit $\omega = 0$ for all binding energies and field strengths! Clearly, this prediction of SFA-VG is unphysical implying that SFA-VG is not applicable in the quasistatic limit for atomic systems. For short-range potentials the integral over χ in (5.80) diverges and one has to consider the term proportional to γ^2 in (A.48). This term removes the divergence and the obtained limit for the ionization rate is now ω independent in accordance with the discussion in [147]. For long-range potentials there is no divergence in (5.80), and thus (5.78) gives the corresponding quasistatic limit of SFA-VG for that case. Clearly, the agreement of the SFA-VG rate with the one predicted by tunneling theories that is obtained for short-range potentials cannot be used as a measure of the validity of the SFA-VG, if long-range potentials are present. However, as is discussed below for the specific example of hydrogen-like atoms, the QSFA-VG results may be used together with tunneling theories to obtain an approximate Coulomb correction factor for SFA-VG.

Since for long-range potentials the SFA-VG rate leads to unphysical results in the quasistatic limit, one would expect that there is very limited interest in its explicit calculation. However, as is shown below, the explicit calculation of $W_{\text{QSFA-VG}}$ is not only useful for obtaining a Coulomb correction factor, but it provides also an alternative recipe for an efficient though approximate calculation of SFA-VG rates for atomic and molecular systems exposed to intense laser fields in a large range of experimentally relevant laser parameters. To demonstrate this, calculations for hydrogen-like atoms using Eqs. (5.78) to (5.80) are discussed in the next subsection.

5.3.2. Quasistatic limit of SFA-VG for hydrogen-like atoms

In the case of bound states of hydrogen-like atoms the functions B in Eq. (5.80) can be calculated analytically. For example, for the 1S_0 state it is simply given by $B_{1\text{S}_0} = 1$. The functions B for all hydrogenic states with principal quantum number $n \leq 3$ are listed in Sec. C.2. Note, for hydrogen-like states the function B is κ-independent and, therefore, the proportionality coefficient R is a function of τ only. The evaluation of R according to Eq. (5.79) can then simply be performed numerically. Since the integrand is a smooth exponentially decaying function, quadrature can easily and very efficiently

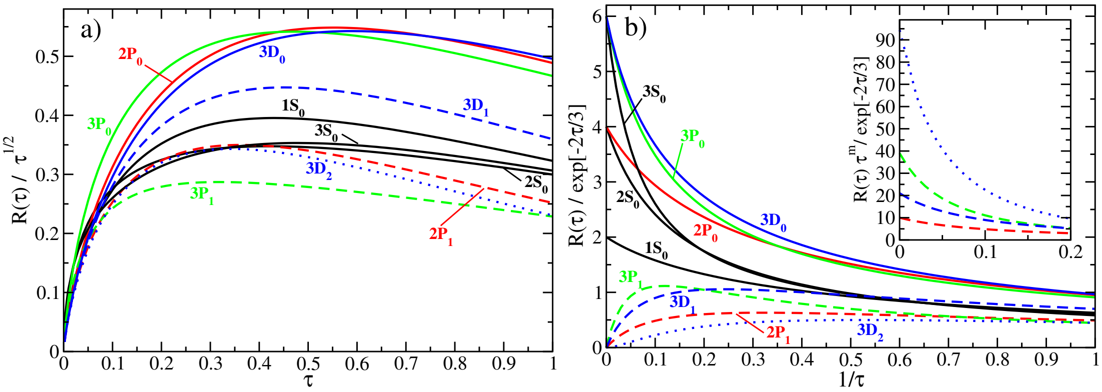

Figure 5.2.: The proportionality coefficient $R(\tau) = W_{\text{QSFA-VG}}/\omega$ (5.79) is shown for the complete range of $\tau = (2E_\text{b})^{3/2}/F$ values for the different hydrogen-like states with $n \leq 3$. a) For small τ (corresponding to a strong field F or a small binding energy E_b) all coefficients decrease with decreasing τ. To partly compensate this effect all coefficients $R(\tau)$ are scaled by factor $\sqrt{\tau}$. b) For large τ (corresponding to a weak field F or a large binding energy E_b) all coefficients are scaled by the factor $\exp[-2\tau/3]$ (in the insert the coefficients for $m > 0$ are also shown scaled by the factor $\tau^{-m}\exp[-2\tau/3]$). In this limit the coefficients $R(\tau)$ tend to those given by (5.81). (Published in [42].)

be performed with high precision.

The proportionality coefficients $R(\tau)$ for a variety of states of hydrogen-like atoms are shown in Fig. 5.2 for the complete range of values of the inverse field parameter τ. In Fig. 5.2 a the range $\tau \leq 1$ is shown. For better visibility the function $R(\tau)/\sqrt{\tau}$ is plotted instead of $R(\tau)$. It is worth noticing that for very small τ the R values for all states approach 0. This is a known failure of SFA-VG, since a larger ratio of the field intensity to the binding energy (and thus smaller τ) should clearly result in a larger and not in a smaller ionization rate [139].

In the τ range shown in Fig. 5.2 a in which the R values follow the expected behavior (decreasing R for increasing τ), the different states behave rather differently as a function of τ. It is clearly visible that R depends mostly on the quantum numbers l and m and only very weakly on n. A different dependence is found for large values of τ as is discussed below.

The weak-field limit $F \to 0$ corresponds to $\tau \to \infty$. Using an asymptotic expansion for the modified Bessel function one finds that the integrand in (5.79) is proportional to $\exp[-2\tau\rho^3/3]$. For large values of τ the integrand decays thus rapidly as ρ increases. Therefore, it is possible to use an expansion in terms of ρ at $\rho = 1$. This procedure yields

$$R_{nlm}(\tau) \to C_{nlm}^{\text{QSFA-VG}}(2\tau)^{-|m|}e^{-2\tau/3}. \tag{5.81}$$

The general expression for the coefficients $C_{nlm}^{\text{QSFA-VG}}$ is quite complicated. A very simple result occurs, however, for $m = 0$ where $C_{nl0}^{\text{QSFA-VG}} = 2n$ is obtained. Note, in this case the coefficient is l independent. For $n \leqslant 3$ the coefficients are given by

$$C_{nlm}^{\text{QSFA-VG}} = 2n\frac{[2n(n-l)+2|m|-1]!!}{[2n(n-l)-1]!!}\,. \tag{5.82}$$

Noteworthy, the l dependence is in fact limited to the circularity of the hydrogenic state, since l appears only in the form $n - l$.

In Fig.5.2 b the function R is shown (after multiplying it with $e^{2\tau/3}$ to remove the exponential dependence on τ) as a function of $1/\tau$. The weak-field limit corresponds thus to $1/\tau \to 0$. As predicted, for $m = 0$ the scaled function R approaches $C_{nl0}^{\text{QSFA-VG}} = 2n$ in this case. Due to the $\tau^{|m|}$ factor appearing in (5.81) the high $|m|$ states are harder to ionize in the weak-field limit. It is also apparent from Fig.5.2 b that the characteristic dependence on the quantum numbers in the weak-field limit is reached only for $1/\tau \leq 0.1$ to 0.2. For example, down to $1/\tau \approx 0.15$ the QSFA-VG ionization rates of the $2S_0$ and $2P_0$ states are almost identical.

It is instructive to compare the quasistatic limit of the SFA-VG-VG ionization rate in the weak-field limit with the well-known quasistatic Popov-Peremolov-Terent'ev (PPT) formula [95],

$$W_{\text{PPT}} = |C_{nl}|^2\, f_{lm}\sqrt{\frac{3}{2\pi}}\,\kappa^2\,(2\tau)^{2n-|m|-3/2}\,e^{-2\tau/3} \tag{5.83}$$

with

$$|C_{nl}|^2 = \frac{2^{2n}}{n(n+l)!(n-l-1)!}, \quad f_{lm} = \frac{(2l+1)(l+|m|)!}{2^{|m|}|m|!(l-|m|)!}\,.$$

The ionization rates $W_{\text{QSFA-VG}}$ and W_{PPT} both include the exponential term $\exp[-2\tau/3]$ and the factor $(2\tau)^{-|m|}$, but differ in the remaining part. Introducing the ratio

$$Q_{\text{PPT}} = \frac{W_{\text{PPT}}}{W_{\text{QSFA-VG}}} = \frac{1}{\omega}\frac{2^{2n-2}|C_{nl}|^2\, f_{lm}}{C_{nlm}^{\text{QSFA-VG}}}\sqrt{\frac{3}{\pi}}\frac{F^{3/2}}{\kappa^{5/2}}\frac{\kappa^{6n}}{F^{2n}} \tag{5.84}$$

it is possible to identify four factors that prevent an agreement between the QSFA-VG and the PPT predictions. One is due to the (unphysical) ω dependence of QSFA-VG. Also the constant factors that depend on the quantum numbers n, l, and m differ. For example, for fixed n and $m = 0$ QSFA-VG predicts the same ionization rate for states with different l whereas the PPT formula predicts an l dependence. Then there is a constant factor ($\sqrt{3/\pi}$) that is, however, very close to 1. Finally, both rates differ in their dependence on field strength and binding energy which is expressed as two factors to stress the n dependent or independent parts.

Note, the popular Ammosov-Delone-Krainov (ADK) formula [96] differs from PPT by the introducing effective quantum numbers n^* and l^* for non-hydrogenic atoms, an application of the Stirling approximation for the evaluation of factorials, and a rearrangement of the final expression. In the here considered case of hydrogen-like atoms the difference between ADK and PPT reduces thus basically to the application of the Stirling formula for $|C_{nl}|^2$. Therefore, the ADK and PPT rates of a specific state differ only by a few percent which is due to their different constant prefactors. A comparison to ADK leads thus to basically the same conclusion as the one to PPT performed above.

Since QSFA-VG is the exact asymptotic limit of SFA-VG, Eq. (5.84) can be used to derive a Coulomb-corrected SFA-VG rate, $W_{\text{CSFA-VG}} = Q_{\text{PPT}}\, W_{\text{SFA-VG}}$. Clearly, the factor Q_{PPT} derived here explicitly for atomic hydrogen could be applied also to other atomic or molecular systems by performing the evident modifications like the introduction of effective quantum numbers [96], such as n^*, l^*, etc. Although the range of validity of $W_{\text{CSFA-VG}}$ for $\omega \neq 0$ is not directly evident, in contrast to $W_{\text{SFA-VG}}$ it at least reaches the tunneling limit. Already in the past efforts have been made to derive Coulomb-correction factors for KFR theories, but so far the resulting rates did not lead to convincing results (see [147] and references therein). Based on some approximations, A. Becker *et al.* [168] have proposed a Coulomb correction factor, C^2. Using this factor, very good agreement is found between experimental and theoretical SFA-VG ionization yields for a large number of atoms and laser frequencies. The comparison is, however, mostly performed on a qualitative level, since the experiments did not provide absolute yields and thus the theoretical and experimental data were adjusted at one common point. In addition, SFA-VG results for atomic hydrogen (with and without C^2 factor) are compared to full numerical solutions of the time-dependent Schrödinger equation in [168] and again good agreement is found (on a logarithmic scale).

For atomic hydrogen one has $C^2 = \kappa^{6n}/F^{2n}$ which corresponds just to the last factor in (5.84). Clearly, the C^2-corrected SFA-VG rate does not approach the tunneling limit for $\omega \to 0$. However, the terms missing in C^2 yield for $\omega = 0.05\,\text{a. u.}$ and the ground state of a hydrogen atom a factor 0.5 - 1.2 for $F = 0.05 - 0.1\,\text{a. u.}$ This can explain the reasonable agreement of the C^2-corrected SFA-VG results with the ones of *ab initio* calculations reported for such parameters in [168]. However, the deviation increases by a factor 10

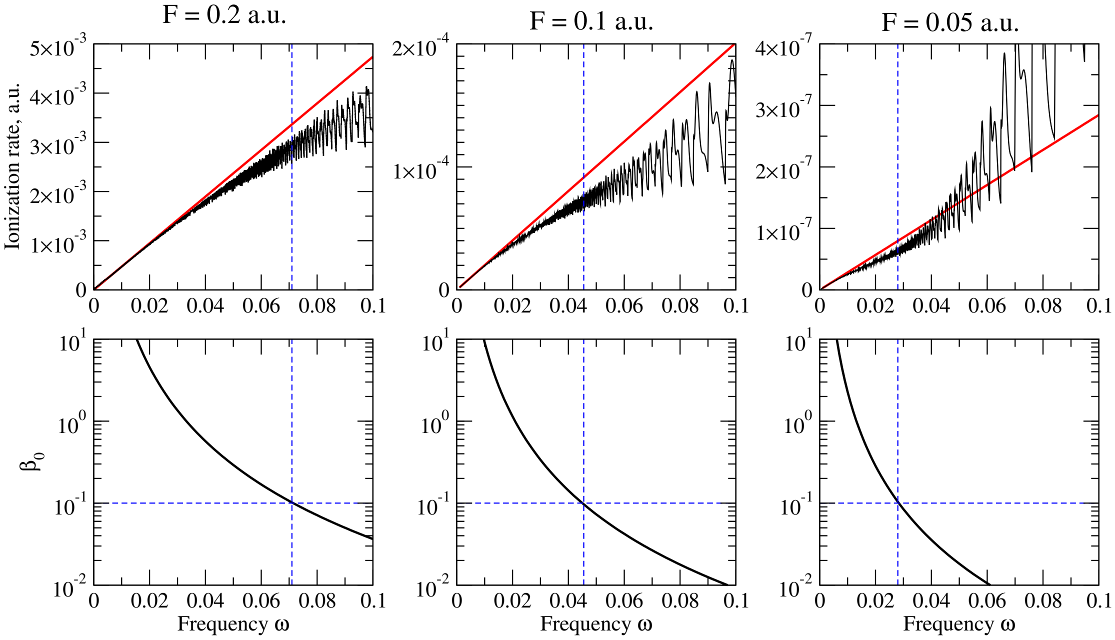

Figure 5.3.: The top panel shows the comparison of SFA-VG (black) and QSFA-VG (red) ionization rates for the 1S state of a hydrogen atom in a range of frequencies from 0 to 0.1 a.u. for different field strength F. The bottom panel shows the corresponding value of the parameter β_0 defined in Eq. (5.85). Blue dashed vertical lines indicate the frequency where $\beta_0 = 0.1$, so that on the right part of the plot the magnetic field effect are expected to be negligible.

for the CO_2 laser frequency or for larger n. It may be noted that although [168] contains also comparisons with experimental data obtained with a CO_2 laser, the present work shows that the found agreement is due to the fact that the comparison is made on a relative scale, as mentioned before. In this case the erroneous ω dependence of SFA-VG (clearly not corrected by the C^2 factor) is, for example, not visible.

As follows from the derivation, $W_{\text{QSFA-VG}}$ in (5.78) is the exact asymptotic form of the SFA-VG ionization rate $W_{\text{SFA-VG}}$ in the limit $\omega \to 0$. It is of course interesting to investigate the validity regime of QSFA-VG for non-zero values of ω. In fact, as is shown now, QSFA-VG provides for a wide range of parameters a good approximation to SFA-VG even for laser wavelengths of around 800 nm or less.

Figure 5.3 shows the comparison of $W_{\text{SFA}-\text{VG}}$ and $W_{\text{QSFA}-\text{VG}}$ for the 1S state of a hydrogen atom in a range of laser frequency $\omega < 0.1$ a.u. for three different values of the field strength F. The ionization rate $W_{\text{SFA}-\text{VG}}$ has been calculated numerically using the scheme described in Sec. A.5. The SFA-VG and QSFA-VG ionization rates approach each other and tend to zero for $\omega \to 0$ indicating the correctness of the derivation of QSFA-VG as well as numerical consistency. An oscillatory behavior of the SFA-VG ionization rate that is due to channel closings is not resolved in QSFA-VG, since the summation over photon number N is transformed into an integration [see Eq. (5.75)]. The oscillation amplitude increases with ω, but the ratio between $W_{\mathrm{SFA-VG}}$ and $W_{\mathrm{QSFA-VG}}$ remains in between about 0.75 and 1.25 in the full frequency range. Therefore, QSFA-VG is correct to within 25%. If one averages over the oscillations, one finds an even much better quantitative agreement between QSFA-VG and SFA-VG. In view of the fact that the SFA-VG rate is known to overestimate the effect of channel closings and that these pronounced channel closing features mostly disappear when averaging over realistic laser parameters (envelope, focal volume etc.), the QSFA-VG can be said to provide a very accurate approximation for the given parameters. Note, $\omega = 0.1\,\mathrm{a.u.}$ corresponds to a laser wave length of about 450 nm and thus the shown frequency range covers a large range of experimentally relevant lasers.

According to [127], the dipole approximation breaks down in the limit $\omega \to 0$ due to the effect of the magnetic field on a free electron. To avoid the onset of magnetic field effects, and thus to maintain the validity of the dipole approximation, the relation

$$\beta_0 = \frac{z}{2c} \ll 1 \tag{5.85}$$

must be valid. The dependence of the parameter β_0 on the laser frequency is also demonstrated in Fig. 5.3. As one can see, SFA-VG and QSFA-VG rates almost coincide for $\beta_0 > 1$, where the applicability of the dipole approximation is questionable. However, even for frequencies with $\beta_0 < 0.1$ the agreement between SFA-VG and QSFA-VG rates is reasonable. Therefore, QSFA-VG allows for a rather accurate prediction of the SFA-VG rate even in the validity regime of the dipole approximation. The large range of applicability of the QSFA-VG is of practical interest, since its numerical evaluation is substantially simpler than the one of the original SFA-VG rate, especially in the IR and far-IR frequency regime. Furthermore, it is very convenient for studies of the frequency dependence of the SFA-VG rate, since the QSFA-VG is, besides a simple proportionality factor, ω independent. Thus the QSFA-VG has to be evaluated for a given system and field strength only once. In turn, the relatively large range of laser frequencies in which QSFA-VG and SFA-VG agree demonstrates that also the SFA-VG rate itself is in a wide range of laser parameters only proportional to ω. An exception is the already mentioned pronounced ω dependence due to channel closings that is not reproduced by QSFA-VG.

5.4. SFA for molecules

SFA theory has been successfully generalized to describe molecules. For example, using velocity-gauge molecular SFA (MO-SFA-VG) the phenomenon of *suppressed* molecular ionization was interpreted by Muth-Böhm *et al.* [141] as an effective destructive interference between the two subwaves of the ionizing electron emerging from the two atomic centers. Alternatively, length-gauge molecular SFA (MO-SFA-LG) was formulated in [142]. In order to consider the nuclear motion in the field, Milošević [19] has proposed two forms of modified MO-SFA-LG, one with the field-free (uM-MO-SFA-LG) and the other with the field-dressed (dM-MO-SFA-LG) initial molecular bound state.

Although SFA appears to be able to predict the main features of the ionization process, it is known to be strongly gauge-dependent. The predictions obtained in length or velocity gauge may differ by 2 or 3 orders of magnitude due to the problem to correctly incorporate the Coulomb correction. Different authors prefer different gauges. The question of which gauge is superior for which problem has often been raised, but never led to any consensus about its answer. The situation is even more complicated due to different additional approximations, used, e.g., to numerically calculate transition amplitudes or to model the initial or the final state. For example, even the application of the same version of SFA, namely MO-SFA-VG, may lead to qualitatively different results obtained by different authors. Whereas Muth-Böhm *et al.* [141] and Usachenko and Chu [169] predict (in agreement with experimental observations) the parallel orientation of N_2 to possess higher ionization rates compared to the perpendicular orientation, the calculations of Kjeldsen and Madsen [142] and Milošević [19] reveal a maximum for perpendicular orientation.

The same simple interference picture which arises in the MO-SFA-VG and seems to plausibly explain the occurrence or absence of suppressed ionization can be applied also for the study of the alignment dependence of the photoelectron spectrum. This section aims to demonstrate theoretically that a clear interference pattern appears in the ratio of energy-resolved spectra for a parallel and a perpendicular alignment of the H_2 molecule. This interference pattern emerges due to the destructive interference caused by the phase shift between the two electronic wavepackets emerging from the two nuclei and moving along the polarization axis.

In the case of a homonuclear diatomic molecule with internuclear separation R a bonding highest occupied molecular orbital (HOMO) Φ built from s-type atomic orbitals ϕ is given within the framework of a linear combination of atomic orbitals as

$$\Phi(\mathbf{r},\mathbf{R}) = a\{\phi(\mathbf{r},-\mathbf{R}/2) + \phi(\mathbf{r},\mathbf{R}/2)\} \tag{5.86}$$

where $\mathbf{r}$ is the electronic coordinate and a the normalization constant. According to MO-SFA-VG [141] (also called first-order IMST) this leads to the N-photon ionization rates (integrated over the directions of the emitted electron)

$$\Gamma_N = N_e \int d\hat{\mathbf{k}}_N \frac{dW^{(N)}}{d\hat{\mathbf{k}}_N} \tag{5.87}$$

in a linearly polarized laser field, if the HOMO is occupied by N_e electrons. The in Eq. (5.87) occurring differential ionization rates are given by

$$\begin{aligned} \frac{dW^{(N)}}{d\hat{\mathbf{k}}_N} &= 2\,\pi\, C^2\, k_N\,(U_p - N\omega)^2 J_N^2\Big(\boldsymbol{\alpha}_0 \cdot \mathbf{k}_N, \frac{U_p}{2\omega}\Big) \\ &\times \Big|2a\langle \mathbf{k}_N|\phi\rangle\Big|^2 \cos^2(\mathbf{k}_N\cdot\mathbf{R}/2)\;. \end{aligned} \tag{5.88}$$

Here, $k_N^2/2 = N\omega - (U_p + E_{\rm ion})$ is the kinetic energy of an electron after absorption of N photons, $U_p = F^2/(4\omega^2)$ is the ponderomotive energy of an electron in a laser field of frequency ω and peak field strength F, $E_{\rm ion} = \kappa^2/2$ is the ionization energy of the molecule, and $C^2 = (\kappa^3/F)^{2/\kappa}$ is a Coulomb correction factor. Finally, $\langle \mathbf{k}|\phi\rangle$ is the Fourier transform of the atomic orbital $\phi(r)$ and $J_n(a,b)$ is a generalized Bessel function of two arguments as defined in [147]. The polarization axis $\boldsymbol{\varepsilon}$ enters the ionization rate only through one of the arguments of the Bessel function, $\boldsymbol{\alpha}_0 = (F/\omega^2)\boldsymbol{\varepsilon}$.

The sum of the N-photon ionization rates for all energetically allowed values of N yield the energy-resolved electron spectra. Since the Fourier transform of spherically symmetric (s-type) orbitals is also spherically symmetric, it depends only on k. Therefore, the ratio of the N-photon ionization rates for parallel and perpendicular orientations of the field polarization vector with respect to the internuclear axis can be written as

$$X_N = \frac{\Gamma_N^{\parallel}}{\Gamma_N^{\perp}} = \frac{\int d\hat{\mathbf{k}}\, J_N^2\Big(g_N\boldsymbol{\varepsilon}\cdot\hat{\mathbf{k}}, b\Big)\cos^2\Big(d_N\hat{\mathbf{k}}\cdot\hat{\mathbf{R}}^{\parallel}\Big)}{\int d\hat{\mathbf{k}}\, J_N^2\Big(g_N\boldsymbol{\varepsilon}\cdot\hat{\mathbf{k}}, b\Big)\cos^2\Big(d_N\hat{\mathbf{k}}\cdot\hat{\mathbf{R}}^{\perp}\Big)} \tag{5.89}$$

where $g_N = \alpha_0\, k_N$, $b = U_p/(2\omega)$, $d_N = R\,k_N/2$, and all factors depending only on the absolute value of $\mathbf{k}_N$ were taken out of the integral and cancel each other, if the ratio is considered.

Fixing the coordinate system in such a way that its z axis agrees with the polarization vector $\boldsymbol{\varepsilon}$, one has $\hat{\mathbf{R}}^{\parallel} = (0,0,1)$, $\hat{\mathbf{R}}^{\perp} = (1,0,0)$, and $\hat{\mathbf{k}} = (\sin\theta\cos\phi, \sin\theta\sin\phi, \cos\theta)$. Then the ratio (5.89) can be rewritten as

$$X_N = \frac{\int_0^\pi d\theta\, \sin\theta\, J_N^2\Big(g_N\cos\theta, b\Big)\cos^2(d_N\cos\theta)}{\int_0^\pi d\theta\, \sin\theta\, J_N^2\Big(g_N\cos\theta, b\Big)[1 + J_0(2d_N\sin\theta)]/2} \tag{5.90}$$

where the identity

$$\int_0^{2\pi} d\phi \cos^2(\delta\cos\phi) = \pi[1 + J_0(2\delta)] \tag{5.91}$$

for the zero-order Bessel function of the first kind was used.

For very strong fields the function $J_N^2(g_N\cos\theta, b)$ peaks usually sharply around $\cos\theta = \pm1$ (i.e. in the case of ionization from a spherically symmetric atom the vast majority of electrons are ejected parallel to the laser polarization axis). On the other hand, the functions $\cos^2(d_N\cos\theta)$ and $J_0\big(2d_N\sin\theta\big)$ vary rather slowly in these regions. They may thus be approximated by their values at $\cos\theta \approx \pm1$:

$$\cos^2(d_N\cos\theta) \approx \cos^2(d_N), \qquad J_0\big(2d_N\sin\theta\big) \approx 1\ . \tag{5.92}$$

Substitution of Eq. (5.92) into Eq. (5.90) results finally in a very simple expression for X_N,

$$X_N \approx \cos^2(d_N) = \cos^2(Rk_N/2)\ . \tag{5.93}$$

Note, that for very small d_N (which means small R or small k_N) both functions in Eq. (5.92) are equal to 1, so the ratio X_N is also 1.

According to Eq. (5.93) MO-SFA-VG predicts a pronounced minimum to occur at the electron energy $E \approx \pi^2/(2R^2)$, if the ratio between the the energy-resolved electron spectra obtained for a parallel and a perpendicular orientation is considered. For the molecular hydrogen, this prediction will be tested in Sec. 7.6 by means of a full solution of the TDSE for both molecular orientations. This numerical test provides a way for checking the interference picture, whereas a direct experimental confirmation of this concept is difficult. Indeed, it requires the measurement of the electron spectra as a function of the alignment between the molecular axis and the laser-field axis. For example, the energy-resolved electron spectra measured in [170] are often seen as an experimental evidence of the concept of symmetry-induced quantum-interference effects as predicted by MO-SFA-VG. However, the spectra measured in [170] are averaged over all orientations, and the obtained results can be explained without using the interference picture [143].

6. Hydrogen atom in a strong laser field

In the remaining part of this work, the main focus will be put on the investigation of the nonlinear ionization of a quantum system. It occurs if the photon energy of the radiation is smaller than the binding energy of the system. In this case, ionization can be considered as the multiphoton transition from an initial state to the continuum via virtual (or resonant) intermediate states. This process is very complex and often depends strongly on both pulse parameters and the level structure of the system. Even for the hydrogen atom the full understanding of all peculiarities in the photoelectron energy spectrum yielded by a full numerical solution of the TDSE is an intricate task. For the hydrogen molecule, one has to face additional effects due to the anisotropy of the electron density and the electron-electron interaction. Thus, the task might become daunting. This is why the hydrogen atom is a perfect candidate for the investigation of the basic aspects of the nonlinear ionization process. Since the full numerical solution of the TDSE is a complicated task by itself, the choice of the hydrogen atom is also motivated by practical reasons. Being the simplest quantum system, the H atom allows accurate ab-initio numerical calculations treating the electron in full dimensionality and a thorough control over convergence is feasible. Hence it is possible to disentangle physical effects from artificial ones occurring due to additionally employed approximations. Last but not least, an extensive numerical investigation of the H atom by means of an accurate numerical technique is of interest by itself. Although a tremendous amount of studies of the ionization of the H atom has been published in literature, most of them employ additional approximations (e.g., reducing the dimensionality of the problem by means of a 1D or a 2D model or just employing a too restricted basis set) and only a minute part of them provides data which can be viewed as being exact. Frequently, exact data provide only a few data points what makes a systematic analysis impossible.

Thus, using the H atom as a case study the present chapter examines the basic aspects of how radiation parameters and internal structure affect the ionization process. After a brief discussion (Sec. 6.1) of the two *ab-initio* numerical techniques employed for the present investigation, peculiarities of photoelectron energy spectra are examined for different radiation parameters. Besides other aspects, it aims to provide a feeling of whether a multipeaked or a continuous spectrum is expected for a given set of parameters and to demonstrate how the spectrum changes when the ionization process passes from the multiphoton to the tunneling regime. The chapter proceeds with a detailed analysis (Sec. 6.3) of the ionization rates for different radiation intensities and photon energies, accompanied by a comparison with the popular SFA and tunneling approximations. Section 6.4 sheds light on the behavior of the atomic bound states in the presence of perturbative and nonperturbative fields. The ionization by ultrashort laser pulses are examined in Sec. 6.5. The chapter closes with a brief discussion of how the dynamics of bound-state populations can be investigated during the pulse and which problems one faces trying to interprete the results obtained in different gauges.

6.1. Ab-initio methods

The numerical study of the laser-matter interaction in the non-perturbative regime can be performed using either Floquet theory [171] or the direct integration of time-dependent Schrödinger equation. Non-perturbative Floquet methods, such as Sturmian-Floquet [172] or R-matrix-Floquet (RMF) theory [173], have been applied extensively to study single multiphoton ionization and high-order harmonic generation for atoms in laser fields with constant or slowly varying intensity. For ultra-short laser pulses, typically in the femtosecond range, the rate concept becomes questionable and a direct integration of the TDSE is more adequate. However, it is computationally expensive, and thus one- or two-dimensional models have been used for a long time to reduce the computational demands [174]. Nevertheless, the first three-dimensional calculations for atoms were carried out by Kulander [175] already in 1987 using a time-dependent finite-difference method. This method, but with different propagation techniques, has also been employed by LaGattuta [176] and Roso-Franco *et al.* [177]. Alternatively, the TDSE has been integrated using time-dependent finite-element methods (e.g., with B splines [178]) as well as by expanding the time-dependent wave function in terms of stationary states [179] or Volkov states [180].

In this section two *ab-initio* numerical methods are briefly discussed which are solely used in the present chapter. The first one, referred to in the following as TDSE method, consists of the direct solution of the TDSE for a given laser pulse using the approach described in [179]. This choice is motivated by the fact that essentially the same concept is further employed for solving the TDSE describing molecular hydrogen exposed to a laser pulse. The code for atomic hydrogen has been rewritten from scratch and extensively used for gaining important experience before turning to the numerical investigation of the intense-field response of molecular hydrogen. The second method is used for solving the TDSE describing the hydrogen atom exposed to an infinitely long, monochromatic laser field by means of Floquet theory. The calculation of ionization rates and AC Stark shifts is performed with the publicly-available package STRFLO [181], which has been slightly improved for a more convenient use taking advantage of recent advances in the Fortran language standard. This package provides also a possibility to calculate the static ionization rates and DC Stark shifts, which are used in the following for an analysis of the low-frequency regime.

6.1.1. TDSE method

Within the TDSE method, the time-dependent wavefunction $\Psi(\mathbf{r},t)$ is expanded in the basis of eigenstates of the H atom, $\psi_{nl}(\mathbf{r})$, i.e. as

$$\Psi(\mathbf{r},t) = \sum_{nl} C_{nl}(t)\psi_{nl}(\mathbf{r}) \tag{6.1}$$

where the $\psi_{nl}(\mathbf{r})$ are expanded in terms of spherical harmonics, with the radial function being expanded in terms of B splines as discussed in Sec. 1.3. For linearly polarized light the Hamiltonian possesses axial symmetry. Therefore, only the axial quantum number $m = 0$ is used in the expansion (6.1), since the current study of ionization of the H atom is restricted to ionization from the 1S ground state and linear polarization. Substitution of Eq. (6.1) into the TDSE results in a system of ordinary differential equations (ODE), whose explicit form depends on the gauge adopted for describing the atom in the field. The system of ODE is then solved numerically employing the NAG routine D02CJF based on a variable-order, variable-step Adams method. Time propagation has been tested for different shapes of the pulse envelope (see Appendix D).

As discussed in Sec. 4.4, the expansion (6.1) is only a particular choice, since the functions $\psi_{nl}(\mathbf{r})$ may be pre-multiplied by an $\mathbf{r}$-dependent phase, depending on the adopted gauge (or a particular choice of the generalized field-free Hamiltonian). This leads to a different time evolution of the basis-state populations, $P_{nl}(t) = |C_{nl}(t)|^2$, as is investigated in the last section of this chapter. However, this does not affect the final observables, such as excitation and ionization probabilities at the end of a pulse, $t = t_f$. For example, the final population of the ground state is given by $P_{1S} = |C_{1S}(t_f)|^2$, the total ionization

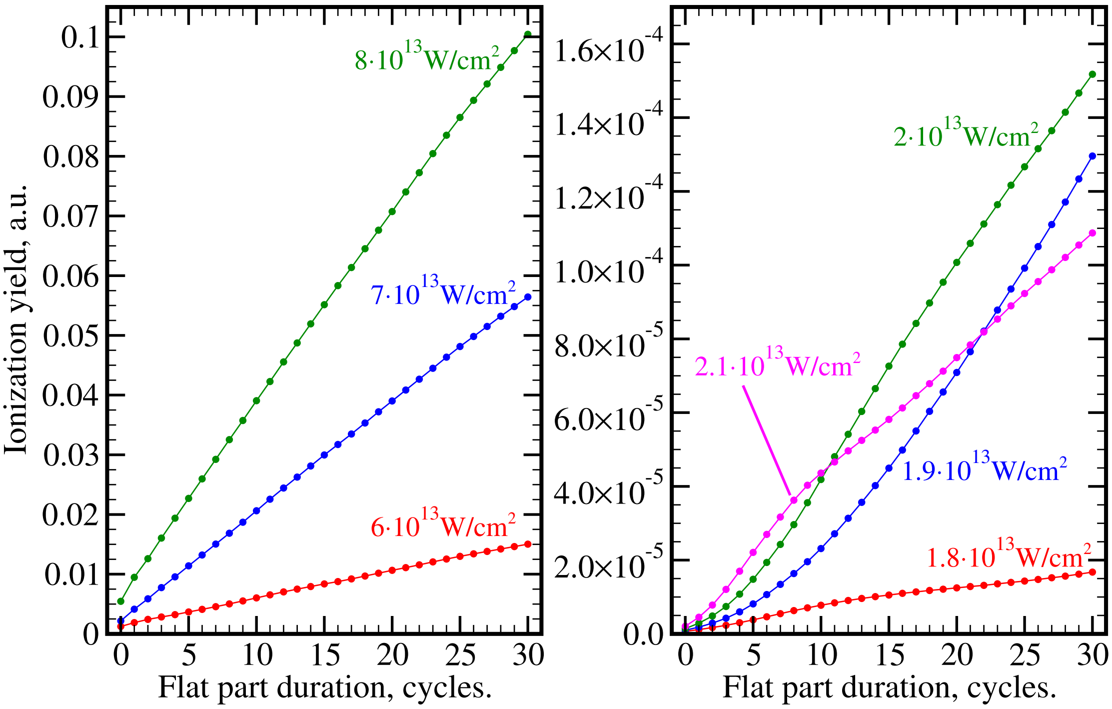

Figure 6.1.: Ionization yields of an H atom for different values of the peak intensity as a function of the duration of the flat part of an 800 nm top-flat pulse with 4 cycles cos^2-shaped up- and down-ramp.

yield is obtained as

$$Y_{\text{ion}} = \sum_{nl(E>0)} |C_{nl}(t_f)|^2, \tag{6.2}$$

and the total excitation yield is given by $Y_{\text{exc}} = 1 - P_{1S} - Y_{\text{ion}}$. The partial photoelectron energy spectrum $\partial P_l/\partial E$ is computed by an interpolation over the final populations of discretized continuum states weighted with the density of states. The total photoelectron energy spectrum is then obtained as

$$\frac{\partial P}{\partial E}(E) = \sum_{l=0}^{l_{\max}} \frac{\partial P_l}{\partial E}(E) \; . \tag{6.3}$$

Although the TDSE method provides the outcome in terms of the ionization yield, it can also be applied to obtain ionization rates. This is achieved by the following procedure. Ionization yields are computed for a series of flat-top pulses with N cycle up- and down-ramp and a M cycle flat part, where M has been varied in the range from 0 to 30 (see Fig. D.2). A typical result of such a variation is demonstrated in Fig. 6.1. In most cases, the obtained function is almost linear (left panel of Fig. 6.1) so that the ionization rate can be determined from its slope. However, in the case of resonant ionization the obtained dependence on the flat part duration might be quite complicated and the slope may change with increasing duration of the flat part (right panel of Fig. 6.1). As one can see, for a peak intensity of $1.9 \times 10^{13}\mathrm{W/cm^2}$ the slope continuously increases with increasing duration of the flat part, whereas for a peak intensity of $2.1 \times 10^{13}\mathrm{W/cm^2}$ the slope suddenly becomes smaller for the durations of the flat part lasting more than 8 cycles. As a consequence, the slope for short durations of the flat part may significantly differ from the slope for long durations of the flat part. In this case ionization rates are determined using the slope of the longest linear part in the range 10 to 30.

6.1.2. Floquet method

According to the Floquet theorem, the wavefunction of a state of the quantum system in a monochromatic electromagnetic field has the form

$$\Psi(\mathbf{r},t) = e^{-\mathrm{i}Et} \sum_K \psi_K(\mathbf{r}) e^{-\mathrm{i}K\omega t} \tag{6.4}$$

where the summation is performed over all integers K, the quasienergy E of the system atom + field is complex and depends both on the frequency ω and the amplitude F_0 of the electric field. The wavefunction $\Psi(\mathbf{r},t)$ is thus a superposition of a number of stationary states with energies $\ldots, E-\omega, E, E+\omega, \ldots$. It is clear from the ansatz (6.4) that the definition of the quasienergy E is not unique, since $E + K\omega$ for any integer K is also a valid quasienergy. The functions $\psi_K(\mathbf{r})$ which are referred to as harmonic components of $\Psi(\mathbf{r},t)$ give different relative contributions to the total wavefunction $\Psi(\mathbf{r},t)$. One can define a measure of this relative contribution, P_K, such that $\sum_K P_K = 1$. (Since the Siegert boundary conditions are used, the normalization is, however, not trivial [181].) By analogy, one can refer to P_K as a population of K-th harmonic component. In certain cases, the system "atom + field" can be well represented by a single dressed state. This is possible if only one harmonic component is effectively populated, so that one can introduce the labeling of the harmonic components in such a way that the dominant one is assigned to $K = 0$. This provides a unique definition of the quasienergy and allows one to define the shift δE of the dressed state with respect to its energy E_0 in the field-free case, $\delta E = \mathrm{Re}\{E\} - E_0$. Since the imaginary part of the quasienergy characterizes the exponential decay of the state, the total ionization rate Γ can be obtained from the quasienergy E as $\Gamma = -2\,\mathrm{Im}\{E\}$.

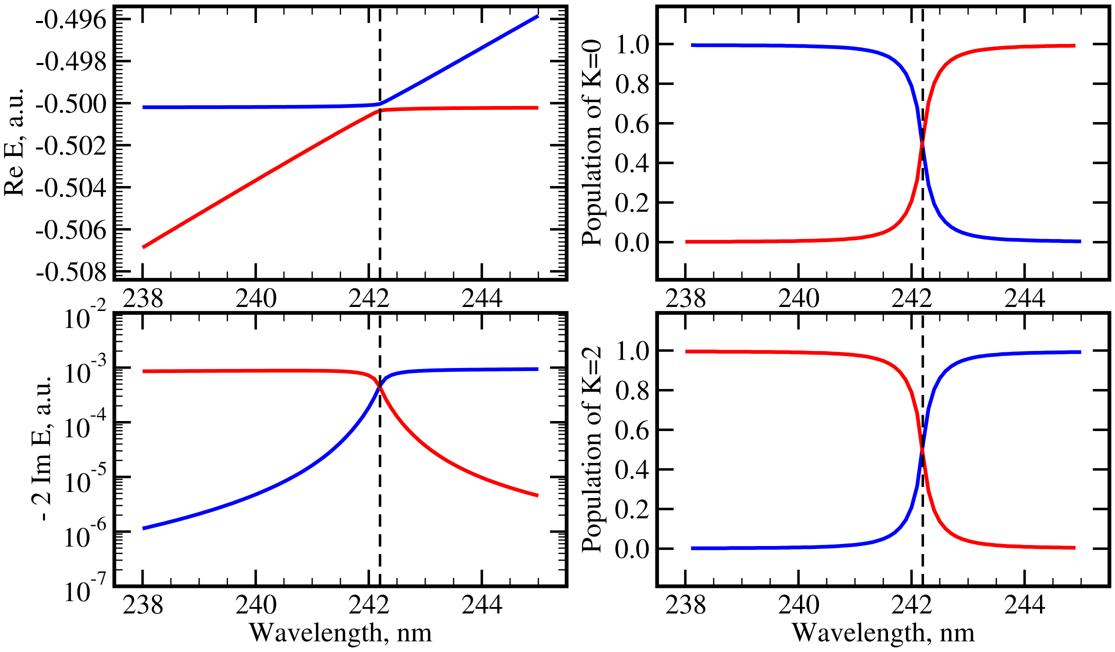

Figure 6.2.: Quasienergies E and harmonic populations P_K for $K = 0, 2$ of two quasienergy states describing an H atom exposed to a harmonic field with the intensity 5×10^{12}W/cm^2 as a function of the radiation wavelength. Blue (red) lines depict the results for the quasienergy state that changes its character from 1S to 2S (from 2S to 1S) with increasing wavelength as a consequence of the resonant two-photon coupling between these states. The position of the avoided crossing is indicated by vertical dashed lines.

In the framework of the Sturmian-Floquet approach [181], the harmonic components $\psi_K(\mathbf{r})$ are expanded in a discrete basis of complex Sturmian functions S (specified by a complex parameter κ) and spherical harmonics,

$$\psi_K(\mathbf{r}) = \sum_{jl} C_{jl}^K \, \frac{1}{r} \, S_{jl}^{\kappa}(r) \, Y_{l0}(\hat{r}) \tag{6.5}$$

where j is the index labeling the Sturmians. The method has been used successfully in the past in a wide range of dynamical regimes, from the weak-field limit to tunneling ionization or above-the-barrier ionization.

Floquet calculations are very helpful for the analysis of resonance enhanced multiphoton ionization (REMPI). In terms of quasienergy states, REMPI occurs if the real part of the quasienergy of the ground state crosses the real part of the quasienergy of a resonant state. An example of such an analysis is presented in Fig. 6.2 where the appearance of (2+1) REMPI through the 2S state when varying the radiation wavelength is demonstrated. At the wavelength 238 nm the two considered quasienergy states can be well described as dressed 1S and 2S states. The total ionization rate ($\Gamma = -2\,\mathrm{Im}\{E\}$) of the H atom in the 1S state is about 10^{-6} a.u., whereas the total ionization rate from the 2S state is about three orders of magnitude larger. Although the real parts of the quasienergy differ only by 0.007 a.u., the harmonic component with $K = 0$ is dominant in the case of the 1S state, whereas for the 2S state the harmonic component with $K = 2$ dominates. Thus, the actual energy spacing between the two dressed states consists in $(2\omega - 0.007)$ a.u., where ω is the photon energy. With increasing radiation wavelength this spacing tends to 2ω, giving rise to an enhanced ionization rate. The harmonic populations are also changing, so that at 242.2 nm both states have $P_0 = P_2 = 0.5$. Note, the dependence of the real parts of the quasienergy as a function of the radiation wavelength exhibit an avoided crossing, so that the 1S quasienergy state continuously changes its character to 2S, and vice versa. This results in an uncertainty when determining AC Stark shifts of states, since none of the quasienergy states can be assigned to a specific dressed state. Noteworthy, as a consequence of the AC Stark shifts of the states the position of the resonance is slightly shifted from its position (243 nm) in the weak-field limit.

6.2. Photoelectron energy spectrum

The present section aims to give a brief review of the features observed in the photoelectron energy spectrum obtained by means of the TDSE method. Depending on the laser parameters, the spectrum can exhibit pronounced peaks or be almost continuous. Furthermore, the main peaks can be distorted by substructures. The dependence of these features on the laser-pulse parameters is investigated emphasizing the changes occurring when going from the multiphoton to the tunneling ionization regime. Among others, the question of whether or not a multipeaked (continuous) spectrum can be always attributed to the multiphoton (tunneling) ionization will be discussed.

6.2.1. Influence of the laser intensity

Some basic intense-field ionization phenomena are illustrated in Fig. 6.3 where photoelectron energy spectra of the H atom in a 500 nm laser pulse are presented for 9 different peak intensities in the range from 10^{12} W/cm^2 to 2×10^{14} W/cm^2. At the lowest intensity shown (10^{12} W/cm^2), the photoelectron energy spectrum exhibits a single pronounced

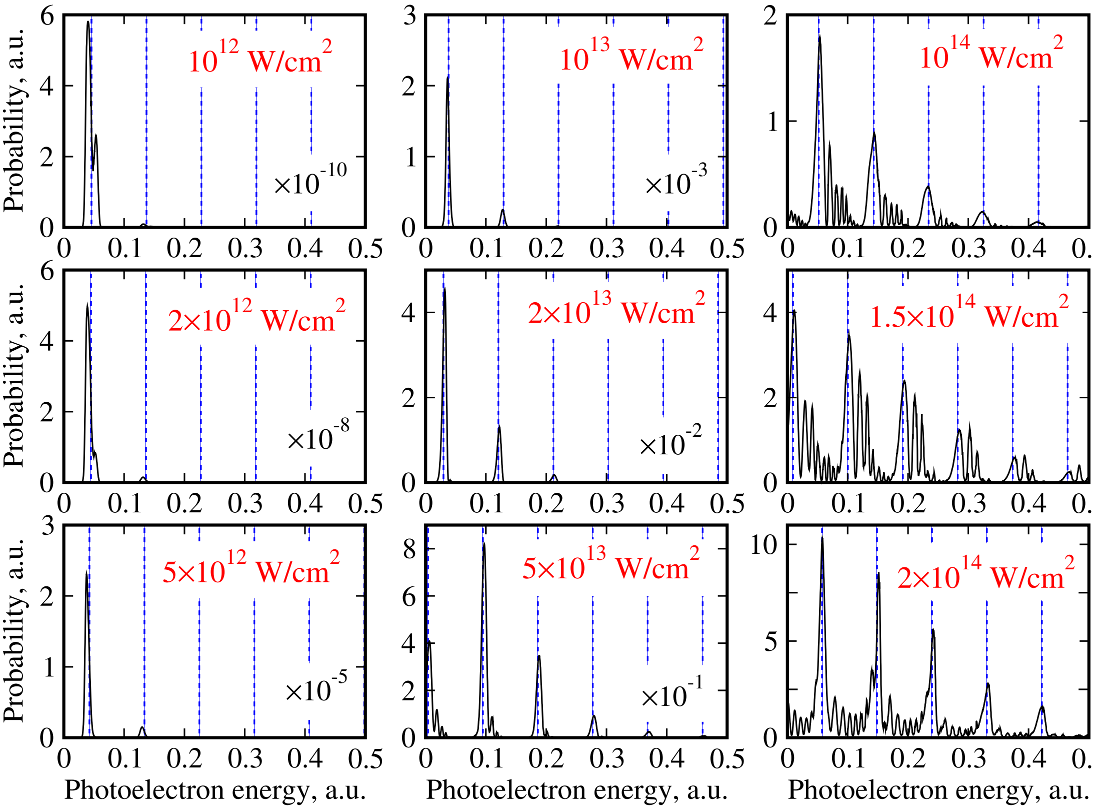

Figure 6.3.: Photoelectron energy spectra of an H atom exposed to a 500 nm Gaussian laser pulse with a duration of 20 fs (FWHM) for various values of the peak intensity. Blue dashed lines indicate the expected spectral peak positions given by the energy conservation law including the dynamic energy shifts.

peak, which is a consequence of the six-photon threshold ionization process[1]. As the intensity increases, two effects become visible. First, a sequential appearance of peaks at higher energies, separated by the photon energy, is a manifestation of the process known as multiphoton above-threshold ionization (ATI)[2]. Second, the shift of the spectral peak positions towards lower energies as a consequence of the increasing intensity-dependent ionization potential. The latter is due to the fact that the laser field must supply enough energy to sustain the field-induced quiver energy of the detached electron in the presence of the laser field. Therefore, the shift is determined by the electron ponderomotive energy U_p and hence increases linearly with the intensity. The intensity-dependent shift

---

[1] Threshold ionization process is the ionization process which takes place by absorption of the minimum (threshold) number of photons required to overcome the ionization potential.

[2] Nowadays, it is common to refer to all spectral peaks as ATI peaks, although originally this term was used to specify only those spectral peaks which arise from absorption of a greater number of photons than required for the threshold ionization process. This section adopts the original terminology.

of the ionization potential is responsible for a further effect known as a multiphoton channel closing. As the laser intensity surpasses a certain threshold, the N-photon ionization process becomes energetically forbidden (in other words, the N-photon ionization channel becomes closed). For example, as is apparent in Fig. 6.3, the 6-photon channel closing occurs when the peak intensity exceeds $5 \times 10^{13}\,\mathrm{W/cm^2}$, whereas the 7-photon channel closing occurs when the peak intensity exceeds $1.5 \times 10^{14}\,\mathrm{W/cm^2}$.

Of course, speaking about a sequential appearance of ATI peaks with increasing intensity is only meaningful, if the photoelectron energy spectra are discussed on a linear scale. On the log scale the ATI peaks are present even at perturbative intensities, although their heights may be orders of magnitude smaller than the height of the threshold ionization peak.

Figure 6.3 reveals also substructures in the peaks observable at both weak and high intensities. For example, the threshold ionization peak at an intensity of $10^{12}\,\mathrm{W/cm^2}$ consists of two clearly distinguishable subpeaks. The substructure of peaks at an intensity of $10^{14}\,\mathrm{W/cm^2}$ and higher is much more involved. The presence of substructures in the photoelectron energy spectrum is a typical situation. Often the photoelectron spectrum imprints images of dynamic resonances [182]. These substructures are called Freeman resonances and their detailed understanding requires the analysis of the field-induced Stark shifts of intermediate states [183]. The distinctive feature of such subpeaks is their weak dependence on the pulse duration. The appearance of substructures on the right-hand side of the spectral peaks (apparent in Fig. 6.3 for the intensities $10^{14}\,\mathrm{W/cm^2}$ and $1.5 \times 10^{14}\,\mathrm{W/cm^2}$) can also be associated with interferences between outgoing waves that have been emitted at slightly different energies due to the time dependence of the intensity during the pulse. The spacing between the emerging subpeaks, known also as Bardsley fringes [184], depends strongly on the duration of the pulse. Similar substructures were reproduced in [185] within the SFA model proving their nonresonant character. An interesting property of these peaks is their energy shift with increasing pulse intensity. In contrast to the main ATI peaks whose energy shift agrees well with the ponderomotive energy, the subpeaks are less shifted due to the smaller intensity the electron experiences during the ionization process.

An increase of the peak intensity is accompanied by a gradual transition from the multiphoton to the tunneling (or above-the-barrier) ionization regime. The transition from one regime to another is thought to occur when the Keldysh (adiabaticity) parameter γ approaches unity, with tunneling being dominant at $\gamma < 1$. For the pulse parameters presented in Fig. 6.3, γ decreases from 17.1 to 1.2 as the peak intensity increases from

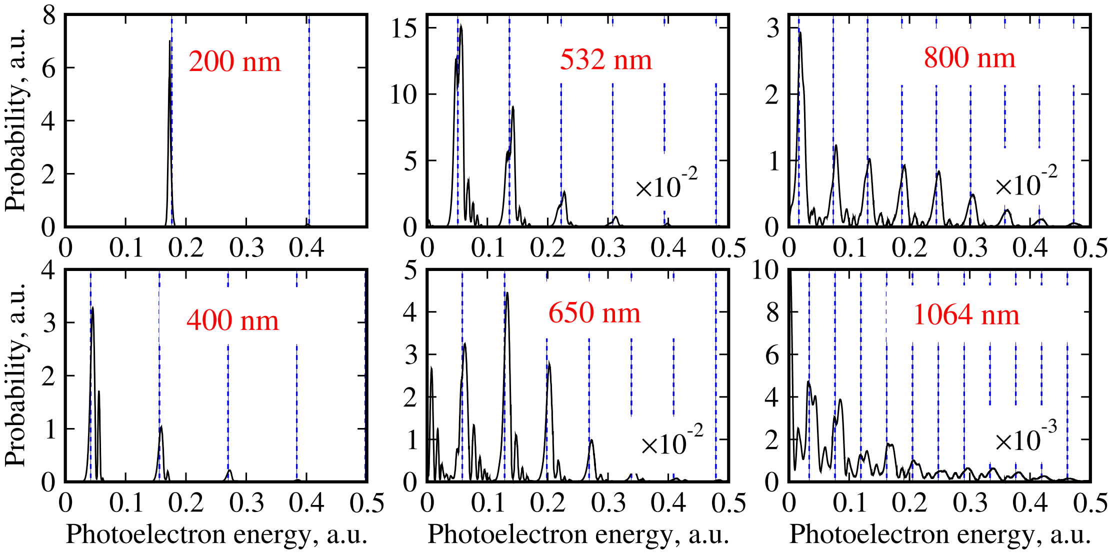

Figure 6.4.: Photoelectron energy spectra of an H atom exposed to a Gaussian laser pulse with a peak intensity of 5×10^{13} W/cm^2 and a duration of 20 fs (FWHM) for various values of the wavelength. Blue dashed lines indicate the expected spectral peak positions given by the energy conservation law including the dynamic energy shifts.

10^{12} W/cm^2 to 2×10^{14} W/cm^2. As is apparent in Fig. 6.3, although the spectrum tends to one characteristic for tunneling ionization (a smooth decay without prominent peaks), at intermediate values ($\gamma \approx 1$) multiphoton effects still play an important role.

6.2.2. Influence of the laser frequency

A gradual transition from the multiphoton to the tunneling (or above-the-barrier) ionization regime may also be observed by increasing the radiation wavelength. This is demonstrated in Fig. 6.4 where the laser wavelength has been varied in the range from 200 nm to 1064 nm with the peak intensity and the pulse width held constant. Such a variation corresponds to a progressive decrease of γ from 6.0 to 1.1. Similar to Fig. 6.3, as the laser wavelength increases, the number of well-resolved spectral peaks also increases and their positions shift towards lower energies. The latter in turn gives rise to channel closings. Unlike the previous study, this shift originates not only from an increase of the dynamic energy shift but also from a decrease of the photon energy. Because of the latter, the peak spacing diminishes as well. In view of the existing substructures and the finite width of the peaks, for higher wavelength (e.g., 1064 nm) this results in complex energy spectra due to the interference between the overlapping peaks. The relation

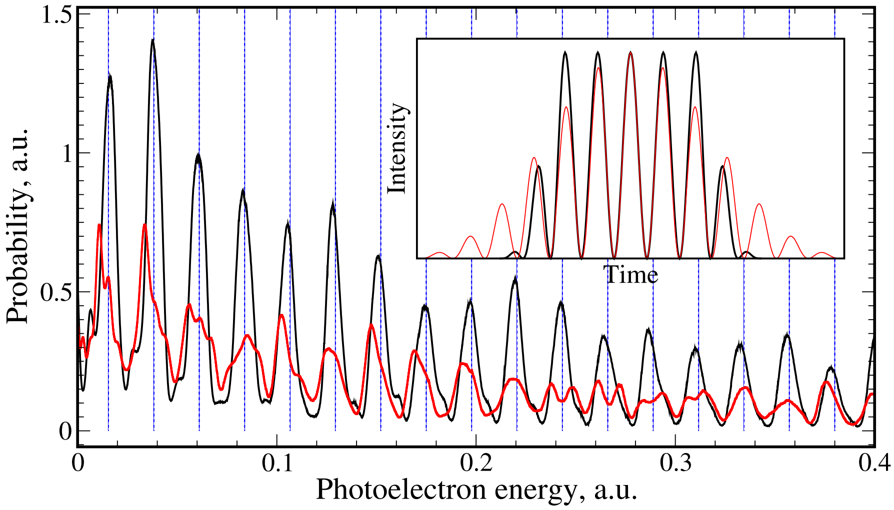

Figure 6.5.: Photoelectron energy spectra of an H atom exposed to 2000 nm laser pulses with a peak intensity of 1.5×10^{14} W/cm^2 and different pulse envelopes: top-flat pulse with 2 cycle flat part and one cycle up- and down-ramp (black) as well as 8-cycle cos^2-shaped pulse (red). The insert shows the corresponding time-dependent intensity of the pulses. Blue dashed lines indicate the expected peak positions given by the energy conservation law including the dynamic energy shifts.

between the heights of neighboring peaks shows non-obvious behavior. For example, at a wavelength of 650 nm the second peak is noticeably higher than the first one whereas for 532 nm and 800 nm the first peak dominates.

An important point to address is whether or not the peaks disappear with a further increase of the laser wavelength which corresponds to going deeper into the tunneling regime. In order to comment on this issue, consider the case (Fig. 6.5) where 113 photons or more are required for ionization and the Keldysh parameter is $\gamma = 0.35$. Although the H atom undergoes the ionization deep in the tunneling regime, pronounced ATI peaks can still be observed, strictly at the expected positions for the top-flat pulse. The cos^2-shaped pulse with a similar duration (see the insert of Fig. 6.5) yields on the other hand a rather a different energy spectrum. The peaks are much less resolved and their positions differ from the expected ones. (A further decrease of γ does not change the situation.) Even though the heights of the peaks yielded by a top-flat pulse are varying slowly from one peak to another, the peaks remain to be well resolvable for sufficiently long pulses and become even narrower for longer pulses. A remarkable feature of such spectra is the virtual absence of substructures, which one can observed for pulses with similar envelopes but smaller wavelength. This indicates that resonances

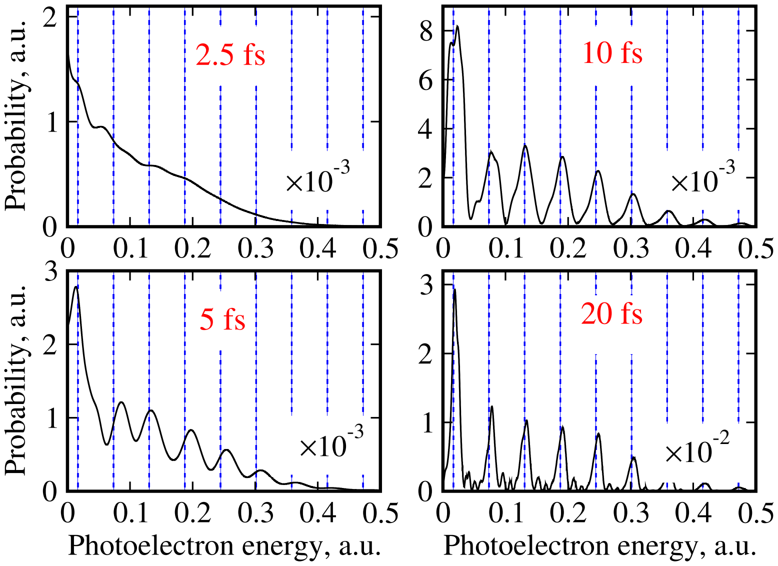

Figure 6.6.: Photoelectron energy spectra of an H atom exposed to an 800 nm Gaussian laser pulse with a peak intensity of 5×10^{13} W/cm^2 for various values of pulse duration (FWHM). Blue dashed lines indicate the expected spectral peak positions given by the energy conservation law including the dynamic energy shifts.

play no role in the ionization process. Because of the latter, the spectra obtained deep in the tunneling regime are especially appropriate for a demonstration of the validity of the energy conservation law. Thus, the important condition required to obtain an almost continuously decaying spectrum (which is usually associated to the spectrum in the tunneling regime) is an intensity variation due to the pulse envelope which changes U_p from cycle to cycle.

6.2.3. Influence of the pulse duration

The pulse duration is another parameter which is particularly relevant when distinguishing between multipeaked and continuous photoelectron energy spectra. Its significance is revealed in Fig. 6.6 which shows the spectra for four different pulse durations in the range from 2.5 fs to 20 fs (compare to the optical cycle period of 2.6 fs for the used 800 nm pulse). As is apparent in Fig. 6.6, with increasing pulse duration the character of the spectra changes drastically from continuous to multipeaked. This transition evidently depends on the widths of the spectral peaks which are in turn related to the Fourier width of the pulse (Sec. D.4). The relation between the spectral width of the peaks and the Fourier width of the pulse in the case of multiphoton ionization is not trivial and may depend on the order of the multiphoton process [186].

Noteworthy, the photoelectron spectrum for 5 fs exhibits peaks whose positions are shifted from the expected ones. This feature is typical for rather short (few-cycle) pulses. Because of the strong nonlinearity of the multiphoton ionization process, the less probable absorption of photons with energies below (or above) the carrier photon energy may result in greater photoelectron yields.

6.2.4. High-energy plateau in ATI spectra

One of the main single-electron features of the ATI spectra is a kind of plateau formed by the high-order ATI peaks. A typical photoelectron energy spectrum consists of an exponential decay from zero energy to about $2U_p$, followed by a plateau extending up to $10U_p$ and ending with a sharp cut-off. This well-known structure has been extensively studied in the past and is understood in terms of direct ionization and rescattering processes. Within the Simpleman model [121, 122] it is assumed that the electron is released with zero velocity and thus its final kinetic energy is equal to $A(t_0)^2/2$, where A is the vector potential and t_0 is the time of the release. Therefore, the electron can gain the maximal energy $A^2_{\text{max}}/2 = 2U_p$ (Simpleman limit), if it is released at the time when the electric field is almost zero. On the other hand, if the electron is released at the maximum of the electric field, its final kinetic energy is almost zero. It is also assumed that the probability of the electron release depends exponentially on the value of the electric field at the release time. Thus, the model predicts an exponential decay from zero to near $2U_p$ energy arising from direct ionization. Depending on the initial time t_0 the electron may return to the ion core, scatter elastically by some angle θ and is then further accelerated by the laser field. The energy of the emerged photoelectrons depends on both t_0 and θ and reaches the maximal value $10U_p$ (rescattering limit) in the case of backscattering ($\theta = \pi$), if the release occurs after the maximum of the electric field with the delay time of 4.15% of the cycle period [187]. Thus, a simple classical rescattering model is able to explain the occurrence of the plateau and a sharp cut-off at $10U_p$. However, the plateau electron spectra are not always similar for different targets and their structure may depend on the laser intensity. A more comprehensive analysis requires a quantitative rescattering theory [188].

The presence of the high-energy plateau in the photoelectron energy spectra of the H atom is reflected in Fig. 6.7. Energy spectra for four different pulses with the same $U_p = 0.39$ a.u. are shown in Fig. 6.7 a. The plateau begins at almost the same energy

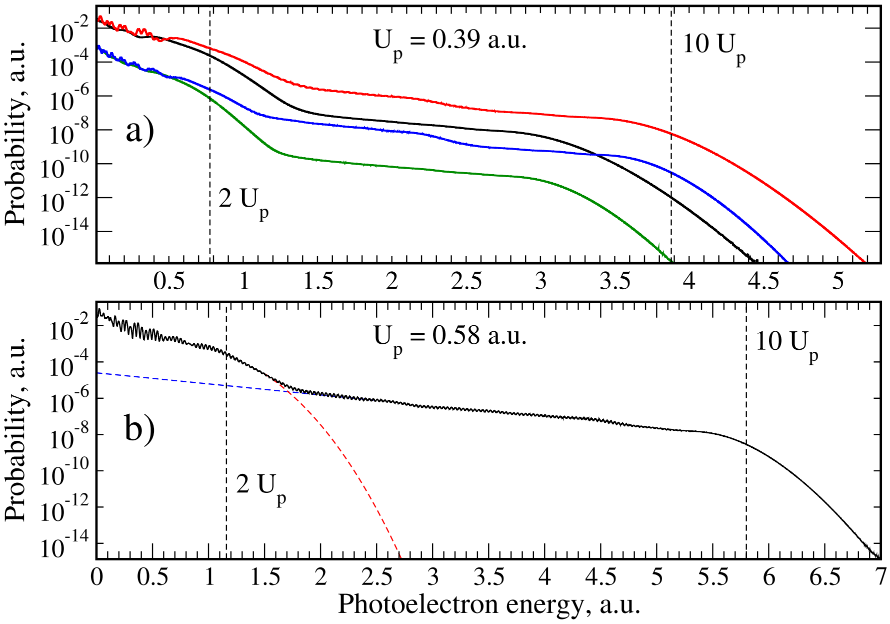

Figure 6.7.: Photoelectron energy spectra of an H atom exposed to (a) a 2-cycle (green curve) and a 4-cycle (blue) $\cos^2$-shaped 1500 nm laser pulse with a peak intensity of 5×10^{13} W/cm^2, a 2-cycle (black) and a 4-cycle (red) $\cos^2$-shaped 1064 nm laser pulse with a peak intensity of 10^{14} W/cm^2 (b) a 6-cycle $\cos^2$-shaped 1300 nm laser pulse with a peak intensity of 10^{14} W/cm^2. The contributions of the direct and the rescattered electrons are shown schematically by the dashed red and blue curves, respectively.

(about $3U_p$) in all presented spectra, the cut-off however occurs earlier for the shorter (2-cycle) pulses compared to the longer (4-cycle) pulses. This effect can also be explained classically. Indeed, the electron requires some time to acquire energy before and after the recollision. For shorter pulses the pulse envelope results in a faster decrease of the pulse intensity and prevents the electron to acquire the same amount of energy as for longer pulses. Another interesting feature is a strong dependence of the plateau height on the pulse duration. As is apparent in Fig. 6.7 a, the direct ionization probability is almost the same (on the log scale) for shorter and longer pulses, whereas the plateau height is substantially enhanced for longer pulses.

The energy spectrum for $U_p = 0.58$ a.u. and an even longer (6-cycle) pulse is presented in Fig. 6.7 b, where the contributions of direct and rescattered electrons to the spectrum are shown explicitly. The cut-off energies which can be extracted from these contributions agree very well with their corresponding classical values of $2U_p$ and $10U_p$.

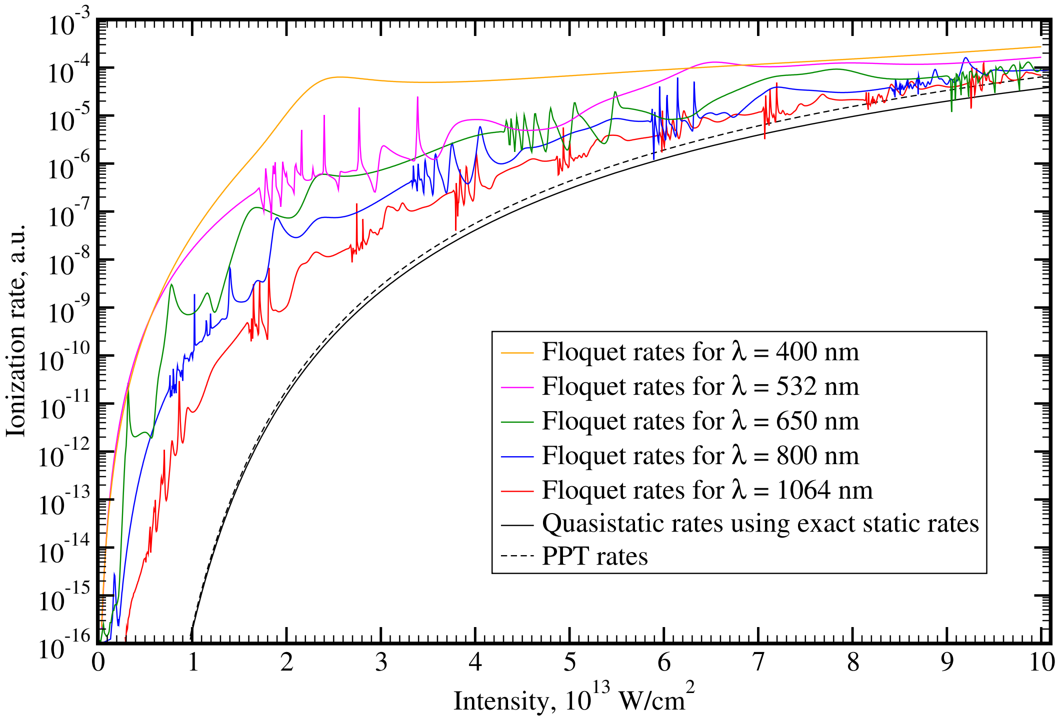

Figure 6.8.: Ionization rates of an H atom vs. radiation intensity. Ionization rates obtained by solving the Floquet equations for different radiation wavelengths are compared to quasistatic rates obtained from exact static rates and using the Popov-Peremolov-Terent'ev formula (5.83) .

6.3. Ionization rates

Consider now the dependence of the ionization rates for the H atom on frequency and intensity of the laser field. Figure 6.8 shows the results of Floquet calculations performed for laser intensities up to 10^{14} W/cm^2 using the laser wavelengths $\lambda = 400, 532, 650, 800$ and 1064 nm. As can be seen from Fig. 6.8, the dependence of the ionization rates on intensity exhibits resonant structures occurring due to the multiphoton coupling of the ground state to Stark-shifted excited states. For a given wavelength the ionization rate primarily increases with increasing radiation intensity, but the slope (on the log scale) becomes smaller. Furthermore, for a given intensity the ionization rate mainly decreases with increasing radiation wavelength and tends to the corresponding quasistatic ionization rate. The latter is very well approximated by the Popov-Peremolov-Terent'ev (PPT) formula (5.83) for smaller intensities, whereas for higher intensities PPT rates evidently overestimate the correct quasistatic rates.

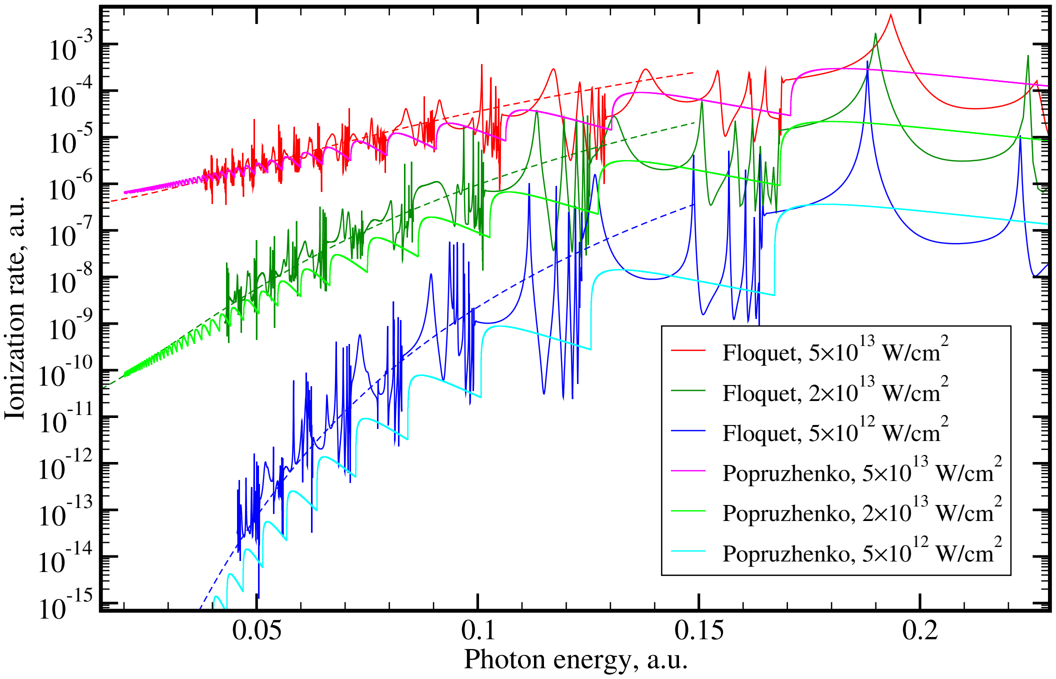

Figure 6.9.: Ionization rates of an H atom vs. photon energy. Ionization rates obtained by solving the Floquet equations for different radiation intensities are compared to ionization rates obtained by using an analytical formula proposed by Popruzhenko *et al.* [189]). Dashed curves indicate the results obtained with Eq. (6.6).

A strong dependence of the ionization rates on the laser wavelength and a substantial deviation from the quasistatic limit (apparent in Fig. 6.8 for small intensities) indicate the multiphoton character of the ionization process. As the intensity increases, the ionization rates depend less on the laser wavelength and the deviation from the quasistatic rate gets smaller. This indicates that the ionization gradually changes its character from multiphoton to quasistatic ionization.

Figure 6.9 presents another view on this transition. It shows Floquet rates for three different radiation intensities plotted as a function of photon energy. As in the previous study, REMPI resonances are clearly visible and the ionization rate may vary by orders of magnitude in a small range of photon energies. Note the evident shift (in the range 0.1 to 0.2 a.u.) of the REMPI peaks towards higher photon energies with increasing radiation intensity, especially well visible for the strong resonances with positions at about 0.19 a.u. Although it makes it difficult to find universal behavior of ionization rates, a general trend is well apparent. Whereas for an intensity of 5×10^{12} W/cm^2 the ionization rate substantially decreases (by 7 orders of magnitude) with decreasing

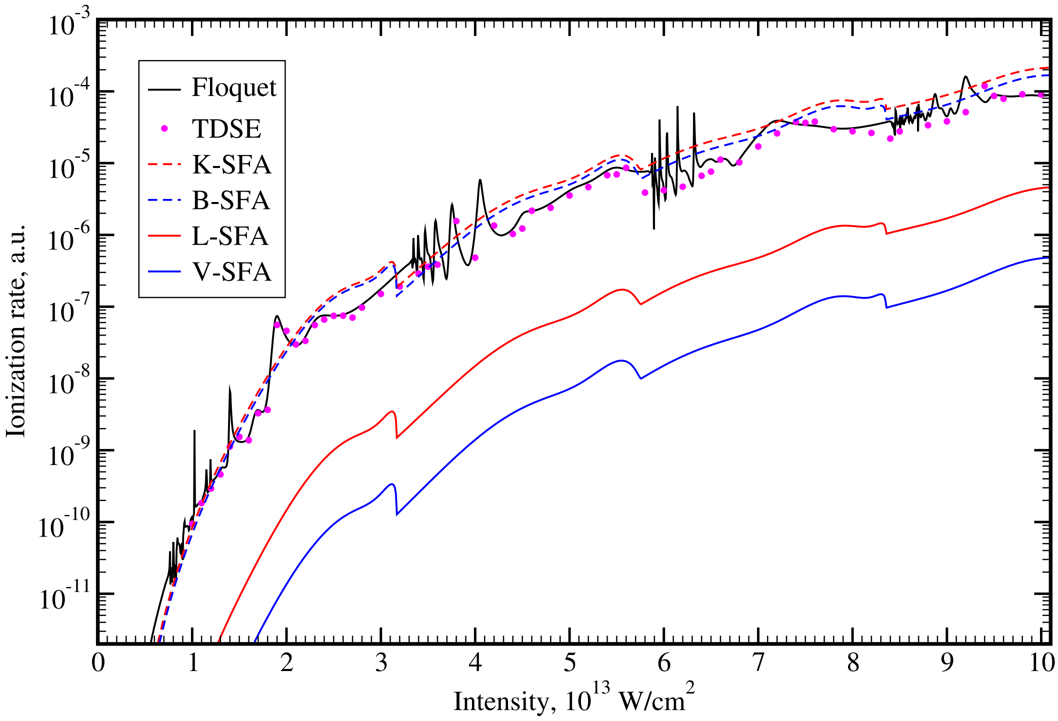

Figure 6.10.: Ionization rates of an H atom for an 800 nm laser field vs. laser intensity. Floquet results are compared with ionization rates yielded by the TDSE method, L-gauge SFA (L-SFA), L-gauge SFA with Krainov's Coulomb correction (K-SFA), V-gauge SFA (V-SFA), and V-gauge SFA with the Coulomb correction of A. Becker *et al.* (B-SFA).

photon energy, the slope of the decrease diminishes with increasing radiation intensity. Surprisingly, for sufficiently low photon energies a very accurate estimation of the slope dependence on photon energy and intensity is provided by a simple correction $C_{\rm cor}$ to the quasistatic rates $\Gamma_{\rm QS}$,

$$\Gamma_{\rm cor} = C_{\rm cor}\Gamma_{\rm QS}, \qquad C_{\rm cor} = \exp\left[\frac{2}{3F}\Big\{1 - g(\gamma)\Big\}\right], \tag{6.6}$$

where the function g, defined as

$$g(\gamma) = \frac{3}{2\gamma}\left\{\left(1+\frac{1}{2\gamma^2}\right)\mathrm{arcsinh}\gamma - \frac{\sqrt{1+\gamma^2}}{2\gamma}\right\}, \tag{6.7}$$

has been introduced by Perelomov *et al.* [95]. A comparison with the recently proposed Coulomb-corrected short-range ionization rates [189] shows a reasonable agreement in the whole range of the photon energies, although the resonances are not described and

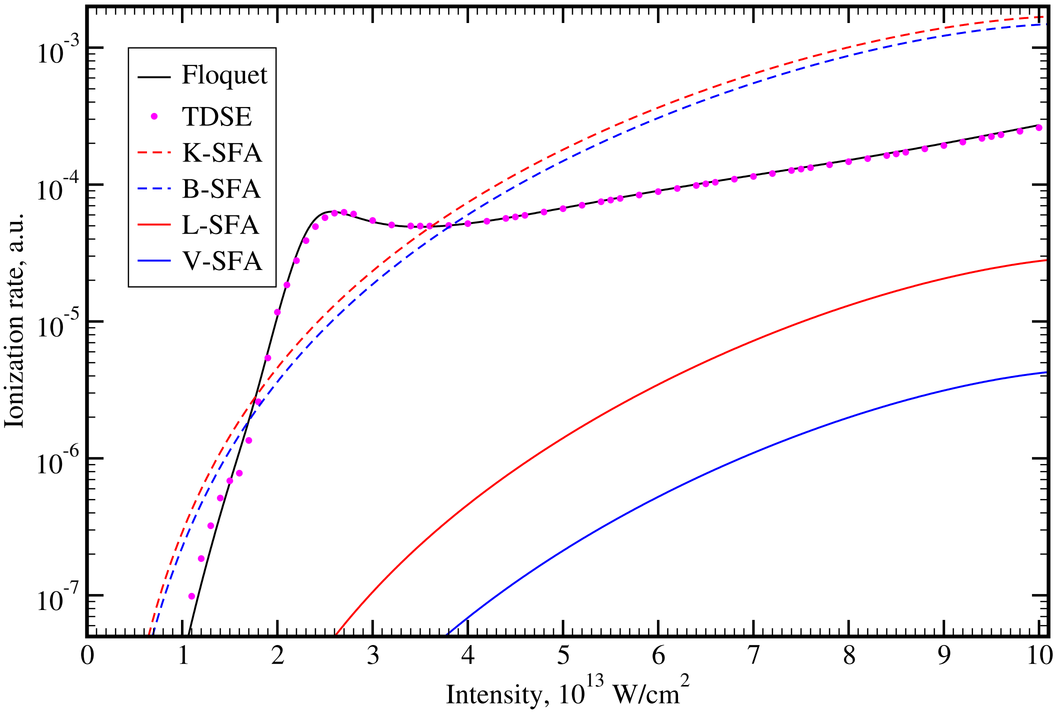

Figure 6.11.: The same as Fig. 6.10 but for an 400 nm laser field.

a slight underestimation can be observed for smaller intensities in the low-energy part of Fig. 6.9, most likely due to the matching technique applied in [189, 190][3].

It is instructive to compare the Floquet ionization rates with the ones obtained using the TDSE method (as discussed in Sec. 6.1.1) and various SFA implementations. Such a comparison is presented in Fig. 6.10 for an 800 nm laser field. Besides the traditional L-gauge and V-gauge SFA, L-gauge SFA with the Coulomb correction of Krainov [192] as well as V-gauge SFA with the Coulomb correction of A. Becker *et al.* proposed in [168] are presented as well.

The largest deviation from the Floquet results (about 3 orders of magnitude) is found for the result of the V-gauge SFA. The L-gauge SFA results are roughly two orders of magnitude smaller than the Floquet ionization rates, whereas the Krainov and A. Becker *et al.* corrections yield ionization rates which are in a very good agreement with the exact result. Finally, the agreement with ionization rates provided by the TDSE

---

[3] The present calculation uses the Coulomb correction defined by Eq. (25) in [189] instead of its approximate version given by Eq. (5) in [190]. The latter yields by about a factor of 2 smaller results for $\gamma \approx 1$. Note, the numerical results presented in [190] were also obtained using the Coulomb correction defined by Eq. (25) [191].

method is almost excellent disregarding small deviations caused by resonances.

Since SFA models do not take into account excited bound states of the H atom, the agreement of the Coulomb corrected SFA models with the exact result becomes worser for those laser parameters at which ionization occurs via an intermediate resonant state. An example of such a situation is presented in Fig. 6.11 where the same type of comparison as in Fig. 6.10 is carried out, but for an 400 nm radiation field. The Floquet ionization rate exhibits a pronounced hump at intensities about $2.5 \times 10^{13}\,\mathrm{W/cm^2}$ which is completely absent in all SFA versions. A more comprehensive analysis shows that this hump is a consequence of (4+1) REMPI through the 4d state. Since the TDSE method takes into account both bound and continuum states, the TDSE rates are again in an excellent agreement with the Floquet rates.

6.4. AC Stark shift of energy levels

In contrast to the shift of the energy levels in a stationary electric field, which is referred to as 'direct-current' (DC) Stark shift, the shift of the levels in a monochromatic electromagnetic field is known as the 'alternating-current' (AC) Stark shift. While the DC Stark shift of atomic levels was discovered by Johannes Stark in 1913 [193], the first observation of the AC Stark effect initiated by laser radiation was made only in 1969 [194]. There are a number of reasons why the AC Stark effect differs dramatically from the DC Stark effect.

The first difference is that while in a static field the perturbation of a nondegenerate bound atomic state reduces to a shift in the energy of that state, in a monochromatic electromagnetic field the initially nondegenerate state is transformed into an assembly of stationary states with the energy difference between adjacent states equal to the energy of the photon of the radiation field (see discussion in Sec. 6.1.2). The second difference is that at a certain frequency of the electromagnetic field a resonance may occur, if this frequency is close to the frequency of a transition from this energy level to another bound state. If this happens, even in a weak electromagnetic field, the resonance level may really become populated. In such a case, Rabi mixing of the energy levels takes place, which is accompanied by a splitting of both the initial and the resonance level into two quasi-energy levels each, where the energy splitting depends linearly on the field strength. This effect is referred to as resonance AC-Stark effect.

Since under laboratory conditions the maximally attainable strength of a DC electric field is by orders of magnitude weaker than the one of a laser field, the DC Stark shift can usually be calculated employing perturbation theory. To the contrary, in a variable laser radiation field the disturbance of a system can be enormous, although the broadening of the levels may remain small. Resonances of a new type may emerge because of this enormous energy shift induced by light. The main peculiarity of such resonances which are referred to as dynamic (or Stark-induced) one- or multiphoton resonances is that for a given frequency of the laser field they occur only within some intensity interval.

6.4.1. Dynamic dipole polarizability

In second-order perturbation theory (PT) the AC Stark shift of a state a is given by

$$\delta E_a(\omega) = -\frac{\alpha_a(\omega)}{4} I \tag{6.8}$$

where α_a is the dynamical dipole polarizability and I is the field intensity. The value of α_a can be found as

$$\alpha_a(\omega) = 2 \sum\!\!\!\!\!\!\!\int_{k \neq a} \frac{|D_{ka}|^2 \omega_{ka}}{\omega_{ka}^2 - \omega^2} \tag{6.9}$$

where ω_{ka} (D_{ka}) is the frequency (dipole matrix element) of a transition from the initial state a to an intermediate state k. In the low-frequency limit the dynamical dipole polarizability $\alpha_a(\omega)$ reduces to the static dipole polarizability $\alpha_a = \alpha_a(0)$.

Fig. 6.12 shows the frequency dependence of the dynamic dipole polarizability for the ground state of the H atom. As is demonstrated in Fig. 6.12 a, the dynamic polarizability has poles if the radiation frequency coincides with the frequencies of allowed dipole transitions to excited states. For small frequencies the polarizability can be well approximated using the following analytical expression[4]

$$\alpha_{1\mathrm{S}}(\omega) = \frac{9}{2} + \frac{319}{12}\omega^2 + \frac{297541}{1728}\omega^4 + \dots \tag{6.10}$$

which is tested in Fig. 6.12 b for $\omega < 0.17$ a.u. As can be seen, the approximation (6.10) works very well for $\omega < 0.12$ a.u. and thus for $\lambda > 400$ nm.

At frequencies exceeding the binding energy of a circular state[5], the dynamic dipole polarizability of this state rapidly tends to the asymptotic value $\alpha(\omega) \to -\omega^{-2}$, so that

---

[4] The expression is obtained by making Taylor expansion of Eq. (6.9) and performing the summation (integration) for the first three terms.

[5] state (n, l) with $l = n - 1$

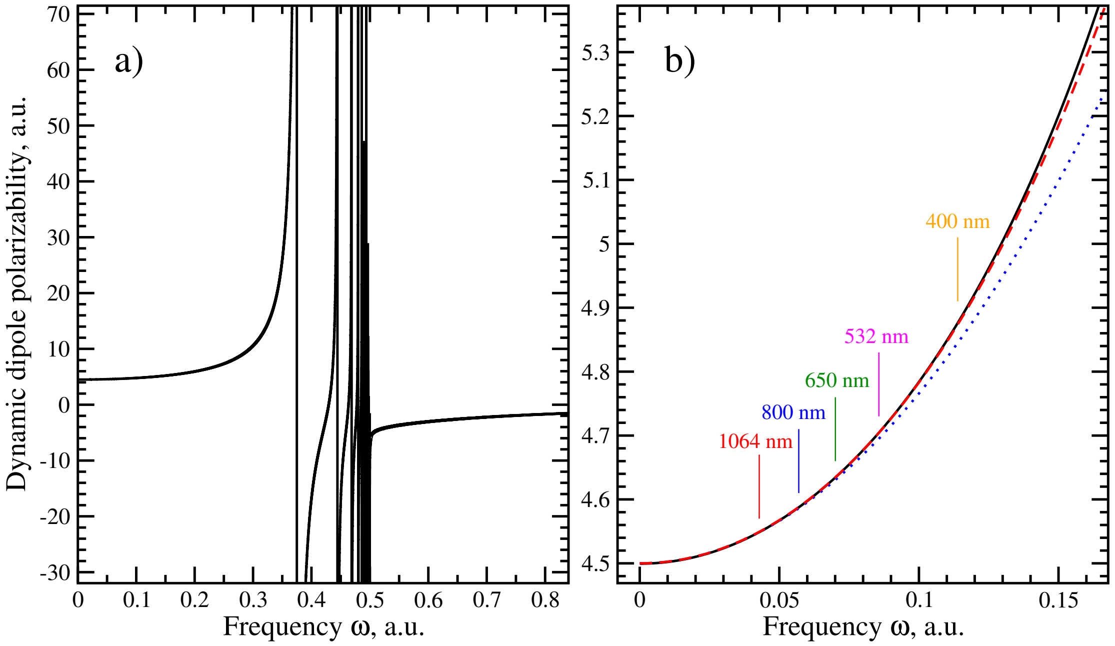

Figure 6.12.: Frequency dependence of the dynamic dipole polarizability for the ground state of an H atom. a) The dynamic polarizability has poles if the radiation frequency coincides with the frequencies of allowed dipole transitions to excited states. b) Exact value (solid line) is compared at low frequencies to the approximate analytical expression (6.10) including either only ω^2 term (dotted line) or additionally also the ω^4 term (dashed line)

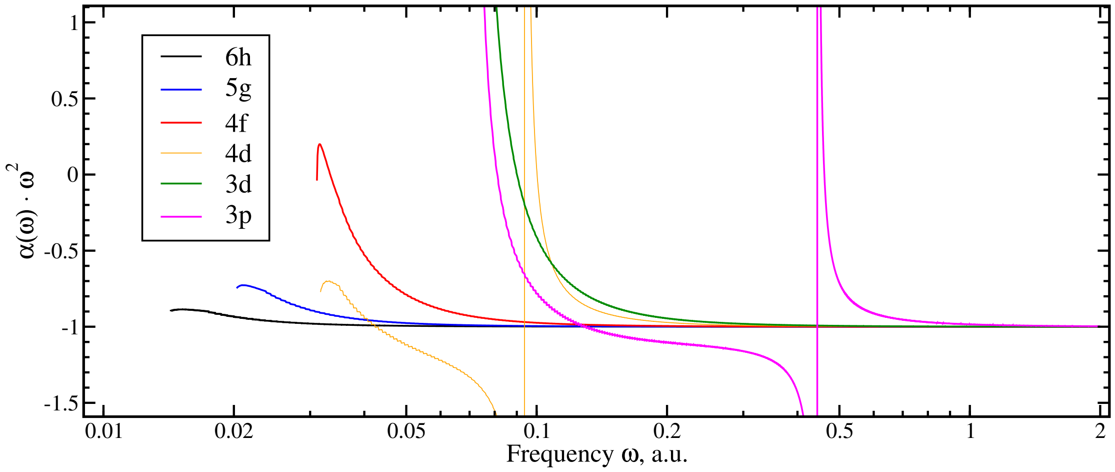

Figure 6.13.: Dynamic dipole polarizability (scaled by factor ω^2) of some excited states of a H atom as a function of radiation frequency ω.

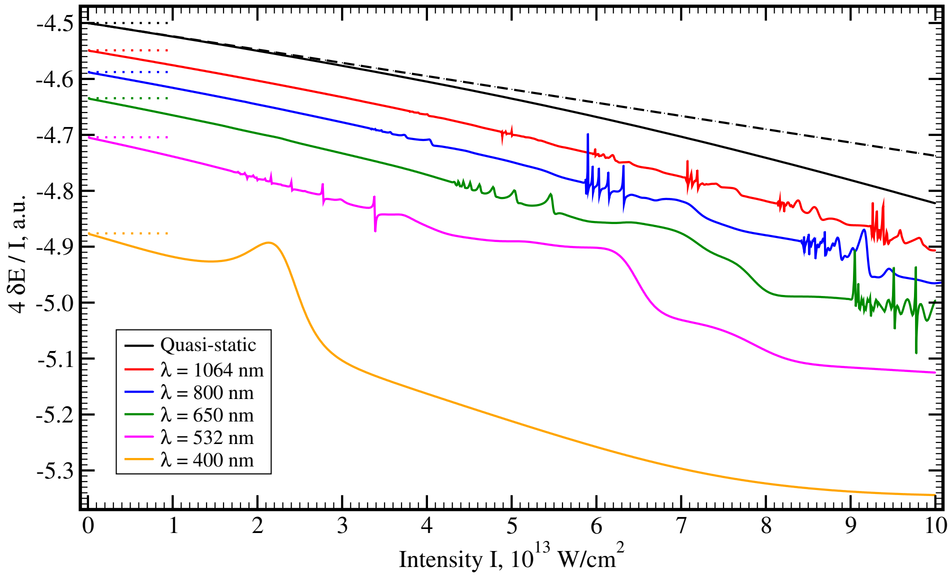

Figure 6.14.: Scaled AC Stark shift δE of the 1S state of a H atom as a function of field intensity I. The results for different wavelengths are obtained from the complex quasienergy of the Floquet state as $\delta E = \mathrm{Re}\{E\} - E_0$ (colored solid lines) and compared in the low-intensity limit to the corresponding dynamic dipole polarizabilities multiplied with -1 (colored dotted lines). The result in the quasi-static limit (black solid line) is compared to the PT prediction (black dashed line) given by Eq. (6.11)

the AC Stark shift of this state tends to the ponderomotive energy $\delta E(\omega) \to I/(4\omega^2) = U_p$. Scaled dynamic dipole polarizabilities of circular states with $n = 3-6$ are shown on Fig. 6.13. The behavior of the dynamic dipole polarizability for states with $l \neq n-1$ is more complicated, since there exist resonances due to transitions to lower bound states. In Fig. 6.13, one can observe these resonances for the 3p and 4d states. However, all such resonances appear only for $\omega < [2(|l-1|+1)^2]^{-1}$, and thus for higher frequencies the asymptotic behavior is also valid.

6.4.2. AC Stark shift in the nonperturbative regime

Consider now the AC Stark shift δE of the ground state of the H atom for various intensities and wavelengths of an external laser field. Figure 6.14 presents the intensity dependence of the Floquet AC Stark shift (see Sec. 6.1.2) for 5 different radiation wavelengths in a range from 400 nm to 1064 nm. For a more detailed analysis, the obtained AC Stark shifts δE are scaled with factor $4/I$ to converge to $-\alpha_{1\mathrm{S}}(\omega)$ in the low-intensity limit [as follows from Eq. (6.8)]. In the low-intensity limit the AC Stark shift reduces to

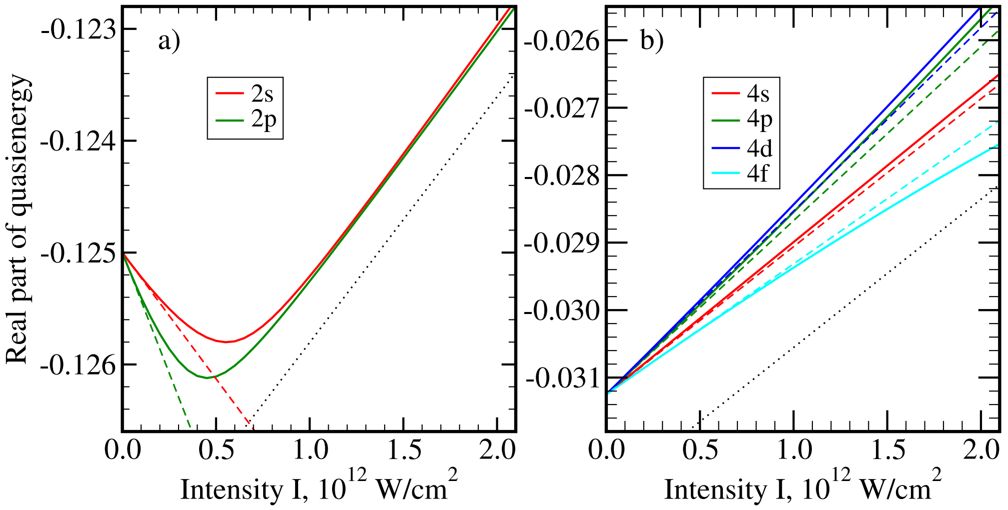

Figure 6.15.: The AC Stark shift (solid curves) for the excited states of the H atom with a) $n = 2$ and b) $n = 4$ in the presence of an 800 nm harmonic field is compared to the corresponding prediction of the second-order PT (dashed lines). The dotted lines show the horizontally shifted ponderomotive energy U_p and serve to guide the eye.

the corresponding dynamic dipole polarizabilities (see Fig. 6.12 b), preliminarily multiplied with -1 for the sake of comparison. For longer radiation wavelengths, the AC Stark shift approaches the quasi-static AC Stark shift obtained by cycle averaging of the complex energy of the Stark resonance. The quasi-static AC Stark shift is in turn compared to the PT prediction (up to fourth order) which reads

$$\delta E_{\mathrm{QS}} = -\frac{9}{8}I - \frac{10665}{512}I^2. \tag{6.11}$$

The narrow resonant structures prominent in Fig. 6.14 originate from the resonant coupling to other excited states and a subsequent uncertainty in the definition of the AC Stark shift (see the discussion related to Fig. 6.2).

In general, for the presented range of parameters, the Floquet AC Stark shift of the ground state differs from the one given by the PT by less than 20 percent. The overall value of the AC Stark shift δE for optical frequencies is quite small and amounts to only about 0.1 eV for a laser intensity of 10^{14}W/cm^2.

The situation is rather different for the excited states of an H atom. Figure 6.15 presents the real part of the quasienergy for the excited states with $n = 2$ and $n = 4$ in an 800 nm radiation field. A comparison with the second-order PT prediction indicates that

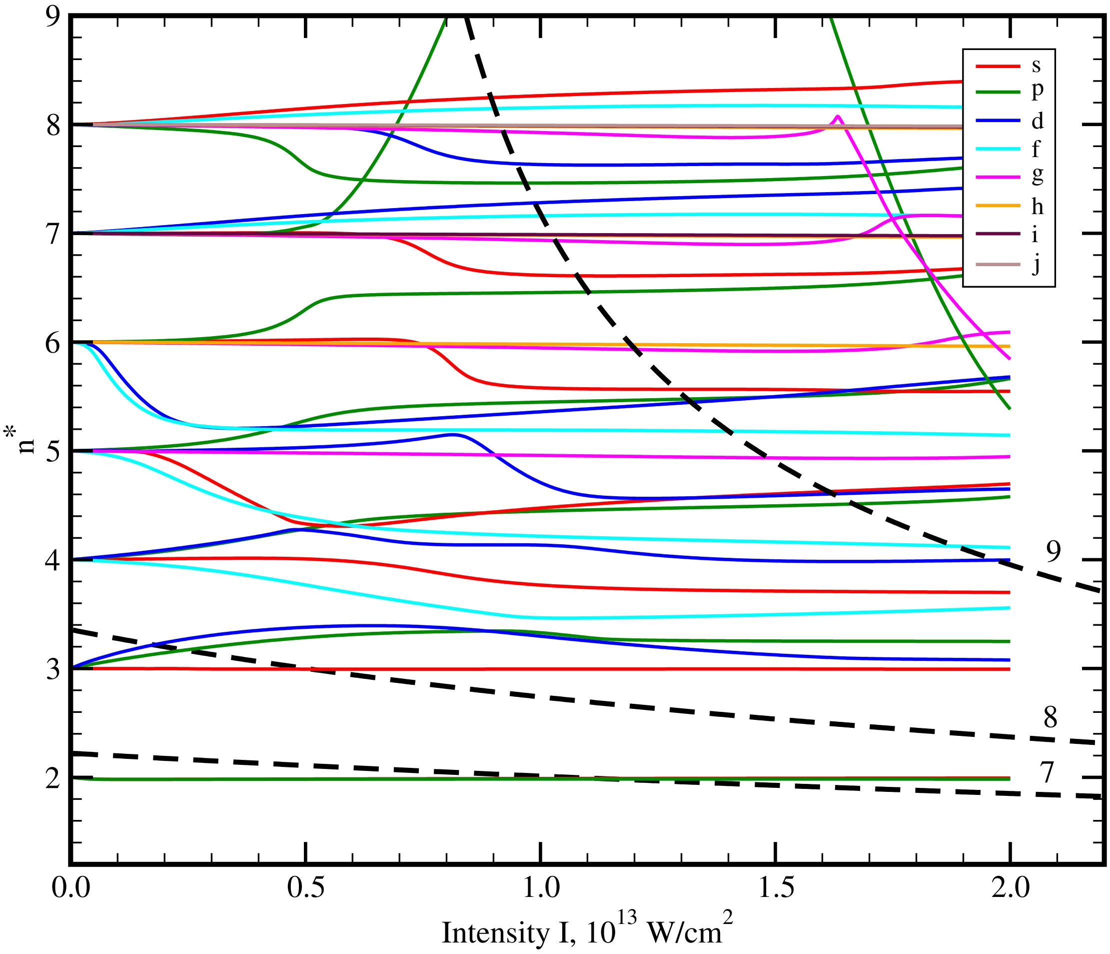

Figure 6.16.: Scaled real part of Floquet energies, $n^*(I) = 1/\sqrt{-(\mathrm{Re}\{E\} - U_p)}$, for the excited states of the H atom with $n \leqslant 8$ in an 800 nm harmonic field. The quasienergy states reducing (in the low-intensity limit) to the atomic bare states with different angular momenta are specified by different colors. The black dashed curves represent the functions $n^*(N, I) = 1/\sqrt{-(\mathrm{Re}\{E_{1\mathrm{S}}\} + N\omega - U_p)}$ for different values of N (explicitly specified on the plot).

the applicability of PT for $n = 2$ states is limited to intensities $I < 2 \cdot 10^{11}\mathrm{W/cm}^2$. For higher intensities the energy of the states increases with a slope similar to the one of the ponderomotive energy U_p. The states with $n = 4$ possess dynamic dipole polarizabilities $\alpha(\omega)$ whose values are approximately equal to $-\omega^{-2}$, so the deviation from the PT prediction is not as significant as for $n = 2$.

As can be inferred from Fig. 6.15, the AC Stark shifts of excited states tend to U_p for higher intensities and n. To substantiate this conclusion, consider the following quantity,

$n^*(I) = 1/\sqrt{-(\mathrm{Re}\{E\} - U_p)}$. It represents the scaled real part of the Floquet energy and has the following two properties. In the low-intensity limit n^* tends to the principle quantum number $n = 1/\sqrt{-\mathrm{Re}E}$ of the state. In the high-intensity limit, provided that n^* is almost independent on the intensity, the AC Stark shift can be approximated as

$$\delta E(I) = U_p(I) - \left[\frac{1}{(n^*)^2} - \frac{1}{n^2}\right] \tag{6.12}$$

where the term in brackets defines an intensity-independent shift. Values of n^* for the excited states with $n \leqslant 8$ in an 800 nm harmonic field are shown in Fig. 6.16. Note that the intensity range in Fig. 6.16 is by a factor of 10 wider as compared to Fig. 6.15. As one can see, the dependence of n^* on intensity is often almost constant. Of course, the simple relation does not work in the case of resonant coupling between excited states which can usually be identified by a fast change of the character of the behavior of $n^*(I)$. On the other hand, for some states, e.g. for 2s, 2p, and 3s, the value of n^* remains almost constant over the whole range of considered intensities.

The functions $n^*(N, I) = 1/\sqrt{-(\mathrm{Re}\{E_{1\mathrm{S}}\} + N\omega - U_p)}$ for different integer values of N are also presented in Fig. 6.16. If the relation $n^*(N, I_r) = n^*(I_r)$ is fulfilled and the function $n^*(I)$ represents a quasienergy state reducing (in the low-intensity limit) to the atomic bare state with the angular momentum l having the same parity as N, the resonant N-photon coupling between the quasienergy state and the 1S state occurs at the intensity I_r.

6.5. Ionization yields

As discussed in Sec. 6.2.3, the total duration of the pulse strongly influences the photoelectron energy spectrum. Its influence on the total ionization yield will now be considered. Figure 6.17 presents TDSE ionization yields for a short (5-cycle) and a long (40-cycle) Gaussian pulse[6]. For the sake of comparison, the ionization yields for the short pulse are multiplied by a factor of 8, that is the ratio of the two pulse durations. If a rate concept is applicable, these scaled ionization yields should agree to the ones for the long pulse. As is apparent in Fig. 6.17, despite showing an overall common trend, the ionization yields differ markedly except for the case of single-photon ionization. This is a manifestation of the nonlinearity of the multiphoton ionization. One of the prominent

---

[6] The used pulse-duration convention for a Gaussian pulse is non-standard. The exact definition of N-cycle Gaussian pulse is given in Sec. D.2. Here and in the following A-based pulses are used.

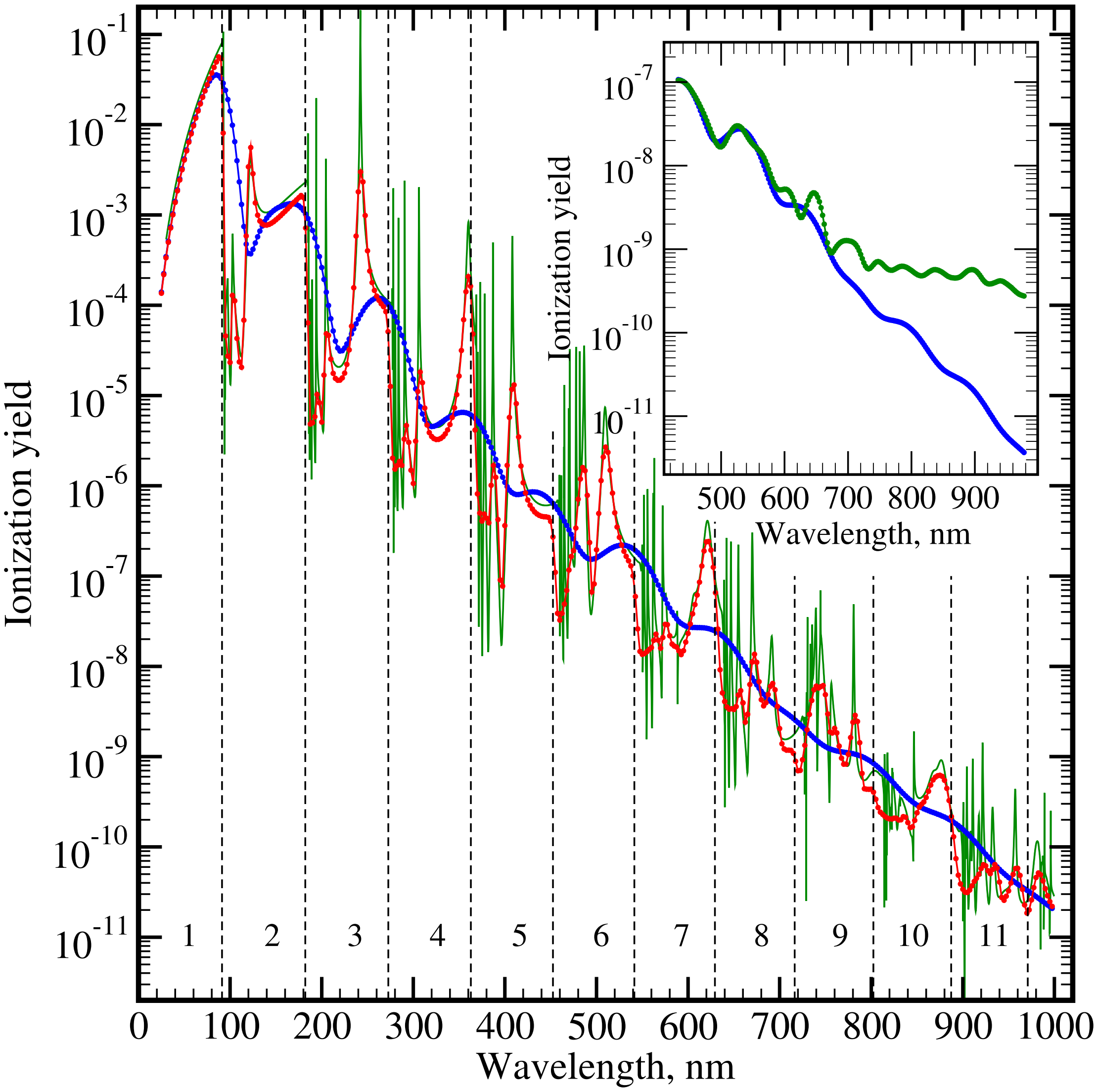

Figure 6.17.: Ionization yield of an H atom as a function of the laser wavelength for a Gaussian pulse with the peak intensity 5×10^{12} W/cm^2. The red curve shows the result for a 40-cycle pulse, whereas the blue curve presents the result for a 5-cycle pulse, multiplied by a factor of 8. The green curve depicts the Floquet ionization rates multiplied by the 'effective' pulse duration (see the text for details). The N-photon ionization thresholds are depicted by dashed vertical lines, with N explicitly indicated in the graph. The insert demonstrates the effect of the pulse envelope on the final result by comparing the ionization yields for a 5-cycle Gaussian pulse (blue curve) and a 5-cycle cos^2-shaped pulse (green curve).

differences between the laser-wavelength dependence of the two ionization yields is their different behavior in the proximity of ionization thresholds. The ionization yields of the long pulse show a sharp decrease when the N-photon ionization channel closes with increasing radiation wavelength. This sharp decrease is about 3 orders of magnitude for $N = 1$ and can still be well resolved for $N < 7$. The ionization yields of the short pulse also exhibit a decrease for small N which is, however, far from being as sharp as for the long pulse. In fact, for longer wavelengths the dependence of the ionization yield on the wavelength becomes almost structureless and tends to a monotonous decrease. The ionization yields for the long pulse show on the other hand prominent resonant structures. It is instructive to compare these resonant structures with those exhibited by Floquet ionization rates. For a consistent comparison, the Floquet ionization rates are multiplied with the 'effective' pulse duration t_{eff} defined as

$$t_{\text{eff}} = 40T_c/\sqrt{\pi(1/2 + \lambda/\lambda_0)} \tag{6.13}$$

where T_c is the cycle period and $\lambda_0 = 91.1\,\text{nm}$ is the threshold of single-photon ionization. The concept of an 'effective' pulse duration can be understood by considering the ratio of the total ionization yield in a Gaussian pulse with the intensity profile $I(t) = I_{\text{peak}} \exp\left\{-(t/t_{\text{sc}})^2\right\}$ to the peak ionization rate Γ_{peak} provided that the ionization rate Γ depends on the laser intensity as $\Gamma = \Gamma_{\text{peak}}(I/I_{\text{peak}})^N$, where N is the number of photons required for ionization and $t_{\text{sc}} = T_{\text{FWHM}}/\sqrt{2\ln 2}$. After some straightforward algebra the desired result is $\sqrt{\pi/N}t_{\text{sc}}$. By definition, t_{sc} equals $40T_c/\pi$ for the long pulse. Equation (6.13) is then obtained replacing N by an approximate but continuous expression $(1/2 + \lambda/\lambda_0)$.

As can be seen from Fig. 6.17, all broader REMPI peaks prominent in the TDSE ionization yields perfectly agree with those found also in the scaled Floquet ionization rates. In contrast, numerous narrower REMPI peaks (especially those caused by resonantly shifted Rydberg states) which prevail in the Floquet results are absent in the TDSE results. This indicates that the transition strength for such resonances is weak and thus even longer pulses are required to observe them.

Ionization yields in few-cycle pulses may strongly depend on the pulse envelope. The insert in Fig. 6.17 shows a comparison of the ionization yields for a 5-cycle Gaussian and a 5-cycle $\cos^2$-shaped pulses. These pulses have an identical high-intensity part of the pulse and differ only in the low-intensity part. Nevertheless, although the ionization yields for the Gaussian pulse continue to decrease with increasing laser wavelength with an almost constant slope (on the log scale), the slope of decrease for the $\cos^2$-shaped

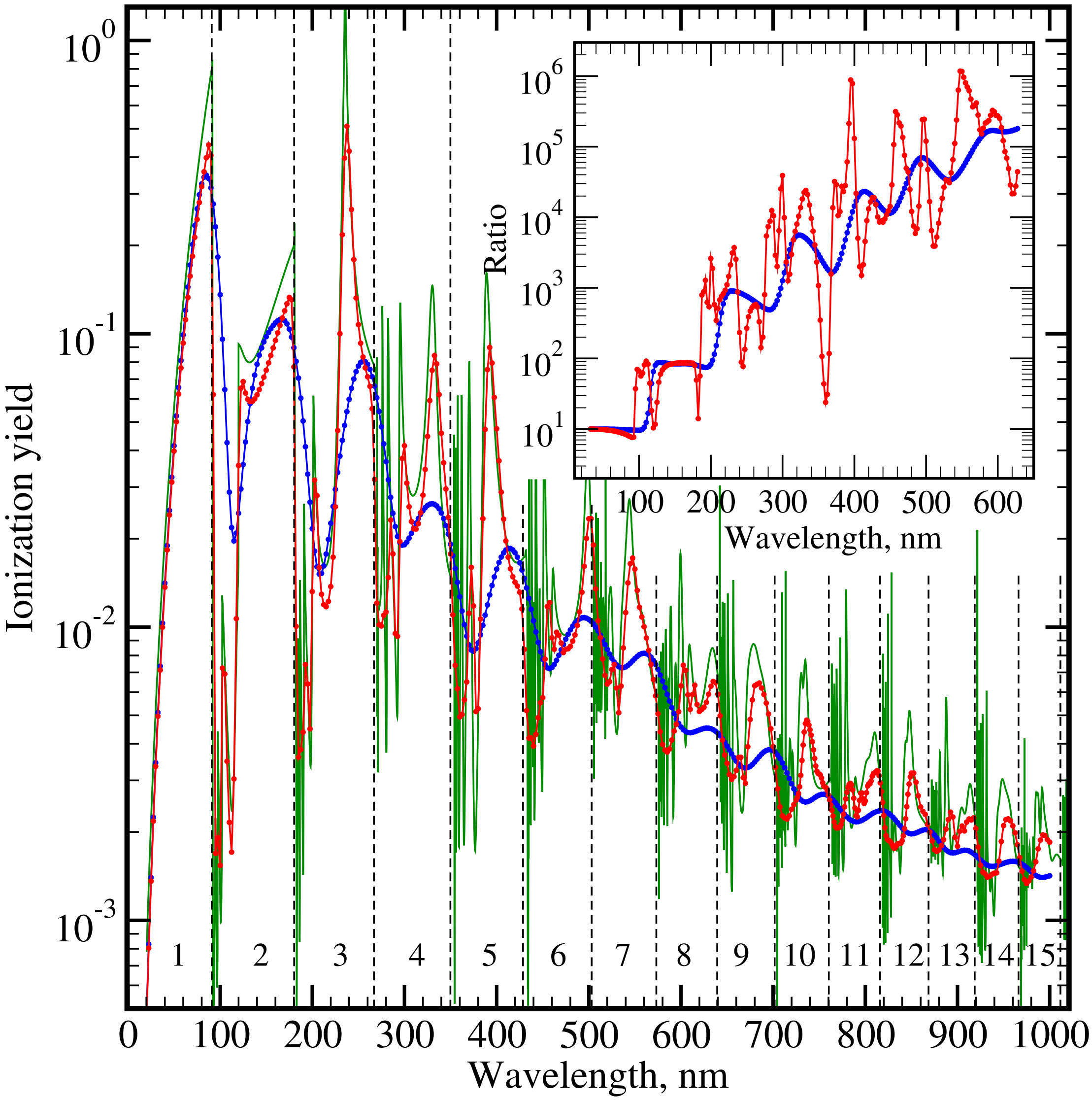

Figure 6.18.: As Fig. 6.17 but for the peak intensity 5×10^{13} W/cm^2. The insert shows the ratio between the ionization yields for this peak intensity and the peak intensity 5×10^{12} W/cm^2 [the red (blue) curve depicts the ratio for the 40-cycle (5-cycle) pulses].

pulses shows a drastic change at about 700 nm. This effect is related to the anomalous ionization efficiency observed in [195] and originates from the much broader spectral wing of a cos^2-shaped pulse compared to a Gaussian pulse with the same pulse duration. In the low-intensity region where multiphoton ionization is the dominant ionization mechanism, the extremely broad spectral bandwidth of the pulse gives rise to the opening of ionization channels accessible with a lower number of photons whose contribution may dominate the one of the main ionization channel due to the high nonlinearity of multiphoton ionization.

For the examined range of laser wavelengths (Fig. 6.17), the ionization yield varies over ten orders of magnitude. As the pulse intensity increases, the dependence on the laser wavelength becomes less pronounced. Thus, at a peak intensity of 5×10^{13} W/cm^2 the ionization yields vary only over two orders of magnitude (Fig. 6.18). Nevertheless, all conclusions drawn for the intensity 5×10^{12} W/cm^2 regarding the influence of the pulse duration hold also for the intensity 5×10^{13} W/cm^2.

It is instructive to examine the ratio of the ionization yields for these two intensities for both pulse durations that have been considered so far. Such a ratio is presented in the insert of Fig. 6.18. Assuming that perturbation theory is applicable, the ratio would be expected to be equal 10^N. As can be seen, for one- and two-photon ionization the observed ratios are basically in accordance with the PT prediction. However, the step from 10^1 to 10^2 occurs for the short pulse at higher wavelengths reflecting the fact that one-photon ionization is still dominant in the range 91 to 110 nm due to the broad spectral width of the short pulse. In contrast, this step is sharp for the long pulse. However, there is a pronounced dip at 120 nm caused by a strong resonance at the intensity 5×10^{12} W/cm^2, which is only weakly resolved at the higher intensity. For longer wavelengths the ratios become smaller than expected manifesting the breakdown of perturbation theory. A distinctive feature of the ratio for the short pulse is its relative smoothness compared to the one for the long pulse. The latter exhibits pronounced peaks and dips. Besides the already mentioned different response to resonant ionization such structures also result from the field-induced shift of the ionization thresholds and the resonance positions (remember the discussion of Fig. 6.9). Thus, the observed ratio at 360 nm amounts to about 30 (local minimum in the insert of Fig. 6.18) instead of the expected value of 10^4-10^5, whereas at 390 nm it amounts to 10^6 instead of the expected value of 10^5. These structures are absent in the ratio for the short pulse. This comparative analysis demonstrates the importance of the pulse duration for the discussion of the strong-field response in the multiphoton regime.

Valuable information on the details of the ionization response can be inferred from the analysis of the residual population of excited states as well as the partial ionization yields Y_l where l is the angular momentum. An example of such an analysis is presented in Fig. 6.19. It examines in detail the two- to four-photon regime for the same peak intensity as in Fig. 6.18 using however a 60-cycle pulse instead of a 40-cycle pulse. A sharp peak at 236 nm which is prominent also in Fig. 6.18 is obviously caused by (2+1)

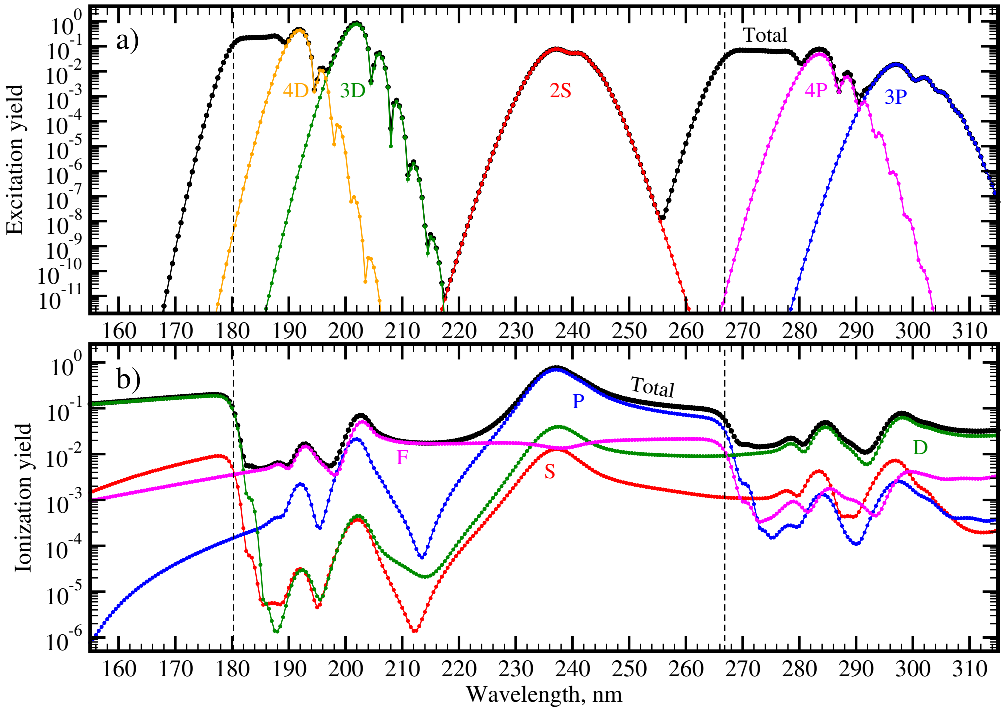

Figure 6.19.: Ionization and excitation yield of an H atom as a function of the laser wavelength in the presence of a 60-cycle Gaussian pulse with a peak intensity of 5×10^{13} W/cm^2. The range of laser wavelengths is split by the vertical dashed lines into two-, three-, and four-photon ionization regimes. a) Final populations of some specific excited states are shown. b) Partial contributions of continuum states with different angular momenta to the total ionization yield are presented.

REMPI through the 2S state, since the residual population of this state exhibits a strong maximum and dominates in the total excitation yield. Besides, the P states prevail over all other symmetries in the continuum. On the other hand, the peaks at 202 nm and 192 nm are due to (2+1) REMPI through the 3D and 4D states, respectively. Note the dominant contribution of F states in the continuum. This indicates the higher transition probability from the 3D and 4D states to the F-continuum manifold compared with those to the P-continuum manifold. A similar effect is observed for (3+1) REMPI through the 3P and 4P states occurring at 397 nm and 284 nm, respectively. An analysis of the partial ionization yield reveals a much higher contribution of the D states as compared to the S states.

The dependence of the final population of the 3D, 4D and 4P states on the laser wavelength shows a clear oscillatory structure (fringes) on the right side of the corresponding peaks. It might be surprising, at first glance, since Gaussian pulses are used and peaks

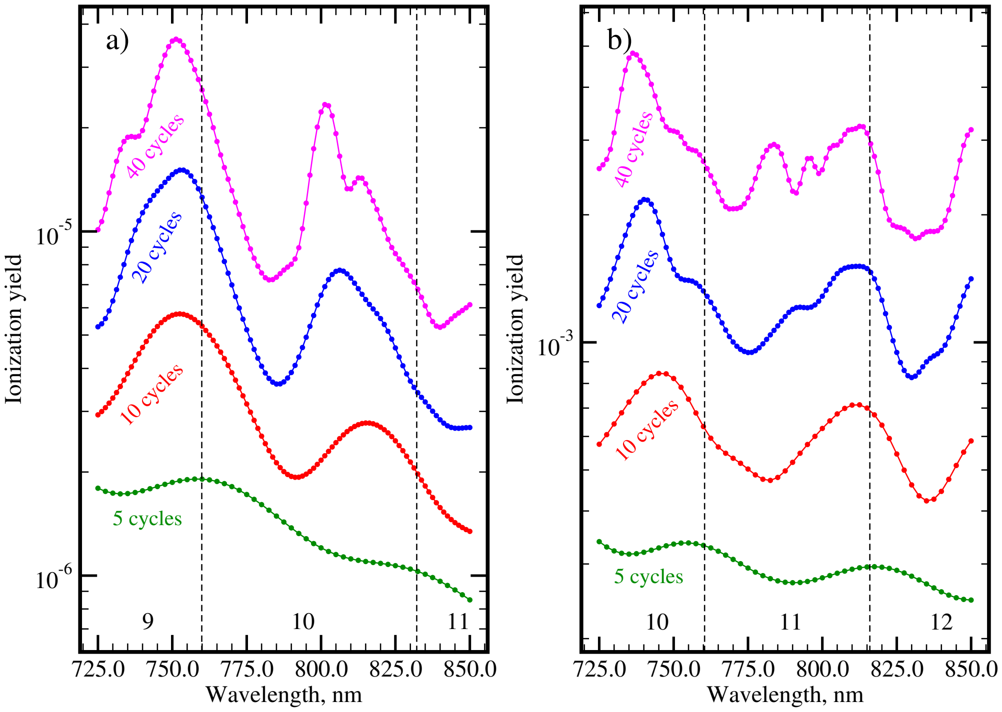

Figure 6.20.: Ionization yield of an H atom as a function of the laser wavelength. Various durations of a Gaussian pulse are presented for peak intensities a) 2×10^{13} W/cm^2 and b) 5×10^{13} W/cm^2. The dashed vertical lines show the positions of channel closings. The numbers at the bottom of the plots specify the minimal number of photons required for ionization.

without fringes are expected (in contrast to the $\cos^2$-shaped pulses where the sharp turn-on and -off leads to an oscillatory behavior in the energy domain and thus in the convolution function, as discussed in Sec. 7.4.2). Similar fringes, but on both sides of the peak, can be obtained within the two-level model because of Rabi oscillations (two-photon resonances can be treated in terms of two-photon Rabi frequencies). The asymmetry observed in Fig. 6.18 could only be reproduced with the two-level model allowing for the intensity-dependent AC Stark shift of the states. Then, if the energy distance between the two states increases with increasing radiation intensity, the fringes on the left side of the peak disappear and vice versa. For a better agreement with the TDSE calculations, it is crucial to extend the two-level system by including also a decay channel due to ionization. A systematic study of two-photon excitation dynamics by means of a two-level system for hydrogenic systems in the presence of laser fields can be found in [196].

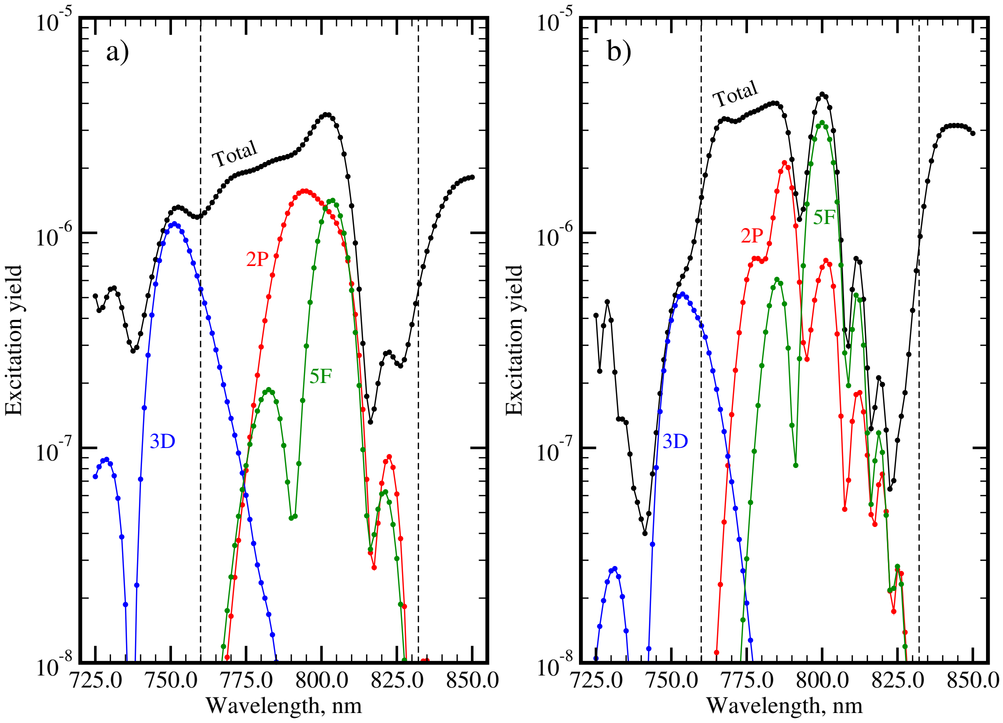

Figure 6.21.: Population of excited states of an H atom as function of the laser wavelength after a Gaussian pulse of the peak intensity 2×10^{13} W/cm^2 and a pulse duration of (a) 20 and (b) 40 cycles.

Now the influence of an increased pulse duration on the ionization yields is discussed. A comparative analysis in the range of radiation wavelengths from 725 nm to 850 nm for the peak intensities of 2×10^{13} W/cm^2 and 5×10^{13} W/cm^2 is presented in Fig. 6.20. The ionization yields in the presence of 5-, 10-, 20-, and 40-cycle pulses are plotted on a log scale. Provided that the rate concept is applicable, the expected result should show four identical curves which are shifted vertically in such a way that the distance between any two adjacent curves is the same. As is apparent from Fig. 6.20, the obtained result is different. Besides the observation of more structures for longer pulses, there is an evident shift of some peaks with increasing pulse duration. On one hand, the position of the peak visible (Fig. 6.20 a) for the 10-cycle pulse at 815 nm shifts gradually towards shorter wavelengths. On the other hand, the position of the peak at 750 nm remains unchanged (for pulse durations longer than 10 cycles). A similar behavior is observed in Fig. 6.20 b, where the position of one peak changes from 745 nm to 735 nm, whereas the position of another peak at about 810 nm remains unchanged (for pulse durations longer than 10 cycles).

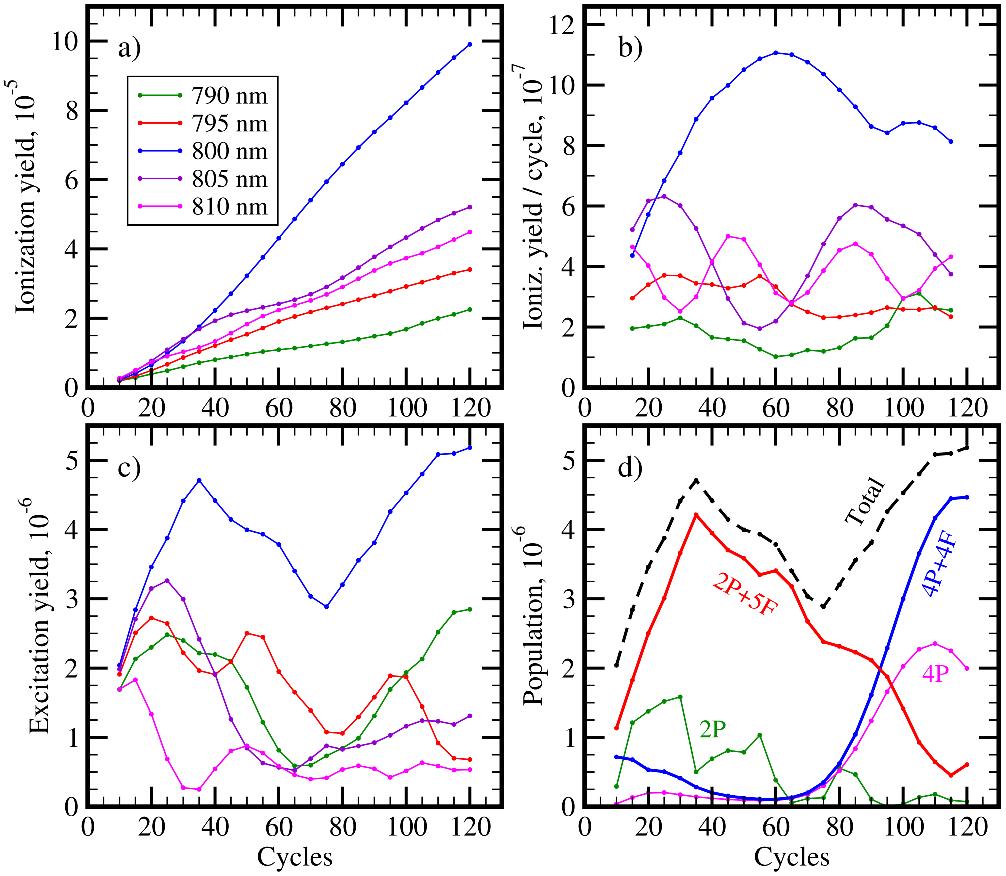

Figure 6.22.: Analysis of the ionization and excitation yields of an H atom in the presence of a Gaussian pulse with a peak intensity of 2×10^{13} W/cm^2 as a function of pulse duration. (a) Ionization yields for various wavelengths in the range from 790 to 810 nm. (b) Derivatives with respect to the number of cycles for the ionization yields provided in a). (c) Excitation yields for the pulses considered in a). (d) Contributions of the final populations of some excited states to the total excitation yield for 800 nm pulses.

In general, the analysis of resonances in the many-photon ionization regime is very complicated. In order to substantiate this statement, the resonance apparent in Fig. 6.20 a at 800 nm is studied in detail. The excitation yields show a complicated dependence on the pulse duration (Fig. 6.21). Thus, the leading contribution of the 2P and 5F states in the total excitation yield indicate a resonant ionization through these states. Of course, it is more proper to consider field-induced quasistates instead of bare states. Therefore, the observed enhanced populations of these two bare states may result from their significant contribution to the resonant quasistate. The final populations exhibit asymmetric fringes and respond differently on an increasing pulse duration. As is apparent from the comparison of Figs. 6.21 a and 6.21 b, the population of the 5F state at 800 nm increases, whereas the population of the 2P state evidently decreases.

The resonant character of ionization at 800 nm is verified in Fig. 6.22 a where the ionization yields at this wavelength are compared to those for slightly longer and shorter wavelengths and for pulse durations up to 120 cycles. However, an analysis of the slope with respect to the pulse duration (Fig. 6.22 b) shows a gradual decrease for durations longer than 60 cycles. Note, the evident oscillatory character of the slope on the pulse duration for 805 and 810 nm pulses. The dependence of the excitation yields on the pulse duration also shows a complicated oscillatory behavior (Fig. 6.22 c). Thus, the excitation yield for 800 nm pulses exhibits a prominent zigzag-like structure. An investigation of the relative contributions of the excited states to the total excitation yield reveals a drastic decrease of the final populations of the 2P and 5F states with the increase of the pulse duration starting from a duration of 35 cycles. The negative slope of the excitation yields changes to a positive one at a duration of 80 cycles when the final populations of the 4P and 4F states become dominant in the total ionization yield. Note the almost negligible populations of these states for shorter pulses (40-60 cycles). As can be seen from Fig. 6.16, there exist a number of avoided crossings between different quasienergy states. Therefore, such a drastic change in the structure of the excitation yield with increasing pulse duration may indicate that the resonant state follows the adiabatic potential curve and thus changes the character of its wavefunction. Undoubtedly, a deeper analysis is required for a full understanding of this effect.

6.6. Investigation of the population dynamics during the pulse in different gauges

The previous section reveals some problems which occur studying REMPI by looking solely onto the final populations of bare states. Therefore, it is tempting to look onto the dynamics of state populations during the pulse. Performing such an investigation one faces a gauge dependence of the obtained result. As has been discussed above, the TDSE can be solved in different gauges by projecting the wavefunction onto the solutions of different generalized field-free Hamiltonians (Sec.4.4). Thus, the populations of states, $P_\alpha(t) = |C_\alpha(t)|^2$, will depend on a specific choice of the functions $\mathbf{G}_i(t)$. Since only a single-electron problem is dealt with here, the electron index is discarded in the following. For the sake of concreteness, the traditional (i.e. $\mathbf{A}(t)$-independent) field-free Hamiltonian is used and thus the function $\mathbf{G}(t)$ depends solely on the adopted gauge.

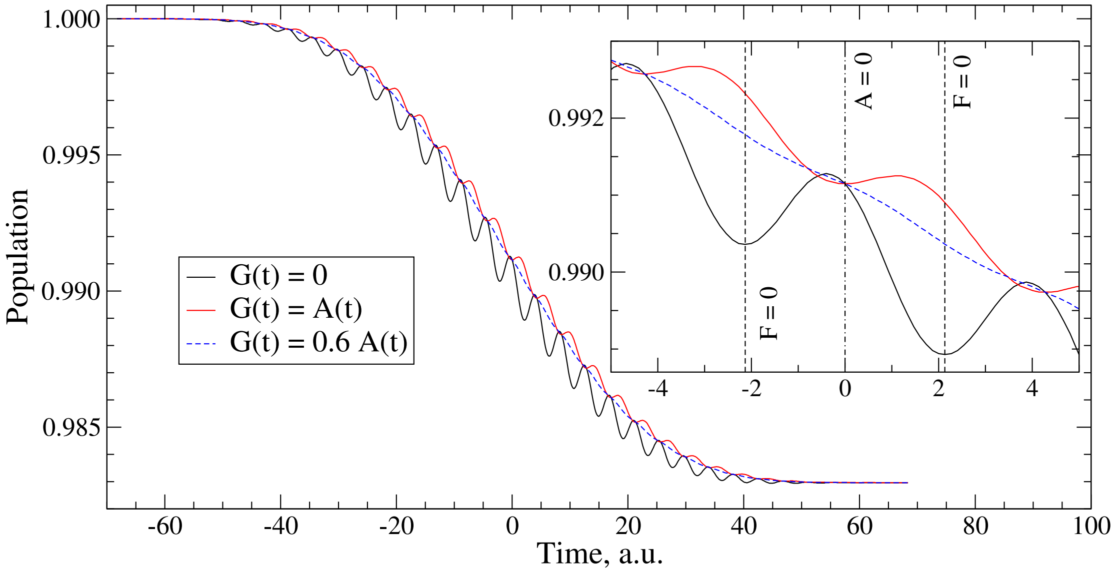

Figure 6.23.: Population of the ground bare state of the H atom in the presence of a cos^2-shaped 16-cycle 20 eV pulse with a peak intensity of 2×10^{13} W/cm^2. The black solid curve line presents the result for traditional L-gauge, the red solid curve shows the result for traditional V-gauge, whereas the blue dashed curve depicts the result obtained using an intermediate gauge specified by $\mathbf{G}(t) = 0.6\mathbf{A}(t)$. The insert shows the population dynamics in the middle of the pulse in more detail.

In order to demonstrate the gauge dependence of the bare-state populations, the population dynamics of the ground bare state of the H atom undergoing single-photon ionization is considered in Fig. 6.23 by using three different functions $\mathbf{G}(t)$. The first one reads $\mathbf{G}(t) = 0$, corresponds to the standard description in the L gauge and results [see Eq. (4.59)] in a system of ordinary differential equations

$$\mathrm{i}\dot{C}_{\alpha'}(t) = \sum_{\alpha} C_{\alpha}(t) \left\langle \Psi_{\alpha'}(t) \left| \mathbf{F}(t) \cdot \mathbf{r} \right| \Psi_{\alpha}(t) \right\rangle \ , \tag{6.14}$$

whereas the second one, $\mathbf{G}(t) = \mathbf{A}(t)$, corresponds to the standard description in the V gauge and yields a system of ordinary differential equations

$$\mathrm{i}\dot{C}_{\alpha'}(t) = \sum_{\alpha} C_{\alpha}(t) \left\langle \Psi_{\alpha'}(t) \left| \mathbf{A}(t) \cdot \mathbf{p}_{\mathrm{c}} \right| \Psi_{\alpha}(t) \right\rangle \ . \tag{6.15}$$

As can be seen from Fig. 6.23, the populations exhibit a different behavior for different gauges during the pulse, although the final populations of the state are the same. Besides an evident depletion of the state population in both gauges, there exists an additional oscillatory structure in the center of the pulse. The population in the L gauge shows a local minimum when the electric field is equal to zero, whereas the population in the V gauge exhibits the opposite behavior. The populations agree when the vector potential is equal to zero, since both descriptions become identical at that moment.

This example reveals a non-triviality in defining instantaneous characteristics during the pulse, for example, an instantaneous state population or an instantaneous ionization. Quantum-mechanically this non-triviality is inherently connected to the uncertainty principle, since the energy uncertainty for the time interval of a quarter of the cycle period is about 4 photon energies. In contrast to the quasistatic regime, this energy range is too wide in the single-photon ionization regime and thus it is impossible to distinguish between bound and continuum states. If the photon picture is used to describe the laser pulse, one could intuitively relate the instantaneous probability of photon absorption to the intensity envelope since it characterizes the photon density. Therefore, one could consider the ionization (and thus the ground state depopulation) as a smooth function of time, which imprints the pulse envelope function. In fact, for the given example, there exists an intermediate gauge specified by $\mathbf{G}(t) = 0.6\mathbf{A}(t)$, which provides such a smooth evolution of the ground-state population. The corresponding system of ordinary differential equations is given by

$$\mathrm{i}\dot{C}_{\alpha'}(t) = \sum_{\alpha} C_{\alpha}(t) \left\langle \Psi_{\alpha'}(t) \left| 0.6\, \mathbf{A}(t) \cdot \mathbf{p}_{\mathrm{c}} + 0.4\, \mathbf{F}(t) \cdot \mathbf{r} \right| \Psi_{\alpha}(t) \right\rangle \ . \tag{6.16}$$

Again, the population of the ground state in the intermediate gauge agrees with those for the L gauge and V gauge when the electric field has its local maximum or minimum ($\mathbf{A}(t) = 0$), but in contrast to the traditional gauges the intermediate gauge predicts a monotonous depopulation of the ground state, where the depopulation rate possesses its maximum in the middle of the pulse (where the pulse intensity has its maximum) and decreases with decreasing pulse intensity. This result might indicate certain advantages of non-traditional gauges in studying strong-field phenomena. Moreover, the results obtained with SFA-like theories formulated in the intermediate gauges provide a smooth transition between the traditional L gauge and V gauge SFA results and may be of interest for the ongoing discussions concerning gauge dependencies of the SFA.

7. Ionization of H_2 in intense ultrashort laser pulses

The full-dimensional *ab initio* numerical treatment of the multiphoton ionization process for molecular hydrogen is a challenge. Up to now, only few studies have been reported. First, an efficient grid point method was used by Harumiya *el al.* [29] in 2002 for the calculation of the electronic wave-packet dynamics of H_2 in a long-wavelength intense field within the fixed-nuclei approximation. The first results with an alternative approach were reported in 2005 [197]. They were obtained by expanding the electronic wave-packet in terms of field-free eigenstates of an H_2 molecule[1] calculated with the electronic-structure method described in chapter 2. Soon thereafter, the spectral method was used with the field-free eigenstates calculated with the one-center approach [31], where the vibrational motion was additionally included within the Born-Oppenheimer approximation[2]. However, only the parallel orientation of the molecular axis with respect to the linear-polarized laser field was considered in these studies. For non-parallel orientations the computational demands are much higher, since the cylindrical symmetry of H_2 is broken and the problem cannot be reduced to five spatial dimensions. Thus, the extension of the grid approach to the case of non-parallel orientations appears infeasible in nearest future. However, a full understanding of the orientation-dependent strong-field response is an important issue in the context of the recently proposed techniques for imaging electrons and nuclear motion with a sub-femtosecond time-resolution [198–200].

The first results for the perpendicular oriented H_2 molecule were reported by the author in 2008 [34]. This chapter presents a pioneering investigation of the orientational dependence of the behavior of H_2 in ultrashort intense laser pulses performed by means of solving the TDSE in full dimensionality. The implementation of the spectral method for an arbitrarily-oriented H_2 molecule[3] is described in Sec. 7.1. The adopted basis-set pa-

---

[1] This approach to the solution of the TDSE is also known as the spectral method.

[2] Since the computational demands are much higher for this approach, the calculations are being performed by means of a supercomputer and the important case of 800 nm laser pulses has not been explored yet.

[3] The corresponding code was written from scratch by the author, since the code used for the time

rameters are discussed in Sec. 7.2. Section 7.3 introduces a simple one-parameter atomic model used to identify the influence of the intrinsic diatomic two-center character of the problem. The investigation of the few-photon ionization regime for two different pulse lengths (10- and 30-cycle pulses) and two different internuclear separations ($1.4\,a_0$ and $2.0\,a_0$) is presented in Sec. 7.4. Section 7.5 examines the effect of zero-point vibrational motion in the context of fixed-nuclei approximation using 400 nm laser pulses. Finally, a simple interference model is tested in Sec. 7.6 using two different internuclear separations ($3\,a_0$ and $4\,a_0$) and 800 nm laser pulses.

7.1. Method

The solution of the TDSE describing molecular hydrogen exposed to a laser field follows closely the approach that has been used for the hydrogen atom in Sec. 6.1.1. The total in-field Hamiltonian is given by

$$\hat{\mathrm{H}} = \hat{\mathrm{H}}_0 + \hat{\mathrm{V}}(t) \tag{7.1}$$

where $\hat{\mathrm{H}}_0$ is the field-free electronic Born-Oppenheimer Hamiltonian of a hydrogen molecule and $\hat{\mathrm{V}}(t)$ is the operator describing its interaction with the (time-dependent) laser field. The non-relativistic approximation is used for both operators, and the interaction with the laser field is described within the dipole approximation and in velocity gauge. For a linearly polarized laser field with the polarization axis $\boldsymbol{\epsilon}$ the interaction operator is given by

$$\hat{\mathrm{V}}(t) = A(t)\boldsymbol{\epsilon} \cdot \mathbf{P}\,. \tag{7.2}$$

Here, $A(t)$ is the magnitude of the vector potential of the laser field and $\mathbf{P}$ is the total momentum operator of the electrons, $\mathbf{P} = -i(\nabla_1 + \nabla_2)$. Without loss of generality, the polarization vector $\boldsymbol{\epsilon}$ can be specified as

$$\boldsymbol{\epsilon} = \cos\theta\,\hat{\mathbf{R}} + \sin\theta\,\hat{\mathbf{x}} \tag{7.3}$$

where the unit vector $\hat{\mathbf{x}}$ is perpendicular to the molecular axis and θ specifies the angle between the polarization axis and the internuclear axis.

The present study is restricted to the case where the H_2 molecule starts in its ground $1^1\Sigma_g^+$ state. Since singlet and triplet states are not coupled by the operator $\hat{\mathrm{V}}(t)$, only singlet molecular symmetries are considered in the following. The number of molec-

---

propagation in [197] could not be easily extended to non-parallel orientations.

ular symmetries involved in the solution of TDSE depends on the orientation of the polarization vector. There are three different cases.

For parallel orientation, $\boldsymbol{\epsilon} \,||\, \mathbf{R}$, only transitions from Σ_g^+ to Σ_u^+ and vice versa are allowed. This reduces the problem effectively to a five-dimensional one, as cylindrical symmetry is preserved. Since only two symmetries have to be considered, this case is much easier to compute.

For perpendicular orientation, $\boldsymbol{\epsilon} \perp \mathbf{R}$, the transitions $\Sigma_g^+ \leftrightarrow \Pi_u \leftrightarrow \Delta_g \leftrightarrow \Phi_u \ldots$ are allowed. Moreover, all states with the symmetries Π, Δ, …, i. e. with the absolute value of the projection of the total angular momentum on the internuclear axis $\Lambda > 0$, are doubly degenerate, since one has for the value of the total angular momentum along the internuclear axis $M = \pm\Lambda$. However, the explicit use of the reflection symmetry (in a plane containing the molecular axis) helps to reduce the dimensionality of the problem. Indeed, both $\hat{\mathrm{H}}_0$ and $\hat{\mathrm{V}}(t)$ are symmetric with respect to the reflection operation and the same is true for the initial $1\Sigma_g^+$ state. Therefore, only the linear combinations of the pairs of degenerate states that are symmetric with respect to the reflection transformation have to be considered. (If the initial state would be $1\Sigma_g^-$, the linear combinations had to be antisymmetric.)

Finally, for an arbitrary orientation, all symmetries are allowed:

$$\begin{array}{ccccccccc}
\Sigma_g^+ & \leftrightarrow & \Pi_u[1] & \leftrightarrow & \Delta_g[2] & \leftrightarrow & \Phi_u[3] & \ldots \\
\updownarrow & & \updownarrow & & \updownarrow & & \updownarrow & \\
\Sigma_u^+[1] & \leftrightarrow & \Pi_g[2] & \leftrightarrow & \Delta_u[3] & \leftrightarrow & \Phi_g[4] & \ldots
\end{array}$$

(In square brackets the minimal number of photons required to populate a given symmetry, N^{ph}, is specified.) The reduction of dimensionality due to reflection symmetry remains possible. Evidently, this case is the most computationally expensive one.

The resulting TDSE

$$\mathrm{i}\,\frac{\partial|\Psi\rangle}{\partial t} \;=\; \hat{\mathrm{H}}|\Psi\rangle \tag{7.4}$$

is solved by expanding the wave function $|\Psi\rangle$ according to

$$|\Psi(t)\rangle \;=\; \sum_{n\Omega} C_{n\Omega}(t)\,|\phi_{n\Omega}\rangle \tag{7.5}$$

in terms of the time-independent wave functions $|\phi_{n\Omega}\rangle$. The latter are solutions of the field-free molecular Schrödinger equation

$$\hat{\mathrm{H}}_0|\phi_{n\Omega}\rangle \;=\; E_{n\Omega}\,|\phi_{n\Omega}\rangle \quad . \tag{7.6}$$

The two-electron wavefunctions $|\phi_{n\Omega}\rangle$ are orthonormal and symmetric with respect to the reflection symmetry. The compound index Ω represents Λ and the parity with respect to inversion symmetry (*gerade* or *ungerade*). The index n just numbers the states with a particular symmetry Ω. It is discrete for all states due to the discretization of the electronic continuum.

In the case of perpendicular orientation the summation in Eq. (7.5) is restricted to $\Lambda \leqslant \Lambda_{\mathrm{max}}$. In the case of arbitrary orientation the summation is restricted to all symmetries with $N^{\mathrm{ph}} \leqslant N^{\mathrm{ph}}_{\mathrm{max}}$.

Since the CI method described in chapter 2 generates only solutions $\psi_{n,\Omega}$ for $M = \Lambda$, they must be adapted for the present purpose. Although for $\Lambda = 0$ they are equivalent to $\phi_{n\Omega}$, for $\Lambda > 0$ the following linear combination has to be used

$$\phi_{n\Omega} \;=\; (\psi_{n,\Omega} + \psi^*_{n,\Omega})/\sqrt{2} \quad . \tag{7.7}$$

As discussed in chapter 2, with a proper normalization of $\psi_{n,\Omega}$ the reflection transformation is equivalent to a complex conjugation of the wavefunction. Therefore, the definition (7.7) ensures that $\phi_{n\Omega}$ is symmetric with respect to reflection.

Substitution of Eq. (7.5) into the TDSE [Eq. (7.4)], multiplication of the result by $\phi^*_{n'\Omega'}$, and integration over the electronic coordinates yields

$$\mathrm{i}\frac{\partial}{\partial t}C_{n'\Omega'}(t) \;=\; E_{n'\Omega'}C_{n'\Omega'}(t) \;+\mathrm{i}A(t)\sum_{n\Omega}\left(\cos\theta\, D^{\|}_{n'\Omega',n\Omega} + \sin\theta\, D^{\perp}_{n'\Omega',n\Omega}\right)\,C_{n\Omega}(t) \tag{7.8}$$

with $D^{\|}_{n'\Omega',n\Omega} = \langle\phi_{n'\Omega'}|\hat{\mathbf{R}}\cdot(\nabla_1+\nabla_2)|\phi_{n\Omega}\rangle$ and $D^{\perp}_{n'\Omega',n\Omega} = \langle\phi_{n'\Omega'}|\hat{\mathbf{x}}\cdot(\nabla_1+\nabla_2)|\phi_{n\Omega}\rangle$. As can be shown using Eq. (7.7), these matrices are related to those obtained in chapter 2, $\bar{D}^{\|}_{n'\Omega',n\Omega} = \langle\psi_{n'\Omega'}|\hat{\mathbf{R}}\cdot(\nabla_1+\nabla_2)|\psi_{n\Omega}\rangle$ and $\bar{D}^{\perp}_{n'\Omega',n\Omega} = \langle\psi_{n'\Omega'}|\hat{\mathbf{x}}\cdot(\nabla_1+\nabla_2)|\psi_{n\Omega}\rangle$ by the relation

$$D^{\|}_{n'\Omega',n\Omega} = \bar{D}^{\|}_{n'\Omega',n\Omega}, \quad D^{\perp}_{n'\Omega',n\Omega} = \begin{cases} \sqrt{2}\bar{D}^{\perp}_{n'\Omega',n\Omega} & \text{for } \Lambda+\Lambda'=1 \\ \bar{D}^{\perp}_{n'\Omega',n\Omega} & \text{otherwise.} \end{cases} \tag{7.9}$$

Here, the reality of $\bar{D}_{n'\Omega',n\Omega}$ and the identity for $\Lambda > 0$,

$$\langle \psi_{n'\Omega'} | \boldsymbol{\epsilon} \cdot (\nabla_1 + \nabla_2) | \psi^*_{n\Omega} \rangle = 0, \quad \text{if } \Lambda' \neq 0 \text{ or } \Lambda \neq 1 \quad , \tag{7.10}$$

was used.

It should be emphasized that with this approach the complete time dependence is incorporated in the coefficients $C_{n\Omega}$. They are calculated by propagating Eq. (7.8) numerically in time using a variable-order, variable-step Adams solver for ordinary first-order differential equations.

7.2. Basis set information

The optimal choice of the basis set parameters is determined by the problem to be solved. Therefore, convergence with respect to different parameters was extensively studied for different laser pulses and internuclear separations before the method has been applied for the investigation of the intense-field response of H_2. This section discusses four basis sets which were found to be reasonable for the investigations described in the present chapter.

For small internuclear separations ($R < 3.0\, a_0$) two different basis sets are chosen, basis A and basis B. Basis A is supposed to be used for shorter wavelengths or pulse durations due to a smaller box size. Basis B is obtained using a larger box size but its application is more expensive.

The basis states $\psi_{n,\Omega}$ were obtained for every symmetry in basis A as follows. A box size (defined implicitly by $\xi_{\max}$ that depends on R) of about $350\, a_0$ is chosen for different R. Along the ξ coordinate 350 B splines of order $k = 10$ with an almost linear knot sequence (the 40 first intervals are increased with geometric progression using $g = 1.05$, all following intervals have the length of 40th one) were used. Along the η coordinate 30 B splines of order 8 were used in the complete interval $-1 \leq \eta \leq +1$, but using the symmetry of a homonuclear system as is described in chapter 2. Out of the resulting 5235 orbitals for every symmetry only 3490 orbitals were further used to construct configurations, whereas those orbitals with highly oscillating angular part (with more than 19 nodes for the η-dependent component) were omitted. In most of the subsequent CI calculations approximately 6000 configurations were used for every symmetry. These states result from very long configuration series (3490 configurations) in which one electron occupies the H_2^+ ground-state $1\,\sigma_g$ orbital while the other one is occupying one of

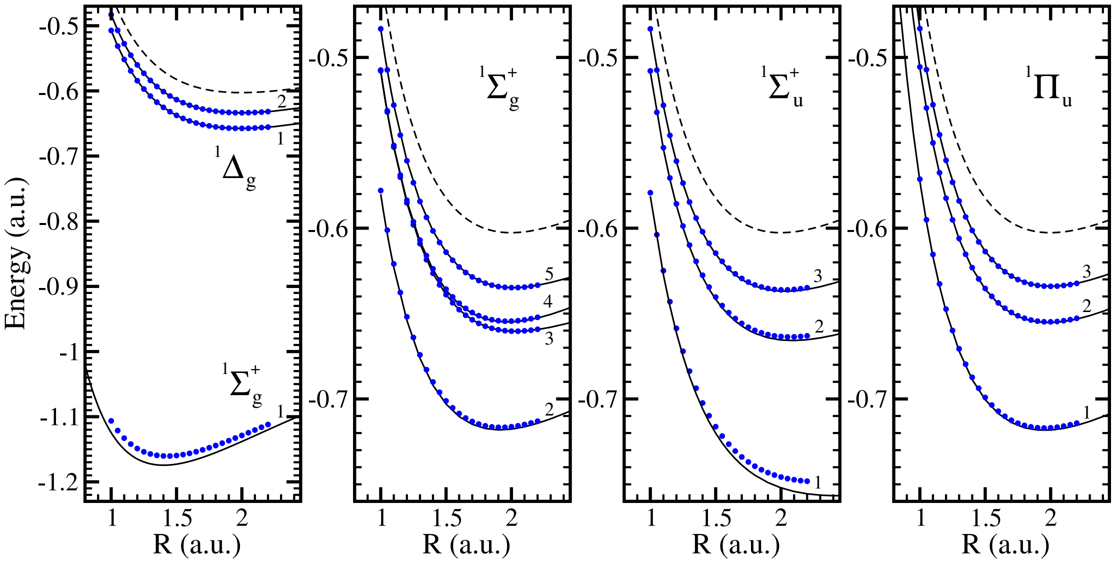

Figure 7.1.: Electronic potential curves of some low-lying states of H_2. The the CI results (blue circles) are compared to the quasi-exact values (solid curves). The dashed line shows the ionization threshold of H_2. The different adiabatic electronic states of a given molecular symmetry are numbered in the order of their energies. (Published in [35].)

the remaining, e. g., $n\,\pi_u$ or $n\,\delta_g$ orbitals. The other configurations represent doubly-excited situations and are responsible for describing correlation (and real doubly-excited states). Finally, out of the obtained CI states only those with an energy below the energy cut-off (here chosen to be 10 a.u. above the ionization threshold) were included in the time propagation (about 5400 states per symmetry).

The preparation of the basis states $\psi_{n,\Omega}$ in basis B differs mainly by using a larger box size, which was chosen to be twice as larger as for basis A (about 700 a_0). Correspondingly, the number of B splines along the ξ coordinate was increased to 500. To reduce the number of orbitals, the number of B splines along the η coordinate was reduced from 30 to 24. Out of the resulting 5988 orbitals for every symmetry only 4990 orbitals were further used to construct configurations, whereas those orbitals with highly oscillating angular part (with more than 19 nodes for the η-dependent component) were omitted. The adopted CI configurations differ from those of basis A only by extending the number of configurations in the leading configuration series (where one electron occupies the $1\,\sigma_g$ orbital) from 3490 to 4990. Thus, for every symmetry the full CI configuration series of basis B is 1500 configurations longer than the one of basis A. Applying the same cut-off results in about 6900 states per symmetry included in the time propagation.

For internuclear separations $R \geqslant 3\,a_0$ the probability to find H_2^+ in the excited $1\sigma_u$ state after ionization process becomes significant. Numerical tests have shown that the discussed basis sets have to be extended in order to obtain converged photoelectron energy spectra. For this purpose, all configurations in which one electron occupies the H_2^+ $1\,\sigma_u$ orbital were additionally included in the configuration series. This resulted in an almost by a factor of 2 larger number of states per symmetry included in the time propagation. These basis sets are labeled C (extended basis set A) and D (extended basis set B).

A variation of the remaining parameter $N_{\max}^{\mathrm{ph}}$ (or $\Lambda_{\max}$) provides an additional convergency test. This parameter can be chosen depending on the problem to be solved and will be specified later.

The CI calculations using all basis sets discussed above yield almost the same electronic energies $E_{n,\Omega}$ for the low-lying states of H_2. Conversely, highly energetic Rydberg states and discretized continuum states have different energies due to a larger box size for basis sets B and D as compared to basis sets A and C. Figure 7.1 shows the electronic energies $E_{n,\Omega}$ of various low-lying states obtained using the discussed basis sets (compared with quasi-exact energies calculated using state-optimized basis set. The agreement is excellent for all states except for $1^1\Sigma_g^+$ and $1^1\Sigma_u^+$ (at larger internuclear distances) where the electronic motion is highly correlated and cannot efficiently be described by a CI calculation employing orbitals with no electron-electron interaction included. Nevertheless, even for these two states the obtained electronic energies are much better than those obtained with the Hartree-Fock approximation. For example, for the ground state of H_2 with the exact electronic energy at $R = 1.4\,a_0$ being equal to $-1.1745\,\mathrm{a.u.}$, the Hartree-Fock limit is $-1.1336\,\mathrm{a.u.}$, whereas the present CI calculation yields $-1.1604\,\mathrm{a.u.}$

For the subsequent discussion it is helpful to keep in mind the relevant energies and transition frequencies (or wavelengths) of a number of electronic bound states of H_2 that can resonantly be excited by a laser with the corresponding photon frequency. Since the exact positions of the resonances depend on the adopted electronic structure model, Table 7.1 reports the energies obtained with the present approach and basis set A. Furthermore, Table 7.1 provides the ground-state energy of H_2^+ which allows to calculate the exact position of the different N-photon thresholds. (The 1-photon threshold is given explicitly.)

Table 7.1.: Electronic energies E (in a. u.) of various H_2 states as they are obtained with the basis set A used in this work and the resulting resonant N-photon transition frequencies ω (in eV) and wavelengths λ (in nm). The last row shows the ground-state energy of H_2^+ and the corresponding 1-photon ionization threshold. (Published in [34].)

State	E^{a}, a.u.	E^{b}, a.u.	N	ω^{a}, eV	ω^{b}, eV	λ^{a}, nm	λ^{b}, nm
$1\ {}^1\Sigma_g^+$ (X)	-1.160351	-1.128787					
$2\ {}^1\Sigma_g^+$ (EF)	-0.690087	-0.716303	2	6.3982	5.6121	193.778	220.922
			4	3.1991	2.8060	387.556	441.844
$3\ {}^1\Sigma_g^+$ (GK)	-0.626453	-0.660305	2	7.2640	6.3739	170.682	194.515
			4	3.6320	3.1870	341.364	389.030
$1\ {}^1\Sigma_u^+$ (B)	-0.702364	-0.745749	1	12.4623	10.4229	99.486	118.953
			3	4.1541	3.4743	298.458	356.859
$2\ {}^1\Sigma_u^+$ (B')	-0.627569	-0.663476	1	14.4975	12.6616	85.520	97.920
$3\ {}^1\Sigma_u^+$ (B")	-0.602079	-0.636115	1	15.1914	13.4063	81.614	92.481
$1\ {}^1\Pi_u$ (C)	-0.687338	-0.716903	1	12.8712	11.2078	96.326	110.622
			3	4.2904	3.7359	288.978	331.866
$2\ {}^1\Pi_u$ (D)	-0.623117	-0.654839	1	14.6187	12.8966	84.811	96.136
$1\ {}^1\Delta_g$ (J)	-0.625213	-0.657517	2	7.2808	6.4119	170.286	193.364
$2\ {}^1\Delta_g$ (S)	-0.601098	-0.633603	2	7.6089	6.7372	162.943	184.026
$1\ \sigma_g$ [H_2^+]	-0.569984	-0.602634	1	16.0645	14.3171	77.178	86.597

[a] For the internuclear distance $R = 1.4\,a_0$ [b] For the internuclear distance $R = 2.0\,a_0$

7.3. Atomic model

A molecule treated in the fixed-nuclei approximation differs from an atom due to the anisotropy of the electronic charge distribution which occurs even for the totally symmetric ground state. Alternatively, this anisotropic charge distribution may be described in the language of the linear combination of atomic orbitals as a multi-centered structure that can give rise to interference phenomena. For the analysis of the effects of the anisotropy and thus the corresponding orientational dependence it is therefore of interest to compare the molecular results with the ones obtained for an artificial atom with an isotropic, single-centered charge distribution. Since strong-field ionization is known to be very sensitive to the electronic binding energy and the exact form of the long-ranged Coulomb potential, it is important that the artificial atom agrees in these properties with the molecule. For this purpose the simple one-parameter model potential

$$V(r) = -\frac{1}{r}\left\{1 + \frac{\alpha}{|\alpha|}\exp\left[-\frac{2r}{|\alpha|^{1/2}}\right]\right\} \tag{7.11}$$

was introduced by the author in [34]. Its performance for describing various physical problems was checked in [201] and it was recently also applied to the calculation of

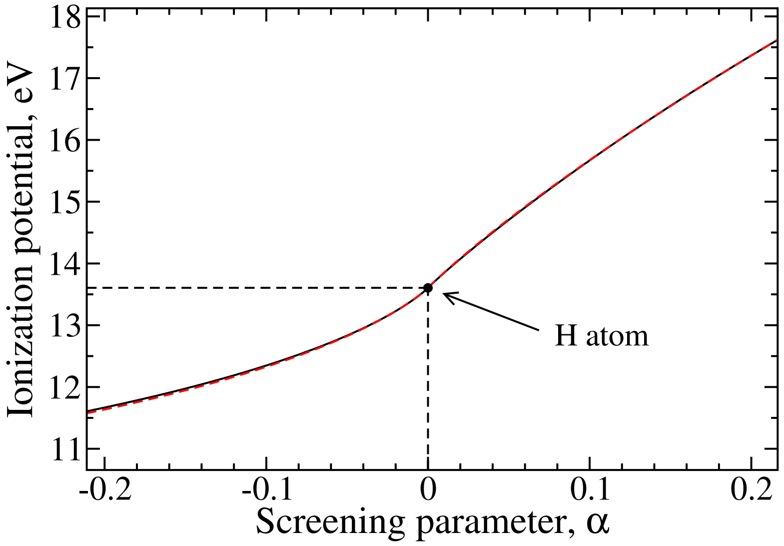

Figure 7.2.: Ionization potential I_p of the atomic-model potential [Eq. (7.11)] as a function of parameter α. The dashed red line shows the approximation given by the expression (7.12).

antiproton–H_2 scattering cross sections and stopping powers [202, 203]. The model potential (7.11) satisfies $V(r) \to -1/r$ for $r \to \infty$ and reduces to the potential of atomic hydrogen, $I_p(\mathrm{H}) = 0.5\,\mathrm{a.u.}$, for $\alpha \to 0$. Although the exact ionization potential I_p for arbitrary values of the parameter α can be obtained only numerically, it can be quite well approximated (Fig. 7.2) by the following expression

$$I_p(\alpha) \approx I_p(\mathrm{H}) + \frac{\alpha}{(1+\sqrt{|\alpha|})^s} \tag{7.12}$$

where $s = 1$ for $\alpha > 0$ and $s = 11/4$ for $\alpha < 0$. For $|\alpha| \ll 1$ the ionization potential is simply given by $I_p(\alpha) \approx I_p(\mathrm{H}) + \alpha$.

Since the molecular ionization potential depends on the internuclear distance R, the value of α should also depend on R in order to compare the atomic-model and the molecular results.

It should be noted that the model atom is a one-electron (hydrogen-like) atom in which the effect of both the anisotropy due to the two nuclei and due to the second electron in H_2 is solely contained as a screening of the Coulomb potential modifying the ionization potential. Therefore, this model does not describe any excitation or relaxation of a second electron that can occur in the H_2 calculation. In order to compare to H_2 the atomic results should be multiplied by a factor 2 in order to account for the two equiv-

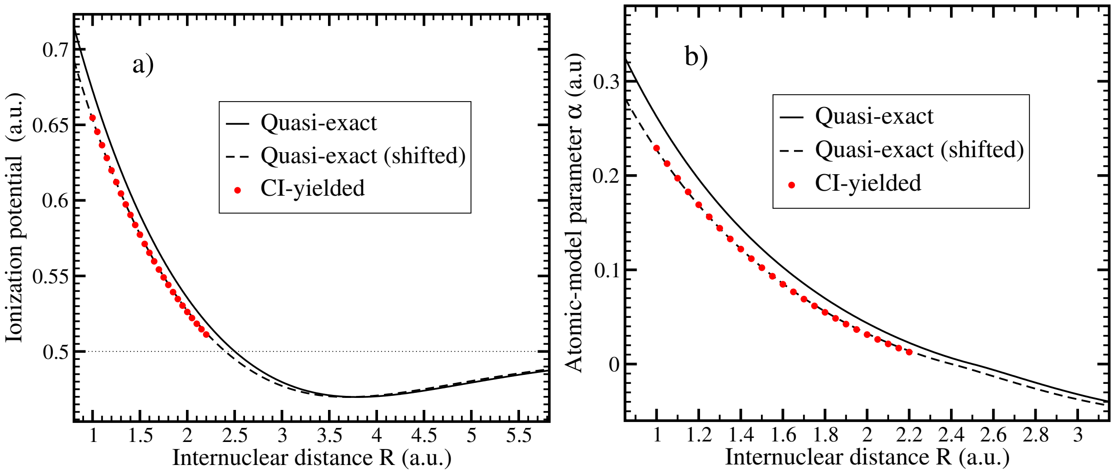

Figure 7.3.: a) Comparison of the R-dependent potential of H_2 obtained in the present CI calculation (red circles) with the quasi-exact one (black solid curve). b) The dependence of the atomic-model parameter α in Eq. (7.11) on the internuclear distance R obtained using the quasi-exact ionization potential $\alpha_{\mathrm{QE}}(R)$ (black solid curve) and the ionization potential $\alpha_{\mathrm{CI}}(R)$ yielded by the present CI calculation (red circles). The dashed curve depicts the solid curve shifted left by $0.1\,a_0$.

alent electrons in H_2. This procedure for comparing SAE results with full two-electron calculations were shown to be reasonable (for not too high ionization yields exceeding about 10 %) in [40].

Since $I_p(\alpha)$ can be found numerically, one can also obtain the corresponding parameter α yielding the necessary ionization potential as $\alpha = \alpha(I_p)$. Also, one can introduce an R-dependent (vertical) ionization potential in order to specify the minimal energy required at a given internuclear separation R for the electronic transition from the ground state of H_2 into the continuum. Clearly, the value of α should also depend on R for comparing atomic-model and the molecular results. Figure 7.3 a shows two R-dependent ionization potentials. The first one is referred to as quasi-exact ionization potential. It is obtained using the quasi-exact electronic energy of the ground state, $E_g^{\mathrm{QE}}(R)$, of molecular hydrogen as $I_p^{\mathrm{QE}}(R) = E_{1\sigma_g}(R) - E_g^{\mathrm{QE}}(R)$. The second one is obtained using the ground state energy $E_g^{\mathrm{CI}}(R)$ yielded by the present CI calculation as $I_p^{\mathrm{CI}}(R) = E_{1\sigma_g}(R) - E_g^{\mathrm{CI}}(R)$. The two resulting R-dependent atomic model parameter, $\alpha_{\mathrm{QE}}(R) \equiv \alpha(I_p^{\mathrm{QE}}(R))$ and $\alpha_{\mathrm{CI}}(R) \equiv \alpha(I_p^{\mathrm{CI}}(R))$, are presented in Fig. 7.3 b.

Besides studying the effects of anisotropy, the atomic model can also be applied for an error estimation. Indeed, comparing results obtained for both $\alpha_{\mathrm{QE}}(R)$ and $\alpha_{\mathrm{CI}}(R)$ provides a way to estimate the error of the molecular calculation due to the inaccurate ionization potential what is virtually impossible by other means. Interestingly, there is a simple approximate relation between the two α functions, $\alpha_{\mathrm{QE}}(R) \approx \alpha_{\mathrm{CI}}(R-0.1)$. It is verified in Fig. 7.3 where the CI-yielded dependence agrees very well with the quasi-exact one shifted left by $0.1\,a_0$. This simple relation allows one to predict the R-dependent ionization yields obtained using $\alpha_{\mathrm{CI}}(R)$ provided that the R-dependent ionization yields obtained using $\alpha_{\mathrm{QE}}(R)$ are known, and vice versa.

7.4. Few-photon regime

In this section the ionization and the electronic excitation are compared for parallel and perpendicular orientations as a function of photon frequency; completely covering the two- to five-photon regime (and partly extending into the one- and six-photon regimes). For these regimes the calculations are performed using the basis set A. The parameter $\Lambda_{\max}$ for perpendicular orientation was varied from 3 to 5 (for longer wavelengths) showing sufficient convergence for total yields already for $\Lambda_{\max} = 3$.

7.4.1. Results for $R = 1.4\,a_0$ and 10-cycle pulses

Figure 7.4 shows the ionization and electronic excitation yields for H_2 exposed to $\cos^2$-shaped laser pulses with a total duration of 10 cycles, a peak intensity $I = 10^{13}\,\mathrm{W/cm^2}$, and a variable photon energy obtained within the fixed-nuclei approximation for the nuclear separation $R = 1.40\,a_0$ that corresponds (to a good approximation) to the equilibrium distance of the field-free H_2 molecule. The excitation yield Y_{exc} is defined as the population of all possible electronically bound excited states, i. e. $Y_{\mathrm{exc}} = 1 - P_{\mathrm{gs}} - Y_{\mathrm{ion}}$ where P_{gs} is the population left in the electronic ground state and Y_{ion} is the ionization yield. (Populations and yields are defined in such a way that a value of 1 corresponds to 100 %.) The results obtained for a parallel orientation of the molecular axis with respect to the field that are shown in the upper graph agree qualitatively to the ones obtained for different laser parameters (the peak intensities were either 2×10^{12} or 2×10^{14} $\mathrm{W/cm^2}$ and the pulse duration was fixed to 15 fs) in an earlier work [197]. However, one notices that the present results are much less structured, despite the larger number of data points and correspondingly higher resolution. Furthermore, the ionization thresholds marking the transition from an N- to an $(N-1)$-photon process are by far not as sharp as in [197]. This is especially evident for the threshold dividing the 1- and 2-photon ionization regimes. The reason is the (especially for those large photon energies) much

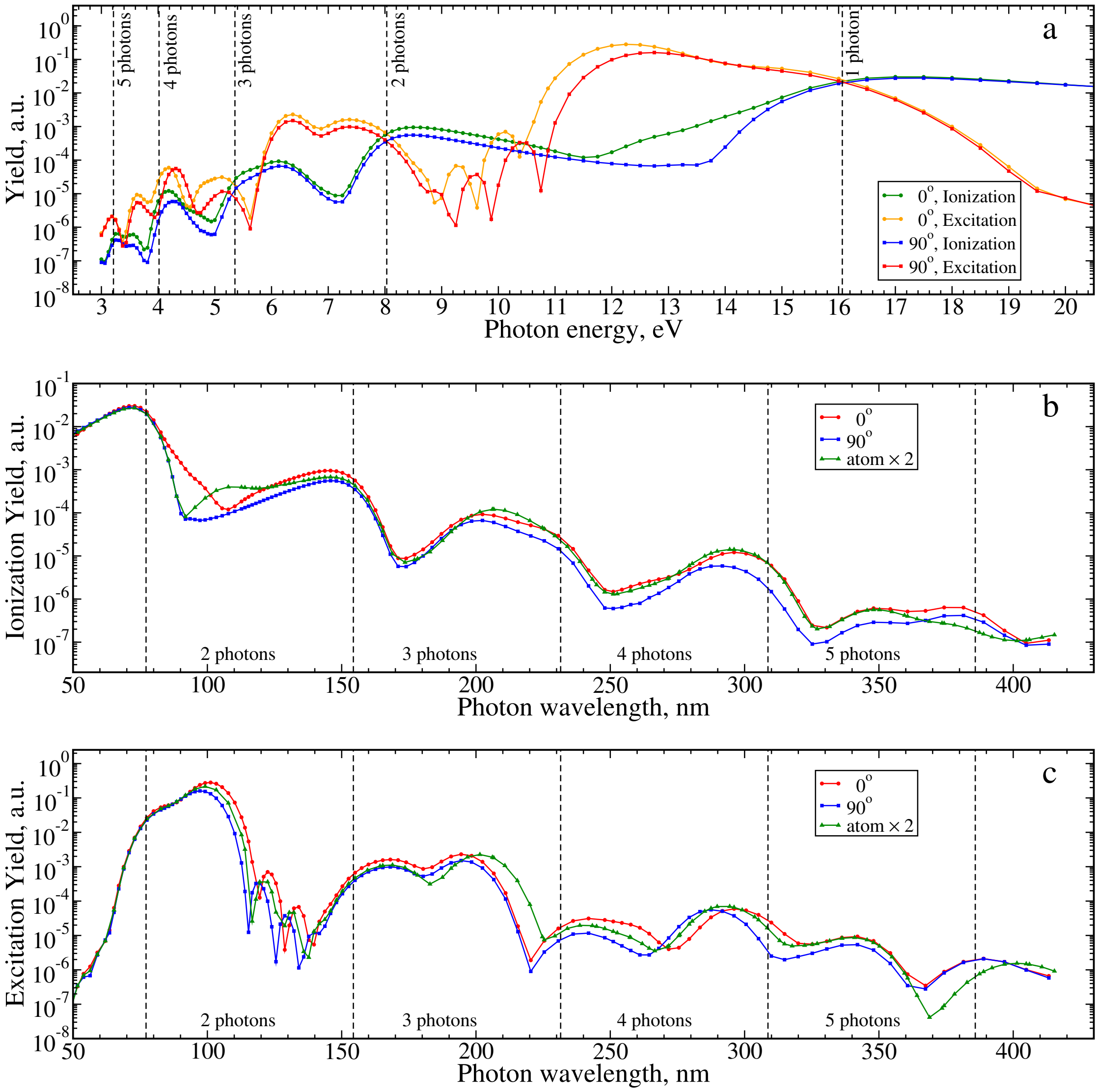

Figure 7.4.: Ionization and excitation yields of an H_2 molecule with fixed internuclear distance $R = 1.4\,a_0$ for a 10-cycle linear-polarized laser pulse with peak intensity $10^{13}\,\mathrm{W/cm^2}$ and either parallel or perpendicular orientation of the molecular axis with respect to the field. Ionization and bound-state excitation yields are shown together as a function of the photon energy in eV (a), while (b) and (c) shows the ionization and excitation yields as a function of photon wavelength, respectively. In (b) and (c) also the yields obtained for a model atom (multiplied by a factor 2, see corresponding discussion in Sec. 7.3) are plotted. The N-photon thresholds (for $N = 1$ to 5) are indicated by vertical dashed lines. (Published in [34].)

shorter pulse duration of the present 10-cycle pulses compared to the 15 fs pulses used in [197].

A short pulse duration leads to a broad spectral width of the Fourier-limited pulse. Fixing the number of cycles instead of the total pulse duration leads, of course, to a variation of the spectral width as a function of the photon energy. On the other hand, a fixed number of cycles has the advantage that one expects the pulses for different photon energy to become better comparable with respect to adiabaticity of the process, since a fixed pulse duration can lead in an extreme case to pulses comprising of in one case many and in the other case even less than a single cycle. An effect of the shorter pulse duration can, for example, be seen for the (1+1)-REMPI peaks that are caused by resonant one-photon transitions to the B and the B' $^1\Sigma_u$ states (cf. Table 7.1). They are clearly visible in both the excitation and ionization yields in [197], but appear in Fig. 7.4 a as an almost structureless broad peak in the excitation yield spanning the photon energy range from about 11 to 16 eV. Another remarkable difference to the earlier result obtained for fixed (longer) pulse length is the fact that in this energy window the resonantly enhanced ionization yield increases almost uniformly with photon energy while in the earlier result there was a pronounced peak at the position of the B state.

7.4.2. Results for $R = 1.4\,a_0$ and 30-cycle pulses

In order to substantiate these arguments even more and to provide a more detailed understanding of the influence of the pulse length on the photon-energy resolved multi-photon spectra, a second series of calculations was performed in which the pulse length was extended to 30 cycles. The results are shown in Fig. 7.5. Clearly, the ionization and excitation spectra become much more structured. For example, in the already discussed energy range from 11 to 16 eV one sees now in both the excitation and ionization yields well separated peaks due to the (1+1)-REMPI process via the B state. Also the B' resonance is clearly visible in the ionization signal and (though less pronounced) also in the excitation yield. Furthermore, the cut-off due to the closing of the one-photon ionization channel is much sharper for the 30-cycle pulse — in direct accordance with the smaller band width with which the threshold is convoluted.

One notices also that the 30-cycle pulse leads to a more pronounced REMPI signal, especially for the B state. This reflects the fact that the REMPI process needs some time to occur, since the pulse has to be sufficiently long to first populate and then ionize the resonant intermediate state. Interestingly, the B' state leads to a larger ionization

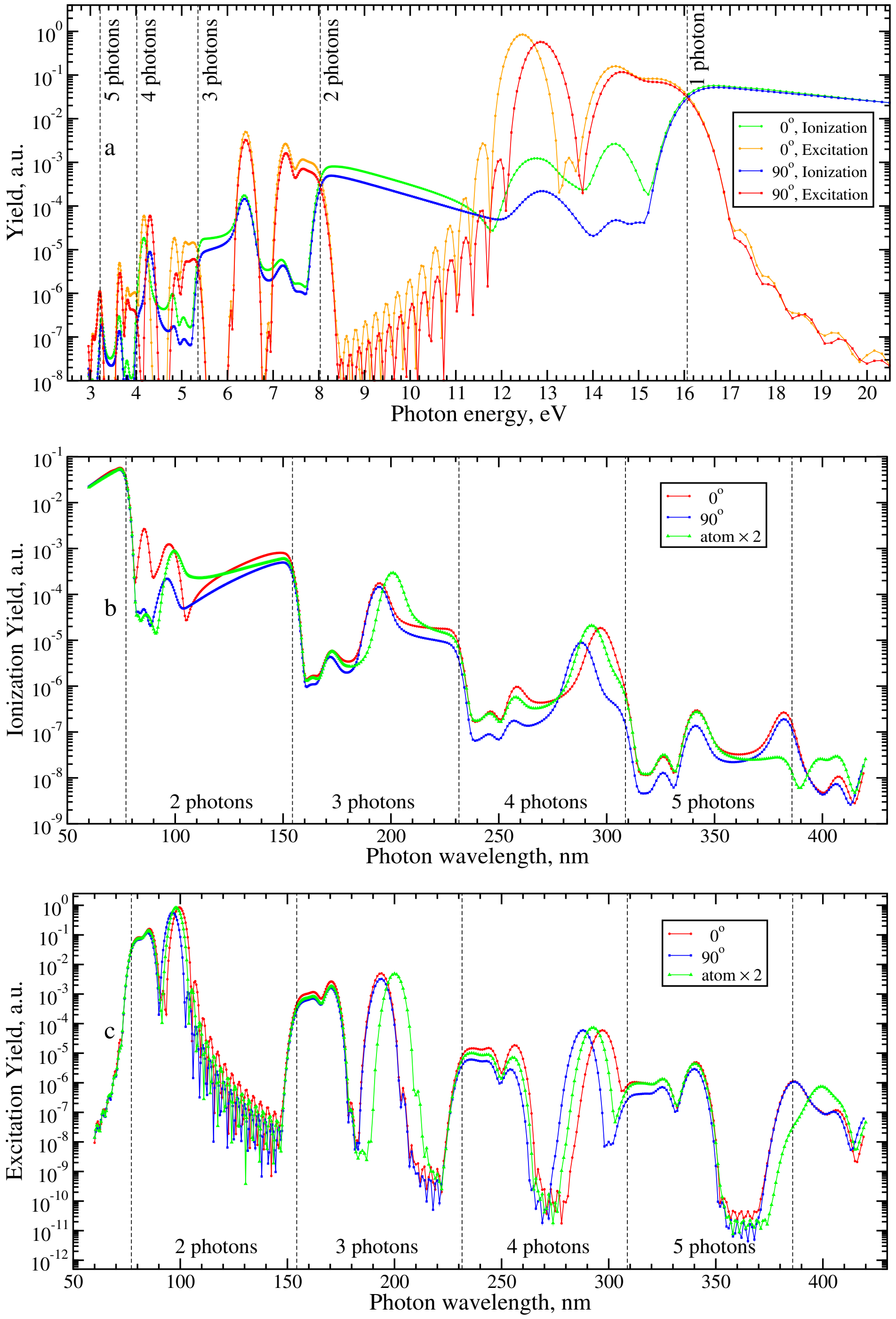

Figure 7.5.: As Fig. 7.4, but for 30-cycle laser pulses with peak intensity $5 \cdot 10^{12}$ W/cm^2. (Published in [34].)

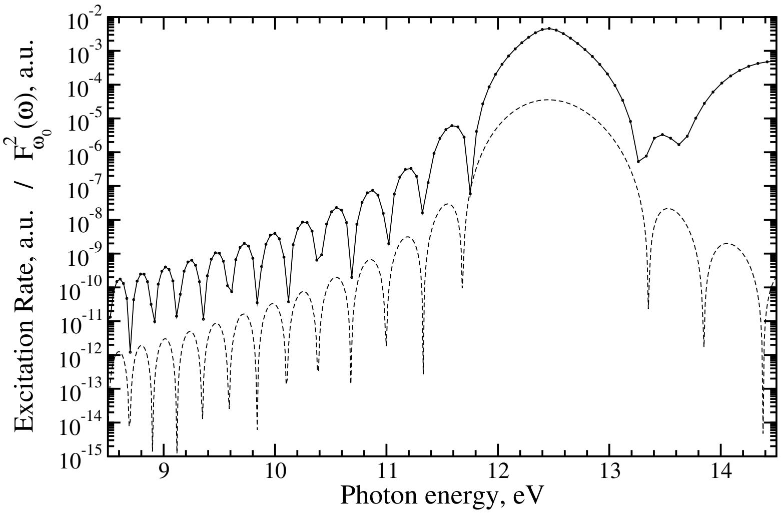

Figure 7.6.: Excitation rate [solid line, extracted from the excitation yield using equation (7.14)] for an H_2 molecule with fixed internuclear distance $R = 1.4\,a_0$, a 30-cycle linear-polarized laser pulse with peak intensity $5 \cdot 10^{12}$ W/cm^2, and a parallel orientation of the molecular axis with respect to the field. It is compared with the square of the Fourier component, $F^2_{\omega_0}(\omega)$ [dashed line, defined in Eq. (7.13)], where ω_0 is the transition frequency from state X to state B. (Published in [34].)

yield than the B state, although the latter is much more populated. Evidently, the B' state is more easily ionized with the given photon frequency than the B state with the photon energy required for its resonant excitation. All these findings for different pulse lengths underline the need for full time-dependent calculations, if ultrashort pulses are considered.

The excitation spectra in Figs. 7.5 a and 7.5 c show in the energy range from about 8.5 to 12 eV (100 to 150 nm) a very pronounced oscillatory structure that is absent for the 10-cycle pulses. The origin of this feature is the chosen pulse profile ($\cos^2$-type envelope function). Its relatively sharp turn-on and turn-off (compared to a Gaussian pulse) which is helpful for numerical calculations, since the pulse has a well defined duration resulting in a well defined interval for the time integration, leads, however, to an oscillatory behavior in the energy domain and thus in the convolution function. A semi-quantitative model for this phenomenon may be obtained in the following way. For the given laser intensity and the photon energy required for a resonant transition to the B state (12.46 eV according to Table 7.1) 1st-order perturbation theory should provide a reasonable approximation for the excitation process. Within lowest-order perturbation theory the rate (and thus for a sufficiently long pulse also the yield) for an N-photon transition is proportional to I^N where $I \propto |F|^2$ is the intensity and F the corresponding electric field strength. The Fourier component of an N_c-cycle laser pulse with carrier frequency ω (and the total pulse duration $T_p = 2\pi N_c/\omega$) at a particular frequency ω_0 can be obtained from the full time-dependent electric field $F(\omega, t)$ by a Fourier analysis (inverse Fourier transform),

$$F_{\omega_0}(\omega) = \frac{2}{T_p} \int_{-T_p/2}^{T_p/2} \mathrm{d}\, t\, F(\omega, t)\, \cos(\omega_0 t) \quad . \tag{7.13}$$

In Eq. (7.13) it was used that the $\cos^2$-shaped laser pulses (with a carrier-envelope phase set to zero) considered in this work lead to an even function $F(\omega, t)$. Therfore, the imaginary part of the Fourier transform vanishes.

Within the perturbative model outlined above the resonant 1-photon transition rate to the B state is convoluted with $|F_{\omega_0}(\omega)|^2$ where ω_0 is equal to the transition frequency from the ground state to state B (12.46 eV). Figure 7.6 shows this convolution function together with the total excitation rate obtained from the numerical solution of the TDSE. In order to obtain a rate from the calculated excitation yield Y_{exc} the approximate relation

$$R_{\text{exc}} \approx -\ln(1 - Y_{\text{exc}})/T_p \tag{7.14}$$

was used. Clearly, the simple model explains very well the observed oscillatory structure.

Although all sharp features (REMPI peaks or ionization thresholds) are, of course, convoluted with the same spectral function, the result is only visible if it stems from a very pronounced, i. e. intense and well isolated, signal like the REMPI peak due to the B state. Owing to its very low relative intensity, this structure is in other cases very easily hidden in the background. For example, the oscillations are symmetric around the position of the B-state resonance, but on the high-energy side all but the first side band are completely covered by the excitation yield due to direct transitions to the B' and higher lying Rydberg states. Thus these oscillations are almost only visible on the low-energy side where due to energy conservation no excited state (B is the lowest-lying one) can directly be populated, while the B state can be reached due to the spectral width of the $\cos^2$-shaped pulse.

The features and trends discussed above mainly for the 2-photon ionization regime (including the range of (1+1)-REMPI processes and the 1-photon ionization threshold) occur also for the other energy ranges considered, but there they are less clearly visible. A better visibility and linearity of the spectrum with respect to the number of photons involved (in a perturbative picture) is obtained, if the yields are shown as a function of the photon wavelength as is done in the middle (lower) panels of Figs. 7.4 and 7.5 for the ionization (excitation) yields. In all considered regimes up to five photons the longer pulses lead to better resolved REMPI peaks and sharper cut-offs at the multi-photon thresholds.

Figures 7.4 and 7.5 show also the results for perpendicular orientation (and $R = 1.40\,a_0$). Clearly, the overall spectra look very similar for parallel and perpendicular orientation, if a logarithmic scale is used. In the case of 10-cycle pulses both parallel and perpendicular excitation yields show clearly one-photon absorption to the electronic excited states in the energy window of 11 to 16 eV. It is, of course, different electronic states that are excited in the two cases, since the dipole selection rule leads to the excitation of $^1\Sigma_g$ states for parallel and of $^1\Pi_u$ states for perpendicular orientation. Noteworthy, the corresponding ionization yield shows almost no trace of enhancement in this energy window, although the excitation to the lowest lying C state is only a factor 2 to 3 lower than the one to the B state, and the excitation to the higher lying states is practically identical.

For the 30-cycle pulses REMPI peaks become clearly visible in this energy window, but they are much weaker than the corresponding peaks obtained for parallel orientation, despite the again very similar excitation yields for the corresponding resonant states. This indicates that the one-photon ionization of the Π_u states (C, C', etc.) with linear-polarized laser light perpendicular to the molecular axis possesses a much lower probability than the corresponding process for the Σ_u states using parallel orientation. Such a pronounced difference between the resonantly-enhanced ionization yield and the excitation yield of the resonant state is, however, only observed for the (1+1)-REMPI processes. Already in the 3-photon regime in which (2+1)-REMPI processes occur the ionization enhancement is to a good approximation proportional to the excitation yield, if REMPI-processes in parallel and perpendicular direction are compared. Within the same orientation (either parallel or perpendicular) the REMPI enhancement is now larger for the dominant excitation peak (at lower energy) than for the one at higher energy.

7.4.3. Analysis of the ionization anisotropy

In fact, as already mentioned, if the region containing (1+1)-REMPI processes is ignored, the parallel and perpendicular ionization yields are very similar. This is even the case for the excitation yields that are only slightly shifted with respect to each other due to

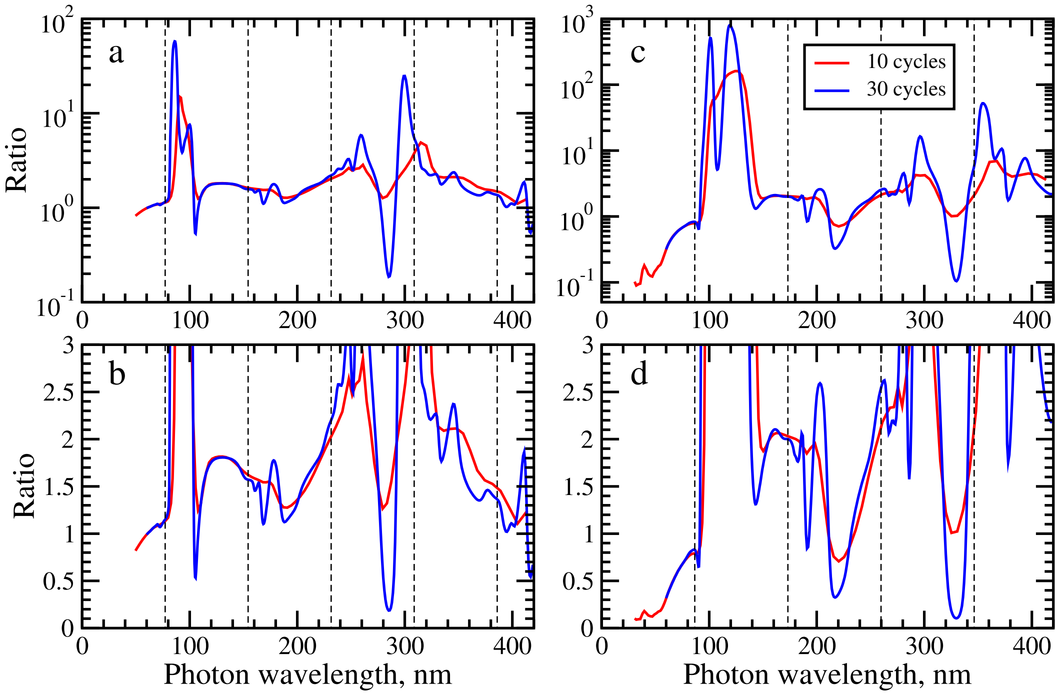

Figure 7.7.: Ratio of the ionization yields for parallel and perpendicular orientation for the internuclear distances $R = 1.4\,a_0$ (a,b) and $R = 2.0\,a_0$ (c,d) on either a logarithmic (a,c) or a linear (b,d) scale. Shown are the results for 10-cycle laser pulses with peak intensity 10^{13} W/cm^2 (red) and for 30-cycle pulses with peak intensity $5 \cdot 10^{12}$ W/cm^2 (blue). (Published in [34].)

the energy differences of the bound states with different angular momentum Λ. A closer look reveals that apart from the the 1-photon regime where parallel and perpendicular yields are almost identical (except the ionization yields at very high photon energies where perpendicular orientation gives higher yields) the ionization and excitation yields are rather uniformly larger for parallel than for perpendicular orientation. The ratio between parallel and perpendicular ionization yields is shown in Fig. 7.7 a for the 10- and 30-cycle pulses (and $R = 1.40\,a_0$). Despite some sharp resonant features that are better resolved for the longer pulses the ratio is rather independent of the pulse duration and varies in between about 1.5 and 2.5 in the whole 2- to 5-photon regime. This overall finding is in reasonable agreement with the corresponding results of 2- and 3-photon lowest-order perturbation theory in [84].

In a recent time-dependent SAE study [204] a rather large deviation to the LOPT result in [84] was found for a photon energy of 10.85 eV ($\approx$ 115 nm). The ratios parallel to perpendicular were about 20 [204] or 1.8 [84]. As is clearly visible from Fig. 7.7, the ratio varies rather drastically around this wavelength. The present work gives a ratio of 1.6 at this photon frequency. However, it increases to about 1.8 already at a wavelength of about 120 nm. On the other hand, in between about 115 and 105 nm the ratio drops down to 0.5 before it sharply increases at about 100 nm. As can be especially seen from Fig. 7.5 a, the reason for this pronounced variation of the ratio is the fact that there is a minimum in the ionization yield for parallel orientation close to this photon energy which may be caused by an interference with the REMPI peak caused by the B state. This minimum together with the REMPI peak that occurs for slightly lower energies than the one due to the C state (perpendicular orientation) leads to the sharp minimum followed by a sharp maximum, if the photon wavelength approaches the region around 125 nm from above. Clearly, depending on the accuracy of the transition energy to the B state provided by a particular electronic-structure model very different results may be obtained for the ratio between parallel and perpendicular orientation at a wavelength around 115 nm.

Similarly, it is difficult to compare to the other recent work discussing orientational dependence of the ionization behavior of H_2 within TD-DFT [205]. The present results agree to that work in the sense that no pronounced (order-of-magnitude) difference between the parallel and perpendicular orientation is found. However, the results in [205] are either close to saturation of single ionization (Fig. 4) or the corresponding value at $R = 1.4\,a_0$ is barely readable from the graph (Fig. 5). Furthermore, at the considered wavelength of 266 nm there is some structure due to REMPI peaks. Therefore, the exact result depends again critically on the corresponding excitation energies (and spectral width of the laser pulse). Noteworthy, the present calculation confirms resonant structure at this wavelength as is also noted (for this R value) in [205].

It is usually assumed that few-photon processes depend heavily on the electronic structure, if not too high intensities are considered, while many-photon processes depend mostly on the ionization potential and shape of the long-range potential experienced by the ejected electron. Accordingly, one would not expect an atomic model like the one described in Sec. 7.3 to yield ionization and excitation yields in reasonable agreement to a full molecular calculation for few-photon processes. However, as is evident from Figs. 7.4 and 7.5, the overall agreement even of the excitation yield is in fact surprisingly good. The ionization yield agrees in the 1-photon regime almost perfectly with the molecular result for perpendicular orientation. Especially for the 30-cycle pulses the agreement continues in the 2-photon regime until the second REMPI peak where the atomic model agrees quantitatively much better with the parallel result. At the threshold between 2- and 3-photon ionization (at about 155 nm) all three curves agree very well for both pulse lengths. Once the parallel and perpendicular results start to disagree, the atomic result follows now more closely the molecular results for parallel orientation. Starting at about 360 nm the atomic results disagree with the molecular ones that agree at these wavelengths rather well with each other. A very similar result is also found for the excitation yields. This confirms that even the position (and dipole moments) of the excited states are very well approximated by the atomic model proposed in this work.

7.4.4. Results for $R = 2.0\,a_0$

Finally, it is interesting to investigate whether the findings reported so far apply only to the case when the internuclear distance is relatively small and thus the ground-state electron density is rather isotropic. A second series of calculations was thus performed in which $R = 2.0\,a_0$ was used. The results are given in Figs. 7.8 and 7.9 as well as in the right panel of Fig. 7.7. This choice of R is motivated by the fact that the ground vibrational wavefunction of H_2 extends to about this distance and it is at the same time the equilibrium distance of the H_2^+ ion created in the ionization process.

Most evidently, the 1- and 2-photon ionization yields disagree for the two orientations much more than for $R = 1.40\,a_0$. Only at the threshold between the two regimes reasonable to good agreement is found. While the 1-photon yield for parallel orientation lies below the perpendicular one, this changes drastically in the 2-photon regime. The latter difference seems to be mainly due to the now even much more pronounced REMPI peaks for parallel orientation. Noteworthy, the excitation yields are very similar for the two orientations, besides the energy shifts due to different excitation energies. In the regimes of 3- to 5-photon ionization the qualitative difference between the two orientations is less pronounced than in the 2-photon case. Compared to $R = 1.4\,a_0$ it is especially the quantitative agreement between the two orientations which becomes worse, if R increases. This is also seen from the corresponding ratio (Fig. 7.7) which covers a larger range of values in this case. It is also interesting to note that a comparison of the results for $R = 1.4$ and $2.0\,a_0$ shows that there is quite good qualitative agreement. The main difference is that with increasing R value the excitation energies become smaller. Together with a decrease of the vertical ionization potential when going from $R = 1.4$ to $2.0\,a_0$ this leads to an effective compression of the wavelength ranges for a given N-photon regime. The results of the atomic model agree not as well with the molecular yields for larger than for smaller R, as is expected. Nevertheless, the atomic model still works reasonably well for a qualitative or even semi-quantitative estimate.

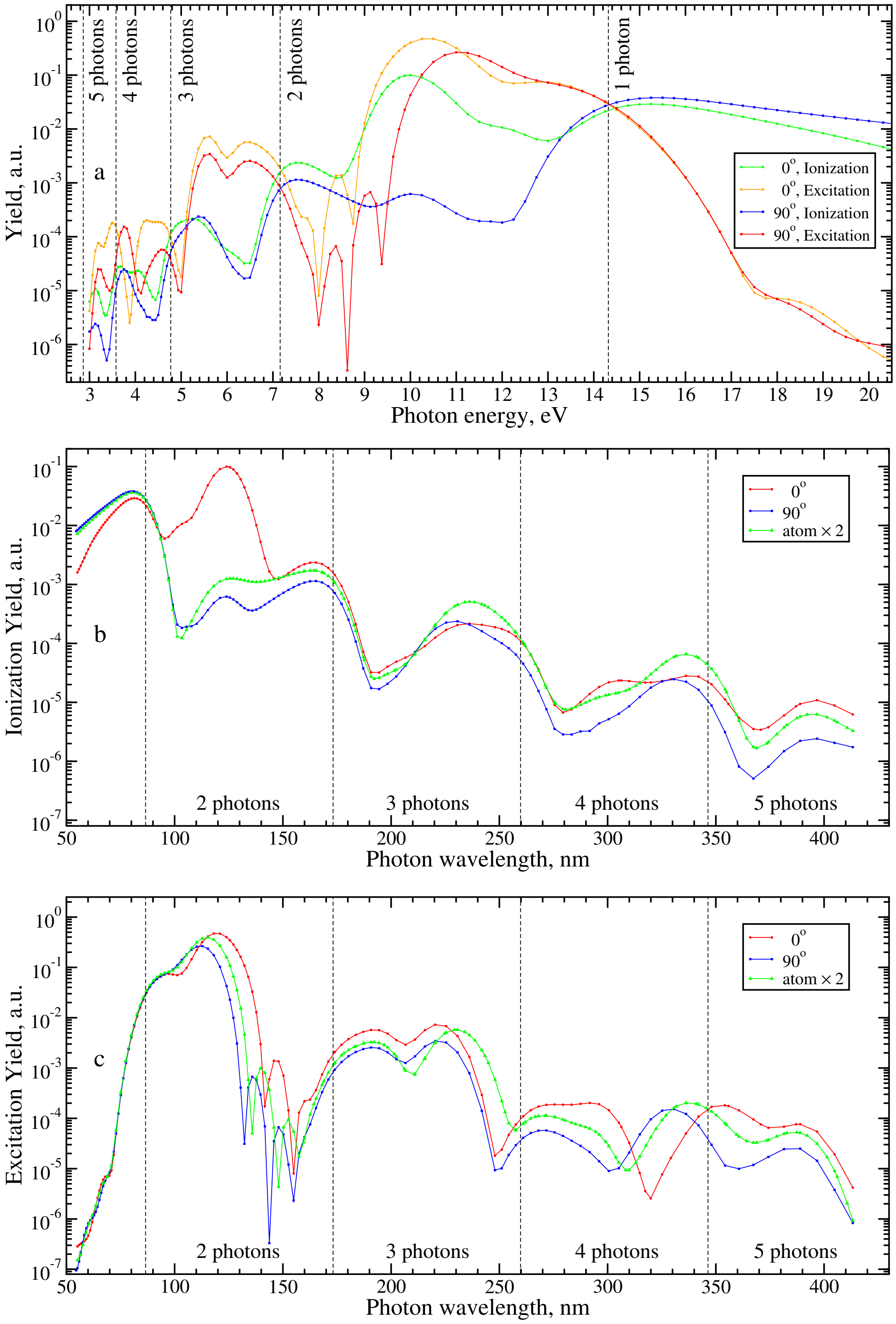

Figure 7.8.: As Fig. 7.4, but for internuclear distance $R = 2.0\,a_0$. (Published in [34].)

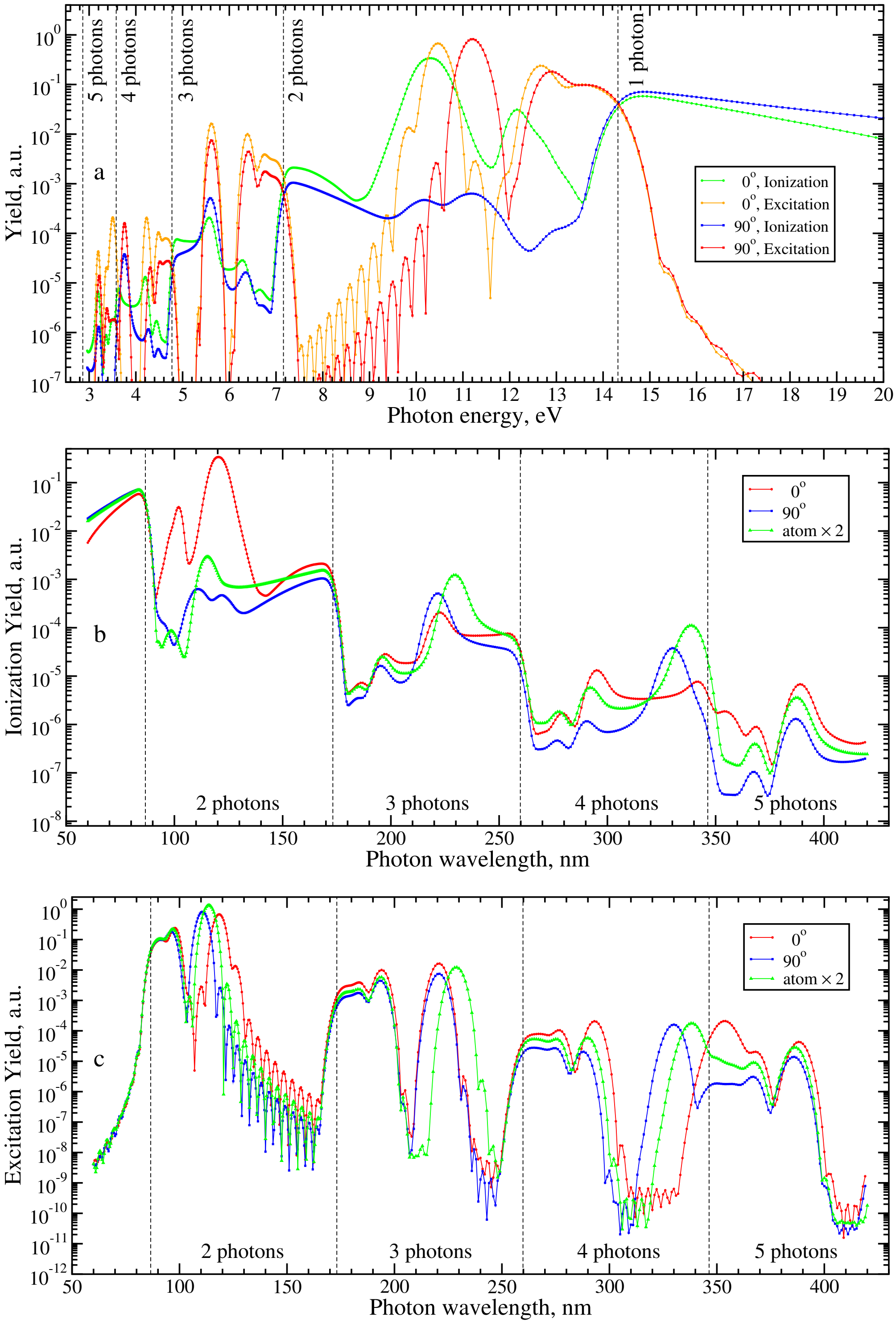

Figure 7.9.: As Fig. 7.5, but for internuclear distance $R = 2.0\,a_0$. (Published in [34].)

7.5. Ionization of H_2 and D_2 by frequency-doubled Ti:Sapphire laser pulses

This section investigates the intense-field single ionization of molecular hydrogen or deuterium oriented either parallel or perpendicular to ultrashort linear-polarized laser pulses with a wavelength of 400 nm, as they are, e. g., experimentally available from a frequency doubling (second-harmonic generation) of a titanium:sapphire laser source. Besides the experimental relevance, the chosen wavelength is also of theoretical interest, since one expects six-photon ionization processes to dominate which lie somehow in the middle between few-photon and many-photon regimes. Thus one expects neither a simple perturbative nor the quasistatic approximation to be applicable. This ambivalent character is shown to be clearly visible, since, e. g., the ionization yield shows a pronounced dependence on the internuclear separation (as is expected for the quasistatic regime), but also clear structures due to resonance-enhanced multiphoton ionization (REMPI). Because of the high intensity of the laser field, the ionization yield in the case of REMPI is sensitive to the position of resonant states in the field, and thus to their AC Stark shifts.

In order to be able to compare the theoretical results for the hydrogen molecule with an experiment, the dependence of the ionization process on the internuclear distance R has to be carefully considered. This is especially important when studying the asymmetry of ionization due to different orientations of molecular axis to the polarization axis of the linear polarized laser field. So far, the ionization asymmetry for diatomic molecules has been theoretically studied only at the equilibrium internuclear distance R_0, where the ground vibrational state of the molecule has the maximum of the probability density. This section sheds light on how significant is the quantum-mechanically unavoidable zero-point vibrational motion for the analysis of the ionization asymmetry.

When discussing REMPI for ultrashort intense laser pulses, it is important to look on the time scale of the process. Therefore, the study is performed for three different durations of the pulse. For the sake of simplicity, all calculations presented in this section were performed with N-cycle $\cos^2$-shaped linear-polarized laser pulses with $N = 10, 20$, and 40. For a wavelength of 400 nm the FWHM of intensity of such pulses corresponds to about 5, 10, and 20 fs. For this regime the calculations are performed using the basis set A. For the perpendicular orientation only molecular symmetries with the absolute value of the component of the total angular momentum along the internuclear axis $0 \leqslant \Lambda \leqslant \Lambda_{\max} = 7$ were included in the time propagation. Note, that the adopted value of $\Lambda_{\max}$ does not only guarantee the convergence of ionization yields, but also provides a reasonable convergence of photoelectron energy spectra.

7.5.1. Integration over internuclear separations

Once the TDSE is solved within the fixed-nuclei approximation for various fixed internuclear separations R of the H_2 molecule exposed to linear-polarized laser pulses with the angle θ between the internuclear and the polarization axis, the ionization yield $Y_{\mathrm{ion}}(R,\theta)$ can further be used to calculate the ionization yield $Y_{\mathrm{ion}}^{(\nu)}(\theta)$ of H_2 (as well as D_2) in a given vibrational state ν described by the vibrational wavefunction $\phi_\nu(R)$. Indeed, if the pulse duration is sufficiently short and depletion of the state during the pulse is insignificant, one can neglect the motion of the wavepacket created during the pulse. Then the transition probability to a vibrational level ν' of the molecular ion which is defined as [131]

$$Y_{\mathrm{ion}}^{(\nu)}(\theta,\nu') = \left| \int \mathrm{d}R\, Y_{\mathrm{ion}}(R,\theta)^{1/2}\, \phi_\nu(R)\, \chi_{\nu'}(R) \right|^2, \tag{7.15}$$

can further be used to calculate the total ionization yield

$$\begin{aligned} Y_{\mathrm{ion}}^{(\nu)}(\theta) &= \sum_{\nu'} Y_{\mathrm{ion}}^{(\nu)}(\theta,\nu') \\ &= \sum_{\nu'} \iint \mathrm{d}R\, \mathrm{d}R'\, Y_{\mathrm{ion}}(R,\theta)^{1/2}\, Y_{\mathrm{ion}}(R',\theta)^{1/2}\, \phi_\nu(R)\, \phi_\nu^*(R')\, \chi_{\nu'}(R)\, \chi_{\nu'}^*(R') \\ &= \iint \mathrm{d}R\, \mathrm{d}R'\, Y_{\mathrm{ion}}(R,\theta)^{1/2}\, Y_{\mathrm{ion}}(R',\theta)^{1/2}\, \phi_\nu(R)\, \phi_\nu^*(R')\, \delta(R-R') \\ &= \int \mathrm{d}R\, Y_{\mathrm{ion}}(R,\theta)\, |\phi_\nu(R)|^2 \end{aligned} \tag{7.16}$$

where the closure property of the orthonormal set of final vibrational states of the molecular ion,

$$\sum_{\nu'} \chi_{\nu'}(R)\, \chi_{\nu'}^*(R') = \delta(R-R') \tag{7.17}$$

has been used.

Application of Eq. (7.16) is further based on the assumption that the molecule has no time to rotate during the pulse and neglect distortion of the electronic ground-state potential curve due to the external field. The latter assumption implies that the index ν of vibrational state should be sufficiently small. In the following, only $\nu = 0$ is considered, but for the two isotopes H_2 and D_2 with their different vibrational wavefunctions (Fig. 7.10). Due to the larger mass the D_2 vibrational ground state is more compact

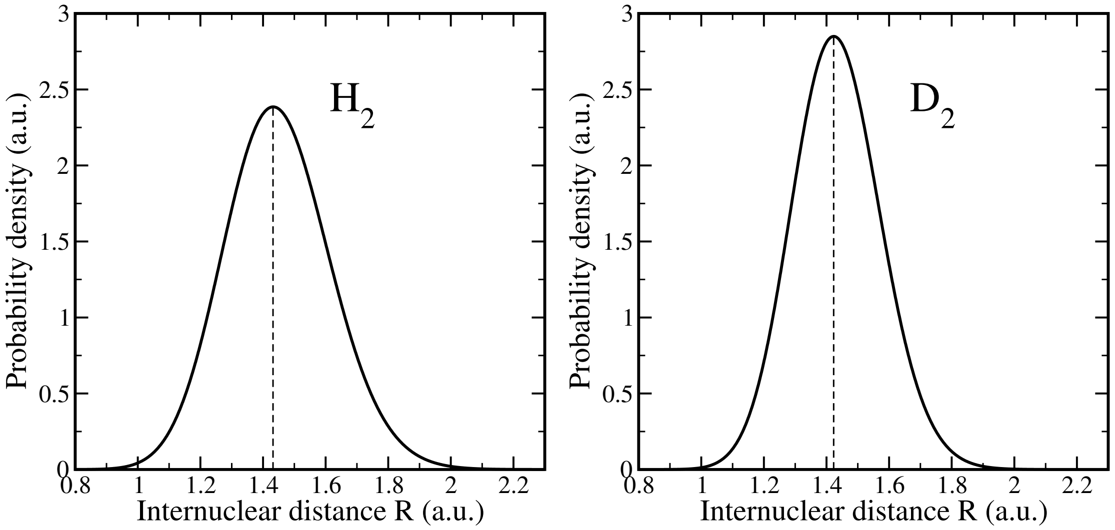

Figure 7.10.: The probability densities of the ground vibrational states of the H_2 (left) and D_2 (left) molecules. The maximum of each probability density is indicated by a vertical dashed line.

than the one of H_2, while the positions of the maximum of the probability density are almost the same ($1.432\,a_0$ for H_2 versus $1.423\,a_0$ for D_2).

7.5.2. Field-induced resonances

For the following discussion of the orientation dependence and isotope effects, it is helpful to obtain a more detailed understanding of the influence of such parameters as peak intensity and wavelength of the pulse or of the internuclear separation on the positions of REMPI peaks and the N-photon ionization thresholds. In order to be able to correctly predict REMPI through some resonant electronic state in intense laser pulses, it is necessary to know the field-induced shift of the resonant state, what is a challenging task by itself. However, if the field is sufficiently intense, one can assume that the field-induced shift (dynamically induced Stark shift) of excited states is almost equal to the ponderomotive energy (remember the discussion in Sec. 6.4.2). With this assumption and using the field-free transition energies of the present CI calculation the positions of the REMPI peaks are expected to depend on the laser parameters and internuclear separation as shown in Fig. 7.11.

The dependence of the expected positions of the REMPI peaks and N-photon ionization thresholds on the internuclear distance R for a 400 nm laser field is given in Fig. 7.11 a. In

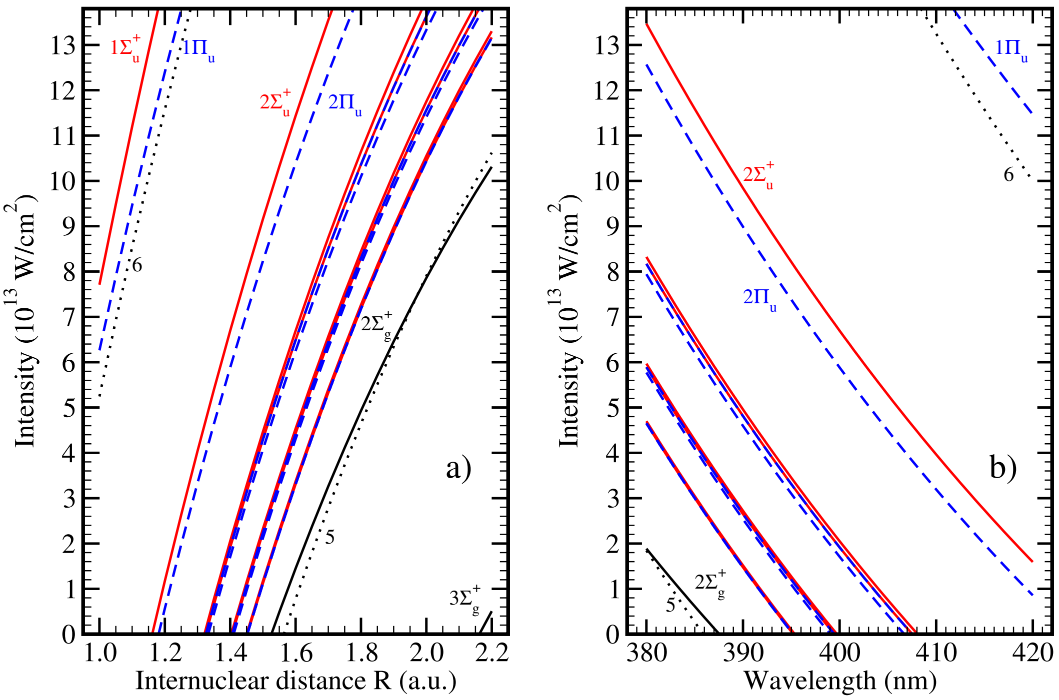

Figure 7.11.: Expected positions of REMPI peaks and N-photon ionization thresholds. Dependence of the resonant intensities I (a) on the internuclear distance R for pulses with a wavelength of 400 nm and (b) on wavelength for the fixed internuclear distance $R = 1.4\,a_0$. Positions of REMPI peaks due to Σ_u^+ (red solid), Π_u (blue dashes), or Σ_g^+ (black solid) intermediate states are shown. Also shown are the N-photon ionization thresholds (dotted lines, with N explicitly indicated in the graph). (Published in [35].)

this R range the ionization process can be referred to as 5-photon (7-photon) ionization in the bottom-right (top-left) part of the figure, or as 6-photon ionization otherwise. Different kinds of REMPI peaks are expected: (5+1) REMPI peaks through $n\Sigma_u^+$ or $n\Pi_u$ electronic states with $n > 1$, (5+2) REMPI peaks through the $1\Sigma_u^+$ or $1\Pi_u$ states, a (4+1) REMPI peak through the $3\Sigma_g^+$ state, and a REMPI peak through the $2\Sigma_g^+$ state. Note, that in the last case the expected position of the resonance crosses the expected position of the 5-photon ionization threshold. Therefore, the resonance can be referred to as (4+1) REMPI for peak intensities smaller than $7.5 \times 10^{13}\,\mathrm{W/cm^2}$, and as (4+2) REMPI for higher intensities. Evidently, the correct character of the resonance is sensitive to the exact intensity dependence of the field-induced shift of the $2\Sigma_g^+$ state, and thus a non-trivial behavior is expected. A similar conclusion is valid for the REMPI through the $1\Sigma_u^+$ or $1\Pi_u$ electronic states, since their exact REMPI positions could in fact cross the 6-photon ionization threshold.

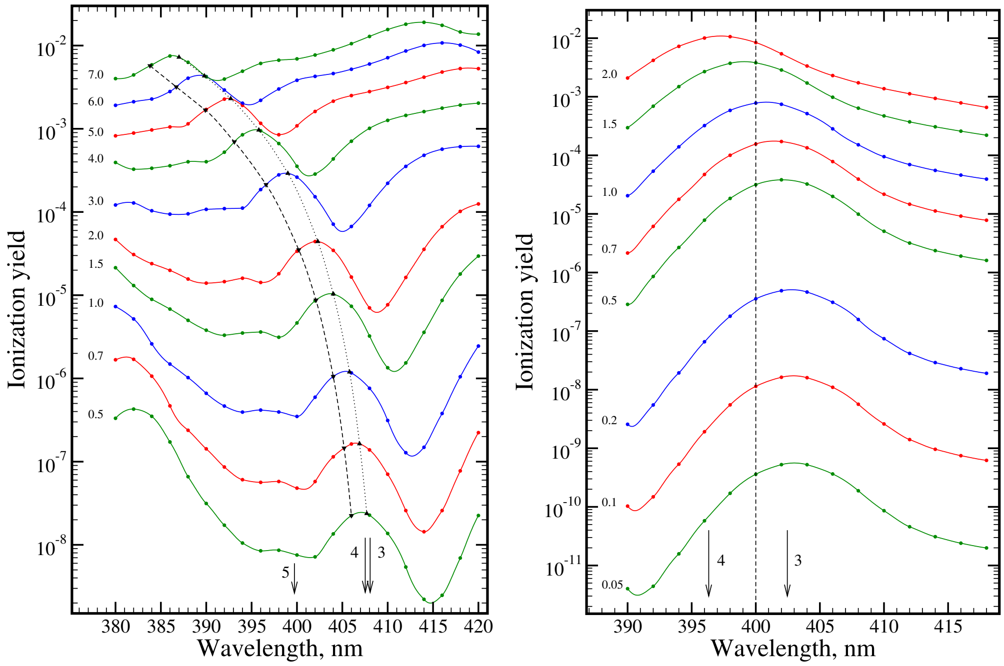

(a) $R = 1.4\,a_0$ (b) $R = 2.2\,a_0$

Figure 7.12.: Wavelength-dependent ionization yields for a parallel orientation of an H_2 molecule at the fixed internuclear distances (a) $R = 1.40\,a_0$ and (b) $R = 2.20\,a_0$ for various peak intensities (specified in units of $10^{13}\,\mathrm{W/cm^2}$) of 40-cycle $\cos^2$-shaped pulses. The arrows indicate the resonant wavelengths (in the low-intensity limit) of REMPI peaks due to $n\Sigma_u^+$ (a) and $n\Sigma_g^+$ (b) intermediate states. The expected (dashes) and found (dots) position of a REMPI peak is also given in (a). (Published in [35].)

Similarly, Fig. 7.11 b shows the dependence of expected positions of REMPI peaks and N-photon ionization thresholds on the laser wavelength for the fixed internuclear distance $R = 1.4\,a_0$. With larger peak intensity the increasing ponderomotive energy leads to an increase of the transition energy between the initial and the resonant state. This increase can be compensated by the increase of the photon energy, and thus the new REMPI position will occur at a smaller wavelength. The calculations at a fixed internuclear separation are more suitable for the investigation of the validity of the assumed field-induced shift of electronic states, since in this case identical sets of field-free electronic wavefunctions are used in the time propagation. For this purpose, a series of 210 calculations for a parallel-oriented H_2 molecule with fixed internuclear distance $R = 1.4\,a_0$ exposed to laser pulses with a total duration of 40 cycles was performed for 21 different values of the wavelength and 10 different values of the peak intensity. The results are shown in Fig. 7.12 a, where every point represents the outcome of one full

TDSE calculation, and curves join the results obtained for the same peak intensity.

Figure 7.12 a shows a pronounced peak whose position moves from 407 nm for a peak intensity of 5×10^{12} W/cm^2 to 387 nm for a peak intensity of 7×10^{13} W/cm^2. From Fig. 7.11 b it follows that this peak can be assigned to REMPI through either one or both of the closely lying $3\Sigma_u^+$ and $4\Sigma_u^+$ electronic states, since the spectral width of the Fourier-limited pulse is too broad to resolve these two resonances. Clearly, the intensity-dependent shift of the peak position is overestimated by the already mentioned simple prediction based purely on the ponderomotive energy ($\delta E(I) = U_p$). Instead, the found intensity dependence of the field-induced energy shift can be well fitted by $\delta E(I) = 0.9U_p - 0.002$. At intensities 5×10^{12} W/cm^2 and smaller it appears as the energy shift of these low-lying excited states (responsible for the REMPI) is already absent. The position of the REMPI peak agrees then much better with the low-intensity limit than with the prediction based on U_p, since the latter would predict a shift of about 2 nm. Such a shift by about 2 nm is, however, found for the (poorly resolved) REMPI peak due to the higher lying $5\Sigma_u^+$ intermediate state. This demonstrates that in the investigated regime of laser parameters different excited states behave differently, and a common prediction for all excited states is impossible.

Figure 7.12 b shows again the results of a series of (this time 120) calculations for a parallel-oriented H_2 molecule, but for the larger internuclear separation $R = 2.2\,a_0$. In this case the spacing of the $3\Sigma_g^+$ and $4\Sigma_g^+$ states that could lead to (4+1) REMPI is rather large, and thus the pronounced peak in Fig. 7.12 b can be entirely assigned to REMPI through the $3\Sigma_g^+$ state. Although the peak position clearly shifts to smaller wavelengths with increasing laser peak intensity, the shift becomes visible only for rather large intensities. As a consequence, the peak position crosses 400 nm at an intensity higher than 10^{13} W/cm^2, whereas according to Fig. 7.11 a the crossing should have occurred at an intensity that is smaller by a factor 2. Thus, although the positions presented in Fig. 7.11 give a satisfactory explanation of the main features, they should only be considered as a rough estimate.

7.5.3. *R*-dependent ionization

If strong-field ionization of H_2 or D_2 initially in their vibrational ground states is considered, it is important to investigate the dependence of the ionization on the internuclear separation R within an R range in which the vibrational wave function is nonvanishing (Franck-Condon window). Therefore, the TDSE describing H_2 within the fixed-nuclei approximation was solved for 25 different values of R (in between $1.0\,a_0$ and $2.2\,a_0$ with a step size of $0.05\,a_0$). This was repeated for 15 different values of peak intensities (in a range from 2×10^{13}W/cm^2 to 1.3×10^{14}W/cm^2).

Figure 7.13 a (left panel) shows the obtained results for a parallel orientation of the molecular axis with respect to the polarization vector and 40-cycle $\cos^2$-shaped (FWHM of about 20 fs) laser pulses. Two main features may be observed. First, the ionization yield increases with R. Second, pronounced structures are visible. The importance of both effects decreases with intensity. The increase with R was first predicted in the quasistatic regime [206]. Its occurrence at 400 nm shows that even for this wavelength clear strong-field phenomena are observable beyond a pure multiphoton picture. On the other hand, the observed structures are due to classical multiphoton phenomena (channel closings and REMPI).

Some pronounced REMPI peaks are visible that should be compared with their predicted positions in Fig. 7.11. The peaks at $R = 1.2\,a_0$ and $R = 1.4\,a_0$ for a laser peak intensity of 2×10^{13}W/cm^2 can thus be assigned to (5+1) REMPI through the $2\,\Sigma_u^+$ and $3-4\,\Sigma_u^+$ states, respectively. The position of the latter peak changes with the peak intensity almost in the expected way as has also been demonstrated in Fig. 7.12 a. On the other hand, the position and amplitude of the REMPI peak arising from the $2\,\Sigma_u^+$ resonant state cannot easily be understood. For a peak intensity of 10^{14}W/cm^2 this REMPI peak is located at $R = 1.6\,a_0$ instead of the expected value of $1.5\,a_0$. Interestingly, the amplitude of the peak that is very large at small intensities is becoming very small for higher intensities, as one may expect when going from the multiphoton in the direction of the quasistatic regime. For intensities between 4×10^{13}W/cm^2 and 6×10^{13}W/cm^2 one can observe something similar to a splitting of the REMPI peak into two peaks. This behavior can evidently not be explained using Fig. 7.11. It is also difficult to explain the pronounced peak located at $R = 1.4\,a_0$ for the highest laser peak intensity (1.3×10^{14}W/cm^2). According to Fig. 7.11 no peak should occur for these values of R and I, since it lies in between the expected positions of the $1\,\Sigma_u^+$ and the $2\,\Sigma_u^+$ REMPI peaks. This may indicate some field-induced coupling of these states and thus a clear strong-field phenomenon. It is also interesting to note that the channel closings indicating the transitions from 5- to 6-photon ionization and from 6- to 7-photon ionization are visible, but not very pronounced. Furthermore, due to the REMPI peaks the channel thresholds are sometimes difficult to identify in the shown ionization yields.

In order to consider the influence of vibrational motion onto the strong-field ionization yields, the results obtained for a fixed nuclear orientation are weighted with the

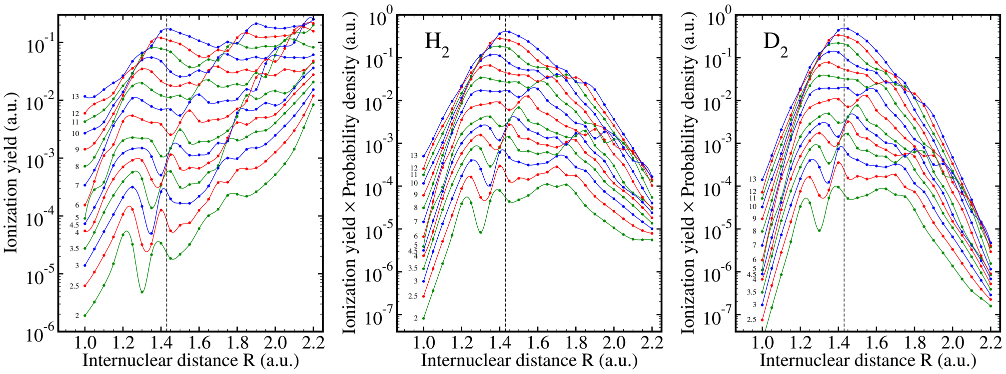

(a) Parallel orientation of the internuclear axis to a linear polarized laser field

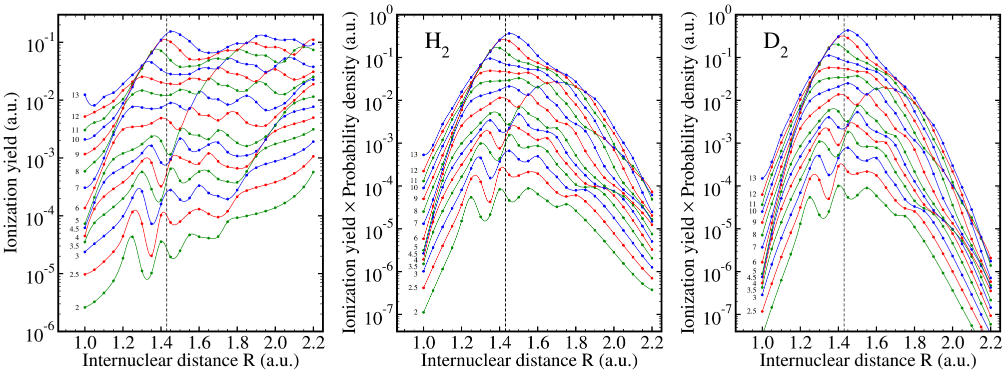

(b) Perpendicular orientation of the internuclear axis to a linear polarized laser field

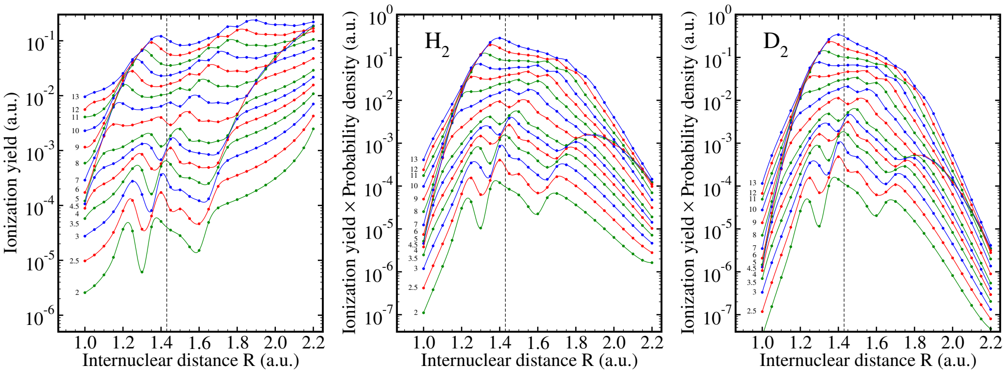

(c) Atomic model calculations (multiplied by a factor 2)

Figure 7.13.: Ionization yields for 40-cycle $\cos^2$-shaped (20 fs) laser pulses with a wavelength of 400 nm and different peak intensities (specified in the graphs in units of 10^{13} W/cm^2). The upper (middle) panel shows the results for a parallel (perpendicular) orientation, while the lower panel shows the results obtained with the atomic model potential in Eq. (7.11). The left panel shows the fixed-nuclei ionization yields, whereas the middle and right panels display the weighted ionization yields for H_2 and D_2, respectively. (Published in [35].)

probability density of the ground vibrational state [see integrand of Eq. (7.16)]. The corresponding result for H_2 is shown in the middle panel of Fig. 7.13. Only in the case of the highest laser peak intensity considered in this work, the maximum of the weighted ionization yield agrees with the maximum of the vibrational wave function. At slightly lower intensities (until about $8 \times 10^{13}\mathrm{W/cm}^2$) the weighted ionization yield is largest for smaller values of R, while for even lower intensities the REMPI peaks due to the $3\,\Sigma_u^+$ and $4\,\Sigma_u^+$ states determine the maximum of the weighted ionization yield. At the lowest laser peak intensity considered ($2 \times 10^{13}\mathrm{W/cm}^2$) the highest weighted ionization yield is found at around $R = 1.7\,a_0$. This maximum should be due to an opening of the 5-photon regime and may be further increased by (4+1) REMPI processes. At this intensity one notices also a very slow decrease of the weighted ionization yield for R values above $2\,a_0$, despite the fact that the vibrational wave function has a very small amplitude. The reason is the already discussed $3\,\Sigma_g^+$ REMPI peak (Fig. 7.12 b).

In the case of D_2 (left panel of Fig. 7.13 a) the narrower vibrational distribution is, however, sufficient to dominate over the resonant effect. In this case the weighted ionization yield decreases rather pronouncedly for internuclear separations larger than $2.0\,a_0$. Close to the minimum of the electronic potential curve at about $1.4\,a_0$ the weighted ionization yields are, however, very similar for H_2 and D_2. Also for D_2 the ionization yield peaks only for the highest intensity considered here at the maximum of the vibrational wavefunction. Consequently, the Franck-Condon approximation would not describe the vibrational distribution of the formed H_2^+ ions properly. A proper calculation of these distributions has to include the effects of channel closings and REMPI, but also of the general increase of the ion yield as a function of internuclear separation. Neither a pure multiphoton nor quasistatic prediction is thus sufficient.

7.5.4. Orientational dependence

For a perpendicular orientation of the molecule with respect to the field (Fig. 7.13 b) the R-dependent ionization yield (left panel) looks on the first glance surprisingly similar to the one for the parallel orientation. For the lowest intensities shown the spectra comprise very pronounced peaks at about $R = 1.25\,a_0$ and $R = 1.4\,a_0$ that can be assigned to (5+1) REMPI through the $2\,\Pi_u$ and the $3-4\,\Pi_u$ states, respectively. It is a peculiarity of H_2 that already the lowest lying excited states of ${}^1\Sigma_u$ and ${}^1\Pi_u$ symmetry and thus REMPI peaks through those states lie energetically very close together. In contrast to the results for parallel orientation a third peak at $R = 1.55\,a_0$ is, however, also well resolved. From Fig. 7.11 it appears very likely that this peak stems from a superposition of (5+1)

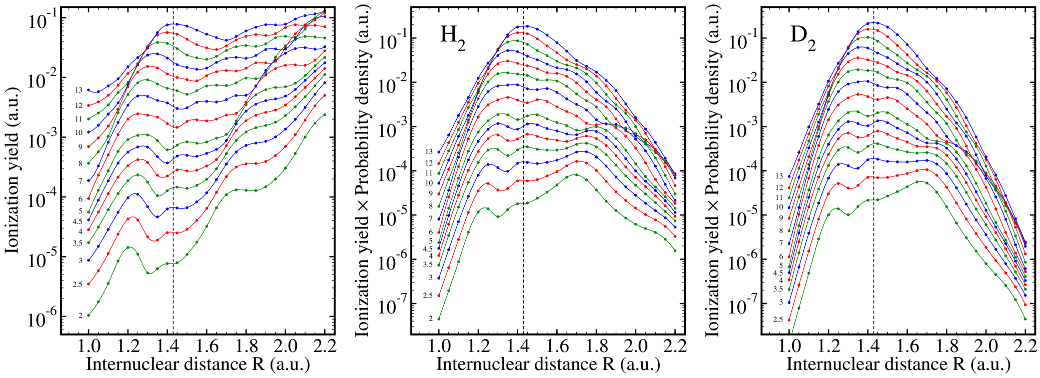

(a) Parallel orientation of the internuclear axis to a linear polarized laser field

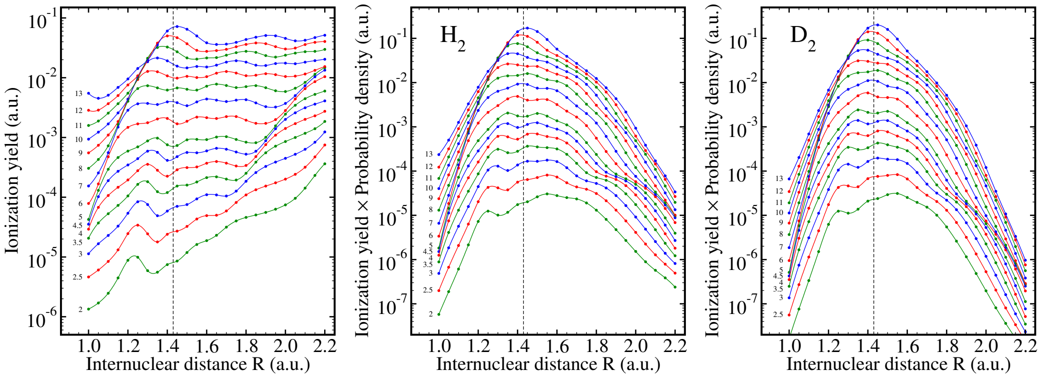

(b) Perpendicular orientation of the internuclear axis to a linear polarized laser field

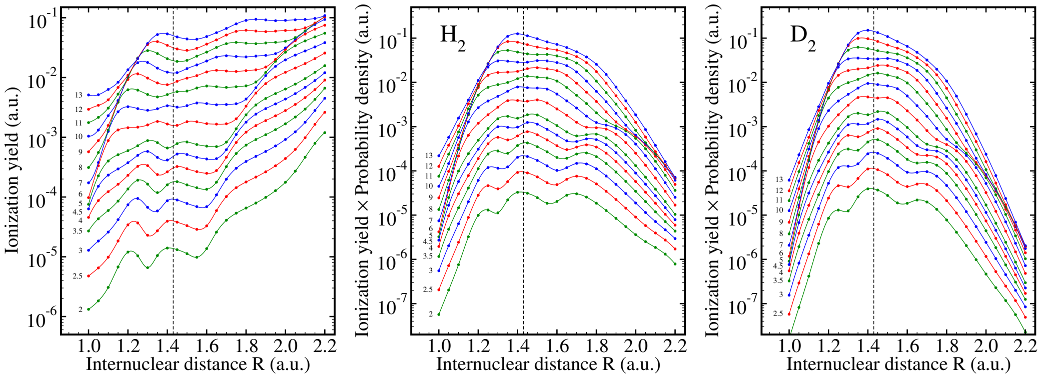

(c) Atomic model calculations (multiplied by a factor 2)

Figure 7.14.: As Figure 7.13, but for 20-cycle $\cos^2$-shaped (10 fs) laser pulses. (Published in [35].)

REMPI processes through the higher excited Π_u states. Especially at lower intensities one notices furthermore that the ionization yield does not increase that evidently for large R values than it does for a parallel orientation. The threshold between 5- and 6-photon ionization is rather well resolved and appears for the different laser peak intensities more or less at the expected R values (Fig. 7.11 a). As a consequence of the smaller slope at large R the weighted ionization yield decays for larger R values much faster for the perpendicular than for the parallel orientation for both H_2 (middle panel of Fig. 7.13 b) and D_2 (right panel).

Figure 7.13 c shows finally the ionization yield obtained with the simple isotropic one-electron model potential given in Eq. (7.11). The agreement of the R-dependent ionization yields obtained with this model and the full molecular two-electron calculation are surprisingly good, especially with the results obtained for the parallel orientation. As in the latter case, the atomic model gives a shifted threshold between the 5-and 6-photon regimes compared to the prediction according to Fig. 7.11. The atomic model yields also a rather pronounced increase in ionization for large R values, especially for low laser peak intensities as was also found for the parallel orientation. A closer look reveals, however, that for small R separations and especially for the first REMPI peak the atomic model agrees slightly better with the molecular results obtained for the perpendicular orientation. The 2nd REMPI peak defines somehow the transition line. For smaller R values the atomic model agrees better with the perpendicular results, while starting with the 2nd REMPI peak the ionization yields obtained for the atomic model and the molecular one for a parallel orientation agree better with each other. The main difference to the molecular calculations is the position of the 3rd REMPI peak that for the lowest shown intensity lies so close to the 2nd one, that it appears in the R-dependent ionization yield as a shoulder. For a laser peak intensity of $2.5 \times 10^{13}\mathrm{W/cm^2}$ the 3rd REMPI peak is shifted more than the 2nd one and is thus visible as a well separated peak. However, for higher intensities it is less well resolved due to its low probability. Despite the overall good agreement of the results for the atomic model with the full molecular calculations (on a logarithmic scale!), the weighted ionization yields still reveal differences. For example, the maximum of the weighted ionization yields for H_2 and D_2 and the largest laser peak intensities is shifted to slightly smaller R values than is found for the full molecular calculations.

A further important laser parameter is the pulse duration. Its influence is demonstrated in Figs. 7.14 and 7.15 that show the corresponding results for 20- and 10-cycle pulses (FWHM of 10 and 5 fs), respectively. The increased laser bandwidth leads to spectra that show much less details compared to the relatively long 40-cycle pulse. The ionization

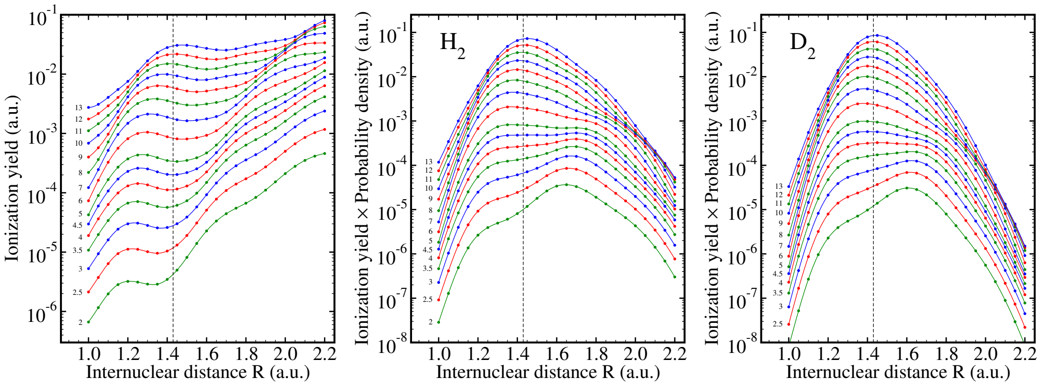

(a) Parallel orientation of the internuclear axis to a linear polarized laser field

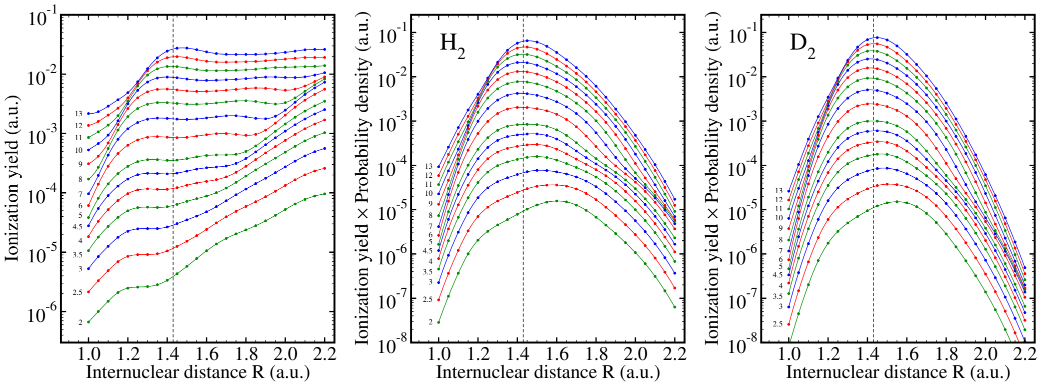

(b) Perpendicular orientation of the internuclear axis to a linear polarized laser field

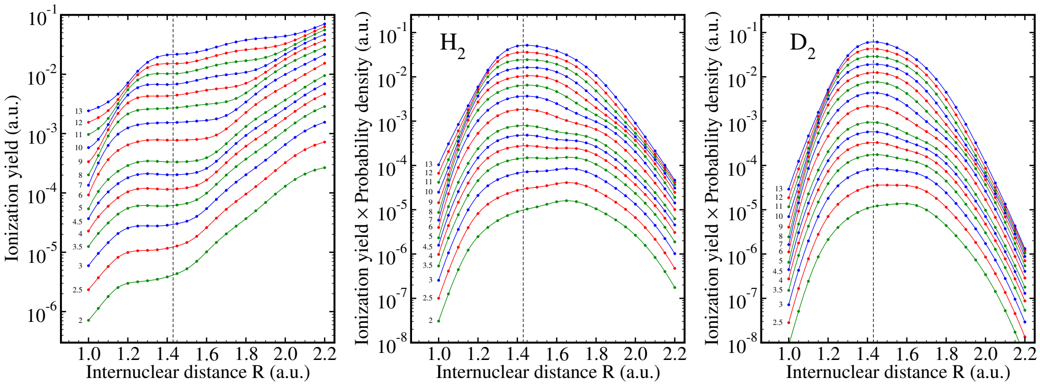

(c) Atomic model calculations (multiplied by a factor 2)

Figure 7.15.: As Figure 7.13, but for 10-cycle $\cos^2$-shaped (5 fs) laser pulses. (Published in [35].)

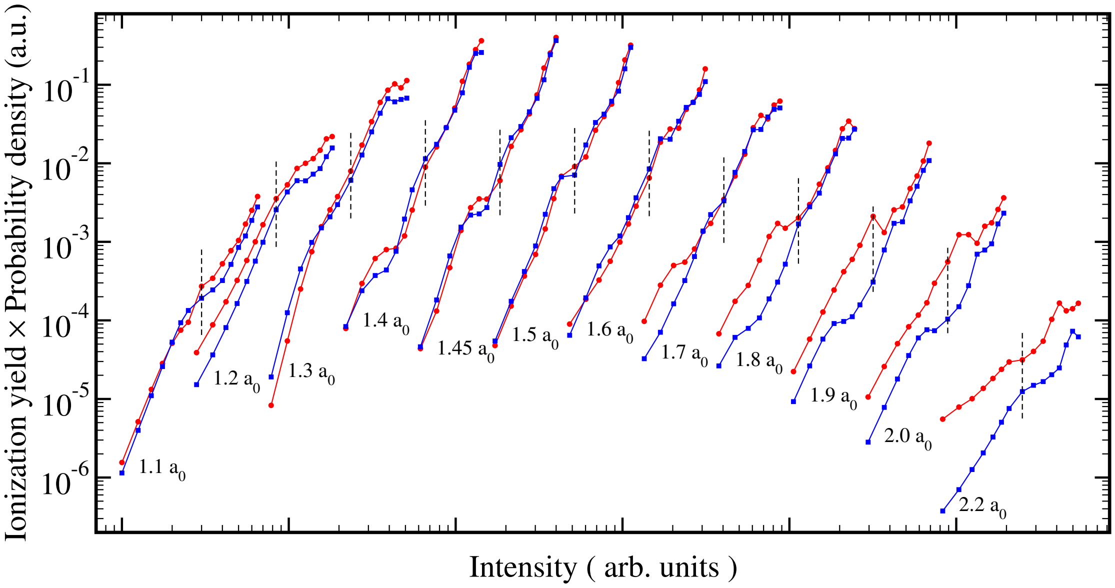

Figure 7.16.: Comparison of ionization yields (in a 20 fs laser pulse) for different internuclear distances R (weighted with the probability density of the ground vibrational state of H_2 at this R) for a parallel (red curves) and a perpendicular (blue curves) oriented H_2 molecule. The R values are specified explicitly in the figure. The vertical dashed lines indicate the position of a peak intensity 6×10^{13}W/cm^2 on the intensity axis for every corresponding pair of curves. (Published in [35].)

yields for the 10-cycle pulse show almost no evidence of REMPI peaks. The curves are fairly smooth and the remaining structures can be explained by the closing and opening of N-photon ionization channels.

Because of the different positions of the REMPI peaks for parallel or perpendicular orientations the ratio of parallel to perpendicular ionization yields may substantially change for a small variation of R. This effect is demonstrated in Fig. 7.16 in which ionization yields (multiplied with the probability density of the ground vibrational state) for parallel and perpendicular oriented H_2 molecule are compared for different internuclear distances. A log-log scale is used and the pairs of curves (parallel and perpendicular orientation for a given value of R) are shifted along the intensity axis for better readability. To guide the eye, the vertical dashed lines indicate the position of the peak intensity 6×10^{13}W/cm^2 on the intensity axis for every pair of curves. The multiplication with the probability density was performed in order to emphasize the relative contributions of different internuclear distances for the total ionization ratio between parallel and perpendicular orientations obtained after integration over R.

As can be seen from Fig. 7.16, the ionization yields for parallel and perpendicular orientation are almost equal in the range $R = 1.3-1.7\,a_0$ for a peak intensity of $6\times10^{13}\mathrm{W/cm}^2$. Whereas the ionization yield for the parallel orientation is larger than for the perpendicular one at $R = 1.3$ and $1.5\,a_0$, the opposite is found at $R = 1.4, 1.45$, and $1.6\,a_0$. At smaller values of R the parallel orientation is slightly easier ionized than the perpendicular one, while for R values larger than $1.8\,a_0$ parallel oriented molecules are much easier ionized. This is a consequence of the slower decay of the ionization yield for a parallel orientation and for large R values that was already discussed in the context of Figs. 7.13 a and b.

The key conclusion that can be drawn from Fig. 7.16 is the need for systematic studies of the intensity and internuclear-separation dependencies of the ratio between the ionization yields for parallel or perpendicular orientation as they are performed in this work, since a calculation for a single laser peak intensity and internuclear separation R can yield any possible result, i. e. the ratio between the ionization yields for parallel and perpendicular orientations may be found to be equal to 1, much smaller than 1, or much larger than 1. Depending on the choice of intensity and R very different conclusions on the orientation dependence of the ionization yield of H_2 in strong laser fields would follow.

7.5.5. Integrated ionization yields

The R-independent ionization yields for H_2 and D_2 molecules (in their vibrational ground states) are finally obtained by an integration of the weighted R-dependent ionization yields over R according to Eq. (7.16). The results for parallel and perpendicular orientation are shown for the different pulse lengths in Fig. 7.17. The curves obtained after R integration are much less structured than the fixed-nuclei ionization yields, as is evident from a comparison with Fig. 7.16). Clearly, the structures due to REMPI processes are smoothed out by the integration over R. As a consequence, the curves look almost like straight lines on the used log-log scale.

In fact, it turns out that the linear dependence on the logarithmic scale is well described, if the yield is fitted with the function

$$Y_s(I,T) = \Omega\, T\, (I/I_0)^{k_s} \tag{7.18}$$

where I is the peak intensity, $I_0 = 3.5094452\times10^{16}$ $\mathrm{W/cm}^2$ is the atomic unit of intensity, and T is the FWHM duration of the pulse in atomic units. For the fit parameters the values $\Omega = 1.55\cdot10^6$ and $k_s = 4.17$ are found. The obtained value of k_s indicates a non-

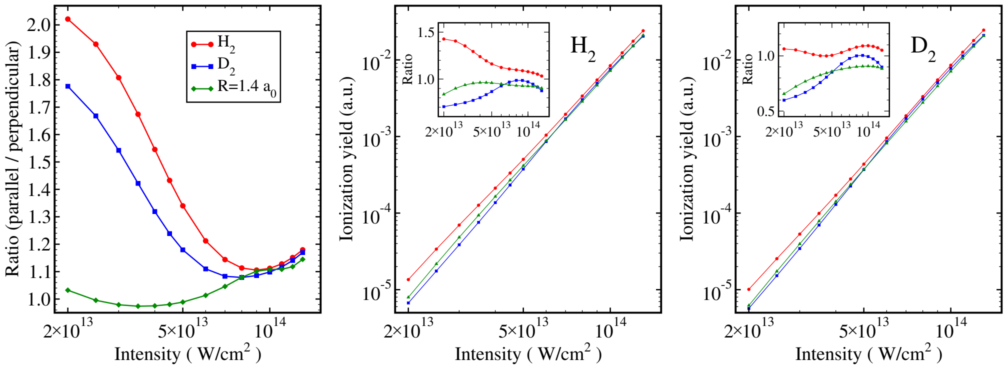

(a) 10-cycle $\cos^2$-shaped (5 fs) laser pulse

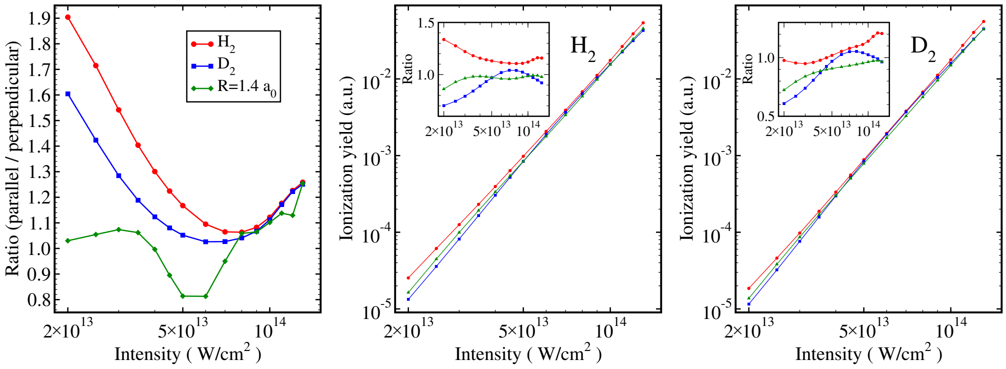

(b) 20-cycle $\cos^2$-shaped (10 fs) laser pulse

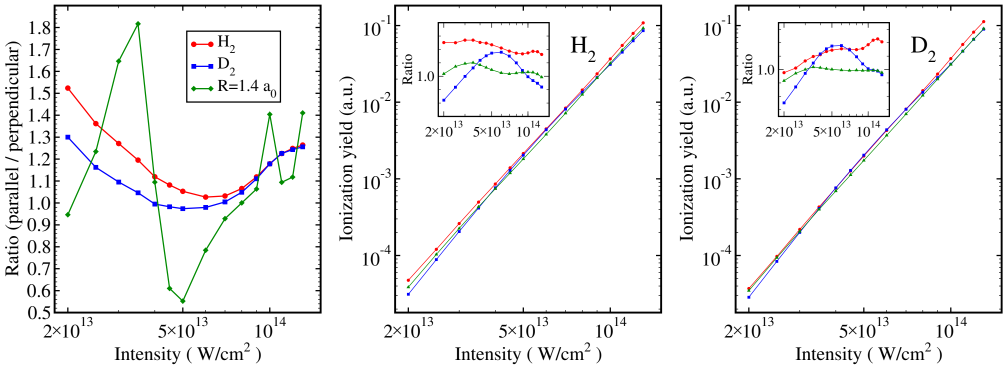

(c) 40-cycle $\cos^2$-shaped (20 fs) laser pulse

Figure 7.17.: Final ionization yields (integrated over R) as a function of the peak intensity for H_2 (middle panel) and D_2 (right panel) and a parallel (red circles) or a perpendicular (blue squares) orientation and a) 10-cycle, b) 20-cycle, or c) 40-cycle laser pulses. Also shown are the results obtained with the atomic model potential (green triangles). The inserts show the ratio of the ionization yields to the fit function in Eq. (7.18). The resulting ratio of parallel to perpendicular ionization yields is shown in the left panel in which also the corresponding ratio obtained for $R = 1.4\,a_0$ is plotted. (Published in [35].)

perturbative behavior, since according to Fig. 7.11 a one would expect mostly 6-photon ionization to occur and thus k_s should be close to 6. The included dependence on the pulse duration T allows to compare the results obtained for different pulse lengths. A linear dependence on T should be found, if a rate concept is applicable.

Dividing the ionization yields by the fit function (7.18) allows a direct comparison of the parallel, perpendicular, and atomic model potential results on a linear scale. They are shown in the inserts of Fig. 7.17. If the vibrational ground state of H_2 is considered (middle panel of Fig. 7.17), the scaled atomic-model results are closest to 1 and thus most accurately described by the fit function. The scaled yield for parallel orientation decreases from a value of 1.5 to about 1.0 for the 10-cycle pulse, but shows an increasing behavior for higher intensities in the case of the 20-cycle pulse. The smallest intensity dependence is found for the longest pulse considered in this work where the scaled yield varies only between about 1.25 and 1.15. Interestingly, the scaled yield for perpendicular orientation shows almost the opposite behavior. The most pronounced intensity dependence is found for the longest pulse. Furthermore, the scaled yield increases for low intensities as a function of intensity. As a consequence, the scaled yields for parallel and perpendicular orientation first approach each other before they separate again for even larger intensities.

Using the same fit function for scaling the D_2 yields one notices that the yields for parallel orientation are now almost flat (shortest pulse) or increase with intensity. Since the vibrational density distribution of D_2 is more localized around R_0, one can conclude that such higher ratio for H_2 can be due to contributions to the ionization from either small or large internuclear distances R. The comparison of the middle and the right panels of Fig. 7.15 a shows that the effect stems from the enhanced ionization at $R > 1.6\,a_0$. Also the scaled yields for perpendicular orientation or the atomic model potential show a larger increase with intensity for D_2 compared to H_2, although this effect is a little bit less pronounced. This indicates that the ionization yield of D_2 possesses a slightly larger slope than the one of H_2, a rather unexpected (though small) isotope effect.

Finally, the ratio of the ionization yields for parallel to perpendicular orientation of the molecular axis as a function of the peak intensity is also shown in Fig. 7.17. For the 10-cycle pulse and H_2 the ratio is about 2 for the peak intensity $2 \times 10^{13}\mathrm{W/cm}^2$ and decreases smoothly to about 1.1 at $9 \times 10^{13}\mathrm{W/cm}^2$, before it increases to 1.18 at $1.3 \times 10^{14}\mathrm{W/cm}^2$. The occurrence of a minimum is due to the maximum found for the scaled yield in the case of the perpendicular orientation, as was discussed in the context of the inserts in the middle and right panels of Fig. 7.17. Increasing the pulse duration does not change the behavior in a qualitative fashion, but the ratio found at small intensities decreases with increasing pulse length. At the same time, the increase at the highest intensities is more pronounced, but this increase is smaller than the decrease seen for the low intensities. In the case of the 40-cycle pulse the ratio starts at about 1.5, decreases to almost 1.0 and increases to 1.26. The turning point shifts also to slightly lower intensities for longer pulses. The intensity dependence of the ratios for D_2 show a similar behavior as was found for H_2. However, at small intensities the ratio is clearly smaller than for H_2, i. e. the anisotropy of the ionization yield is less pronounced. For high intensities the ratios found for H_2 and D_2 agree on the other hand almost perfectly with each other. An isotope effect occurs thus only for low intensities.

The importance of the inclusion of nuclear motion is evident from the ratio of parallel to perpendicular ionization yields obtained for a fixed internuclear separation ($R = 1.4\,a_0$) that is also shown in Fig. 7.17. In the case of a 10-cycle pulse the ratio is also smooth, but increases with intensity. The pronounced decrease found for the R-integrated ratio at low intensities is thus completely absent. Interestingly, the agreement with the ratio found for H_2 is very good for high intensities for which also the H_2 and D_2 ratios agreed well with each other. This indicates that for high intensities the ratio is less sensitive to R. The reason is the less pronounced R dependence of the ionization yields for high intensities that was found in general and discussed in the context of the weighted R-dependent ionization yields in Figs. 7.13 to 7.15. One of the consequences of this reduced R dependence was, e. g., that the maximum of the ionization yield was more or less found for the R value at which the vibrational density had its maximum. For longer pulses pronounced intensity-dependent maxima and minima become visible. As a consequence, the ratio found for a single R value differs clearly from the R-integrated results. For example, in the case of a 40-cycle pulse and $R = 1.4\,a_0$ the ratio decreases to about 0.5 at a laser peak intensity of $5 \times 10^{13}\mathrm{W/cm}^2$ which means that perpendicular oriented H_2 ionizes much better than parallel oriented one. This is in complete contrast to the R-integrated results for which the perpendicular orientation never ionizes faster than parallel oriented molecules in the considered range of laser peak intensities.

7.5.6. Photoelectron energy spectra

The integration over internuclear separations can also be applied in order to obtain R-independent photoelectron energy spectrum. Indeed, the R-dependent ionization yield

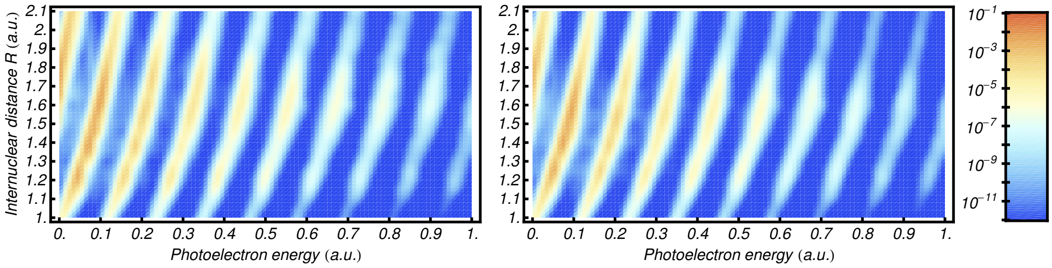

(a) Peak intensity of $2 \times 10^{13} \mathrm{W/cm^2}$

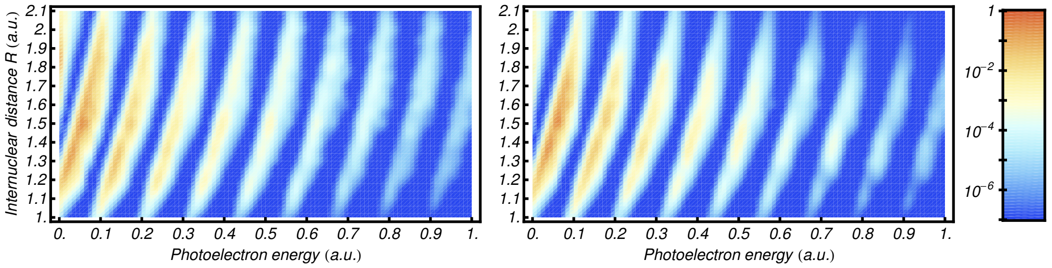

(b) Peak intensity of $5 \times 10^{13} \mathrm{W/cm^2}$

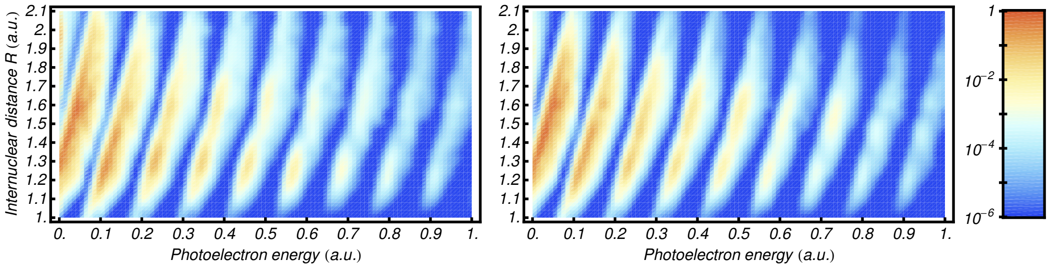

(c) Peak intensity of $7 \times 10^{13} \mathrm{W/cm^2}$

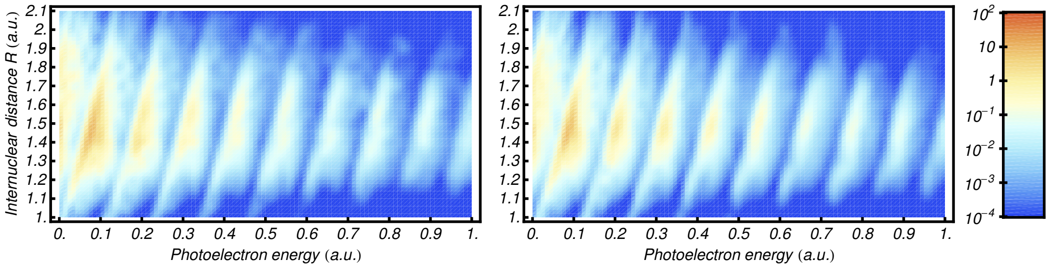

(d) Peak intensity of $1.3 \times 10^{14} \mathrm{W/cm^2}$

Figure 7.18.: The interpolated photoelectron energy spectra (weighted with the probability density of the ground vibrational state of H_2) for parallel (left) and perpendicular (right) orientations of an H_2 molecule in the presence of 40-cycle $\cos^2$-shaped 400 nm laser pulses with different peak intensities.

is related to the R-dependent photoelectron spectrum, $P_{\rm ion}(E, R, \theta)$, as

$$Y_{\rm ion}(R, \theta) = \int \mathrm{d}E \, P_{\rm ion}(E, R, \theta). \tag{7.19}$$

Substituting Eq. (7.19) into Eq. (7.16) and interchanging the order of integration, the R-independent ionization yield can be written as

$$Y^{(\nu)}_{\rm ion}(\theta) = \int \mathrm{d}E \, P^{(\nu)}_{\rm ion}(E, \theta). \tag{7.20}$$

Here, $P^{(\nu)}_{\rm ion}(E, \theta)$ is the R-independent photoelectron energy spectrum which is obtained by integrating over the weighted R-dependent photoelectron energy spectra

$$P^{(\nu)}_{\rm ion}(E, \theta) = \int \mathrm{d}R \; P_{\rm ion}(E, R, \theta) \, |\phi_\nu(R)|^2. \tag{7.21}$$

In order to obtain the R-independent photoelectron energy spectrum, the weighted R-dependent spectra $[P_{\rm ion}(E, R, \theta) \, |\phi_0(R)|^2$; only $\nu = 0$ is used in the following] for all 25 values of the internuclear separation R are calculated using a dense energy grid. Further, for every energy point, a spline interpolation over R is performed on the log scale. Figure 7.18 presents such interpolated weighted spectra both for parallel and perpendicular orientations of an H_2 molecule for 40-cycle pulses with four different peak intensities.

As is apparent from Fig. 7.18, the photoelectron spectrum for a given R exhibits pronounced ATI peaks spaced by the photon energy (0.114 a. u.). The positions of the peaks shift towards higher energies with increasing internuclear separation R as a consequence of corresponding decrease of the molecular binding energy. The peaks are better resolved for lower peak intensities and become broader for higher intensities. The results for parallel and perpendicular orientations are almost the same on the log scale, with the only difference that the amplitudes of the peaks for the perpendicular orientation at $R > 1.7 \, a_0$ are smaller than for the parallel orientation.

Figure 7.19 a provides a more detailed comparison of the weighted R-dependent photoelectron spectra for a perpendicular oriented H_2 molecule exposed to a 40-cycle laser pulse of a peak intensity of 2×10^{13}W/cm^2. As discussed above, for this peak intensity the R-dependent ionization yield comprises three pronounced peaks at $R = 1.25, 1.4$ and $1.55 \, a_0$. As is apparent from Fig. 7.19 a, the peaks for these internuclear separations clearly dominate those obtained for the neighboring R. Therefore, one can expect that

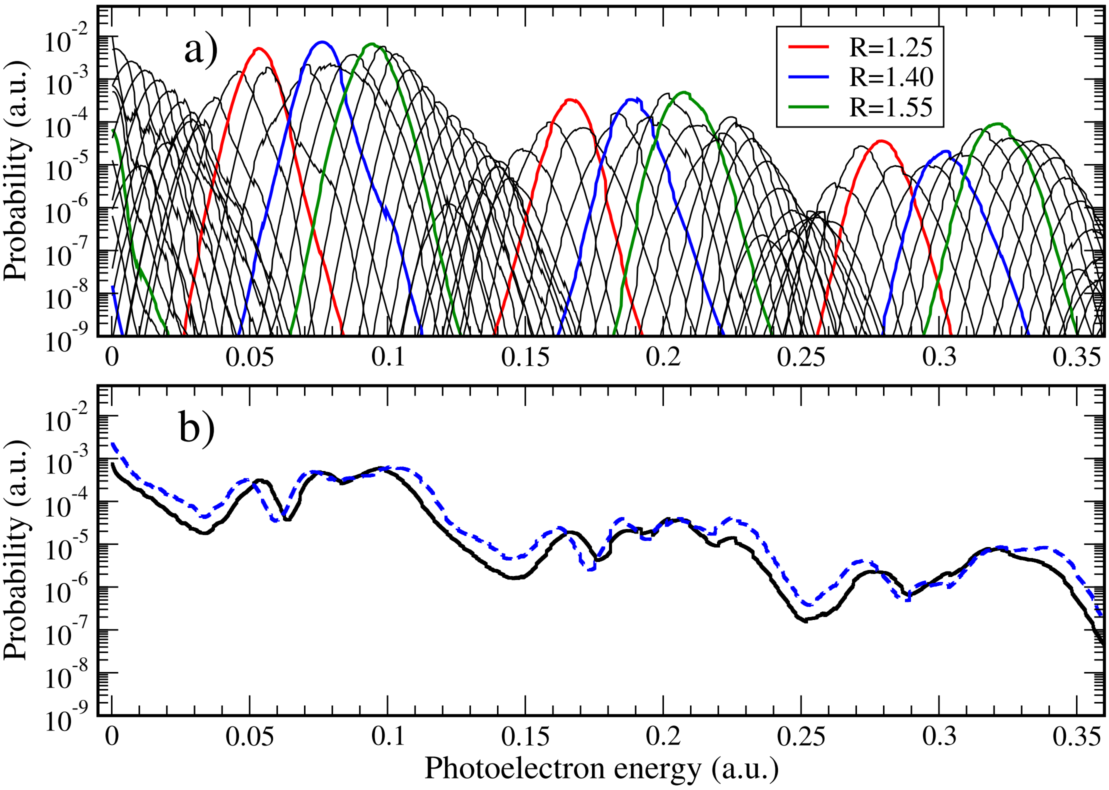

Figure 7.19.: Photoelectron energy spectra for an H_2 molecule exposed to a 40-cycle $\cos^2$-shaped 400 nm laser pulse with a peak intensity of 2×10^{13}W/cm^2. (a) The weighted R-dependent spectra for the perpendicular orientation of H_2 obtained for various fixed internuclear separations R. To guide the eye, the results for $R = 1.25, 1.4$ and $1.55\,a_0$ are presented in color, whereas the results for the other R values are plotted in black. (b) Comparison of the R-independent photoelectron spectra (integrated over R) for perpendicular (black solid) and parallel (blue dashed) orientations of H_2 molecule.

the R-independent photoelectron spectrum should exhibit peaks at the same photoelectron energies, although the integration over R results in an almost complete smearing out of spectral details. This expectation is confirmed in Fig. 7.19 b, where one can observe the maxima emerged at the expected positions due to the resonant ionization. In fact, the R dependence of the weighted ionization yields is someway imprinted in the R-independent photoelectron spectrum (compare to Fig. 7.13 b) due to the gradual decrease of the R-dependent ionization potential (Fig. 7.3). Besides, this decrease gives rise to the same positions of the peaks at, for example, $R = 1.1\,a_0$ and $R = 2.0\,a_0$, as can be seen in Fig. 7.19 a.

Figure 7.19 b provides also a comparison to the R-independent photoelectron spectrum obtained for the same pulse but a parallel oriented H_2 molecule. Again, the main deviation occurs due to different contributions coming from the larger internuclear separations (e.g. in the ranges from 0 to 0.03 a.u. and from 0.1 to 0.15 a.u.) where the spectrum for the parallel orientation is larger by more than a factor of 2. Note also a slight shift towards smaller photoelectron energies compared to the perpendicular orientation which can be observed for the maxima that result from the resonant ionization at $R = 1.25\,a_0$. However, this shift should not change the total ionization yield. Therefore, the obtained ratio (about 1.5, see Fig. 7.17 c) of the total ionization yields for the parallel to the perpendicular orientation should arise solely from the higher ionization yields for the parallel orientation at larger internuclear separations.

7.6. Investigation of two-center destructive interference.

As has been discussed in Sec. 5.4, MO-SFA-VG predicts a pronounced minimum to occur at the photoelectron energy $E \approx \pi^2/(2R^2)$, if the ratio between the energy-resolved electron spectra obtained for a parallel and a perpendicular orientation is considered. This effect should be especially pronounced for larger internuclear separations R, since at these distances the HOMO of H_2 is extremely well described by two hydrogenic 1s orbitals. There are, in fact, two more reasons for choosing a larger R value. If the predicted minimum lies at too high energies, rescattering that is not incorporated in the first-order SFA theory could dominate and cover the interference phenomenon. Furthermore, the energy-resolved spectra obtained from the TDSE calculation converge more easily for lower energies, due to their fast exponential decay.

Therefore, two series of calculations have been performed, one for $R = 3\,a_0$ and the second one for $R = 4\,a_0$. The basis set of type D has been used and the molecular symmetries with $\Lambda \leqslant \Lambda_{\max} = 9$ have been included in the time propagation for the perpendicular orientation. The pulse length of the 800 nm $\cos^2$-shaped laser pulse has been fixed to 10 cycles (about 10 fs FWHM) in order to prevent possible reflections from the box boundaries to alter the photoelectron energy spectrum for the energies of interest[4]. Figure 7.20 shows the obtained results for two different values of the peak intensity, 2×10^{13}W/cm^2 and 5×10^{13}W/cm^2. As can be seen, for all considered cases the TDSE results disagree with the behavior predicted by MO-SFA-VG. In fact, the effect is almost opposite. Indeed, at the energies $E \approx \pi^2/(2R^2)$ the ionization probability

---

[4] Note, the time propagation with the present basis set is substantially more expensive compared to those performed in the previous chapters. Thus, a single time propagation for the perpendicular orientation lasts 8-10 days and requires 25GB of memory

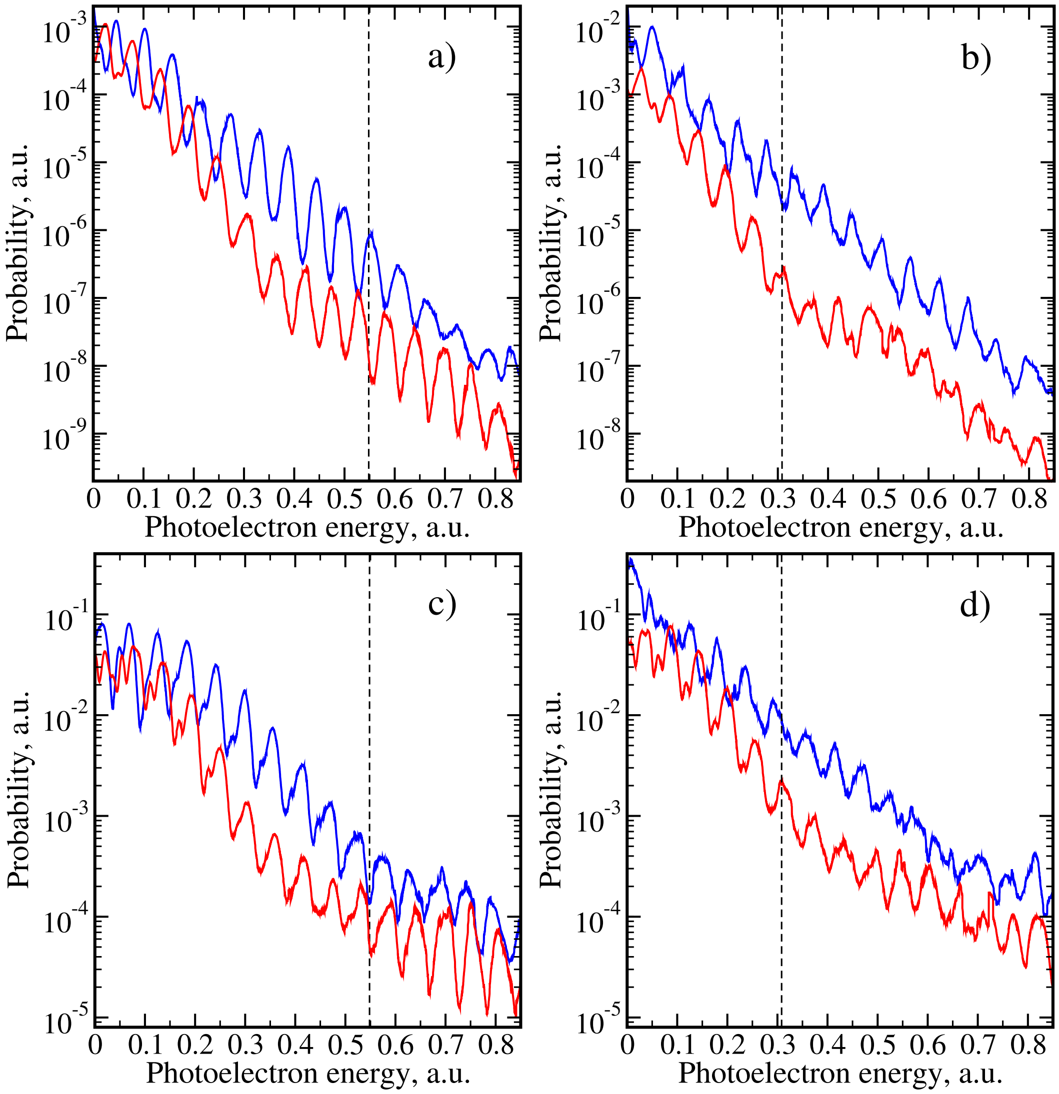

Figure 7.20.: Photoelectron energy spectra for parallel (blue) and perpendicular (red) orientations of an H_2 molecule with fixed internuclear separations (a,c) $R = 3\,a_0$ and (b,d) $R = 4\,a_0$ exposed to a 10-cycle laser pulse with the peak intensity (a,b) $2 \times 10^{13}\,\mathrm{W/cm^2}$ and (c,d) $5 \times 10^{13}\,\mathrm{W/cm^2}$. The black dashed curves indicate the corresponding electron energies $E = \pi^2/(2R^2)$ where MO-SFA-VG predicts significantly smaller ionization probability for the parallel orientation compared to the perpendicular orientation.

for the parallel orientation is clearly higher than for the perpendicular orientation. The positions of the peaks for both orientations are different due to different polarizabilities and the rather short pulse duration. Therefore, the ratios of parallel to perpendicular photoelectron

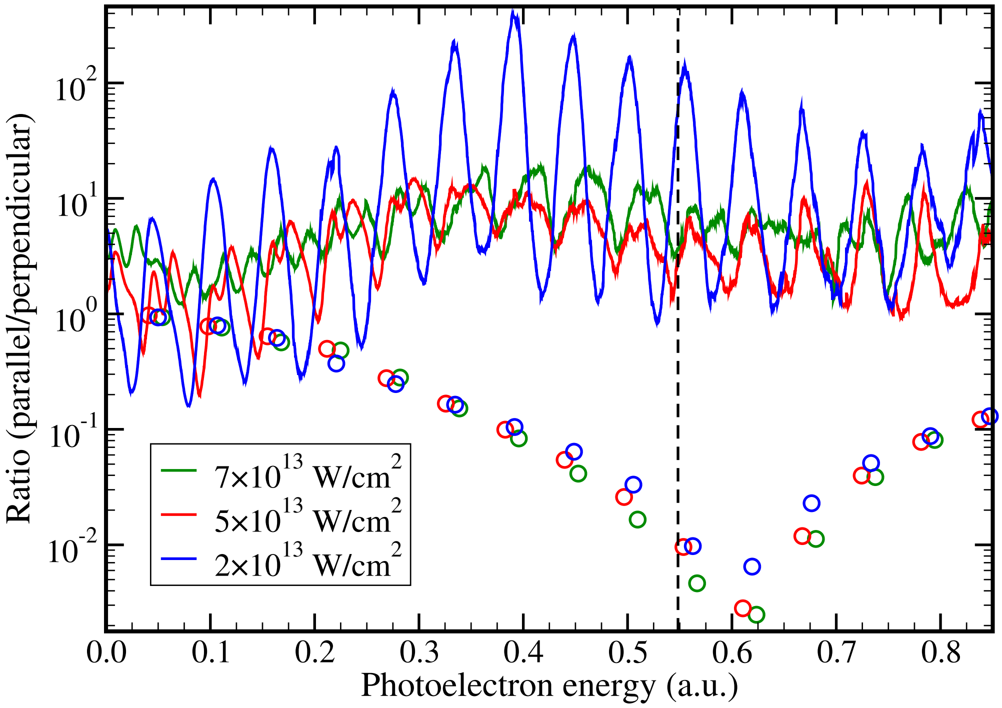

Figure 7.21.: Ratio of parallel to perpendicular energy-resolved electron spectra of H_2 ($R = 3.0\,a_0$) for 10-cycle cos^2-shaped 800 nm laser pulse and three different peak intensities. The ratios predicted by MO-SFA-VG in Eq. 5.90 are also shown using circles. Black dashed curve indicate the electron energy $E = \pi^2/(2R^2)$.

spectra obtained from the TDSE results (Fig. 7.21) exhibit strong oscillations. Nevertheless, the TDSE results indicate a rather universal overall behavior of the ratio independent of the laser intensity. The ratio first clearly increases with increasing electron energy and remains on average above unity. The ratio predicted by MO-SFA-VG in Eq. (5.90) is also almost intensity independent but its behavior is completely different. Note, the approximate expression for the minimum of the ratio ($E \approx \pi^2/(2R^2)$) predicts a somewhat lower energy than the one that is obtained with Eq. (5.90). This is due to the fact that the majority of photoelectrons are not ejected strictly parallel to the laser polarization axis but with a small deflection.

Thus, the obtained TDSE results seem to indicate the failure of the simple interference picture predicted by MO-SFA-VG. Therefore, it is certainly of interest to compare the TDSE results with other molecular SFA models.

Conclusions and Outlook

In this thesis, the full-dimensional time-dependent Schrödinger equation describing a two-electron diatomic molecule exposed to an ultrashort intense laser pulse is solved in two steps. First, the stationary Schrödinger equation is numerically solved. Second, the time-dependent wave function is expanded in terms of the obtained (in the first step) field-free states and propagated in time. For solving the field-free problem a novel molecular *ab initio* electronic-structure method has been developed and implemented. The method employs the prolate spheroidal coordinate system, a B-spline basis set, and a configuration-interaction approach. In contrast to a similar one-center approach, the present method makes full use of the molecular symmetry and its applicability is not limited to the case of small internuclear separations. Furthermore, the method was extended for the numerical treatment of alkali dimers by means of a model potential.

The applicability of the developed electronic-structure method extends beyond the scope of strong-field physics. For example, the calculated doubly-excited Q(2) states of H_2 were successfully used for scattering calculations describing low-temperature collisions between spin-polarized metastable hydrogen atoms.

This thesis presents the first results on the orientational dependence of intense-field ionization of an H_2 molecule. Results are obtained for both parallel and perpendicular orientations of the molecular axis with respect to the laser field. An extensive systematic numerical study has been performed for ultrashort 400 nm laser pulses. A key conclusion of this study is the importance of consideration of the nuclear vibrational motion for the interpretation of experiments. So far, it is taken into account by means of an integration of the fixed-nuclei ionization yields multiplied with the corresponding vibrational probability over the internuclear separation. Therefore, the full incorporation of nuclear motion is an important direction for future developments. Besides, calculations for arbitrary oriented H_2 molecule are definitely of interest and will be performed in the future.

Presently, the study is extended to longer wavelengths (especially the popular 800 nm of the Ti:sapphire laser). These calculations demand more computer memory and computational time. However, in view of existing experimental results and on-going research of time-resolved imaging, the study of this regime is of a great importance. For relatively long pulses and arbitrarily oriented H_2 molecules such calculations require computer resources that are provided nowadays only by supercomputers. However, in view of the recent computer development, these requirements appear to be fulfilled for normal workstations in the near future.

A direct comparison to experimental data requires a complete theoretical treatment of all degrees of freedom and is at the same time hampered by experimentally enforced averagings over, e.g., spatio-temporal pulse forms as well as uncertainties (exact pulse shape, peak intensity, etc.). Therefore, the developed theoretical approach is of great importance, since it allows a detailed test of other theoretical approaches and simplified models. The validity of the single-active-electron approximation, the molecular Ammosov-Delone-Krainov tunneling model, and some versions of the molecular strong-field approximation (MO-SFA) was investigated on the basis of a comparison with the results yielded by the present method. A key result is that the calculated energy-resolved spectra show no evidence of the simple interference pattern predicted by MO-SFA in the velocity gauge. This finding is of great importance in view of the popularity of this model for the interpretation of experimental results, e.g., for explaining the phenomenon of suppressed ionization of molecules. Another interesting investigation to be done in the future is a test of existing recollision models by means of calculating high-order harmonic spectrum produced by the molecule exposed to a low-frequency laser pulse. All required data (time-dependent wavefunctions and dipole moments) are already available.

The comparison with simplified models has led to an in-depth study of their formulations and implementations. Undoubtedly, the most surprising finding was the significantly different behavior of the length-gauge and velocity-gauge SFA ionization rates in the low-frequency limit. It was shown that the velocity-gauge SFA ionization rate does not converge to the tunneling limit for weak fields, if long-range Coulomb interactions are present. The study of the length-gauge SFA has revealed an incorrect application of the residue theorem within the so-called generalized Keldysh theory. This resolved the corresponding puzzling discrepancies found in literature. Finally, a further interesting finding was obtained in an investigation of the gauge problem within the SFA. Introducing the concepts of a generalized gauge and a generalized field-free Hamiltonian it has been demonstrated that identical S-matrix expansions can be obtained in different gauges, if the Hamiltonian is properly partitioned.

Appendices

A. Quasi-classical action in the complex plane

This appendix provides an outline of the derivations leading to the expressions used in Secs. 5.2 and 5.3.

The quasi-classical action $S_{\mathbf{p}}(t)$ involved in the calculation of transition amplitudes in the framework of the strong field approximation is given for the linear polarized harmonic laser field $\mathbf{F}(t) = \mathbf{F}\cos\omega t$ in the single-active-electron approximation as

$$S_{\mathbf{p}}(t) = \int\limits_{0}^{t} dt' \left[E_{\mathrm{b}} + \frac{1}{2}\boldsymbol{\pi}^2(t') \right] \quad . \tag{A.1}$$

where $E_b = \kappa^2/2$ is the binding energy of the initial bound state and $\boldsymbol{\pi}(t)$ is the mechanical (drift) momentum of the electron, $\boldsymbol{\pi}(t) = \mathbf{p} - (\mathbf{F}/\omega)\sin\omega t$.

The transition amplitude $A(\mathbf{p})$ can be presented in a general form as follows:

$$A(\mathbf{p}) = \frac{1}{T}\int\limits_{0}^{T} dt\, G(\mathbf{p},t)\, e^{\mathrm{i}S_{\mathbf{p}}(t)} \tag{A.2}$$

where $T = 2\pi/\omega$ is the field period and the function $G(\mathbf{p},t)$ depends on the gauge. [The definition of $G(\mathbf{p},t)$ in the length and velocity gauge can be inferred from Eqs. (5.54) and (5.69), respectively.]

A.1. Integration in the complex plane

Since the function $S_{\mathbf{p}}(t)$ is a rapidly varying function of time t, it is useful to shift the path of the integration over t in Eq. (A.2) into the complex plane by means of the transformation $\tilde{t} = t + i\epsilon$ where ϵ is an infinitesimally small positive number. The

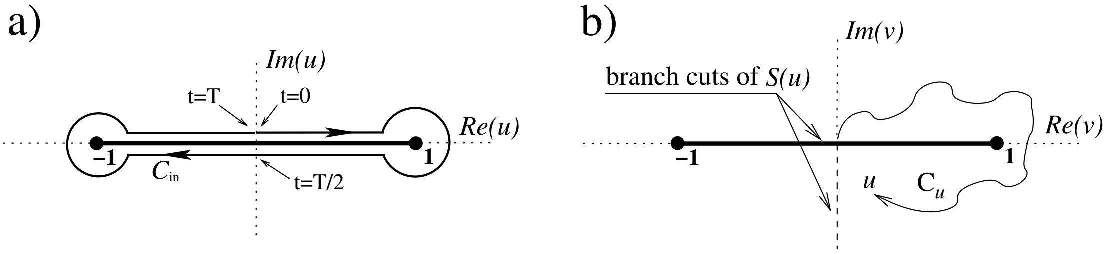

Figure A.1.: (**a**) The path C_{in} of the contour integration for $A(\mathbf{p})$. (**b**) The path C_u of the contour integration for $S(u)$.

introduction of the new complex variable $u = \sin\omega\tilde{t} = \sin\omega t + i\epsilon\cos\omega t$ transforms the integration $\int_0^T dt$ into one on the closed contour C_{in} which encloses the interval $(-1, 1)$ (see Fig. A.1 a). Applying the same procedure to the integral contained in the function $S_{\mathbf{p}}(t)$ [Eq. (A.1)] yields

$$A(\mathbf{p}) = \oint_{C_{\text{in}}} du\, \tilde{G}(u)\, e^{\mathrm{i}S_{\mathbf{p}}(u)} \tag{A.3}$$

where

$$\tilde{G}(u) = \frac{G(u)}{2\pi f(u)}, \qquad S_{\mathbf{p}}(u) = \int_{C_u} \frac{dv}{f(v)} \left[\frac{E_{\text{b}}}{\omega} + \frac{1}{2\omega}\left(\mathbf{p} - \frac{\mathbf{F}}{\omega}v\right)^2\right]. \tag{A.4}$$

Note, that usually (see, e.g., [138]) $\sqrt{1-u^2}$ is used in Eq. (A.4) instead of $f(u)$. However, the square root is defined in a standard way to possess a non-negative real part which can in the present context be misleading and cause a sign error. Therefore, the function

$$f(v) = \operatorname{sgn}[\operatorname{Im}(v)]\sqrt{1-v^2}, \tag{A.5}$$

is introduced, which is analytical in the whole complex plane except its branch cut $[-1, 1]$. The path of integration C_u specifies the path around the branch cut (see Fig. A.1 b) starting at $v = i\epsilon$ and terminating at $v = u$. Since $S(u)$ is a multivalued function, the branch cut along the negative imaginary axis is selected.

Both Eqs. (A.2) and (A.3) can equivalently be used for performing a numerical integration to yield an exact result. However, the use of Eq. (A.3) provides more flexibility, since the contour C_{in} can be deformed in a convenient way.

Due to the energy conservation law, one needs to calculate $A(\mathbf{p})$ only for $|\mathbf{p}| = p_N = \sqrt{2(N\omega - E_{\text{b}} - U_p)}$, where N is the number of photons involved in the process and $U_p = F^2/(4\omega^2)$ is the electron quiver (ponderomotive) energy due to the field. Then one can rewrite Eq. (A.1) as

$$\begin{aligned} S_{\mathbf{p}}(t) &= \int_0^t dt'\omega\left[N - z\cos 2\omega t' + \xi\sin\omega t'\right] \\ &= N\omega t - \frac{z}{2}\sin 2\omega t + \xi(1-\cos\omega t) \end{aligned} \tag{A.6}$$

with

$$z = \frac{U_p}{\omega} = \frac{F^2}{4\omega^3}, \qquad \xi = -\frac{\mathbf{p}\cdot\mathbf{F}}{\omega^2} = -\frac{p_N F\cos\theta_{pF}}{\omega^2}, \tag{A.7}$$

whereas Eq. (A.4) can be rewritten as

$$\begin{aligned} S(u) &= \int_{C_u} \frac{dv}{f(v)}\left[N + z(2v^2-1) + \xi v\right] \\ &= \xi - \mathrm{i}N\ln[f(u)+\mathrm{i}u] - zf(u)u - \xi f(u). \end{aligned} \tag{A.8}$$

In contrast to $S(u)$, $e^{\mathrm{i}S(u)}$ is a single-valued function and can be given as

$$e^{\mathrm{i}S(u)} = e^{\mathrm{i}\xi}[f(u)+\mathrm{i}u]^N e^{-zu[\mathrm{i}f(u)]-\xi[\mathrm{i}f(u)]}\ . \tag{A.9}$$

A.2. Saddle points

There exist two saddle points $u_\pm$ of $S(u)$ in the complex plane u that are defined by $S'(u_\pm) = 0$. From Eq. (A.8) follows

$$4zu_\pm^2 + 2\xi u_\pm + 2(N-z) = 4zu_\pm^2 + 2\xi u_\pm + (p_N^2+\kappa^2)/\omega = 0 \tag{A.10}$$

and $u_\pm$ can be explicitly given by

$$u_\pm = \frac{1}{4z}\left\{-\xi \pm \mathrm{i}\sqrt{4z(p_N^2+\kappa^2)/\omega - \xi^2}\right\} = \gamma(q_\parallel \pm \mathrm{i}\rho) \tag{A.11}$$

with

$$\rho = \sqrt{1+q_N^2\sin^2\theta_{pF}}, \quad q_\parallel = q_N\cos\theta_{pF} \tag{A.12}$$

where $\gamma = \kappa\omega/F$ is the Keldysh parameter and $q_N = p_N/\kappa$ is a scaled momentum.

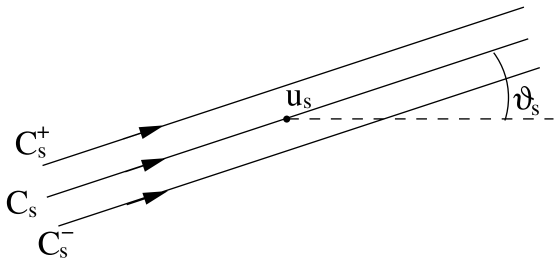

Figure A.2.: Integration paths C_s and $C_s^\pm$ passing through the steepest descent of $\exp[\mathrm{i}S(u)]$, where C_s passes through the the saddle point u_s and C_s^+ (C_s^-) passes slightly above (below) u_s.

Using Eq. (A.12) the first derivative $S'(u)$ can be expressed as

$$S'(u) = 2z\frac{(u-u_+)(u-u_-)}{f(u)} \tag{A.13}$$

and the values of the second $S''(u)$ and third $S'''(u)$ derivatives at $u = u_\pm$ are given by

$$S''(u_\pm) = \pm\frac{\tau\rho\,\mathrm{i}}{\gamma^2 f(u_\pm)}, \quad S'''(u_\pm) = \frac{6z-2N}{f^3(u_\pm)} \tag{A.14}$$

where the inverse field parameter $\tau = \kappa^3/F = 4z\gamma^3$ is introduced.

A.3. Contours through steepest descent

We introduce the straight contours C_s ($C_s^\pm$) that go through (slightly above or below) the saddle point u_s (the index $s = \pm$ specifies one of the two saddle points). They are given parametrically as

$$u(x, Q_s) = u_s + (x + \mathrm{i}k\varepsilon)Q_s, \quad -\infty < x < \infty, \;\; \varepsilon \to 0^+ \tag{A.15}$$

starting at $x \to -\infty$, where $k = \pm 1$ for the contours $C_s^\pm$ and $k = 0$ for C_s. The contours are schematically presented in Fig. A.2. The values of $Q_\pm$ are chosen in such a way that the contours are passing through the steepest descent, i. e. as

$$Q_\pm = \sqrt{\frac{2\mathrm{i}}{S''(u_\pm)}} = \gamma\sqrt{\pm\frac{2f(u_\pm)}{\tau\rho}} = Qe^{\mathrm{i}\vartheta_\pm}. \tag{A.16}$$

The absolute value Q and the argument $\vartheta_\pm$ of Q_s defined by (A.16) can be written as

$$Q = \gamma\sqrt{\frac{2}{\rho\tau}}\left\{\left[1+\gamma^2(1+q_N^2)\right]^2 - 4\gamma^2 q_\parallel^2\right\}^{1/8}, \tag{A.17}$$

$$\tan 4\vartheta_\pm = \mp\frac{2\rho q_\parallel}{\gamma^{-2}+\rho^2-q_\parallel^2}, \quad -\frac{\pi}{4} < \vartheta_\pm < \frac{\pi}{4}. \tag{A.18}$$

Representing $\exp[\mathrm{i}S(u)]$ as

$$e^{\mathrm{i}S(u)} = e^{\mathrm{i}S(u_s)}e^{-Q_s^{-2}(u-u_s)^2}e^{\mathrm{i}R(u)} \tag{A.19}$$

where $R(u) = S(u) - S(u_s) - (1/2)S''(u_s)(u-u_s)^2$, one obtains for u given by the function $u(x, Q_s)$ in Eq. (A.15)

$$e^{\mathrm{i}S(u)} = e^{\mathrm{i}S(u_s)}e^{-x^2-2\mathrm{i}k\varepsilon+k^2\varepsilon^2}e^{\mathrm{i}R(u)}\ . \tag{A.20}$$

Performing a Taylor expansion of the function $R(u)$ at $u = u_s$ yields

$$e^{\mathrm{i}R(u)} = 1 + \frac{\mathrm{i}S'''(u_s)}{6}(u-u_s)^3 + \dots \tag{A.21}$$

A.4. Power series expansions at infinity

For $u \to \infty$ the function $f(u)$ can be expanded in the following power series

$$f(u) = \mathrm{i}\left\{-u + \frac{1}{2u} + \sum_{n=2}^{\infty}\frac{(2n-3)!!}{2^n n!}\frac{1}{u^{2n-1}}\right\} \tag{A.22}$$

The second term on the right-hand side of Eq. (A.9) can be expanded as

$$[f(u)+\mathrm{i}u]^N = \sum_{n=0}^{\infty}\frac{a_n(N)}{u^{N+2n}}, \qquad a_n(N) = \left(\frac{\mathrm{i}}{2}\right)^N \frac{NC_n^{N+2n}}{4^n(N+2n)} \tag{A.23}$$

whereas the third term on the right-hand side of Eq. (A.9) can be separated into two parts using the identities

$$\frac{1}{u+\mathrm{i}f(u)} = u - \mathrm{i}f(u), \qquad \frac{1}{2}\frac{u-\mathrm{i}f(u)}{u+\mathrm{i}f(u)} + \frac{1}{2} = u^2 - \mathrm{i}uf(u) \tag{A.24}$$

as

$$e^{-zu[\mathrm{i}f(u)]-\xi[\mathrm{i}f(u)]} = e^{z/2} e^{-zu^2-\xi u} \exp\left\{\frac{z}{2}\frac{u-\mathrm{i}f(u)}{u+\mathrm{i}f(u)}\right\} \exp\left\{\frac{\xi}{u+\mathrm{i}f(u)}\right\} \tag{A.25}$$

All terms can be expanded in a series expansion, namely

$$e^{-zu^2-\xi u} = \sum_{n=0}^{\infty} b_n(\xi,z) u^n, \qquad b_n(\xi,z) = \sum_{k=0}^{[n/2]} \frac{(-z)^k}{k!}\frac{(-\xi)^{n-2k}}{(n-2k)!} \tag{A.26}$$

$$\exp\left\{\frac{z}{2}\frac{u-\mathrm{i}f(u)}{u+\mathrm{i}f(u)}\right\} = \sum_{n=0}^{\infty}\frac{c_n(z)}{u^n}, \quad c_n(z) = \sum_{k=0}^{n-1}\frac{C_k^{2n} z^{n+k}}{2^{3n+k} n\,(n-k-1)!} \tag{A.27}$$

$$\exp\left\{\frac{\xi}{\mathrm{i}f(u)+u}\right\} = \sum_{n=0}^{\infty}\frac{d_n(\xi)}{u^n}, \quad d_n(\xi) = \sum_{k=0}^{[n/2]}\frac{C_k^n \xi^{n-2k}}{2^n n(n-2k-1)!} \tag{A.28}$$

where $c_0(z) = d_0(\xi) = 1$.

Note, that the behavior of $e^{\mathrm{i}S(u)}$ at infinity is determined by the term e^{-zu^2}. Since $z > 0$ and $u^2 = (\mathrm{Re}\,u)^2 - (\mathrm{Im}\,u)^2 + 2\mathrm{i}(\mathrm{Re}\,u)(\mathrm{Im}\,u)$ one finds for $u \to \infty$

$$e^{\mathrm{i}S(u)} \to \begin{cases} 0 & \text{for } |\mathrm{Re}\,u| > |\mathrm{Im}\,u| \\ \infty & \text{for } |\mathrm{Re}\,u| < |\mathrm{Im}\,u| \end{cases} \tag{A.29}$$

where $e^{\mathrm{i}S(u)}$ grows (vanishes) exponentially.

For $x \to \pm\infty$ one has for $u(x, Q_s)$ defined in Eq. (A.15)

$$\frac{|\mathrm{Im}\,u(x,Q_s)|}{|\mathrm{Re}\,u(x,Q_s)|} \to \frac{|\mathrm{Im}\,Q_s|}{|\mathrm{Re}\,Q_s|} = |\tan\vartheta_\pm| < 1 \quad , \tag{A.30}$$

where the inequality (A.18) has been used.

Whenever the function $\tilde{G}(u)$ in Eq. (A.4) has the following power series expansion

$$\tilde{G}(u) = \sum_{n=0}^{\infty}\frac{G_n}{u^{n_0+n}} \tag{A.31}$$

then the integrand in Eq. (A.3) can be presented as a power series

$$\tilde{G}(u) e^{\mathrm{i}S(u)} = e^{z/2+\mathrm{i}\xi} \sum_{n,i,j,k,l=0}^{\infty} G_n a_i b_j c_k d_l u^{j-(n_0+N)-n-2i-k-l} \tag{A.32}$$

Using Eq. (A.32) one can calculate the residue of $\tilde{G}(u)e^{\mathrm{i}S(u)}$ at infinity. Since infinity is an essential singularity of the function $\tilde{G}(u)e^{iS(u)}$, the residue is equal to the coefficient at u^{-1},

$$\operatorname*{Res}_{u=\infty}[\tilde{G}e^{\mathrm{i}S}] = e^{z/2+\mathrm{i}\xi} \sum_{n,i,k,l=0}^{\infty} G_n a_i c_k d_l b_{(n_0+N-1)+n-2i-k-l} \tag{A.33}$$

A.5. Function *L* in the quasistatic limit

The function $L(\mathbf{p})$ which is defined as

$$L = L(\mathbf{p}) = \frac{1}{T} \int_0^T e^{iS_{\mathbf{p}}(t)} dt \tag{A.34}$$

can simply be expressed for $\mathbf{p} = p_N \hat{\mathbf{p}}$ using the generalized Bessel functions (we use for them Reiss' definition [117] which differs slightly from the one of Faisal [147]) as

$$L(p_N \hat{\mathbf{p}}) = (-\mathrm{i})^N e^{\xi \mathrm{i}} J_N(\xi, -z/2) \tag{A.35}$$

In the high-frequency and low-intensity regime the generalized Bessel functions can be very efficiently calculated using an expansion over products of ordinary Bessel functions,

$$J_N(a,b) = \sum_{m=-\infty}^{\infty} J_{N-2m}(a) J_m(b) \quad , \tag{A.36}$$

where only a few terms are required to yield high accuracy.

It is convenient to describe the quasistatic limit $\omega \to 0$ as $\gamma \to 0$ by rewriting all parameters as functions of γ and an (inverse) field parameter $\tau = \kappa^3/F$ which is ω independent. Then

$$\xi = \frac{\tau q_N \zeta}{\gamma^2}, \quad z = \frac{\tau}{4\gamma^3}, \quad N_0 = \frac{\tau}{4\gamma^3}(1 + 2\gamma^2) \tag{A.37}$$

where $\zeta = -\hat{\mathbf{p}} \cdot \hat{\mathbf{F}}$. Since the numerical values of q_N and ζ are usually of the order of one, both arguments and the index of the generalized Bessel function in Eq. (A.35) tends to infinity. In this case it is very problematic to use Eq. (A.36) in numerical calculations, since very many terms are required and their amplitudes are much larger than the final result. This can lead to large cancellation errors. A very efficient way for the numerical computation of $L(p_N \hat{\mathbf{p}})$ is possible by means of performing the integration through the saddle points, as will be discussed in the following paragraph.

Introduction of the new complex variable $u = \sin\omega t$ allows to rewrite Eq. (A.34) as

$$L = \oint_{C_{\mathrm{in}}} \frac{e^{\mathrm{i}S(u)}}{2\pi f(u)} du \ . \tag{A.38}$$

Deforming the contour C_{in} to pass along the contour C_- in positive direction, along C_+ in negative direction (see Sec. A.3 for the definitions of $C_\pm$), and connecting the ends of these contours at infinity one obtains

$$L = L_+ - L_- \tag{A.39}$$

where the integrals $L_\pm$ can be calculated using Eq. (A.15) as

$$L_\pm = \int_{-\infty}^{\infty} Q_\pm \mathcal{F}(u_\pm + Q_\pm x) dx \quad . \tag{A.40}$$

It is sufficient to calculate only L_+. Indeed, using

$$f(u^*) = -f^*(u), \quad Q^*_\pm = Q_\mp, \tag{A.41}$$

$$e^{\mathrm{i}S(u^*)} = (-1)^N \exp[2\xi\mathrm{i}] \left\{ e^{\mathrm{i}S(u)} \right\}^* \tag{A.42}$$

one obtains

$$L_- = -(-1)^N \exp\left[2\xi\mathrm{i}\right] L^*_+ \quad . \tag{A.43}$$

Substituting Eq. (A.43) into Eq. (A.39) yields

$$L = L_+ + (-1)^N \exp\left[2\xi\mathrm{i}\right] L^*_+ \quad . \tag{A.44}$$

Introducing the absolute value $\mathcal{L}$ and the argument Ω of L_+ we obtain for the generalized Bessel function

$$J_N(\xi, -z/2) = 2\mathcal{L} \cos(\xi - \Omega - N\pi/2) \tag{A.45}$$

and

$$|L|^2 = 2\mathcal{L}^2 \left[1 + \cos(2\xi - 2\Omega - N\pi)\right]. \tag{A.46}$$

It follows from Eq. (A.11) that $u_+ \to 0$ in the limit $\gamma \to 0$. The function $f(u)$ is then nearly 1 in the interval $(0, u_+)$ and $S(u_+)$ can be calculated using the Taylor expansion of $f^{-1}(u)$ at $u = 0$ for $\mathrm{Im}(u) > 0$,

$$f^{-1}(u) = 1 + \frac{u^2}{2} + \frac{3u^4}{8} + \dots \tag{A.47}$$

Substitution of Eq. (A.47) into Eq. (A.4) and integration yields

$$\mathrm{i}S(u_+) = -\frac{\tau\rho^3}{3} - \frac{\tau\rho^3\chi(3+\chi^2)}{6}\,\mathrm{i} + O(\gamma^2) \tag{A.48}$$

where $\chi = -q_N\zeta/\rho$.

Performing the Taylor expansion of $S(u)$ at $u = u_+$ gives

$$\mathrm{i}S(u_+ + Q_+x) = \mathrm{i}S(u_+) - x^2 + \mathrm{i}\frac{\sqrt{2}}{3\sqrt{\tau\rho^3}}x^3 + O(\gamma^2) \tag{A.49}$$

where

$$Q_+ = \gamma\sqrt{\frac{2f(u_+)}{\tau\rho}} = \gamma\sqrt{\frac{2}{\tau\rho}} + O(\gamma^3) \tag{A.50}$$

has been used. Due to the smallness of Q_+, the function $e^{\mathrm{i}S(u)}$ decays quickly in the vicinity of u_+. Since the expansions (A.49) and (A.47) are expected to be valid in this region, the integrand of L_+ can be rewritten as

$$Q_\pm\mathcal{F}(u_\pm + Q_\pm x) = \gamma\, C\,\exp\left[-x^2 + \mathrm{i}\frac{\sqrt{2}x^3}{3\sqrt{\tau\rho^3}}\right] + O(\gamma^3) \tag{A.51}$$

where

$$C = \frac{1}{2\pi}\sqrt{\frac{2}{\tau\rho}}\exp\left[-\frac{\tau\rho^3}{3} - \frac{\tau\rho^3\chi(3+\chi^2)}{6}\,\mathrm{i}\right]\,. \tag{A.52}$$

Integration over x yields for the absolute value $\mathcal{L}$ and the argument Ω of L_+

$$\mathcal{L} = \gamma\frac{\rho}{\sqrt{3}\pi}K_{1/3}\left(\frac{\tau\rho^3}{3}\right) + O(\gamma^3) \tag{A.53}$$

$$\Omega = -\frac{\tau\rho^3\chi(3+\chi^2)}{6} + O(\gamma^2) \tag{A.54}$$

where K_ν is the modified Bessel function of the second kind of order ν.

B. Method of steepest descent

One can numerically calculate the contour integrals

$$I_C = \int\limits_C du\, \tilde{G}(u)\, e^{\mathrm{i}S(u)} \tag{B.1}$$

where C is one of the contours discussed in Sec. A.3. However, the approach called *method of steepest descent* (MSD) (or *saddle point approximation*) can be employed to approximate them.

B.1. Simple MSD formula

If the function $\tilde{G}(u)$ has no singularity at a saddle point u_s (see Sec. A.2), the integrals over $C_s, C_s^{\pm}$ are equal and thus only integral over C_s (i.e. I_s) needs to be discussed. The vicinity of u_s is expected to give the main contribution to the integral. Besides, it is assumed that the functions $\tilde{G}(u)$ and $R(u)$ (see Eq. A.19) are slowly varying functions in the vicinity of u_s. Then, the integral I_s can be approximated as

$$I_s \approx \int\limits_{-\infty}^{\infty} \mathrm{d}x\, Q_s\, \tilde{G}(u_s)\, e^{\mathrm{i}S(u_s)} e^{-x^2} = \sqrt{\pi}\, Q_s\, \tilde{G}(u_s)\, e^{\mathrm{i}S(u_s)} \tag{B.2}$$

However, if the function $\tilde{G}(u)$ has a pole of order ν at u_s,

$$\tilde{G}(u) = \frac{g_s(u)}{(u - u_s)^{\nu}}\ , \tag{B.3}$$

the integration cannot be performed over C_s, and the integrals over $C_s^{\pm}$, $I_s^{\pm}$, should give different results. From Eq. (A.15) the relation

$$\frac{1}{(u_x - u_s)^{\nu}} = \frac{(\pm 1)^{\nu}}{(\mathrm{i}Q_s)^{\nu}} \frac{1}{(\epsilon \mp \mathrm{i}x)^{\nu}} \tag{B.4}$$

follows. Similar to the previous case, the vicinity of u_s is assumed to give the main contribution to the integral. However, the function $\tilde{G}(u)$ cannot be seen as slowly varying function in the vicinity of u_s. Instead, the functions $g_s(u)$ and $R(u)$ are assumed to be slowly varying functions in the vicinity of u_s. Then, using the identity

$$\frac{1}{(a \mp \mathrm{i}b)^\nu} = \frac{1}{\Gamma(\nu)} \int_0^\infty d\eta \eta^{\nu-1} e^{-\eta a} e^{\pm \mathrm{i}\eta b}, \quad a > 0\,, \tag{B.5}$$

one obtains

$$I_s^\pm \approx (\pm 1)^\nu \frac{g_s(u_s) e^{\mathrm{i}S(u_s)}}{\mathrm{i}^\nu Q_s^{\nu-1} \Gamma(\nu)} \int_0^\infty \mathrm{d}\eta\, \eta^{\nu-1} e^{-\eta\epsilon+\epsilon^2} \int_{-\infty}^{\infty} \mathrm{d}x\, e^{-x^2 \pm \mathrm{i}(\eta-2\epsilon)x}. \tag{B.6}$$

The integration over x and η yields

$$I_s^\pm \approx I_{s,\mathrm{MSD}}^\pm = g_s(u_s) \bar{I}_s^\pm(\nu), \qquad \bar{I}_s^\pm(\nu) = (\pm 1)^\nu \frac{\pi e^{iS(u_s)}}{i^\nu Q_s^{\nu-1} \Gamma(\frac{\nu+1}{2})}. \tag{B.7}$$

Therefore, MSD predicts I_s^+ and I_s^- to be equal for even ν and to differ only by the sign for odd ν. For $\nu = 0$ Eq. (B.7) reduces to Eq. (B.2).

B.2. Corrected MSD formula

The result of Eq. (B.7) can often be significantly improved by taking into account the behavior of the functions $g_s(u)$ and $R(u)$ in the vicinity of u_s. Performing a Taylor expansion of $g_s(u)$ at $u = u_s$,

$$g_s(u) = \sum_{m=0}^{\infty} g_s^{(m)} (u - u_s)^m, \tag{B.8}$$

and using Eq. (A.21), one can represent the function $\tilde{G}(u) e^{\mathrm{i}R(u)}$ in the vicinity of u_s by a sum over terms containing different non-positive powers of $(u - u_s)$,

$$\tilde{G}(u) e^{\mathrm{i}R(u)} \approx \frac{g_s(u_s)}{(u-u_s)^\nu} + \sum_{m=1}^{\nu} \frac{g_s^{(m)}}{(u-u_s)^{\nu-m}} + \frac{\mathrm{i}S'''(u_s)}{6} \sum_{m=0}^{\nu-3} \frac{g_s^{(m)}}{(u-u_s)^{\nu-3-m}}\,. \tag{B.9}$$

Applying the procedure described in Sec. B.1 to every term in Eq. (B.9), the corrected MSD formula

$$I^{\pm}_{s,\mathrm{cMSD}} = I^{\pm}_{s,\mathrm{MSD}} + \sum_{m=1}^{\nu} g_s^{(m)} \bar{I}_s^{\pm}(\nu - m) + \frac{\mathrm{i}S'''(u_s)}{6} \sum_{m=0}^{\nu-3} g_s^{(m)} \bar{I}_s^{\pm}(\nu - m - 3) \tag{B.10}$$

is obtained as approximation for $I_s^{\pm}$.

C. Hydrogenlike atom

Consider some properties of hydrogenlike atom with potential $U(\mathbf{r}) = Z/r$, where Z is the charge of the nucleus.

C.1. Function $\tilde{\mathbf{V}}_\mathbf{0}(\mathbf{u})$ for the *n*s states

The Fourier transform of a hydrogenic ns state is given by

$$\tilde{\Phi}_0(\mathbf{q}) = \frac{8\sqrt{\pi}}{\kappa^{3/2}} \sum_{k=0}^{n-1} (-1)^k \, 2^{2k} \, C_{2k+1}^{n+k} \left(\frac{\kappa^2}{\mathbf{q}^2 + \kappa^2} \right)^{k+2} \tag{C.1}$$

where C_k^n are binomial coefficients and $\kappa = Z/n$. Using the identity $\nabla_\mathbf{q} f(q^2) = 2\mathbf{q}\partial f(q^2)/(\partial q^2)$ one obtains for $V_0(\mathbf{q}) = \mathrm{i}\mathbf{F} \cdot \nabla_\mathbf{q} \tilde{\Phi}_0(\mathbf{q})$ the expression

$$V_0(\mathbf{q}) = \frac{4\pi(\mathbf{F} \cdot \mathbf{q})}{\kappa F} \sum_{k=3}^{n+2} D_n^{(k)} \left(\frac{\kappa^2}{\mathbf{q}^2 + \kappa^2} \right)^{k} \tag{C.2}$$

where

$$D_n^{(k)} = (-1)^k \, (k-1) \, 2^{2k-4} \, C_{2k-5}^{n+k-3} \frac{\mathrm{i}F}{\sqrt{\pi}\kappa^{5/2}}. \tag{C.3}$$

The function $\tilde{V}_0(u)$ defined by the relation

$$\tilde{V}_0(u) = \frac{1}{2\pi} V_0 \left(\mathbf{p} - \frac{\mathbf{F}}{\omega} u \right) \tag{C.4}$$

can be given in terms of

$$P_\pm(u) = \frac{\gamma}{u - u_\pm} \tag{C.5}$$

using the identities

$$\mathbf{F} \cdot \mathbf{q} = -\frac{F\kappa}{2} [P_+^{-1}(u) + P_-^{-1}(u)], \quad \frac{\kappa^2}{\mathbf{q}^2 + \kappa^2} = P_+(u) P_-(u)$$

as

$$\tilde{V}_0(u) = -\sum_{k=3}^{n+2} D_n^{(k)}\, G_k, \quad G_k = P_+^{k-1} P_-^{k} + P_+^{k} P_-^{k-1}. \tag{C.6}$$

Here $u_\pm$ are the points defined in Eq. (A.11). It is evident from Eqs. (C.5) and (C.6) that the function $\tilde{V}_0(u)$ has poles of order $n+2$ at $u = u_\pm$ and vanishes for $u \to \infty$ as

$$\tilde{V}_0(u) \to -\frac{2\gamma^5 D_n^{(3)}}{u^5}. \tag{C.7}$$

Introducing $R_\pm = P_\pm(u_\mp) = \pm\mathrm{i}/(2\rho)$ and using the Taylor expansion of $P_\pm^k(u)$ at $u \approx u_\mp$,

$$P_\pm^k(u) = \sum_{m=0}^{\infty} (-1)^m\, C_m^{k+m-1}\, R_\pm^{k+m}\, P_\mp^{-m}(u), \tag{C.8}$$

one can rewrite $\tilde{V}_0(u)$ as a Laurent series at $u \approx u_\pm$

$$\tilde{V}_0(u) = \sum_{\nu=-\infty}^{n+2} \frac{M_\pm^{(n,\nu)}}{(u-u_\pm)^\nu} \tag{C.9}$$

where

$$M_\pm^{(n,\nu)} = -\gamma^\nu \sum_{r=\max(\nu,3)}^{n+2} D_n^{(r)}\, Q_{r-\nu}^{(r)}\, R_\mp^{2r-\nu-1}, \tag{C.10}$$

and

$$Q_m^{(k)} = (-1)^m \{C_m^{k+m-2} - C_{m-1}^{k+m-2}\}, \quad Q_0^{(k)} = 1. \tag{C.11}$$

Then the function $g_\pm(u) = \tilde{V}_0(u)(u-u_\pm)^{n+2}$ that has no poles at $u_\pm$ can be expanded at $u \approx u_\pm$ as

$$g_\pm(u) = \sum_{m=0}^{\infty} M_\pm^{(n,n+2-m)} (u-u_\pm)^m, \tag{C.12}$$

where at $u = u_\pm$ one obtains

$$g_\pm(u_\pm) = M_\pm^{(n,n+2)} = -(\pm 2)^{n-1} \frac{\mathrm{i}^n\,(n+1)\,\gamma^{2n+3}\,F}{\sqrt{\pi}\,\rho^{n+1}\,\kappa^{5/2}}. \tag{C.13}$$

An expansion of $\tilde{V}_0(u)$ at $u \to \infty$ can be obtained using the identities

$$R_-(P_+P_-) = P_+ - P_-, \qquad (P_+P_-)T_k = R_- T_{k+1} - R_-(P_+P_-)T_{k-1} \tag{C.14}$$

where

$$T_k = P_+^k - (-P_-)^k = \sum_{m=0}^{\infty} \frac{T_m^k}{u^m}, \quad T_m^k = C_{k-1}^{m-1} \gamma^k \left[u_+^{m-k} - (-1)^k u_-^{m-k} \right]. \tag{C.15}$$

Indeed, it is sufficient to represent G_k as an expansion over $\{T_p\}$. From Eq. (C.14) one obtains

$$G_3 = R_-^2 T_3 - R_-^3 T_2, \qquad G_4 = R_-^3 T_4 - 2R_-^4 T_3 + 2R_-^5 T_2 \tag{C.16}$$

and the further terms are obtained using $G_{k+1} = (P_+ P_-) G_k$ and the identity which follows from Eq. (C.14),

$$(P_+ P_-) T_k = \sum_{i=1}^{k} (-1)^{i-1} R_-^i T_{k+2-i} \ . \tag{C.17}$$

For example, for $n = 1$ the function $\tilde{V}_0(u)$ can be expanded at $u \to \infty$ as

$$\begin{aligned} \tilde{V}_0(u) = \frac{8\,\mathrm{i}\,F\,\gamma^5}{\sqrt{\pi}\,\kappa^{5/2}} \sum_{m=5}^{\infty} \frac{1}{u^m} \Bigg\{ & \frac{(m-1)(m-2)}{2(2\rho\gamma\mathrm{i})^2} \big(u_+^{m-3} + u_-^{m-3} \big) \\ & + \frac{(m-1)}{(2\rho\gamma\mathrm{i})^3} \big(u_+^{m-2} - u_-^{m-2} \big) \Bigg\} \end{aligned} \tag{C.18}$$

where the terms for $m < 5$ are all equal to zero.

C.2. Functions $\mathrm{B}(\rho)$ for different states with $\mathrm{n} \leqslant 3$

The function

$$B(\rho, \kappa) = \rho^8 \left(\frac{\kappa}{4\pi} \right)^3 \int_{-\infty}^{\infty} d\chi \, (1 + \chi^2)^2 \, \tilde{\Phi}(\rho, \chi), \quad \tilde{\Phi} = \int_0^{2\pi} d\phi |\tilde{\Psi}_0|^2, \tag{C.19}$$

where $\tilde{\Psi}_0$ is the Fourier transform of the hydrogenic state, can be analytically calculated using the identity

$$\int_{-\infty}^{\infty} \frac{d\chi}{(1 + \chi^2)^n} = \pi \frac{(2n-3)!!}{(2n-2)!!} \tag{C.20}$$

to perform the integration over χ. For example, the Fourier transform of the $1S_0$ state is given by

$$\tilde{\Psi}_0 = \frac{16\pi}{\kappa^{3/2}} \frac{1}{(1+q_N^2)^2} \frac{1}{\sqrt{4\pi}} \tag{C.21}$$

resulting in

$$\tilde{\Phi}(\rho,\chi) = \frac{2^7\pi^2}{\kappa^3\rho^8(1+\chi^2)^4} \,. \tag{C.22}$$

Substitution of Eq. (C.22) into Eq. (C.19) and integration over χ yields $B_{1\mathrm{S}_0} = 1$. The other functions $B(\rho)$ for all hydrogenic states with principal quantum number $n \leq 3$ (note, for hydrogenlike atoms function B is independent of κ) read

$$\begin{aligned}
B_{2\mathrm{S}_0}(\rho) &= 4 - 12\rho^{-2} + 10\rho^{-4} \\
B_{2\mathrm{P}_0}(\rho) &= 2\rho^{-2} \\
B_{2\mathrm{P}_1}(\rho) &= 5\rho^{-2} - 5\rho^{-4} \\
B_{3\mathrm{S}_0}(\rho) &= 9 - 72\rho^{-2} + 220\rho^{-4} - 280\rho^{-6} + 126\rho^{-8} \\
B_{3\mathrm{P}_0}(\rho) &= 12\rho^{-2} - 30\rho^{-4} + 21\rho^{-6} \\
B_{3\mathrm{P}_1}(\rho) &= 30\rho^{-2} - 135\rho^{-4} + \frac{399}{2}\rho^{-6} - \frac{189}{2}\rho^{-8} \\
B_{3\mathrm{D}_0}(\rho) &= \frac{47}{4}\rho^{-4} - \frac{49}{2}\rho^{-6} + \frac{63}{4}\rho^{-8} \\
B_{3\mathrm{D}_1}(\rho) &= \frac{21}{2}\rho^{-4} - \frac{21}{2}\rho^{-6} \\
B_{3\mathrm{D}_2}(\rho) &= \frac{189}{8}\rho^{-4} - \frac{189}{4}\rho^{-6} + \frac{189}{8}\rho^{-8} \,.
\end{aligned}$$

D. Theoretical description of a laser pulse

D.1. Physical conditions

The exact form of experimentally realized ultrashort intense laser pulses is unknown. In theoretical studies one usually adopts a simple model of the pulse. It is, however, important to select a pulse model such that it does not lead to unphysical results.

Realistic laser pulses always satisfy two principle conditions. The first is

$$\mathbf{F}(-\infty) = \mathbf{F}(\infty) = \mathbf{0}\,. \tag{D.1}$$

The second is the so-called zero-net-force condition

$$\int_{-\infty}^{\infty} \mathrm{d}t\, \mathbf{F}(t) = 0 \tag{D.2}$$

which is equivalent to $\mathbf{A}(-\infty) = \mathbf{A}(\infty)$.

D.2. Various pulse specifications

In order to specify the pulse, two different concepts are used. Within the first concept the pulse envelope is defined via the vector potential $A(t)$,

$$A(t) = A_{\mathrm{peak}}\, f_{\mathrm{env}}(t) \sin(\omega t + \phi) \qquad \text{[A-based pulse]} \tag{D.3}$$

whereas within the second concept the pulse envelope is defined via the electric field $F(t)$,

$$F(t) = F_{\mathrm{peak}}\, f_{\mathrm{env}}(t) \cos(\omega t + \phi) \qquad \text{[F-based pulse]} \tag{D.4}$$

Here, ω is the carrier frequency, ϕ is the carrier-envelope phase (CEP), and A_{peak} (F_{peak}) is the peak amplitude of the vector potential (electric field). The envelope function

$f_{\mathrm{env}}(t)$ is non-zero only in the time interval $t \in [t_{\mathrm{i}}, t_{\mathrm{f}}]$, and can be defined in general as

$$f_{\mathrm{env}}(t) = \begin{cases} g_{\mathrm{env}}\left(-\dfrac{t}{t_{\mathrm{sc}}}\right) & \text{for} \quad t_{\mathrm{i}} \leqslant t < 0, \\ 1 & \text{for} \quad 0 \leqslant t \leqslant T_{\mathrm{flat}}, \\ g_{\mathrm{env}}\left(\dfrac{t - T_{\mathrm{flat}}}{t_{\mathrm{sc}}}\right) & \text{for} \quad T_{\mathrm{flat}} < t \leqslant t_{\mathrm{f}}. \end{cases} \tag{D.5}$$

where the duration of the flat part of the pulse T_{flat} can also be equal to 0. The function $g_{\mathrm{env}}(x)$ specifies the shape of the pulse edge (ascent and descent) and the parameter t_{sc} specifies the duration of the pulse (its detailed meaning depends on the used edge shape). The following edge shapes have been implemented:

$$\text{Linear:} \quad g_{\mathrm{env}}(x) = g_{\mathrm{L}}(x) = 1 - x, \qquad t_{\mathrm{sc}} = T_{\mathrm{edge}} \tag{D.6}$$

$$\text{Parabolic:} \quad g_{\mathrm{env}}(x) = g_{\mathrm{P}}(x) = 1 - x^2, \qquad t_{\mathrm{sc}} = T_{\mathrm{edge}} \tag{D.7}$$

$$\cos^2\text{:} \quad g_{\mathrm{env}}(x) = g_{\mathrm{C}}(x) = (\cos x)^2, \qquad t_{\mathrm{sc}} = (2/\pi)\, T_{\mathrm{edge}} \tag{D.8}$$

$$\text{Gaussian:} \quad g_{\mathrm{env}}(x) = g_{\mathrm{G}}(x) = \exp(-x^2), \qquad t_{\mathrm{sc}} = T_{\mathrm{FWHM}}/\sqrt{2\ln 2} \tag{D.9}$$

$$\text{sech:} \quad g_{\mathrm{env}}(x) = g_{\mathrm{S}}(x) = \mathrm{sech}(\sqrt{2}x) \qquad t_{\mathrm{sc}} = \sqrt{2}\tau \tag{D.10}$$

Whereas the first three shapes represent finite pulses and their duration can be specified using the duration T_{edge} of the edge part of the pulse (ascend or descent) as $t_{\mathrm{i}} = -T_{\mathrm{edge}}$ and $t_{\mathrm{f}} = T_{\mathrm{flat}} + T_{\mathrm{edge}}$, Gaussian and sech shapes represent infinite pulses and to specify their duration one uses either the full-width-at-half-maximum duration T_{FWHM} (especially for Gaussian shape) or just the time-parameter τ (for sech shape). This makes the comparison of results obtained with different edge shapes difficult. However, there exist a unique and physically motivated way to specify the duration based on the fact that usually most of the effect of the laser pulse comes from the top part of the pulse (i.e. where $x \approx 1$). For such x all shapes (except the linear one) satisfy $g_{\mathrm{env}}(x) \approx 1 - x^2$. Therefore, pulses with different edge shapes and the same t_{sc} will have a nearly identical top part, as shown in Fig. D.1. Since $\cos^2$ pulses are popular, it is convenient to specify the duration of pulses with other shapes using the one with $\cos^2$. For example, $2N$-cycle $\cos^2$ pulses (without the flat part) possess $T_{\mathrm{edge}} = 2\pi N/\omega$ and they are identical (in the sense discussed above) to parabolic pulses with $T_{\mathrm{edge}} = 4N/\omega$, Gaussian pulses with $T_{\mathrm{FWHM}} = 4\sqrt{2\ln 2}\, N/\omega$ and sech pulses with $\tau = 4N/(\sqrt{2}\,\omega)$. For the sake of simplicity, in the present work such pulses are referred to as $2N$-cycle parabolic, Gaussian or sech pulses. Similarly, N-M-N-cycle pulses are the same as the previous ones but with $T_{\mathrm{flat}} = 2\pi M/\omega$.

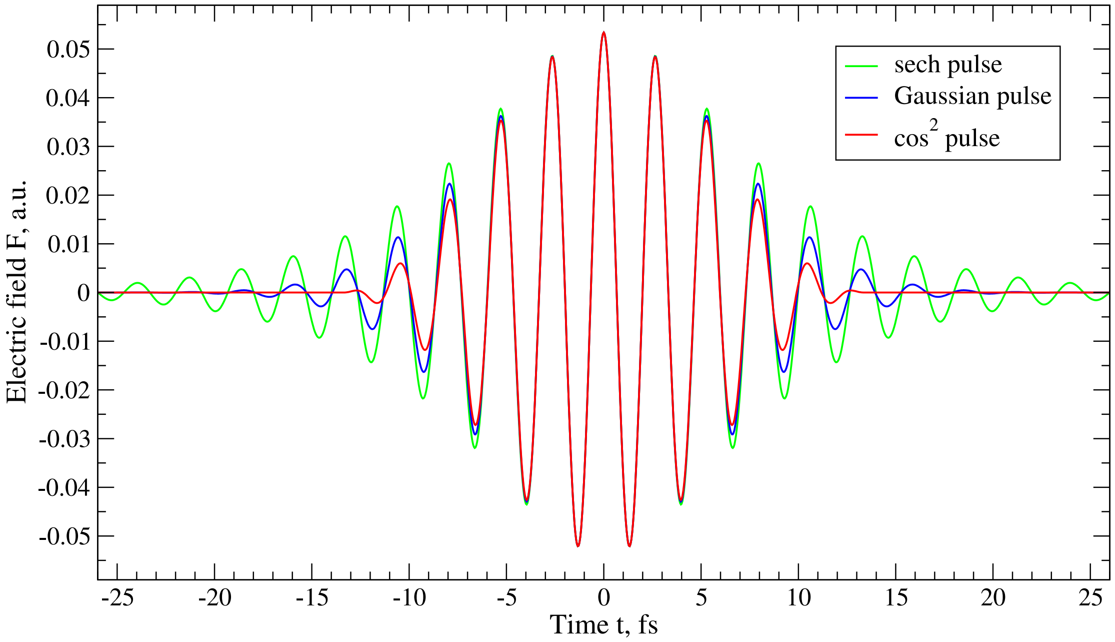

Figure D.1.: Electric field as a function of time for different pulse shapes with the same $t_{\mathrm{sc}} = 8.494\,$fs, peak intensity $I_{\mathrm{peak}} = 10^{14}$ W/cm^2, and wavelength $\lambda = 800\,$nm. The cos^2 pulse (*CF514a*) has a real duration of 10 cycles, while the two infinite pulses can for simplicity be referred to as (approximate) 10-cycle Gaussian (*GF514a*) and 10-cycle sech (*SF514a*) pulses.

The peak intensity I_{peak} is defined as the intensity of the harmonic electromagnetic plane wave with the amplitude F_{peak} (A_{peak}) of the electric field (vector potential), that fulfills $I_{\mathrm{peak}} = F^2_{\mathrm{peak}} = \omega^2 A^2_{\mathrm{peak}}$ (in atomic units with the atomic unit of intensity $I_0 = 3.509 \cdot 10^{16}$ W/cm^2). It should, however, be noted that I_{peak} can differ for very short pulses from the real maximum of intensity (see [6] for a discussion on the definition of the intensity of few-cycle pulses). The definitions (D.3) and (D.4) are chosen such that the value I_{peak} should be the closest to the real maximum of the intensity for the CEP ϕ equal to 0. Note, the last condition is fulfilled for all laser pulses used in the present work.

D.3. Pulse acronyms

For a convenient data processing (storage of results in a database, data selection from the database) pulse acronyms were introduced, which make it possible to specify the whole pulse characteristics using only a few letters. The following scheme is used in the developed code. The pulse acronym consists of 6 (or 7) characters:

- The first character specifies the shape of the pulse edge and whether the pulse is defined according to Eq. (D.3) or Eq. (D.4). A-based pulses are specified by a capital letter, e.g. C stands for $\cos^2$ shape, G stands for Gaussian shape, and S stands for sech pulse, whereas F-based pulses are specified by the same but small letter.
- The second character specifies the carrier-envelope frequency ω. For example, the frequency of a Ti:Sapphire laser and its harmonics is specified by F ($\lambda = 800$ nm), C (400 nm), and A (200 nm), whereas the frequency of a Nd:YAG laser and its harmonics is specified by G (1064 nm), D (532 nm), and B (266 nm).
- The third character specifies the edge duration, i.e. the duration of ascending (descending) part of the pulse. For example, the digit $N = 1..9$ stands for an N-cycle ascent and an N-cycle descent (in the sense discussed above).
- The middle character specifies the duration of the flat part of the pulse, e.g., the digit $M = 1..9$ stands for a flat part consisting of M cycles. For pulses without flat part this character is absent.
- The following two characters specify the peak intensity of the pulse. If both are digits, then the peak intensity is given by $I_{\text{peak}} = x \cdot 10^{10+y}$ W/cm^2, where x (y) denotes the first (second) character of the pair.
- The last character specifies the CEP, the most common cases are a ($\phi = 0$) and b ($\phi = \pi/2$).

For example, the pulse acronym *CG453a* (see Fig. D.2) stands for an 8-cycle 1064 nm laser pulse defined by Eq. (D.3) with the peak intensity $I_{\text{peak}} = 5 \cdot 10^{13}$ W/cm^2, carrier-envelope phase $\phi = 0$ and an envelope function that has a 4-cycle ascent and 4-cycle descent, both of $\cos^2$ shape. The pulse acronym *CG4753a* stands for a 15-cycle pulse which is identical to the previous one but possesses additionally a flat part with a duration of 7 cycles.

D.4. Fourier transform of the pulse

The knowledge about the Fourier transform of a pulse is important for understanding certain features of the final result, e.g., details in the ATI spectrum. Applying the

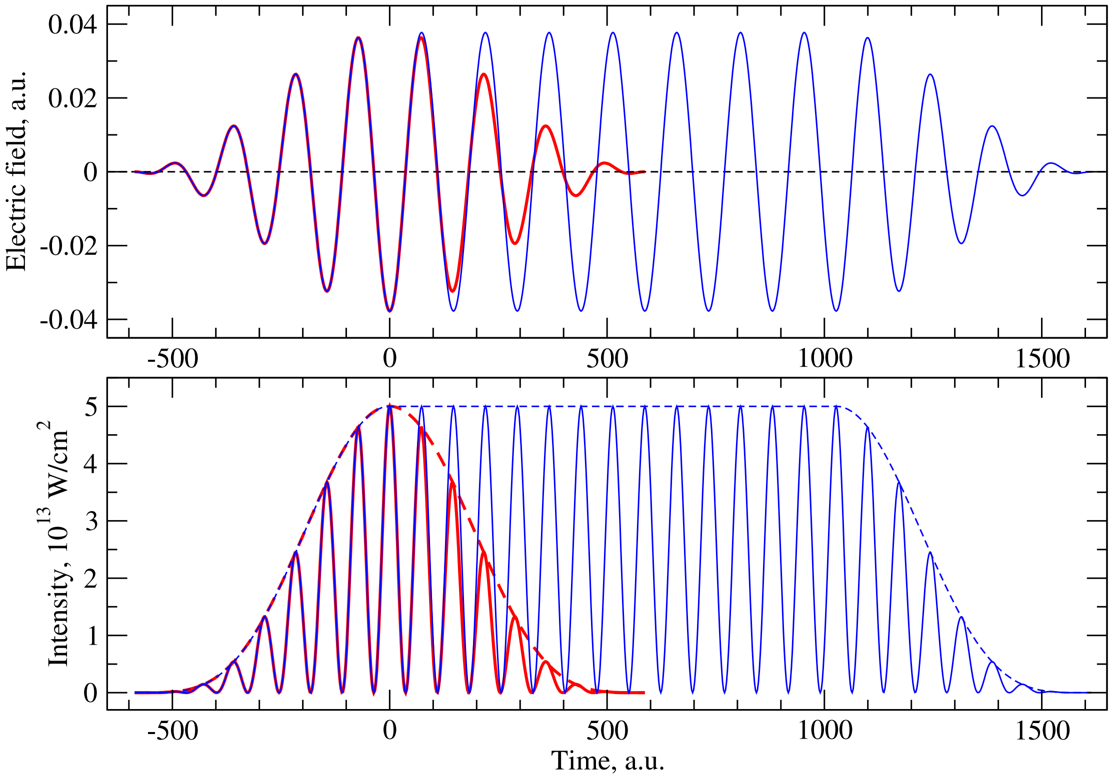

Figure D.2.: Electric field and intensity as a function of time for *CG453a* (red thick line) and *CG4753a* (blue thin line) pulses.

Fourier transform to Eqs. (D.3) and (D.4) one obtains

$$A(\bar{\omega}) = A_{\text{peak}}\left[f^{+}_{\text{env}}(\bar{\omega})\sin\phi + \mathrm{i}f^{-}_{\text{env}}(\bar{\omega})\cos\phi\right] \qquad \text{[A-based]} \qquad \text{(D.11)}$$

$$F(\bar{\omega}) = -F_{\text{peak}}\,(\bar{\omega}/\omega)\left[f^{-}_{\text{env}}(\bar{\omega})\cos\phi - \mathrm{i}f^{+}_{\text{env}}(\bar{\omega})\sin\phi\right] \qquad \text{[A-based]} \qquad \text{(D.12)}$$

$$F(\bar{\omega}) = F_{\text{peak}}\left[f^{+}_{\text{env}}(\bar{\omega})\cos\phi - \mathrm{i}f^{-}_{\text{env}}(\bar{\omega})\sin\phi\right] \qquad \text{[F-based]} \qquad \text{(D.13)}$$

where

$$f^{\pm}_{\text{env}}(\bar{\omega}) = \frac{f_{\text{env}}(\bar{\omega}-\omega) \pm f_{\text{env}}(\bar{\omega}+\omega)}{2}, \qquad f_{\text{env}}(\bar{\omega}) = \frac{1}{\sqrt{2\pi}}\int_{-\infty}^{\infty}\mathrm{d}t\, f_{\text{env}}(t)\, e^{\mathrm{i}\bar{\omega}t}\,. \qquad \text{(D.14)}$$

For example, within the first-order PT the transition probability from a ground state with energy E_0 to a continuum state with energy E is equal to

$$P(E) = 2\pi|D(E)|^2|F(E-E_0)|^2\rho(E)\,. \qquad \text{(D.15)}$$

Applying the Fourier transformation to Eq. (D.5) one obtains

$$f_{\text{env}}(\bar{\omega}) = \frac{t_{\text{sc}}}{\sqrt{2\pi}}\Big[\tilde{g}^{*}_{\text{env}}\big(\bar{\omega}t_{\text{sc}}\big) + e^{\mathrm{i}\bar{\omega}T_{\text{flat}}}\tilde{g}_{\text{env}}\big(\bar{\omega}t_{\text{sc}}\big)\Big] - \mathrm{i}\frac{e^{\mathrm{i}\bar{\omega}T_{\text{flat}}} - 1}{\sqrt{2\pi}\bar{\omega}} \tag{D.16}$$

where the envelope-dependent function $\tilde{g}_{\text{env}}(k)$ given by

$$\tilde{g}_{\text{env}}(k) = \int_{0}^{x_{\text{env}}} \mathrm{d}x\, g_{\text{env}}(x) e^{\mathrm{i}kx} \tag{D.17}$$

can be obtained for each of the used edge shapes. The value of the parameter $x_{\text{env}} = T_{\text{edge}}/t_{\text{sc}}$ for ideal pulses is given by

$$x_{\text{L}} = x_{\text{P}} = 1, \qquad x_{\text{C}} = \pi/2, \qquad x_{\text{G}} = x_{\text{S}} = \infty\ . \tag{D.18}$$

However, in numerical computations x_{env} is typically fixed to some finite value.

Consider now transitions to continuum states with energy $E = E_0 + \omega + \delta E$, where δE is small. Then the identity

$$f^{\pm}_{\text{env}}(\omega + \delta E) = [f_{\text{env}}(\delta E) \pm f_{\text{env}}(2\omega + \delta E)]/2 \approx f_{\text{env}}(\delta E)/2, \tag{D.19}$$

is valid which leads to

$$|F(\omega + \delta E)|^2 = \frac{1}{4}F^2_{\text{peak}}|f_{\text{env}}(\delta E)|^2 = \frac{t^2_{\text{sc}}F^2_{\text{peak}}}{2\pi}\, W_{\text{env}}(k, q) \tag{D.20}$$

where the function

$$W_{\text{env}}(k, q) = \Big\{\mathrm{Re}\big[e^{\mathrm{i}kq}\tilde{g}_{\text{env}}(k)\big] + \frac{\sin(kq)}{k}\Big\}^2 \tag{D.21}$$

depends only on two parameters, $k = \delta E\, t_{\text{sc}}$ and $q = T_{\text{flat}}/(2t_{\text{sc}})$. For $k \approx 0$ the right part of Eq. (D.20) reduces to $F^2_{\text{peak}}T^2_{\text{eff}}/(2\pi)$, where $T_{\text{eff}} = \gamma_{\text{env}}t_{\text{sc}} + T_{\text{flat}}/2$ and

$$\gamma_{\text{L}} = \frac{1}{2}, \qquad \gamma_{\text{P}} = \frac{2}{3}, \qquad \gamma_{\text{C}} = \frac{\pi}{4}, \qquad \gamma_{\text{G}} = \frac{\sqrt{\pi}}{2}, \qquad \gamma_{\text{S}} = \frac{\pi}{2\sqrt{2}}. \tag{D.22}$$

In the case $T_{\text{flat}} = 0$, the function $|F(\omega + \delta E)|^2$ is proportional to the function $W_{\text{env}}(k, 0)$ whose dependence on the envelope of the pulse is presented in Fig. D.3. The key feature is that even for the same t_{sc} the height (γ^2_{env}) and width of the peak differs for different envelope functions. The sech-shaped pulse gives the highest and narrowest peak, while the parabolic pulse leads to the lowest and widest peak. Another impor-

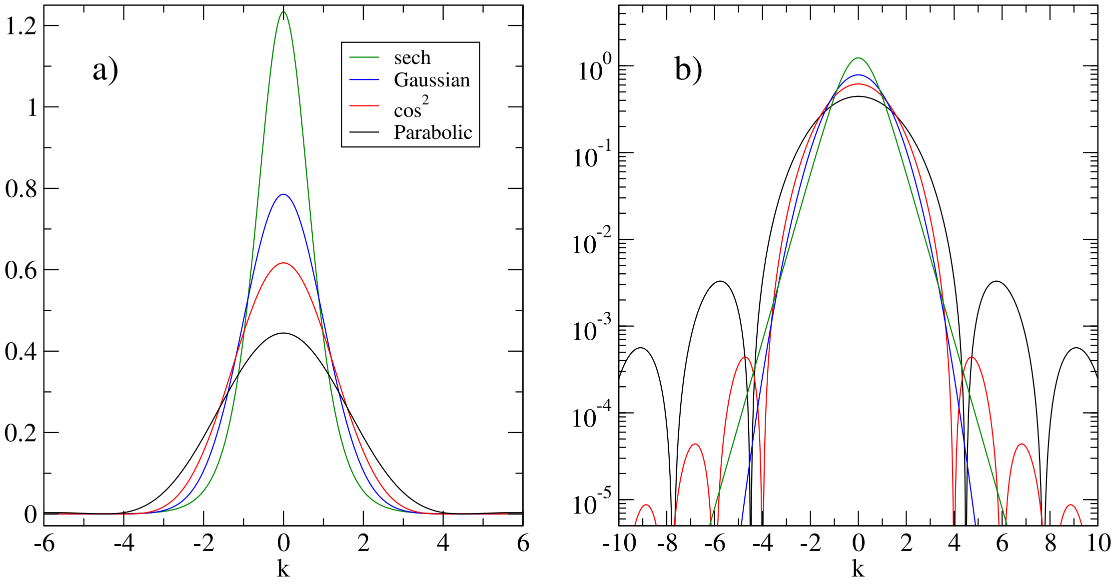

Figure D.3.: Function $W_{\text{env}}(k, 0)$ for different pulse shapes plotted on a linear (a) and logarithmic (b) scale.

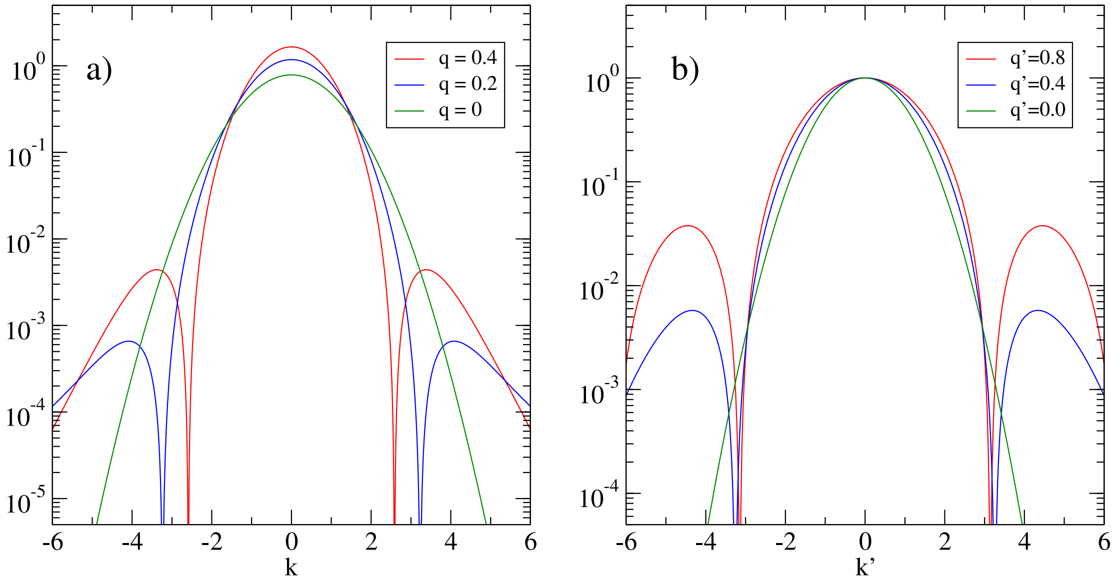

Figure D.4.: (a) Function $W_{\text{G}}(k, q)$ for different values of q. (b) Function $W'_{\text{G}}(k', q')$ for different values of q'.

tant feature is that for finite pulses additional subpeak structures appear with peaks at $|\delta E|\, t_{\rm sc} = 4.73, 6.81, \dots$ for the $\cos^2$ pulse and $|\delta E|\, t_{\rm sc} = 5.75, 9.11, \dots$ for the parabolic pulse. Similar subpeak structures appear also for infinite pulses in the case $T_{\rm flat} \neq 0$. Figure D.4a demonstrates this effect for a Gaussian pulse. With an increase of $T_{\rm flat}$ (and, therefore, q) the subpeaks become more and more pronounced.

Although the scaled variable k is useful to discuss the form of the peaks for the same $t_{\rm sc}$, to discuss the form of peaks with the same height it is convenient to introduce $k' = \delta E\, T_{\rm eff}$ and $q' = T_{\rm flat}/(2T_{\rm eff})$. The dependence on $T_{\rm flat}$ for fixed $T_{\rm eff}$ can thus be studied by varying the parameter q' in the interval between 0 (no flat part) and 1 ($T_{\rm flat} \gg t_{\rm sc}$). For this purpose, Eq. (D.20) can be rewritten in the form

$$|F(\omega + \delta E)|^2 = \frac{T_{\rm eff}^2 F_{\rm peak}^2}{2\pi}\, W'_{\rm env}(k', q') \tag{D.23}$$

where

$$W'_{\rm env}(k', q') = \left\{ \frac{1-q'}{\gamma_{\rm env}} {\rm Re} \left[e^{{\rm i}k'q'} \tilde{g}_{\rm env} \Big(\frac{1-q'}{\gamma_{\rm env}} k' \Big) \right] + \frac{\sin(k'q')}{k'} \right\}^2 . \tag{D.24}$$

The function $W'_{\rm env}(k', q')$ is shown in Fig. D.4 b for a Gaussian pulse and different values of q'. In the limit $q' \to 1$ it reduces to $(\sin k'/k')^2$.

List of Abbreviations

AC	Alternating Current
ADK	Ammosov-Delone-Krainov (approximation)
ATI	Above-Threshold Ionization
CI	Configuration Interaction (method)
DFT	Density Functional Theory
IMST	Intense-field Many-body S-matrix Theory
FWHM	Full Width at Half Maximum
GKT	Generalized Keldysh Theory
HOMO	Highest Occupied Molecular Orbital
KFR	Keldysh-Faisal-Reiss (approximation)
LAPACK	Linear Algebra PACKage
LOPT	Lowest-Order Perturbation Theory
MSD	Method of Steepest Descent
OESE	One-Electron Schrödinger Equation
OTBI	Over-The-Barrier Ionization
PPT	Popov-Peremolov-Terent'ev (approximation)
PT	Perturbation Theory
REMPI	Resonant Enhanced MultiPhoton Ionization
SAE	Single-Active Electron (approximation)
SFA	Strong Field Approximation
TDSE	Time-Dependent Schrödinger Equation

Acknowledgments

I would like to express my deepest gratitude to my supervisor, PD Dr. Alejandro Saenz, for his guidance and many fruitful discussions contributing to this work. I benefited a lot from his intimate professional knowledge and expertise, practical ideas and constructive criticism. I am very indebted to him for giving me a lot of freedom to work on my own schedule, for giving me the scientific freedom, which is always required for successful work, and for supporting my ideas. Additionally, I wish to express my grateful appreciation of his contributions and his support in various private matters during my stay in Germany.

I would like to thank my group members for interesting work together and for their share in creating the friendly atmosphere I enjoyed during my PhD time. Special thanks to Armin, Irina, and Simon who helped me a lot by correcting my English.

I would like to thank all colleagues from the QOM and NANO groups at the Hausvogteiplatz, who worked here from the very beginning and who came recently for the nice environment.

Last but not the least, I would like to express my deep thanks and appreciation to my family, especially to my dear wife Aliona and my lovely daughter Nicole, the source of my happiness, encouragement and motivation.

Bibliography

[1] *T. Brabec and F. Krausz*: Intense few-cycle laser fields: Frontiers of nonlinear optics. *Rev. Mod. Phys. 72*, 545 (2000).

[2] *U. Keller*: Recent developments in compact ultrafast lasers. *Nature 424*, 831 (2003).

[3] *T. Udem, R. Holzwarth, and T. W. Hänsch*: Optical frequency metrology. *Nature 416*, 233 (2002).

[4] *A. Baltuška, T. Udem, M. Uiberacker, M. Hentschel, E. Goulielmakis, C. Gohle, R. Holzwarth, V. S. Yakovlev, A. Scrinzi, T. W. Hänsch, and F. Krausz*: Attosecond control of electronic processes by intense light fields. *Nature 421*, 611 (2003).

[5] *T. Fuji, J. Rauschenberger, C. Gohle, A. Apolonski, T. Udem, V. S. Yakovlev, G. Tempea, T. W. Hänsch, and F. Krausz*: Attosecond control of optical waveforms. *New J. Phys. 7*, 116 (2005).

[6] *D. B. Milošević, G. G. Paulus, D. Bauer, and W. Becker*: Above-threshold ionization by few-cycle pulses. *J. Phys. B 39*, R203 (2006).

[7] *T. Wittmann, B. Horvath, W. Helml, M. G. Schätzel, X. Gu, A. L. Cavalieri, G. G. Paulus, and R. Kienberger*: Single-shot carrier–envelope phase measurement of few-cycle laser pulses. *Nature Phys. 5*, 357 (2009).

[8] *T. Pfeifer, C. Spielmann, and G. Gerber*: Femtosecond x-ray science. *Rep. Prog. Phys. 69*, 443 (2006).

[9] *E. Goulielmakis, M. Schultze, M. Hofstetter, V. S. Yakovlev, J. Gagnon, M. Uiberacker, A. L. Aquila, E. M. Gullikson, D. T. Attwood, R. Kienberger, F. Krausz, and U. Kleineberg*: Single-cycle nonlinear optics. *Science 320*, 1614 (2008).

[10] *A. H. Zewail*: Laser femtochemistry. *Science 242*, 1645 (1988).

[11] *D. M. Neumark*: Time-resolved photoelectron spectroscopy of molecules and clusters. *Annu. Rev. Phys. Chem. 52*, 255 (2001).

[12] *T. Seideman*: Time-resolved photoelectron angular distributions: Concepts, applications, and directions. *Annu. Rev. Phys. Chem. 53*, 41 (2002).

[13] *H. Stapelfeldt and T. Seideman*: Colloquium: Aligning molecules with strong laser pulses. *Rev. Mod. Phys. 75*, 543 (2003).

[14] *J. A. Davies, R. E. Continetti, D. W. Chandler, and C. C. Hayden*: Femtosecond time-resolved photoelectron angular distributions probed during photodissociation of NO_2. *Phys. Rev. Lett. 84*, 5983 (2000).

[15] *J. Itatani, J. Levesque, D. Zeidler, H. Niikura, H. Pépin, J. C. Kieffer, P. B. Corkum, and D. M. Villeneuve*: Tomographic imaging of molecular orbitals. *Nature 432*, 867 (2004).

[16] *M. Meckel, D. Comtois, D. Zeidler, A. Staudte, D. Pavičić, H. C. Bandulet, H. Pépin, J. C. Kieffer, R. Dörner, D. M. Villeneuve, and P. B. Corkum*: Laser-induced electron tunneling and diffraction. *Science 320*, 1478 (2008).

[17] *A. Jaroń-Becker, A. Becker, and F. H. M. Faisal*: Ionization of N_2, O_2, and linear carbon clusters in a strong laser pulse. *Phys. Rev. A 69*, 023410 (2004).

[18] *T. K. Kjeldsen and L. B. Madsen*: Comment on "Strong-field ionization of laser-irradiated light homonuclear diatomic molecules: A generalized strong-field approximation–combination of atomic orbitals model". *Phys. Rev. A 73*, 047401 (2006).

[19] *D. B. Milošević*: Strong-field approximation for ionization of a diatomic molecule by a strong laser field. *Phys. Rev. A 74*, 063404 (2006).

[20] *V. I. Usachenko*: Reply to "Comment on 'Strong-field ionization of laser-irradiated light homonuclear diatomic molecules: A generalized strong-field approximation–combination of atomic orbitals model' ". *Phys. Rev. A 73*, 047402 (2006).

[21] *D. A. Telnov and S.-I. Chu*: Effects of electron structure and multielectron dynamical response on strong-field multiphoton ionization of diatomic molecules with arbitrary orientation: An all-electron time-dependent density-functional-theory approach. *Phys. Rev. A 79*, 041401 (2009).

[22] *A. Saenz*: Enhanced ionization of molecular hydrogen in very strong fields. *Phys. Rev. A 61*, 051402(R) (2000).

[23] *A. Saenz*: Molecular hydrogen exposed to a suddenly turned-on strong electric field or low-frequency laser. *J. Phys. B 33*, 3519 (2000).

[24] *A. Saenz*: Behavior of molecular hydrogen exposed to strong dc, ac, or low-frequency laser fields: I. Bond softening and enhanced ionization. *Phys. Rev. A 66*, 063407 (2002).

[25] *A. Saenz*: Behavior of molecular hydrogen exposed to strong dc, ac, or low-frequency laser fields: II. Comparison of ab initio and Ammosov-Delone-Krainov (ADK) rates. *Phys. Rev. A 66*, 063408 (2002).

[26] *A. Saenz*: Electronically excited states of molecular hydrogen exposed to strong direct current, alternative current, or low-frequency laser fields. *J. Phys. B 35*, 4829 (2002).

[27] *A. Saenz*: Molecular Hydrogen in Strong Laser Fields: Bond Softening, Enhanced Ionisation, and Coherent Control. *Physica Scripta T110*, 126 (2004).

[28] *K. Harumiya, I. Kawata, H. Kono, and Y. Fujimura*: Exact two-electron wave packet dynamics of H_2 in an intense laser field: Formation of localized ionic states H^+H^-. *J. Chem. Phys. 113*, 8953 (2000).

[29] *K. Harumiya, H. Kono, Y. Fujimura, I. Kawata, and A. D. Bandrauk*: Intense laser-field ionization of H_2 enhanced by two-electron dynamics. *Phys. Rev. A 66*, 043403 (2002).

[30] *H. Kono, Y. Sato, M. Kanno, K. Nakai, and T. Kato*: Theoretical investigations of the electronic and nuclear dynamics of molecules in intense laser fields: Quantum mechanical wave packet approaches. *Bull. Chem. Soc. Jpn. 79*, 196 (2006).

[31] *A. Palacios, H. Bachau, and F. Martín*: Enhancement and control of H_2 dissociative ionization by femtosecond VUV laser pulses. *Phys. Rev. Lett. 96*, 143001 (2006).

[32] *Y. V. Vanne, A. Saenz, A. Dalgarno, R. C. Forrey, P. Froelich, and S. Jonsell*: Doubly excited autoionizing states of H_2 converging to the $H(n = 2) + H(n' = 2)$ limit. *Phys. Rev. A 73*, 062706 (2006).

[33] *R. C. Forrey, A. Dalgarno, Y. V. Vanne, A. Saenz, and P. Froelich*: Nonadiabatic coupling in cold collisions of spin-polarized metastable hydrogen atoms. *Phys. Rev. A 76*, 052709 (2007).

[34] *Y. V. Vanne and A. Saenz*: Ionization of H_2 in intense ultrashort laser pulses: parallel versus perpendicular orientation. *J. Mod. Opt. 55*, 2665 (2008).

[35] *Y. V. Vanne and A. Saenz*: Ionization of molecular hydrogen and deuterium by frequency-doubled Ti:sapphire laser pulses. *Phys. Rev. A 80*, 053422 (2009).

[36] *I. A. Bocharova, H. Mashiko, M. Magrakvelidze, D. Ray, P. Ranitovic, C. L. Cocke, and I. V. Litvinyuk*: Direct Coulomb-explosion imaging of coherent nuclear dynamics induced by few-cycle laser pulses in light and heavy hydrogen. *Phys. Rev. A 77*, 053407 (2008).

[37] *A. Staudte, S. Patchkovskii, D. Pavičić, H. Akagi, O. Smirnova, D. Zeidler, M. Meckel, D. M. Villeneuve, R. Dörner, M. Y. Ivanov, and P. B. Corkum*: Angular tunneling ionization probability of fixed-in-space H_2 molecules in intense laser pulses. *Phys. Rev. Lett. 102*, 033004 (2009).

[38] *M. Magrakvelidze, F. He, S. De, I. Bocharova, D. Ray, U. Thumm, and I. V. Litvinyuk*: Angular dependence of the strong-field ionization measured in randomly oriented hydrogen molecules. *Phys. Rev. A 79*, 033408 (2009).

[39] *T. Wilbois and H. Helm*: On the complex momentum spectra of photoelectrons formed from H_2 in a strong laser field. *Laser Phys. 18*, 579 (2008).

[40] *M. Awasthi, Y. V. Vanne, A. Saenz, A. Castro, and P. Decleva*: Single-active-electron approximation for describing molecules in ultrashort laser pulses and its application to molecular hydrogen. *Phys. Rev. A 77*, 063403 (2008).

[41] *Y. V. Vanne and A. Saenz*: Exact Keldysh theory of strong-field ionization: Residue method versus saddle-point approximation. *Phys. Rev. A 75*, 033403 (2007).

[42] *Y. V. Vanne and A. Saenz*: Quasistatic limit of the strong-field approximation describing atoms and molecules in intense laser fields. *Phys. Rev. A 75*, 063403 (2007).

[43] *Y. V. Vanne and A. Saenz*: Generalized gauge-invariant formulations of the strong-field approximation. *Phys. Rev. A 79*, 023421 (2009).

[44] *I. J. Schoenberg*: Contribution to the problem of approximation of equidistant data by analytic functions. *Quart. Appl. Math. 4*, 45 (1946).

[45] *C. de Boor*: *A Practical Guide to Splines* (Springer, New York, 1978).

[46] *M. Brosolo, P. Decleva, and A. Lisini*: Accurate variational determination of continuum wavefunctions by a one-centre expansion in a spline basis. An application to H_2^+ and HeH_2^+ photoionization. *J. Phys. B 25*, 3345 (1992).

[47] *H. Bachau, E. Cormier, P. Decleva, J. E. Hansen, and F. Martín*: Applications of B-splines in atomic and molecular physics. *Rep. Prog. Phys. 64*, 1815 (2001).

[48] *L. D. Thomas, M. H. Alexander, B. R. Johnson, W. A. Lester, Jr, J. C. Light, K. D. McLenithan, G. A. Parker, M. J. Redmon, T. G. Schmalz, D. Secrest, and R. B. Walker*: Comparison of numerical methods for solving the second-order differential equations of molecular scattering theory. *J. Comp. Phys. 41*, 407 (1981).

[49] *M.Aymar, C. H. Greene, and E. Luc-Koenig*: Multichannel Rydberg spectroscopy of complex atoms. *Rev. Mod. Phys. 68*, 1015 (1996).

[50] *C. Marzok, B. Deh, C. Zimmermann, P. W. Courteille, E. Tiemann, Y. V. Vanne, and A. Saenz*: Feshbach resonances in an ultracold ^{7}Li and ^{87}Rb mixture. *Phys. Rev. A 79*, 012717 (2009).

[51] *S. Grishkevich, P.-I. Schneider, Y. V. Vanne, and A. Saenz*: Mimicking multichannel scattering with single-channel approaches. *Phys. Rev. A 81*, 022719 (2010).

[52] *C.-C. Chen, H. Chang, and C.-S. Hsue*: A highly accurate calculation for the electronic states of H_2^+ in B-spline basis. *Chem. Phys. Lett. 217*, 486 (1994).

[53] *H. Bachau*: Multiphoton ionization of one-electron diatomic molecules: the discretization approach for the two-centre problem. *J. Phys. B 35*, 509 (2002).

[54] *L. Wolniewicz*: Relativistic energies of the ground state of the hydrogen molecule. *J. Chem. Phys. 99*, 1851 (1993).

[55] *J. Rychlewski, W. Cencek, and J. Komasa*: The equivalence of explicitly correlated Slater and Gaussian functions in variational quantum chemistry computations. the ground state of H_2. *Chem. Phys. Lett. 229*, 657 (1994).

[56] *E. R. Davidson*: The iterative calculation of a few of the lowest eigenvalues and corresponding eigenvectors of large real-symmetric matrices. *J. Comput. Phys. 17*, 87 (1975).

[57] *S. Magnier, P. Millié, O. Dulieu, and F. Masnou-Seeuws*: Potential curves for the ground and excited states of the Na_2 molecule up to the (3s+5p) dissociation limit: Results of the different effective potential calculations. *J. Chem. Phys. 98*, 7113 (1993).

[58] *P. Lambropoulos, P. Maragakis, and J. Zhang*: Two-electron atoms in strong fields. *Phys. Rep. 305*, 203 (1998).

[59] *F. Martín*: Ionization and dissociation using B splines: photoionization of the hydrogen molecule. *J. Phys. B 32*, R197 (1999).

[60] *R. C. Forrey, S. Jonsell, A. Saenz, P. Froelich, and A. Dalgarno*: Cold collisions of metastable hydrogen atoms. *Phys. Rev. A 67*, 040701(R) (2003).

[61] *Y. V. Vanne and A. Saenz*: Numerical treatment of diatomic two-electron molecules using a B-spline based CI method. *J. Phys. B 37*, 4101 (2004).

[62] *E. L. Mehler and K. Ruedenberg*: Two-center exchange integrals between Slater-type atomic orbitals. *J. Chem. Phys. 50*, 2575 (1969).

[63] *J. D. Weeks, A. Hazi, and S. A. Rice*: On the use of pseudopotentials in the quantum theory of atoms and molecules. *Adv. Chem. Phys. 16*, 283 (1969).

[64] *J. N. Bardsley*: Pseudopotentials in atomic and molecular physics. *Case studies in atomic physics 4*, 299 (1974).

[65] *A. Dalgarno*: Model and pseudopotential calculations. *Atomic Physics 4*, 325 (1975).

[66] *A. Hibbert*: Model potentials in atomic structure theory. *Adv. Atom. Molec. Phys. 18*, 309 (1982).

[67] *G. Peach*: Long-range interactions in atoms and diatomic molecules, in *Atoms in Astrophysics*, edited by *P. G. Burke, W. B. Eissner, D. G. Hummer, and I. C. Percival*, p. 115 (Plenum, New York, 1983).

[68] *P. Durand and J. P. Matieu*: Effective hamiltonians and pseudo operators as tools for rigorous modeling, in *Ab Initio Methods in Quantum Chemistry*, edited by *K. P. Lawley*, p. 321 (Wiley, New York, 1987).

[69] *C. Laughlin and G. A. Victor*: Model-potential methods. *Adv. Atom. Molec. Phys. 25*, 163 (1988).

[70] *A. Dalgarno, C. Bottcher, and G. A. Victor*: Pseudo-potential calculation of atomic interactions. *Chem. Phys. Lett. 7*, 265 (1970).

[71] *C. Bottcher*: An iterative perturbation solution of the inverse potential problem. *J. Phys. B 4*, 1140 (1971).

[72] *D. K. Watson, C. J. Cerjan, S. Guberman, and A. Dalgarno*: Potential energy curves for Li_2. *Chem. Phys. Lett. 50*, 181 (1977).

[73] *M. Klapisch*: A program for atomic wavefunction computations by the parametric potential method. *Comput. Phys. Commun. 2*, 239 (1971).

[74] *M. Aymar*: Influence of core-polarisation effects on the photoionisation cross sections of the ground level and excited ns levels of neutral sodium. *J. Phys. B 11*, 1413 (1978).

[75] *S. Magnier and F. Masnou-Seeuws*: Model potential calculations for the excited and Rydberg states of the Na_2^+ molecular ion: Potential curves, dipole and quadrupole transition moments. *Mol. Phys. 89*, 711 (1996).

[76] *S. Magnier, S. Rousseau, A. R. Allouche, G. Hadinger, and M. Aubert-Frécon*: Potential energy curves of 58 states of Li_2^+. *Chem. Phys. 246*, 57 (1999).

[77] *S. Magnier and M. Aubert-Frécon*: Model potential calculations for the ground and various excited states of $LiNa^+$. *J. Phys. Chem. A 105*, 165 (2001).

[78] *M. Aymar, S. Azizi, and O. Dulieu*: Model-potential calculations for ground and excited Σ states of Rb_2^+, Cs_2^+ and $RbCs^+$. *J. Phys. B 36*, 4799 (2003).

[79] *S. Magnier, M. Aubert-Frécon, J. Hanssen, and C. L. Sech*: Two-electron wavefunctions for the ground state of alkali negative ions. *J. Phys. B 32*, 5639 (1999).

[80] *G. Staszewska and L. Wolniewicz*: Adiabatic energies of excited ${}^1\Sigma_u$ states of the hydrogen molecule. *J. Mol. Spec. 212*, 208 (2002).

[81] *L. Wolniewicz and G. Staszewska*: ${}^1\Sigma_u^+ \to X\,{}^1\Sigma_g^+$ transition moments for the hydrogen molecule. *J. Mol. Spec. 217*, 181 (2003).

[82] *L. Wolniewicz and G. Staszewska*: Excited ${}^1\Pi_u$ states and the ${}^1\Pi_u^+ \to X\,{}^1\Sigma_g^+$ transition moments for the hydrogen molecule. *J. Mol. Spec. 220*, 45 (2003).

[83] *K. Dressler and L. Wolniewicz*: Improved theoretical $^1\Sigma_u^+$ and $^1\Pi_u$ wavefunctions, energies, and transition moments for the H_2 molecule. *Ber. Bunsenges. Phys. Chem. 99*, 246 (1995).

[84] *A. Apalategui and A. Saenz*: Multiphoton ionization of the hydrogen molecule H_2. *J. Phys. B 35*, 1909 (2002).

[85] *I. Sánchez and F. Martín*: Doubly excited autoionizing states of H_2 above the second ionization threshold: the Q(2) resonance series. *J. Chem. Phys. 110*, 6702 (1999).

[86] *A. Saenz*: Photoabsorption and photoionization of HeH^+. *Phys. Rev. A 67*, 033409 (2003).

[87] *D. Landhuis, L. Matos, S. C. Moss, J. K. Steinberger, K. Vant, L. Willmann, T. J. Greytak, and D. Kleppner*: Inelastic collision rates of trapped metastable hydrogen. *Phys. Rev. A 67*, 022718 (2003).

[88] *J. Tennyson*: Resonance parameters and quantum defects for superexcited H_2. *Atomic Data and Nuclear Data Tables 64*, 253 (1996).

[89] *S. Jonsell, A. Saenz, P. Froelich, R. C. Forrey, R. Cote, and A. Dalgarno*: Long-range interactions between two 2s excited hydrogen atoms. *Phys. Rev. A 65*, 042501 (2002).

[90] *S. L. Guberman*: The doubly excited autoionizing states of H_2. *J. Chem. Phys. 78*, 1404 (1983).

[91] *S. I. Nikitin, V. N. Ostrovskii, and N. V. Prudov*: Interaction between two excited hydrogen atoms at large separations. *Sov. Phys. JETP 64*, 745 (1986), note, the English translation includes several typos in the definition of the transformations. It should read $P_0 : \mathbf{r}_{1a} \to -\mathbf{r}_{1a}, \mathbf{r}_{2b} \to -\mathbf{r}_{2b}; P_1 : \mathbf{r}_{1a} \to -\mathbf{r}_{1a}, \mathbf{r}_{2b} \to \mathbf{r}_{2b}$.

[92] *I. Dumitriu, Y. V. Vanne, M. Awasthi, and A. Saenz*: Photoionization of the alkali dimer cations Li_2^+, Na_2^+ and $LiNa^+$. *J. Phys. B 40*, 1821 (2007).

[93] *J. R. Oppenheimer*: Three notes on the quantum theory of aperiodic effects. *Phys. Rev. 31*, 66 (1928).

[94] *L. D. Landau and E. M. Lifshitz*: *Quantum Mechanics* (Pergamon Press, Oxford, 1965).

[95] *A. M. Perelomov, V. S. Popov, and M. V. Terent'ev*: Ionization of atoms in an alternating electric field. *Sov. Phys. JETP 23*, 924 (1966).

[96] *M. V. Ammosov, N. B. Delone, and V. P. Krainov*: Tunnel ionization of complex atoms and of atomic ions in an alternating electromagnetic field. *JETP 64*, 1191 (1986).

[97] *W. Kaiser and C. G. B. Garrett*: Two-photon excitation in CaF_2:Eu^{2+}. *Phys. Rev. Lett. 7*, 229 (1961).

[98] *I. D. Abella*: Optical double-photon absorption in cesium vapor. *Phys. Rev. Lett. 9*, 453 (1962).

[99] *M. Göppert-Mayer*: Über Elementarakte mit zwei Quantensprüngen. *Ann. Phys. 9*, 273 (1931).

[100] *W. Zernik*: Two-photon ionization of atomic hydrogen. *Phys. Rev. 135*, 1A (1964).

[101] *H. B. Bebb and A. Gold*: Multiphoton ionization of hydrogen and rare-gas atoms. *Phys. Rev. 143*, 1 (1966).

[102] *G. S. Voronov and N. B. Delone*: Ionization of the xenon atom by the electric field of ruby laser emission. *Sov. Phys. JETP Letters 1*, 66 (1965).

[103] *P. Lambropoulos*: Multiphoton ionization of one-electron atoms with circularly polarized light. *Phys. Rev. Lett. 29*, 453 (1972).

[104] *P. Lambropoulos*: Topics on multiphoton processes in atoms. *Adv. At. Mol. Phys. 12*, 87 (1976).

[105] *R. G. Evans and P. C. Thonemann*: Laser produced dissociation and ionisation of residual hydrocarbons in a high vacuum system. *Phys. Lett. A 38*, 398 (1972).

[106] *E. A. Martin, Jr. and L. Mandel*: Electron energy spectrum in laser-induced multiphoton ionization of atoms. *Appl. Opt. 15*, 2378 (1976).

[107] *P. Agostini, F. Fabre, G. Mainfray, G. Petite, and N. K. Rahman*: Free-free transitions following six-photon ionization of xenon atoms. *Phys. Rev. Lett. 42*, 1127 (1979).

[108] *L. A. Lompré, G. Mainfray, C. Manus, and G. Farkas*: Multiphoton absorption by electrons. *Phys. Rev. Lett. 43*, 1243 (1979).

[109] *Y. Gontier, M. Poirier, and M. Trahin*: Multiphoton absorptions above the ionisation threshold. *J. Phys. B 13*, 1381 (1980).

[110] *Y. Gontier and M. Trahin*: Energetic electron generation by multiphoton absorption. *J. Phys. B 13*, 4383 (1980).

[111] *F. Fabre, G. Petite, P. Agostini, and M. Clement*: Multiphoton above-threshold ionisation of xenon at 0.53 and 1.06μm. *J. Phys. B 15*, 1353 (1982).

[112] *P. Kruit, J. Kimman, H. G. Muller, and M. J. van der Wiel*: Electron spectra from multiphoton ionization of xenon at 1064, 532, and 355 nm. *Phys. Rev. A 28*, 248 (1983).

[113] *L. A. Lompré, G. Mainfray, C. Manus, and J. Kupersztych*: The energy distributions of electrons produced in multiphoton ionisation of rare gases. *J. Phys. B 20*, 1009 (1987).

[114] *L. V. Keldysh*: Ionization in the field of a strong electromagnetic wave. *Sov. Phys. JETP 20*, 1307 (1965).

[115] *D. M. Volkov*: Über eine Klasse von Lösungen der Diracschen Gleichung. *Z Phys. 94*, 250 (1935).

[116] *F. H. M. Faisal*: Multiple absorption of laser photons by atoms. *J. Phys. B 6*, L89 (1973).

[117] *H. R. Reiss*: Effect of an intense electromagnetic field on a weakly bound system. *Phys. Rev. A 22*, 1786 (1980).

[118] *A. L'Huillier and P. Balcou*: High-order harmonic generation in rare gases with a 1-ps 1053-nm laser. *Phys. Rev. Lett. 70*, 774 (1993).

[119] *B. Yang, K. J. Schafer, B. Walker, K. C. Kulander, P. Agostini, and L. F. DiMauro*: Intensity-dependent scattering rings in high order above-threshold ionization. *Phys. Rev. Lett. 71*, 3770 (1993).

[120] *G. G. Paulus, W. Nicklich, H. Xu, P. Lambropoulos, and H. Walther*: Plateau in above threshold ionization spectra. *Phys. Rev. Lett. 72*, 2851 (1994).

[121] *H. B. van Linden van den Heuvell and H. G. Muller*: Limiting cases of excess-photon ionization, in *Multiphoton Processes*, edited by *S. J. Smith and P. L. Knight*, p. 25 (Cambridge Univ. Press, 1988).

[122] *T. F. Gallagher*: Above-threshold ionization in low-frequency limit. *Phys. Rev. Lett. 61*, 2304 (1988).

[123] *P. B. Corkum*: Plasma perspective on strong field multiphoton ionization. *Phys. Rev. Lett. 71*, 1994 (1993).

[124] *K. J. Schafer, B. Yang, L. F. DiMauro, and K. C. Kulander*: Above threshold ionization beyond the high harmonic cutoff. *Phys. Rev. Lett. 70*, 1599 (1993).

[125] *M. Lewenstein, P. Balcou, M. Y. Ivanov, A. L'Huillier, and P. B. Corkum*: Theory of high-harmonic generation by low-frequency laser fields. *Phys. Rev. A 49*, 2117 (1994).

[126] *H. R. Reiss*: Inherent contradictions in the tunneling-multiphoton dichotomy. *Phys. Rev. A 75*, 031404(R) (2007).

[127] *H. R. Reiss*: Limits on tunneling theories of strong-field ionization. *Phys. Rev. Lett. 101*, 043002 (2008).

[128] *B. Walker, B. Sheehy, L. F. DiMauro, P. Agostini, K. J. Schafer, and K. C. Kulander*: Precision measurement of strong field double ionization of helium. *Phys. Rev. Lett. 73*, 1227 (1994).

[129] *J. B. Watson, A. Sanpera, D. G. Lappas, P. L. Knight, and K. Burnett*: Nonsequential double ionization of helium. *Phys. Rev. Lett. 78*, 1884 (1997).

[130] *A. D. Bandrauk* (editor): *Molecules in Laser Fields* (Marcel Dekker, New York, 1993).

[131] *J. H. Posthumus*: The dynamics of small molecules in intense laser fields. *Rep. Prog. Phys. 67*, 623 (2004).

[132] *G. N. Gibson, R. R. Freeman, and T. J. McIlrath*: Dynamics of the high-intensity multiphoton ionization of N_2. *Phys. Rev. Lett. 67*, 1230 (1991).

[133] *S. L. Chin, Y. Liang, J. E. Decker, F. A. Ilkov, and M. V. Ammosov*: Tunnel ionization of diatomic molecules by an intense CO_2 laser. *J. Phys. B 25*, L249 (1992).

[134] *T. D. G. Walsh, J. E. Decker, and S. L. Chin*: Tunnel ionization of simple molecules by an intense CO_2 laser. *J. Phys. B 26*, L85 (1993).

[135] *A. Talebpour, C.-Y. Chien, and S. L. Chin*: The effects of dissociative recombination in multiphoton ionization of O_2. *J. Phys. B 29*, L677 (1996).

[136] *C. Guo, M. Li, J. P. Nibarger, and G. N. Gibson*: Single and double ionization of diatomic molecules in strong laser fields. *Phys. Rev. A 58*, R4271 (1998).

[137] *I. V. Litvinyuk, K. F. Lee, P. W. Dooley, D. M. Rayner, D. M. Villeneuve, and P. B. Corkum*: Alignment-dependent strong field ionization of molecules. *Phys. Rev. Lett. 90*, 233003 (2003).

[138] *K. Mishima, M. Hayashi, J. Yi, S. H. Lin, H. L. Selzle, and E. W. Schlag*: Generalization of Keldysh theory. *Phys. Rev. A 66*, 033401 (2002).

[139] *J. Bauer*: Low-frequency-high-intensity limit of the Keldysh-Faisal-Reiss theory. *Phys. Rev. A 73*, 023421 (2006).

[140] *D. Bauer, D. B. Milošević, and W. Becker*: Strong-field approximation for intense-laser-atom processes: The choice of gauge. *Phys. Rev. A 72*, 023415 (2005).

[141] *J. Muth-Böhm, A. Becker, and F. H. M. Faisal*: Suppressed molecular ionization for a class of diatomics in intense femtosecond laser fields. *Phys. Rev. Lett. 85*, 2280 (2000).

[142] *T. K. Kjeldsen and L. B. Madsen*: Strong-field ionization of N_2: length and velocity gauge strong-field approximation and tunnelling theory. *J. Phys. B 37*, 2033 (2004).

[143] *T. K. Kjeldsen and L. B. Madsen*: Strong-field ionization of diatomic molecules and companion atoms: Strong-field approximation and tunneling theory including nuclear motion. *Phys. Rev. A 71*, 023411 (2005).

[144] *B. Bergues, Z. Ansari, D. Hanstorp, and I. Y. Kiyan*: Photodetachment in a strong laser field: An experimental test of Keldysh-like theories. *Phys. Rev. A 75*, 063415 (2007).

[145] *H. R. Reiss*: Velocity-gauge theory for the treatment of strong-field photodetachment. *Phys. Rev. A 76*, 033404 (2007).

[146] *F. H. M. Faisal*: Gauge-invariant intense-field approximations to all orders. *J. Phys. B 40*, F145 (2007).

[147] *A. Becker and F. H. M. Faisal*: Intense-field many-body S-matrix theory. *J. Phys. B 38*, R1 (2005).

[148] *H. R. Reiss*: Comment on "Photodetachment in a strong laser field: An experimental test of Keldysh-like theories". *Phys. Rev. A 77*, 067401 (2008).

[149] *B. Bergues, Z. Ansari, D. Hanstorp, and I. Y. Kiyan*: Reply to "Comment on 'Photodetachment in a strong laser field: An experimental test of Keldysh-like theories' ". *Phys. Rev. A 77*, 067402 (2008).

[150] *J. H. Bauer*: Simple proof of gauge invariance for the S-matrix element of strong-field photoionization. *Phys. Scr. 77*, 015303 (2008).

[151] *F. H. M. Faisal*: Gauge-equivalent intense-field approximations in velocity and length gauges to all orders. *Phys. Rev. A 75*, 063412 (2007).

[152] *S. Hassani*: *Mathematical Physics: A Modern Introduction to Its Foundations* (Springer-Verlag New York, Inc, 1999).

[153] *K. Mishima, M. Hayashi, J. Yi, S. H. Lin, H. L. Selzle, and E. W. Schlag*: Theoretical studies of the long range Coulomb potential effect on photoionization by strong lasers. *Phys. Rev. A 66*, 053408 (2002).

[154] *K. Mishima, K. Nagaya, M. Hayashi, and S. H. Lin*: Theoretical studies of high-power laser ionization of molecules in the tunneling region. *Phys. Rev. A 70*, 063414 (2004).

[155] *S. D. Chao*: Influence of intense incident electromagnetic fields on weakly bound electrons: An exact Keldysh approximation. *Phys. Rev. A 72*, 053414 (2005).

[156] *K. Nagaya, K. Mishima, M. Hayashi, and S. Lin*: Distortion effects of the initial electronic states on tunneling photo-ionization of hydrogen atom. *Chem. Phys. Lett. 414*, 438 (2005).

[157] *K. Mishima, K. Nagaya, M. Hayashi, and S. H. Lin*: Towards the realization of the quantum chemistry approach to tunneling photoionization processes in strong laser fields. *J. Chem. Phys. 122*, 024104 (2005).

[158] *K. Mishima, K. Nagaya, M. Hayashi, and S. H. Lin*: Effect of quantum interference on tunneling photoionization rates of N_2 and O_2 molecules. *J. Chem. Phys. 122*, 104312 (2005).

[159] *K. Mishima, M. Hayashi, and S. H. Lin*: Keldysh-type photoionization rate of large polyatomic molecules in the tunneling region. *Phys. Rev. A 71*, 053411 (2005).

[160] *K. Nagaya, K. Mishima, and M. Hayashi*: Theoretical studies on tunneling ionizations of helium atom in intense laser fields. *J. Chem. Phys. 124*, 144303 (2006).

[161] *K. Nagaya, H. Mineo, K. Mishima, A. A. Villaeys, M. Hayashi, and S. H. Lin*: Theoretical studies on sequential multiple ionizations of benzene and hexafluorobenzene in high-power lasers. *Phys. Rev. A 75*, 013402 (2007).

[162] *K. Nagaya, H. Lu, H. Mineo, K. Mishima, and M. Hayashi*: Theoretical studies on tunneling ionizations from the doubly degenerate highest occupied molecular orbitals of benzene in intense laser fields. *J. Chem. Phys. 126*, 024304 (2007).

[163] *H. Mineo, S. Chao, K. Nagaya, K. Mishima, M. Hayashi, and S. Lin*: Rigorous contour integral analysis of generalized Keldysh theory of strong laser photoionization. *Chem. Phys. Lett. 439*, 224 (2007).

[164] *C. Figueira de Morisson Faria, D. B. Milošević, and G. G. Paulus*: Phase-dependent effects in bichromatic high-order harmonic generation. *Phys. Rev. A 61*, 063415 (2000).

[165] *H. R. Reiss and V. P. Krainov*: Generalized Bessel functions in tunnelling ionization. *J. Phys. A 36*, 5575 (2003).

[166] *J. Bauer*: Comment on 'Generalized Bessel functions in tunnelling ionization'. *J. Phys. A 38*, 521 (2005).

[167] *H. R. Reiss and V. P. Krainov*: Further 'Comment on 'Generalized Bessel functions in tunnelling ionization''. *J. Phys. A 38*, 527 (2005).

[168] *A. Becker, L. Plaja, P. Moreno, M. Nurhuda, and F. H. M. Faisal*: Total ionization rates and ion yields of atoms at nonperturbative laser intensities. *Phys. Rev. A 64*, 023408 (2001).

[169] *V. I. Usachenko and S. Chu*: Strong field ionization of laser-irradiated light homonuclear diatomic molecules: A generalized strong-field approximation-linear combination of atomic orbitals model. *Phys. Rev. A 71*, 063410 (2005).

[170] *F. Grasbon, G. G. Paulus, S. L. Chin, H. Walther, J. Muth-Böhm, A. Becker, and F. H. M. Faisal*: Signatures of symmetry-induced quantum-interference effects observed in above-threshold-ionization spectra of molecules. *Phys. Rev. A 63*, 041402(R) (2001).

[171] *M. G. Floquet*: Équations différentielles linéires a coefficients périodiques. *Ann. de l'École Normale Supérieure 12*, 47 (1883).

[172] *R. M. Potvliege and R. Shakeshaft*: Nonperturbative treatment of multiphoton ionization within the Floquet framework, in *Atoms in Intense Laser Fields*, edited by *M. Gavrila*, p. 373 (Academic Press, 1992).

[173] *P. G. Burke, P. Francken, and C. J. Joachain*: R-matrix-Floquet theory of multiphoton processes. *J. Phys. B 24*, 761 (1991).

[174] *S. Geltman*: Ionization of a model atom by a pulse of coherent radiation. *J. Phys. B 10*, 831 (1980).

[175] *K. C. Kulander*: Multiphoton ionization of hydrogen: A time-dependent theory. *Phys. Rev. A 35*, 445 (1987).

[176] *K. J. LaGattuta*: Laser effects in photoionization. II. Numerical solution of coupled equations for atomic hydrogen. *Phys. Rev. A 41*, 5110 (1990).

[177] *L. Roso-Franco, A. Sanpera, M. L. Pons, and L. Plaja*: Photoionization of the hydrogen atom: Three-dimensional results and pseudo-one-dimensional model. *Phys. Rev. A 44*, 4652 (1991).

[178] *E. Cormier and P. Lambropoulos*: Above-threshold ionization spectrum of hydrogen using B-spline functions. *J. Phys. B 30*, 77 (1997).

[179] *X. Tang, H. Rudolph, and P. Lambropoulos*: Nonperturbative approach to atomic multiphoton processes under intense, short laser pulses. *Phys. Rev. Lett. 65*, 3269 (1990).

[180] *L. A. Collins and A. L. Merts*: Solutions to the time-dependent three-dimensional Schrödinger equation: Atoms in intense electric fields. *Phys. Rev. A 40*, 4127 (1989).

[181] *R. M. Potvliege*: STRFLO: a program for time-independent calculations of multiphoton processes in one-electron atomic systems. I. Quasienergy spectra and angular distributions. *Comp. Phys. Comm. 114*, 42 (1998).

[182] *R. R. Freeman, P. H. Bucksbaum, H. Milchberg, S. Darack, D. Schumacher, and M. E. Geusic*: Above-threshold ionization with subpicosecond laser pulses. *Phys. Rev. Lett. 59*, 1092 (1987).

[183] *R. Wiehle, B. Witzel, H. Helm, and E. Cormier*: Dynamics of strong-field above-threshold ionization of argon: Comparison between experiment and theory. *Phys. Rev. A 67*, 063405 (2003).

[184] *J. N. Bardsley, A. Szöke, and M. J. Comella*: Multiphoton ionisation from a short-range potential by short-pulse lasers. *J. Phys. B 21*, 3899 (1988).

[185] *M. Wickenhauser, X. M. Tong, and C. D. Lin*: Laser-induced substructures in above-threshold-ionization spectra from intense few-cycle laser pulses. *Phys. Rev. A 73*, 011401(R) (2006).

[186] *L. A. A. Nikolopoulos and P. Maragakis*: Gradual broadening of successive above-threshold-ionization peaks. *Phys. Rev. A 64*, 053407 (2001).

[187] *G. G. Paulus, W. Becker, W. Nicklich, and H. Walther*: Rescattering effects in above-threshold ionization: a classical model. *J. Phys. B 27*, L703 (1994).

[188] *Z. Chen, A.-T. Le, T. Morishita, and C. D. Lin*: Quantitative rescattering theory for laser-induced high-energy plateau photoelectron spectra. *Phys. Rev. A 79*, 033409 (2009).

[189] *S. V. Popruzhenko, V. D. Mur, V. S. Popov, and D. Bauer*: Multiphoton ionization of atoms and ions by high-intensity X-ray lasers. *JETP 108*, 947 (2009).

[190] *S. V. Popruzhenko, V. D. Mur, V. S. Popov, and D. Bauer*: Strong field ionization rate for arbitrary laser frequencies. *Phys. Rev. Lett. 101*, 193003 (2008).

[191] *S. V. Popruzhenko*: Private communication.

[192] *V. P. Krainov*: Ionization rates and energy and angular distributions at the barrier-suppression ionization of complex atoms and atomic ions. *J. Opt. Soc. Am. B 14*, 425 (1997).

[193] *J. Stark*: Beobachtungen über den Effekt des elektrischen Feldes auf Spektrallinien I. Quereffekt. *Annalen der Physik 43*, 965 (1914).

[194] *A. M. Bonch-Bruevich, N. N. Kostin, V. A. Khodovoi, and V. V. Khromov*: Changes in the atomic absorption spectrum in the field of a light wave. *Sov. Phys. JETP 29*, 82 (1969).

[195] *C. Liu and T. Nakajima*: Anomalous ionization efficiency by few-cycle pulses in the multiphoton ionization regime. *Phys. Rev. A 76*, 023416 (2007).

[196] *M. Haas, U. D. Jentschura, C. H. Keitel, N. Kolachevsky, M. Herrmann, P. Fendel, M. Fischer, T. Udem, R. Holzwarth, T. W. Hänsch, M. O. Scully, and G. S. Agarwal*: Two-photon excitation dynamics in bound two-body Coulomb systems including ac Stark shift and ionization. *Phys. Rev. A 73*, 052501 (2006).

[197] *M. Awasthi, Y. V. Vanne, and A. Saenz*: Non-perturbative solution of the time-dependent Schrödinger equation describing H_2 in intense short laser pulses. *J. Phys. B 38*, 3973 (2005).

[198] *S. Baker, J. S. Robinson, C. A. Haworth, H. Teng, R. A. Smith, C. C. Chirilă, M. Lein, J. W. G. Tisch, and J. P. Marangos*: Probing Proton Dynamics in Molecules on an Attosecond Time Scale. *Science 312*, 424 (2006).

[199] *E. Goll, G. Wunner, and A. Saenz*: Formation of ground-state vibrational wavepackets in intense ultrashort laser pulses. *Phys. Rev. Lett. 97*, 103003 (2006).

[200] *T. Ergler, B. Feuerstein, A. Rudenko, K. Zrost, C. D. Schröter, R. Moshammer, and J. Ullrich*: Quantum-phase resolved mapping of ground-state vibrational D_2 wave packets via selective depletion in intense laser pulses. *Phys. Rev. Lett. 97*, 103004 (2006).

[201] *A. Lühr, Y. V. Vanne, and A. Saenz*: Parameter-free one-center model potential for an effective one-electron description of molecular hydrogen. *Phys. Rev. A 78*, 042510 (2008).

[202] *A. Lühr and A. Saenz*: Antiproton collisions with molecular hydrogen. *Phys. Rev. A 78*, 032708 (2008).

[203] *A. Lühr and A. Saenz*: Stopping power of antiprotons in H, H_2, and He targets. *Phys. Rev. A 79*, 042901 (2009).

[204] *L. A. A. Nikolopoulos, T. K. Kjeldsen, and L. B. Madsen*: Three-dimensional time-dependent hartree-fock approach for arbitrarily oriented molecular hydrogen in strong electromagnetic fields. *Phys. Rev. A 76*, 033402 (2007).

[205] *M. Uhlmann, T. Kunert, and R. Schmidt*: Non-adiabatic quantum molecular dynamics: ionization of many-electron systems. *J. Phys. B 39*, 2989 (2006).

[206] *A. Saenz*: On the influence of vibrational motion on strong-field ionization rates in molecules. *J. Phys. B 33*, 4365 (2000).

List of Figures

List of Tables

Selbständigkeitserklärung

Hiermit erkläre ich, die vorliegende Arbeit selbständig ohne fremde Hilfe verfasst und nur die angegebene Literatur und Hilfsmittel verwendet zu haben.

Ich habe mich anderwärts nicht um einen Doktorgrad beworben und besitze einen entsprechenden Doktorgrad nicht.

Ich erkläre die Kenntnisnahme der dem Verfahren zugrunde liegenden Promotionsordnung der Mathematisch-Naturwissenschaftlichen Fakultät I der Humboldt-Universität zu Berlin.

Berlin, den 07.12.2009 Yulian V. Vanne